APMM 2019

International Conference on Asia Pacific Mining and Metallurgy
Venue : International Conference Hall NCKU, Tainan, Taiwan
Date : 2019/11/17 ~ 2019/11/20
Supported by :
Ministry of Science and Technology
Central Geological Survey, MOEA
Bureau of Mine, MOEA

International Conference on
Asia Pacific Mining and Metallurgy

APMM 2019

Tainan, Taiwan
November 17-20, 2019

International Conference on Asia Pacific Mining and Metallurgy

Tainan, Taiwan, November 17-20, 2019

Organized by:

Department of Resources Engineering, National Cheng Kung University

Department of Materials Science and Engineering, National Cheng Kung University

Institute of Mineral Resources Engineering, National Taipei University of Technology

Chinese Institute of Mining and Metallurgical Engineers

Co-organized by:

Taiwan Ceramic Society

The Society of Power Technology, Japan

Korean Power Metallurgy Institute

Vacuum Society of the Philippines

Slovak Silicate Scientific-Technological Society

Taiwan Association for Coating and Thin Film Technology

Materials Research Society of Taiwan

Sponsored by:

Ministry of Science and Technology

Central Geological Survey, MOEA	China Steel Express Corporation
Bureau of Mine, MOEA	CPC Corporation, Taiwan
China Steel	Calderys Taiwan Co., Ltd.
Dragon Steel	Good Furnace Refractory IND. Co., Ltd.
Kuan-Ho Refractories IND. Corporation	I HSIN MACHINE CO.,LTD.
Mayer Steel Pipe Co.	C.S. Aluminium Co.
Patio Engineering Corp.	Tung Ho Steel

International Committee:

Sanki Kwon	R. Ananthakumar
Jian-Xun Fu	Xinong Xie
Peigang He	

Chairman:

Dr. Jow-Lay Huang

Department of Materials Science and Engineering, National Cheng Kung Uni.

No.1, University Road, Tainan City 701, Taiwan (R.O.C)

Tel: +886-6-2348188

Fax: +886-6-275-4410

Email: JLH888@mail.ncku.edu.tw

Honor Chairman:

Woei-Shyan Lee

Deputy Chairman:

Kuo-Chin Hsu

Executive Secretary:

Bieng-Zih Hsieh

Secretary General:

Yen-Hsun Su

Program Chair:

Yu-Hsu Chang

Local Organizing Committee:

Kuo-Chin Hsu	Bing-Sheng Yu
Yen-Hsun Su	Yu-Hsu Chang
Wu-Cheng Chi	Ting-To Yu
Yung-Chin Ding	Bieng-Zih Hsieh
Jhewn-Kuang Chen	Muh-Jung Lu
Yen-Pei Fu	Yu-Chuan Wu
Ta-Wui Cheng	Ming-Sheng Ko

Secretariat:

Cheng-Yueh Wu   Yi-Ting Cheng   En-Ting Shen

Edited by:

Bing-Sheng Yu and Jow-Lay Huang

General Information

Schedule for APMM 2019

	Sun.	Mon.	Tues.	Wed.
	11/17	11/18	11/19	11/20
a.m.		Program	Program	CIMME
p.m.	Registration	Program	City Tour	Annual
18:00-20:00	Reception		Banquet	Meeting

Conference Venue

The international Conference Hall of National Cheng Kung University.

Floor Plans

1F

Multifunction Room

Registration Lobby

B1

International Conference Hall

3rd Lecture Room

2nd Lecture Room

1st Lecture Room
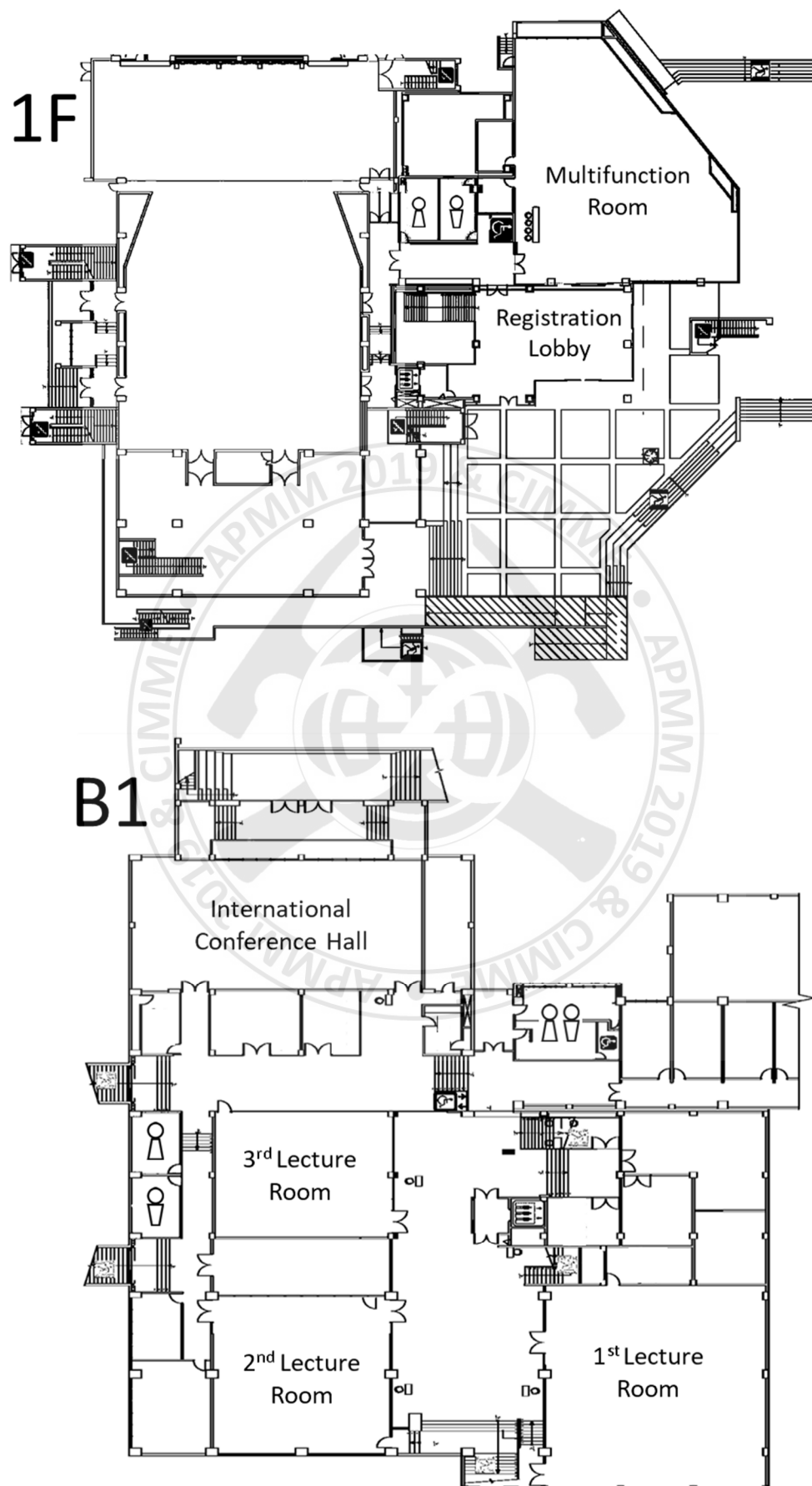
Reception

The reception of APMM 2019 for all participants will be held in the evening of November 17th, 2019, at Multifunction Room next to the international conference hall.

Banquet

Participants are welcome to join the APMM 2019 Banquet held in the evening of November 19th, 2019, at Hotel Tainan. There will be a staff waiting at the international conference hall, the front desk of Zenda Suites and the front desk of Shangri-La's Far Eastern Plaza Hotel, Tainan at 17:45 and guide you to the restaurant.

City Tour

The organizing committee is arranging a half-day city tour for the participants in the afternoon of 19th November to visit some must-go spots in Tainan City. We will visit Anping Old Street, Anping Tree House and Old Tait & Co. Merchant House. The bus will leave at 13:30 from the gate of the campus near the conference venue. Please do register at the information desk, if you are interested in joining the city tour.
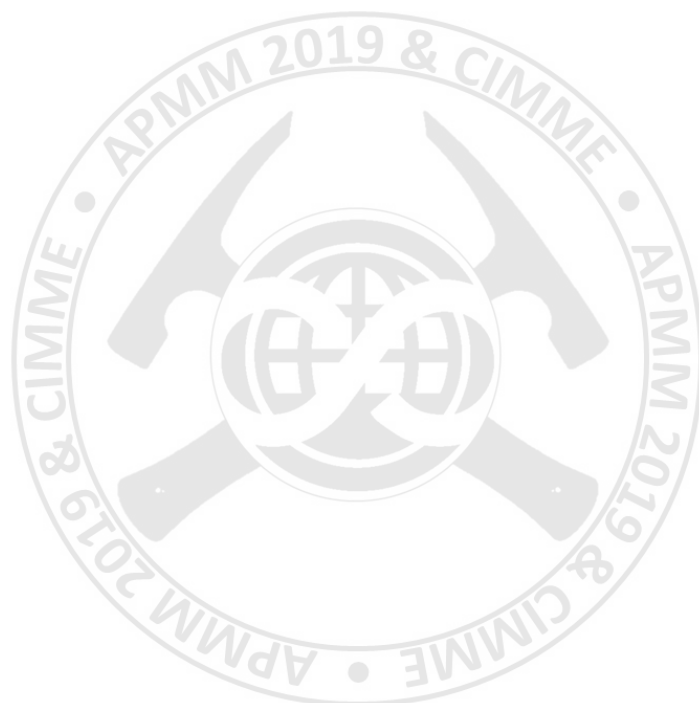
International Conference on Asia Pacific Mining and Metallurgy

APMM 2019
Program

Tainan, Taiwan
November 17-20, 2019

Organized by
Department of Resources Engineering, National Cheng Kung University
Department of Materials Science and Engineering, National Cheng Kung University
Institute of Mineral Resources Engineering, National Taipei University of Technology
Chinese Institute of Mining and Metallurgical Engineers

在看不見的地方,給你最安全的保護

耐震 從選擇ＳＮ鋼材開始

THAS　　　CNS　SN400YB

東和鋼鐵
TUNG HO STEEL

International Conference on Asia Pacific Mining and Metallurgy

Tainan, Taiwan, November 17-20, 2019

November 17, 2019 (Sunday)
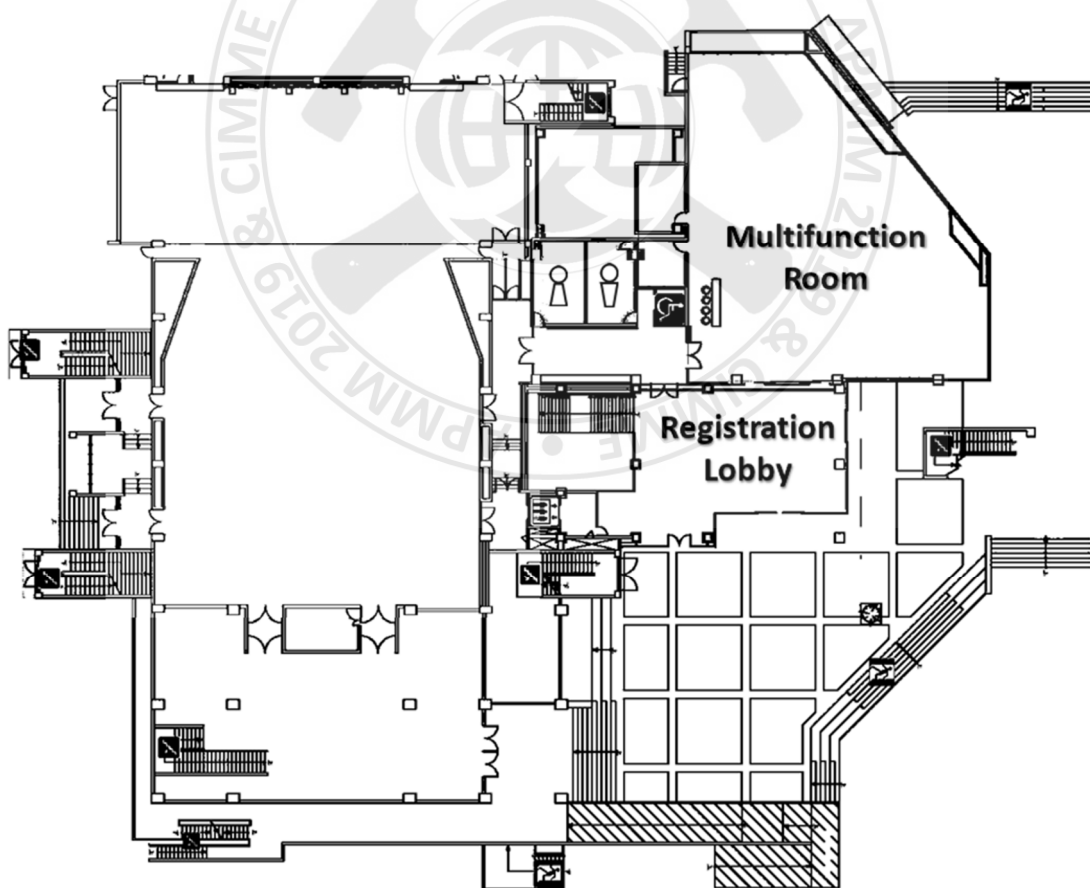
16：00 – 18：00	Registration	**Registration Lobby**
18：00 – 20：00	Reception	**Multifunction Room**

International Conference on Asia Pacific Mining and Metallurgy
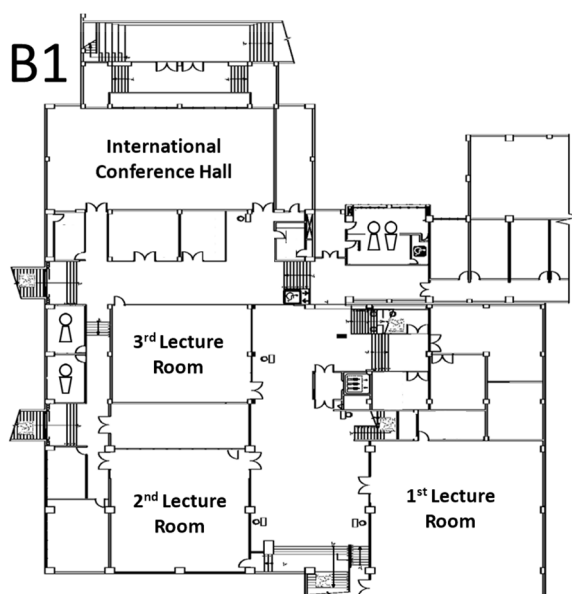## Tainan, Taiwan, November 17-20, 2019

November 18, 2019 (Monday)

08：30 – 09：00	Registration	**Registration Lobby**
09：00 – 09：30	Opening	**1st Lecture Room**
09：30 – 10：10	*Keynote Speech* <u>Syd S. Peng</u> *Automation of Longwall Mining*	**1st Lecture Room**
10：10 – 10：20	Group Photo	**1st Lecture Room**
10：20 – 10：40	Tea Break	**B1 Hallway**
10：40 – 11：20	*Keynote Speech* <u>Shinya Kitamura</u> *Extract of P and Mn from Steelmaking Slag*	**1st Lecture Room**
11：20 – 12：00	*Keynote Speech* <u>Hwan-Tang Tsai</u> *Sustainable Development of Automotive Steels*	**1st Lecture Room**
12：00 – 13：00	Lunch Break	**Multifunction Room**
13：00 – 14：50	Session 1	**Lecture Rooms**
14：50 – 15：10	Tea Break	**B1 Hallway**
15：10 – 17：00	Session 2	**Lecture Rooms**
17：00 – 18：00	Poster	**B1 Hallway**

International Conference on Asia Pacific Mining and Metallurgy
Tainan, Taiwan, November 17-20, 2019

November 19, 2019 (Tuesday)

08：30 – 09：10	***Keynote Speech***	**1st Lecture Room**
Takeshi Tsuji		
	Characterization of Gas-Hydrate and Free-Gas around Japanese Island	

09：10 – 09：50	***Keynote Speech***	**1st Lecture Room**
Jien-Wei Yeh		
	High-Entropy Materials and Their Applications	

09：50 – 10：10	Tea Break	**B1 Hallway**
10：10 – 12：00	Session 3	**Lecture Rooms**
12：00 – 13：00	Lunch Break	**Multifunction Room**
13：00 – 17：00	City Tour	
18：00 – 20：00	Banquet	**Hotel Tainan**

International Conference on Asia Pacific Mining and Metallurgy

Tainan, Taiwan, November 17-20, 2019

<u>**November 20, 2019 (Wednesday)**</u>

| 08：00 – 18：00 | CIMME Annual Meeting | **1st Lecture Room** |

08：00 – 18：00　　CIMME Annual Meeting　　　　**1ˢᵗ Lecture Room**
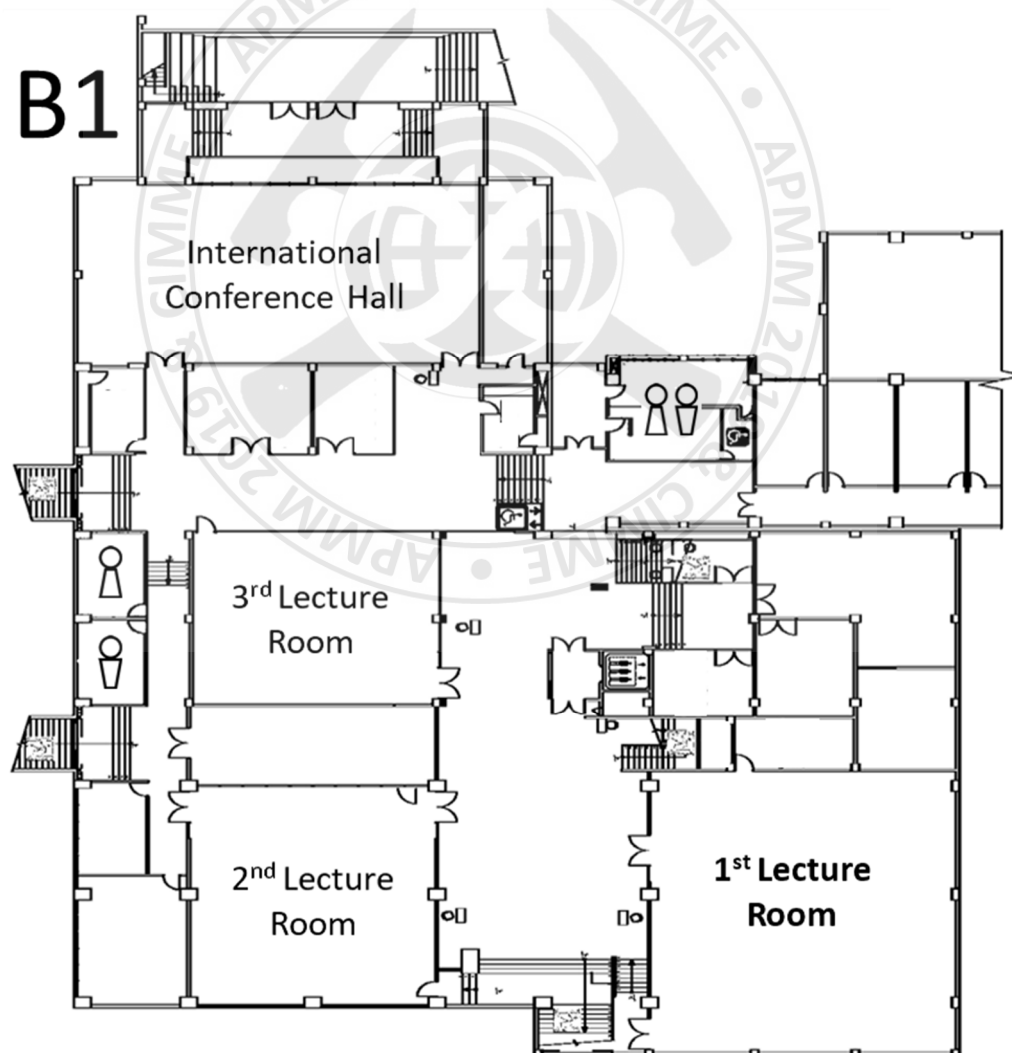
International Conference on
Asia Pacific Mining and Metallurgy

APMM 2019
Keynote Speech

Tainan, Taiwan
November 17-20, 2019

BE STRONG!

讓台灣的孩子
幸福起來

台灣中油 用愛灌溉教育心田
激發下一代無限潛能
探索能源永續新生活

2019堅持勇敢｜台灣中油　為幸福加油

台灣中油股份有限公司
CPC Corporation, Taiwan

Automation of Longwall Mining

Syd S. Peng

Charles E. Lawall Chair in Mining Engineering (emeritus)
Department of Mining Engineering, West Virginia University, WV, USA
Syd.Peng@mail.wvu.edu

ABSTRACT

Since longwall mining consists of three major machines, shearer, AFC, and shields, there are two types of "automation": "automation" for each machine and "automation" for the longwall system (i.e. the three machines are mutually communicated and operate automatically for coal production). Since each machine has its level of automation developed at certain specific time period, the precise level of automation for the whole system at any instant is difficult to specify. Besides, there remains many unknown and unexpected events to be defined for automation for each machine and longwall system before "full automation" is realized. Consequently, it is important to recognize that the word "automation" is qualitative, not quantitative in this book.

Automation of individual shield is to add a pilot valve and an electromagnetic solenoid valve to the hydraulic valve to control all movement steps in a cycle such that with a light touch of a button, the three separate steps of shield advancing cycle is performed automatically in sequence, rather than a push button for each of the cycle steps when only the manual hydraulic valve is available. This is electrohydraulic shield that is much faster and safer than only with the hydraulic valve. The shield control unit (SCU. i.e., PMC-R or RS20s) mounted on every shield is in fact a computer. Since there are many units of shields in a face, those SCUs form an internet, enabling multiple shields, up to the whole face, to operate in sequential order accurately by programmed menu.

Shearer automation is the most difficult part among the three face machines because it has many components doing different interacting tasks that cover and therefore require all aspects of human intelligence: seeing, hearing and feeling.

An automated shearer will cut the coal and stay in-seam cut after cut without the need for human intervention. In order for the shearer to perform those tasks replacing human, it has to have ''seeing, hearing and feeling" ability that human uses to perform the tasks. For the shearer, it means electronic "sensors." Since a shearer has many components that perform different functions, each component needs one or more different types of sensors to accomplish its assigned tasks. For the shearer as a unit, it needs to know its location at the face, and direction and speed of travel (or acceleration and deceleration); for the drums, it needs to know its elevations with respect to the interfaces of roof/coal and floor/coal and shearer's location; for the cowl, it needs to know it is on the head or tail side anywhere at the face. Those features must be able to display in screen all in real time.

Since panline is stationary and attached to, and rely on, shield to move, it does not need to be automated. Automation of AFC thus concentrates on drive motors to ensure smooth running of chain strand and consists of soft start, load sharing, overload protection, and optimum chain speed control as well as chain tension.

The AFC drive system requires static and dynamic power reserves, start-up against high loads and handling of slack chain. In the 1980s, due to smaller chain size and chain strength, sudden overload of

AFC often occurred that caused chain breakage and/or drive motor burnout. So the soft start technology was developed for AFC drives in 1994 to handle heavy-load start up, to guarantee load sharing among the drive motors and avoid slack chain at the head drive frame. It will stop when a sudden overload occurs to relief the pressure and re-clutch quickly. In recent years, the application of variable frequency drive (VFD) will slow down the conveyor speed when encountering overloads.

Automation of longwall machine and system follows the advancement of sensor and communication (or data transmission) technologies and big data analysis. As the sensors are getting more sophisticated and more types of sensors as well as faster communication technology (e.g. 5G) developed and introduced for mining application, the level and reliability of longwall automation will advance further.

The state-of-the-art semi-automated longwall system consists of: electrohydraulic control shields and doubled-ended ranging drum shearer operated in shearer-initiated-shield advance (SISA) mode with the memory cut cutting algorithm for the whole face.

Recent adoption and application of remote control of shearer is the correct approach from miner's health and safety as well as coal production points of view considering the complicated mining and geological conditions where many unexpected events can occur suddenly.

The pre-requisite for longwall automation is very high equipment reliability, i.e., 100% reliable all time if a man-less system is to be achievable.

Various sensors for detecting unexpected underground events as well as their software control algorithm due to complicated mining and geological conditions must be identified, developed and tested successfully in advance before full automation is feasible.

Adoption of automation of longwall system does not guarantee reduction in face crew. The highest level automation of longwall system today requires 4-10 crew members at various mines. Obviously mine/crew practices and mining and geological conditions still dictate the manpower need at the longwall face.

Extract of P and Mn from Steelmaking Slag

SHIN-YA KITAMURA

Institute of Multidisciplinary Research for Advanced Materials
Tohoku University, Japan
shinya.kitamura.e7@tohoku.ac.jp

ABSTRACT

Steelmaking slag contains considerable amount of Mn and P, and in Japan, for resource security, the recycling them is an important issue. Since Mn is an alloy added to enhance the steel quality, while P is a harmful impurity in the steel product, they need to be separated for recycling. For this purpose, two principles are considerable. One is to use the different property of each mineralogical phase in slag, and the other is to use the different thermodynamic property of each element in slag.

In steelmaking slag, P is enriched in the dicalcium silicate phase (C_2S) and form the solid solution with tricalcium phosphate (C_3P). As the solubility of this phase to the aqueous solution is widely different from that of other phases in slag, we have proposed the leaching treatment to separate C_2S-C_3P phase from slag. The dissolution ratio of P from the synthesized slag has reached about 91%. After the separation of residue, pH of the leachate increased to precipitate phosphate. 80% or more of the P in the leachate was precipitated and the phosphate content of the precipitate was about 25% after calcination.

The reduction of steelmaking slag was conducted by many researchers to recover Fe and P. However, by the simple reduction, Mn was also reduced and the product of C saturated iron with high content of Mn and P is hard to reuse. In thermodynamics, MnO is basic oxide but P_2O_5 is acid oxide, and the temperature dependences of the equilibrium constants of their reduction reactions are widely different. We have already found the possibility of separating Mn and P from steelmaking slag by selectively reducing P_2O_5 and FeO while suppressing the reduction of MnO. By the fundamental study, it was found that a decrease in slag basicity suppressed the reduction rate of Mn while enhancing that of P. To analyze this result, the activity coefficients of both Mn and P in the Fe-P-Mn-C(sat.) alloy (2.5–15.2 mass% of P and 2.9–12.8 mass% of Mn), which is obtained by the reduction of steelmaking slag were investigated. A comparison with the results obtained by reduction experiment indicated that the activity coefficients of P and Mn obtained in the study were applicable.

# Sustainable Development of Automotive Steel at ArcelorMittal

Dr. Hwan-Tang Tsai

Principal Scientist Global R & D Center ArcelorMittal USA
H.Tsai@arcelormittal.com

ABSTRACT

Production of motor vehicle in China has grown from 5% of the world production in 2001 to 30% in 2016. ArcelorMittal produced over 17 million tons of steel for the automotive industry worldwide. ArcelorMittal Global R&D with 1,500 full time researchers focused on the innovation of automotive steel development and its applications. Since June 2014, ArcelorMittal has successfully launched a joint venture (Valin ArcelorMittal Automotive Co.) in Hunan, China with a capacity of 1.5 million tons per annual. A clean steel platform has been established which helps to stabilize the production of high-quality automotive steel. The origin of sliver was identified as alumina, spinel and calcium aluminates from the deoxidation and re-oxidation products, mold powder entrainment, argon bubbles and other mechanically induced defects. Systematic analyses of the sliver defects and countermeasures taken at steelmaking and continuous casting have greatly improved the steel surface quality downstream. Sustainable growth of steel industry in the future is built on low carbon, clean air and a circular economy. For the sustainable development of automotive steel, ArcelorMittal has initiated the S-in motion which provided solutions to reduce car weight with hot stamped parts and laser welded blanks at the same cost with better safety. The lightest BiW, hang-on parts and chassis have resulted in a weight reduction of 16% in the C-class vehicle. Saving of 73 kg for the whole vehicle induces a reduction of 6.23-gram CO_2/km during its life cycle.
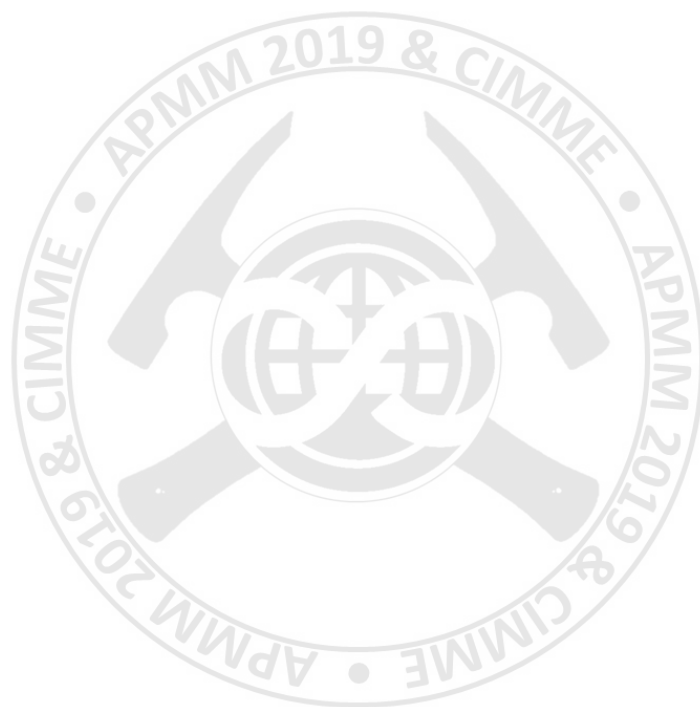
Characterization of Gas-Hydrate and Free-Gas around Japanese Island

Takeshi Tsuji

Department of Earth Resources Engineering, Kyushu University
tsuji@mine.kyushu-u.ac.jp

ABSTRACT

Gas Hydrate is crystalline solids like ice bonding both water and gas molecules. In gas hydrate, mainly methane is trapped within water molecules forming as a rigid lattice cages. They occur in the permafrost region and deep water sediments where are high pressure and low temperature condition (Kvenvolden, 1993; Sloan and Koh, 2007). Significant amount of hydrocarbon clogged in the hydrate phase represents the unconventional and potential energy resources (Milkov, 2004). One cubic foot of gas hydrate approximately yields 163 cubic feet of gas (Hardage and Roberts, 2006). The gas hydrates contribute to global climate change and potential drilling hazards (Ruppel and Kessler, 2017). Furthermore, the destabilized gas hydrate seepage in marine sediments could cause geologic hazards such as submarine slumps and induced earthquakes (Xu and Germanovich, 2006). Therefore, characterization of hydrocarbon reservoirs is also crucial to predict future climate change and geohazards. Here we show methane hydrate and free gas distribution in the Nankai Trough.

Gas hydrates are widely distributed in the Kumano forearc basin, which is located above accretionary prism in the Nankai margin off the Kii peninsula, Japan. Bottom-Simulating Reflector (BSR) at the base of gas hydrate stability zone has been imaged as a strong acoustic impedance contrast on the reflection seismic profiles. In order to better define the accumulations of gas hydrates and free gases, we performed a high-resolution seismic velocity analysis to 3D seismic data using a method of conventional semblance spectra via automatic velocity picking algorithm. The results revealed that gas hydrate-bearing sediments above the BSR and free gas-bearing sediments below the BSR are characterized by P-wave velocities of 1900-2500 m/s and 1000-1800 m/s, respectively. Then, the velocity model was converted into gas hydrate and free gas saturation using rock physics approaches. The results indicated that saturation of gas hydrates ranges from 0% to 45% in the pore space, and highly concentrated around the outer ridge where faults are densely developed. Additionally, concentrations of free gas ranging from 0% to 20% in the pore space are widely distributed below BSRs and are considerably high above ridge structure generated by displacement of large fault splayed from the deep plate boundary décollement. Based on these results, we suggest that the gas hydrates concentrated due to the free gas influx which migrated upward through the steeply dipping strata and faults (or fractures) cutting through the basin. The accumulations of gas and/or hydrates are further controlled by fault movements in the accretionary prism beneath the forearc basin. Therefore, these factors generated by intensive tectonic movements in the plate subduction zone control the distribution and saturation pattern of gas hydrate and free gas formations.

High-Entropy Materials and their applications

Jien-Wei Yeh

High Entropy Materials Center,
Department of Materials Science and Engineering, National Tsing Hua University, Taiwan
jwyeh@mx.nthu.edu.tw

ABSTRACT

"High-Entropy Materials (HEMs)" has become an emerging field since the high-entropy alloys (HEAs) concept was disclosed in 2004. Total number of journal papers on HEMs has exceeded 3000 from 2004 to the end of 2018. The HEAs are featured with high entropy effect by which their high mixing entropy can enhance the formation of solution-type phases and avoid the formation of many complex and brittle intermetallic compounds. This simplification of constituent phases renders HEAs feasible to be synthesized, studied, and used. Another three core effects, i.e., severe lattice distortion, sluggish diffusion and cocktail, accompanying high entropy effect have significant influences on kinetics, microstructure and properties of HEAs. Thus, HEAs have a wide range of microstructure and properties. In 2005, the concept of HEAs was first extended to HEMs by the publication of research on high-entropy nitrides which was formed by reactive magnetron sputtering. Afterwards, high-entropy ceramics and composites were designed and researched based on HEAs concept and core effects. It has been widely accepted that a HEM with suitable composition design as well as suitable process design will exhibit superior properties in mechanical, physical, chemical or functional aspect and thus have advanced applications. In this talk, several possible breakthrough applications are pointed out and emphasized. They include materials for turbine engines, molds and dies, cutting tools, hard coatings, hardfacings, and radiation damage resistant parts, etc.
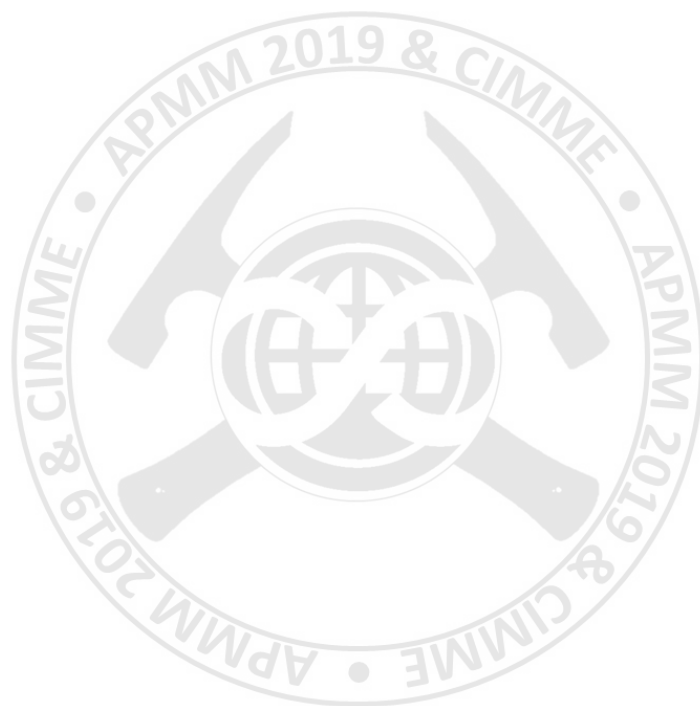
International Conference on Asia Pacific Mining and Metallurgy

APMM 2019
Abstract Volume

Tainan, Taiwan
November 17-20, 2019

International Conference on Asia Pacific Mining and Metallurgy
Tainan, Taiwan, November 17-20, 2019

Section 1：Metallurgical Engineering

13：00 – 14：50　　　1st Lecture Room

13:00-14:50	Session Chair:	Prof. **Jhewn-Kuang Chen** National Taipei University of Technology
13:00-13:30	CIMME108186	**Dr. Eungsoo Choi** POSTCO, Korea *The New Trend in Ironmaking Technology*
13:30-13:50	CIMME108015	**Tsung-Yen Huang** China Steel Corporation, Taiwan *Characteristic of Iron Ore-Coal Composite during Reduction* *under a Similar Heating and Gas Composition Condition of Blast Furnace*
13:50-14:10	CIMME108027	**Chao-Han Wu** China Steel Corporation, Taiwan *Zinc Control on Blast Furnace Raw Materials*
14:10-14:30	CIMME108005	**Yao-Feng Chang** China Steel Corporation, Taiwan *Investigation of Slag Reducing Operation in BOF Steelmaking*

The New Trend in Ironmaking Technology

Eungsoo Choi
Ironmaking Research Group, POSCO, Pohang, Korea
papageno@posco.com

ABSTRACT

The face of the research in the ironmaking field has dramatically changed during the last decade. The competitive steel market has demanded the severe cost reduction and tight government regulations on the environment has restricted activities of the steel mill. As a result, the technologies based on the artificial intelligence and cost-value evaluation have been intensively developed in POSCO and the trend is expected to keep moving forward in the future.

Characteristic of Iron Ore-Coal Composite during Reduction under a Similar Heating and Gas Composition Condition of Blast Furnace

Tsung-Yen Huang,[1]* Daisuke Maruoka,[2] Taichi Murakami[2] and Eiki Kasai[2]

1) *Iron & Steel Research and Development Department, China Steel Corporation, No. 1, Chung Kang Rd., Hsiao Kang, Kaohsiung 81233, Taiwan. *Corresponding author:* 172833@mail.csc.com.tw*

2) *Graduate School of Environmental Studies, Tohoku University, 6-6-02, Aramaki-Aza Aoba, Aoba-ku, Sendai, 980-8579 Japan.*

ABSTRACT

For sustainable development and environmental protection, decreasing CO_2 emission and energy consumption are always indispensable task. Using iron ore-coal composite as the raw material of BF is a promising way to mitigate the above issues.

In this study, we conducted an experiment procedure to simulate the reduction of an iron ore-coal composite travelling from the top zone to the cohesive zone of BF. Reduction behavior, morphology changes and carburization characteristic of the composites with the variables of C/O (Carbon to Oxygen) ratio were investigated.

As C/O ratio was increased from 0 to 0.6, the reduction rate of composite was accordingly enhanced. It was found that the composite was swelling severely when C/O ratio was lower than 0.4. The swelling occurred in the temperature range from 800ºC to 1100ºC which was just under the stage of reduction from Wustite to iron. The composite was shattering obviously starting from 1160ºC when C/O ratio was higher than 0.4. It is because the remained free carbon is surplus in reduced iron, causing shattering and powdering. Hence, C/O = 0.4 was suggested to the composite for being charged into BF.

INTRODUCTION

Blast Furnace (BF) is the most important reactor among the global steel industry. The usage amount of reducing agent in BF is based on carbon which is concerned not only energy consumption but also CO_2 emission. According to RIST diagram and Fe-C-O diagram, it is possible to improve a further step of CO gas utilization efficiency by lowing the temperature at thermal reserve zone (TRZ) of BF [1]. Using iron ore-carbon composite as raw material of BF is expected to lower the TRZ temperature [2]. Iron ore-carbon composite is recognized as a micro-reactor for conducting the reduction of iron oxide because the distance between iron oxide and carbonaceous material is in the range of micrometer [3]. Laboratory scale experiment on iron ore-carbon composite had presented the starting temperature of endothermic reaction, which is nearly the same with the TRZ temperature in BF, was lowered [4] and the gasification reaction, which is recognized as solution loss reaction, was improved.

In this study we conducted an experiment procedure which was to simulate the reduction of an iron ore-coal composite passing from the top zone of BF to approaching the cohesive zone of BF. Meanwhile, the off gas composition was analyzed to calculate gas generation, gas consumption and furthermore the reduction degree of composite. The shape of composite was recorded simultaneously

by camera during the reduction to identify the changes of morphology. Finally, the microstructure and carbon content in the reduced iron and in metallic iron were inspected.

EXPERIMENTAL METHOD

Raw materials used in this study are iron ore concentrate and regular sinter made by China Steel Corporation. Iron ore concentrate here is usually called as pellet feed fines. The reductant was Pulverized Coal (PC) which was usually injected together with hot air in tuyer of blast furnace. Iron ore and PC powders were well mixed and was press-shaped into a tablet. The study on reduction behavior of iron ore-coal composite was conducted by a vertical infrared image furnace equipped with a gas chromatography (GC) which can continuously measure the concertation of gases in the outlet gas. The sample was heated by a heating profile with its gas concentration profile which was considered to simulate the condition of an iron-bearing material passing from the top zone of BF to near the cohesive zone of BF. On the other hand, we carried out the direct observation experiment on morphology changes by a horizontal electric resistance furnace. Three benchmark experiments were carried out using sinter as raw material, the tablet of iron ore concentrate, and iron ore-coal composite reduced under 50%N_2/Ar atmosphere. The main independent variables were C/O ratio shown in **Table 2**.

Table 1. Sample preparation and experimental conditions.

| Group name	Sample name	Ore	C/O	Basicity
Benchmark experiment	B1	Sinter	-	1.90
	B2	Concentrate	0.0	0.04
	B3*	Concentrate	0.4	0.04
Effect of C/O ratio	C1(B2)	Concentrate	0.0	0.04
	C2	Concentrate	0.2	0.04
	C3	Concentrate	0.4	0.04
	C4	Concentrate	0.6	0.04
	C5	Concentrate	0.8	0.04

B3* experiment was under 50%N_2/Ar atmosphere.

RESULTS AND DISCUSSION

Benchmark experiments of sinter particle (B1) and iron ore concentrate tablet (B2) were carried out. Here, concentrate tablet was without adding carbonaceous material and binder. **Figure 1** is the changes in reduction degree and the ratio of $CO/(CO+CO_2)$ with temperature on the phase diagram of Fe-C-O system from the experiment of sinter (B1) and concentrate tablet (B2). The reduction rate of B2 sample is significantly higher than that of B1. Noted that the curve of $CO/(CO+CO_2)$ ratio of B2 exists a peak at 450°C and passes through the equilibrium curve of FeO-Fe at 850°C. At the temperature of 450°C and 850°C, the reduction degree is about 12 and 32%, which are identified as the beginning point of reduction of magnetite and wustite, respectively. In contrast, B1 sample needs higher temperature and higher $CO/(CO+CO_2)$ ratio to achieve the same reduction degree with B2.

Figure 2 shows the changes in the CO_2 gas generation and CO gas consumption from C/O = 0 to 0.6 of composite with temperature. B3 experiment was reacted under a constant of 50%N_2/Ar atmosphere for reference. The positive and negative value of gas generation means that the gas is generated and is consumed on the basis of introduced gas, respectively. Three peaks of C1-C4 samples at 450-550, 780, and 1000°C are recognized as the reduction stage of hematite, magnetite and wustite, respectively. In

contrast, CO_2 peaks of B3 sample appears at 700, 980, and 1100°C, which means that reaction under inert gas has relatively higher reduction temperature of each stage. Further, when increasing the C/O ratio, the amount of CO consumption and CO_2 generation at high temperature range decreases. Moreover, high C/O ratio condition is able to lower the temperature at end point of gas generation and consumption indicated by arrow which is also recognized as the end of reduction. For example, the reduction of the C/O = 0.6 sample is completed at 1100°C, because there are nearly no CO consumption and therefore no CO_2 generation.
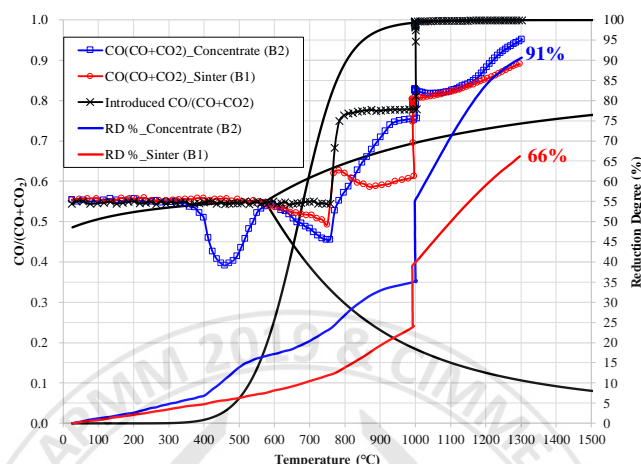

Fig. 1. Changes in reduction degree and the ratio of $CO/(CO+CO_2)$ with temperature on the phase diagram of Fe-C-O system.

When the composites were under reduction, the shape were recorded to compare the morphology changes with temperature. **Figure 2** reveals the shape pictures of composite at the reduction temperature of 1200°C and 1300°C. Comparing samples with the same C/O ratio of B3 and C3, where their difference was reacted under 50%N_2/Ar and 50%N_2/CO/CO_2 atmosphere, the projected area of B3 was significantly smaller than that of C3. Therefore, it is sure that the CO and CO_2 atmosphere affected the morphology changes of composite. Among the images of C/O=0 (C1), 0.2 (C2) and 0.4 (C3), the projected area of C3 was the smallest one; that of C1 was the largest one; that of C2 was under shrinkage from the top part of tablet. On the other hand, as the C/O ratio was higher than 0.4, the top portion of tablet turned into fluffy in the sample of C4 and C5 shown in **Fig. 2 e) and g)** at 1200°C. Furthermore, when the temperature was increased, the fluffy structure shattered into powder and dropped down. **Figure 2 f) and h)** showed the tablet collapsing into powder at 1300°C especially in the sample of C/O=0.8 (C5).

In addition to the microstructure observation, the carbon concentration in as-reduced sample and in metallic iron were measured, individually, shown in **Fig. 3**. Moreover, when the total carbon is subtracted the dissolved carbon, the value stands for free carbon over the reduced iron. All of the as-reduced irons contained residual carbon, implying that the addition amount of coal in green composite was surplus for reduction under simulating the atmosphere of BF. It is comprehensible that when increasing the C/O ratio, the remained carbon in reduced iron are also increased. Further, carburization indeed occurred because the carbon existed in the metallic iron. The total remained carbon of 7.4% and 13.9% in mass in the reduced iron of C/O=0.6 and 0.8, respectively, are suggested that the carbon addition was too much in both green composites. Especially, there are still 5.3 mass % and 10.5 mass % free carbon in reduced sample. It can imagine that free carbon occupied a lot of space in reduced sample because the density of carbon is much lower than that of iron. Reference reported that carbon remained in reduced iron is benefit to the carburization [5]. However, too much free carbon existed in reduced iron was likely to segregate the metallic iron particles each other rather

than contacting together.
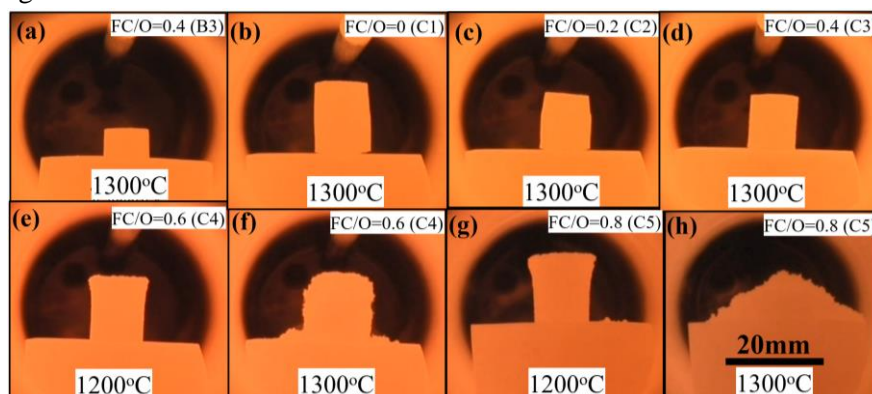
Fig. 2. Shape pictures of composite at the reduction temperature of 1200°C and 1300°C. a) C/O=0.4 (B3) under 50%N$_2$/Ar reaction; b-h) C/O=0, 0.2, 0.4, 0.6 and 0.8 respectively reacted under 50%N$_2$/CO/CO$_2$ atmosphere.
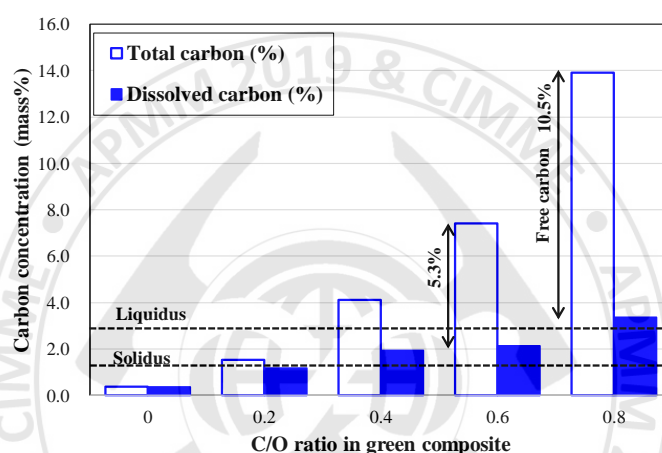
Fig. 3. Comparison of carbon concentration of reduced iron in the variable of C/O ratio. Total carbon and dissolved carbon stand for the carbon concentration in as-reduced sample and in the metallic iron, respectively. Free carbon is the difference between total carbon and dissolved carbon. The liquidus point and solidus point at 1300°C of Fe-C phase are drawn for reference.

CONCLUSIONS

C/O = 0.4 was suggested to a suitable ratio, because when C/O ratio was lower than 0.4, the sample volume was swelling severe, while when C/O ratio was higher than 0.4, the sample became shattering starting from 1160°C. Swelling of iron ore-coal composite occurred during the temperature range of 800°C to 1100°C which was under the stage of reduction from wustite to iron.

REFERENCES

[1] T. Ariyama, R. Murai, J. Ishii and M. Sato: ISIJ Int., 45(2005), 1371.
[2] A. Kasai, H. Toyota, K. Nozawa and S. Kitayama: ISIJ Int., 51(2011), 1333.
[3] S. Ueda, K. Yanagiya, K. Watanabe, T. Murakami, T. Inoue and T. Ariyama: ISIJ Int., 49(2009), 827.
[4] A. Kasai and Y. Matsui: *ISIJ Int.*, 44(2004), 2073.
[5] T. Murakami and K. Nagata: *Miner. Process. Extr. Metall. Rev.*, 24(2003), 253.

Zinc Control on Blast Furnace Raw Materials

Chao-Han Wu

*Ironmaking Department, China Steel Corporation, Taiwan*
w2s4@ mail.csc.com.tw

ABSTRACT

During the 143-day revamping of one blast furnace at China Steel Corporation (CSC), another one shouldered the burden of disposal of double residuals. This process made the zinc load of the latter exceed the control limit for a long time, resulting in a series of abnormal furnace conditions and repeated shutdowns, which caused considerable production losses. In addition to restoring normal production of the blast furnace as soon as possible, the ironmaking department also took advantage of this opportunity to construct a complete zinc circulation process and control mechanism. For integrated steel plants, it is inevitable for an increasing amount of residuals and waste to be disposed of internally. CSC demonstrated good practice of controlling the zinc content in blast furnace (BF) raw materials in this incident.

INTRODUCTION

Zinc is a harmful element for BF. It exists in iron ore mostly in the forms of zincite (ZnO) and sphalerite (ZnS) and also in sinter in the form of ferrites. With a low melting point (420°C) and boiling point (907°C), zinc is easy to circulate and concentrate continuously in BF, thereby affecting the operation and furnace campaign of the BF. The hazards of zinc are described below.

Zinc-containing compounds rapidly decompose into zinc oxide after entering BF. Endothermic reactions, such as reduction and gasification, occur at the lower part of the furnace. Then, as the furnace gas rises, the reaction products move to the upper part of the furnace, where exothermic reactions, such as oxidation and condensation, occur. This process moves the furnace heat from the furnace bosh to the shaft and consumes CO from the lower part of the furnace. It not only causes fuel loss and an increase in the slag viscosity, but also hinders hot metal desulfurization and furnace ventilation as shown in the work by Esezobor *et al.* (2006) and Jiao *et al.* (2017). The reaction formulas of zinc in the furnace are as follows.

$$\text{At the upper part of the furnace} \quad Zn(g)+CO_2 \; \rightarrow \; ZnO(s)+CO$$
$$\text{At the lower part of the furnace} \quad ZnO(s)+CO \; \rightarrow \; Zn(g)+CO_2$$
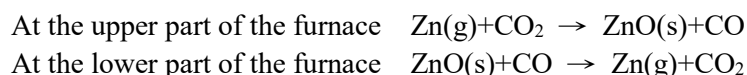
Because the furnace lining comprises mostly porous refractory materials, zinc vapor is easy to penetrate and condense inside the lining. As zinc accumulates, the volume of the lining increases, resulting in an internal stress increase and, eventually, damage of the lining as shown in the work by Zhang *et al.* (2011). Consequently, the furnace campaign is jeopardized. Zinc vapor may also condense on the lining surface, further accumulate, and agglomerate as shown in the work by Trinkel *et al.* (2017), which impedes the burden descending and gas rising. If the scaffold or accretion falls off, it may cause hearth chilling and deterioration of the liquid permeability of the furnace core. In serious

cases, the tuyeres are even smashed or distorted, and the furnace is shut down urgently, resulting in production losses in steel plants.

BACKGROUND

In recent years, because of rising environmental awareness, the difficulty in the disposal of residuals and waste in plants is increasing with each passing day. As an integrated steel plant, CSC has been committed to recycling resources for a long time, which not only reduces the total amount of waste to be disposed of, but also lowers the cost. Taking the ironmaking department as an example, the iron-containing BF and basic oxygen furnace (BOF) dust and sludge are smelted into sinter and pellet by sintering, cold-bonded granulation, and the rotary hearth furnace (RHF), and are then charged into the BF with other ironmaking raw materials.

Although both environmental protection and cost reduction can be achieved by processing furnace dust and sludge and charge them into BF again, as mentioned above, there is a risk that harmful elements will accumulate continuously in BF. Alkali metals can be removed from the BF by adjusting the slag basicity. Zinc with a low boiling point continuously circulates, corroding the furnace lining or agglomerating inside BF; only part of the zinc is discharged in the form of BF dust. During the revamping of one blast furnace, the residuals to be disposed of by the furnace were taken over by another one. Eventually, the furnace conditions of the latter deteriorated rapidly from early February 2018, and slipping and channeling occurred frequently. By mid-March, there were seven temporary shutdowns caused by breaking and distortion of tuyeres because of the falling accretion, resulting in considerable production losses.

METHODS AND RESULTS

A cross-department task force was set up immediately after the accident in the ironmaking department to figure out the causes of the accident and measures to prevent its recurrence. It was first presumed that zinc was the most likely responsible for the abnormal furnace conditions. There were four reasons. (1) The alkali metal load of all the blast furnaces in CSC have never exceeded the control limit for a long time. (2) The suffered blast furnace maintained a high sinter ratio of 72%–74% for a long time. (3) Blast furnaces in CSC needed to dispose of the cold-bonded pellet (CBP) and direct reduced iron (DRI) generated from processed residuals. DRI is the product of RHF dezincification, and only its zinc content was still as high as 0.3%. (4) During the revamping of one blast furnace, the amount of CBP and DRI disposed of by another one doubled, resulting in a zinc load of 0.253–0.272 kg/THM, which exceeded the control limit of 0.20 kg/THM for several months.

To confirm the above hypothesis further, the task force first needed to construct a complete zinc circulation process in the ironmaking department. Figure 1 is the result of the investigation. The flow chart shows that the main sources of residuals added to BF are dust and sludge from itself and BOF. The task force immediately arranged for periodic sampling and analysis of the above-mentioned residuals to clarify the main source of zinc and then removed it from the production process and found alternative disposal methods. In addition, optimizing RHF operation and increasing the removal rate of zinc can further reduce the zinc load of BF.
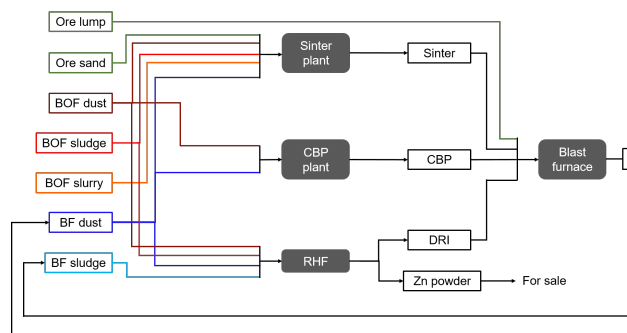
Figure 1. Zinc circulation flow chart in the ironmaking department

Through sampling analysis and comparison, the highest zinc content was found in BOF dust among all residuals. The reason is that raw materials for BOF include zinc-containing scrap steel. The task force immediately requested that charging zinc-containing scrap steel into BOF be stopped and asked the sales department to open up external sales channels for it as soon as possible. Figure 2 is the analysis result of BOF dust sampling and shows that its zinc content decreased significantly after stopping charging of zinc-containing scrap steel. The zinc content of 1–3 BOF dust decreased by 71% after control, which demonstrates a remarkable effect.
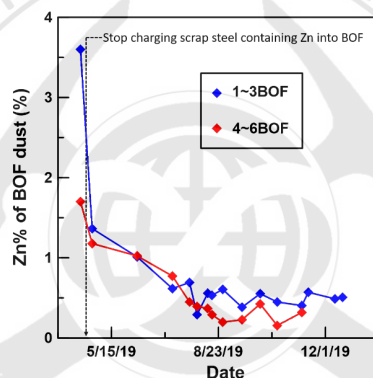
Figure 2. Trend chart of zinc content in BOF dust

Figure 3 is the analysis result of zinc content in sinter. It shows that the zinc content of sinter at different plants decreases gradually when the addition of zinc-containing scrap steel in BOF is stopped, and the decreasing trend is not as obvious as that for BOF dust and has occasional fluctuation. The reason is that, in addition to iron ore, the raw materials of the sinter plant also include residuals, such as dust, sludge and slurry, which are influenced by various factors.
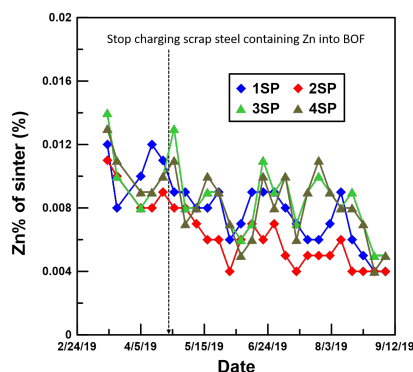

Figure 3. Trend chart of zinc content in sinter

Figure 4 is the trend chart of the RHF operation rate. It shows that the removal rate of zinc has been steadily improved by continuously adjusting and optimizing various operating conditions and remained stable at more than 85% of the control limit. In addition to increasing the profit of external sales of zinc powder, the most important thing was to reduce effectively the zinc content of DRI and the zinc load of the BF.
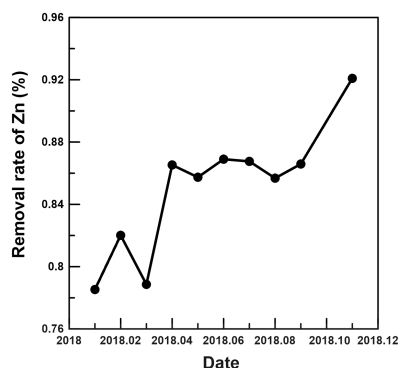

Figure 4. Trend chart of RHF operation rate

CONCLUSIONS

At the beginning of 2018, a series of abnormal furnace conditions and shutdowns occurred in the suffered blast furnace caused by excessive zinc load, resulting in considerable production losses. Fortunately, with rapid response, the task force effectively coordinated with relevant departments to clarify the causes and took measures to reduce the zinc load of the BF and stabilize operation. This is not as simple a process as it may seem. It involves additional periodic sampling and testing of furnace dust with limited manpower, redesigning of the throughput of furnace dust and scrap steel in the storage area with limited hinterland, and selling of valuable scrap steel to reduce inventory pressure. In addition, the operation conditions need to be optimized to improve the zinc removal rate of RHF. The cooperation of all relevant departments is necessary to complete the above work. Considering the factors of environmental protection, it is inevitable that, for the steel plants, the difficulty of disposal of waste and residuals by taking them outside of the plants will increase gradually. In other words, it is an inevitable trend to increase the in-plant recycling of residuals. How to control harmful elements and avoid their enrichment in the BF is a subject that must be continuously refined for integrated steel plants.

REFERENCES

Esezobor, D. E, and Balogum, S. A. (2006). "Zinc accumulation during recycling of iron oxide wastes in the blast furnace," Ironmaking and Steelmaking 3(5): 419-425.

Jiao, K. X., Zhang, J. L., Liu, Z. J., Chen, C. L., and Liu, F. (2017). "Circulation and accumulation of harmful elements in blast furnace and their impact on the fuel consumption," Ironmaking and Steelmaking 44(5): 344-350.

Zhang, F., An, S., Luo, G., and Zhang, S. (2011). "Behavior of zinc and lead in blast furnace of Baotao iron and steel group co.," Advanced Materials Research 194-196: 306-309.

Trinkel, V., Aschenbrenner, P., Thaler,C., Rechberger, H., Mallow, O., and Fellner, J. (2017). "Distribution of Zn, Pb, K, and Cl in the blast furnace lining," Steel Research International 88(1): 1-7(1600153).

Investigation of slag reducing operation in BOF steelmaking

Yao-Feng Chang, Shui-Sheng Hung
Department of steelmaking, China steel corporation, Taiwan
184713@mail.csc.com.tw, 143438@mail.csc.com.tw

Ku-Ling Chang, Chen-Chi Hou
Technology division, China steel corporation, Taiwan
150334@mail.csc.com.tw, 149914@*mail.csc.com.tw*

ABSTRACT

Industrial tests were carried out the double-slag process in a 150-metric ton converter at the CSC Steel Corporation to effect on the reduction of lime consumption and the BOF slag volume simultaneously. A low oxygen lance height was operated in the dephosphorization period for the double-slag process to disrupt the slag/steel interface and promote the dephosphorization reaction in temperature 1665 ± 10K. For the endpoint of the dephosphorization period, the desiliconization ratio (η_{Si}) and decarburization ratio (η_c) were $90\pm5\%$ and $30\pm5\%$, respectively, and the dephosphorization ratio (η_P) was concentrated in 45%. The phosphorus distribution ratio (L_p) of the double-slag process with relative low basicity is superior to the conventional single-slag process. After adopting the double-slag process, lime consumption is reduced by an average of 14 kg per metric ton steel and the BOF slag volume was decreased by 9.4 kg per metric ton of steel.

KEYWORDS: BOF, The double-slag, Dephosphorization

INTRODUCTION

In Taiwan, BOF slag cannot be buried or reclaimed, and only a small amount of slag can be used for road construction. Therefore, decreasing the generation of BOF slag is the most important issue for steelmaking plant. Less-slag steelmaking process refers to a kind of steel-making technology that reduces the total amount of slag during steelmaking. In less-slag steelmaking process, the main purpose of adding slag-forming agent is aiming to protect the furnace brick and cover the molten steel to reduce the loss of molten steel. In this case, it is no longer to operate with high basicity to maintain the efficiency of dephosphorization at high temperatures. Therefore, the prerequisite for less-slag steelmaking process is that the molten iron must be dephosphorized. At present, there are three kinds of major pretreatment processes in steelmaking plant. One is that molten iron is first added to the converter after desulfurization, dephosphorization and desulfurization treatment; the second is smelting by duplex melting process; the third is the double-slag process. The first two types of pretreatment process need to have sufficient space and the large-scale equipment transformation. The double-slag process does not need to add additional equipment investment, and make production scheduling more flexible.

Double-slag process principle

The characteristic of the double-slag process is that carried out the dephosphorization and the decarburization continuously in the same converter. The dephosphorization reaction operated in low temperature during the early stages of the double-slag process, which is a conducive thermodynamic condition for dephosphorization, and then discharging the slag after dephosphorization period could reduce rephosphorization in the later smelting stage. After that, the decarburization is operated in the same converter and the end-point slag, which had less dephosphorization ability at high temperature was reserved in the converter as the pre-melting slag for dephosphorization in the low-temperature stage of

the subsequent furnace (because the slag dephosphorization was restored in the low temperature), as shown in Fig. 1.
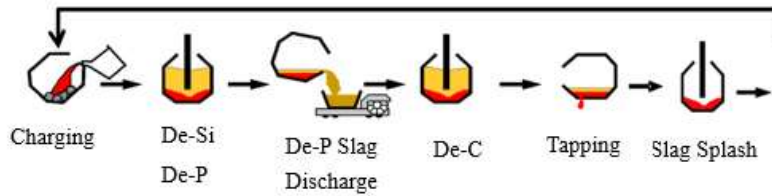

Figure 1. The pictorial of the double-slag process

EXPERIMENTAL PROCESDURE

At China steel corporation, an industrial experiment was carried out in three 150 ton converters which combined top and bottom blowing. In order to reduce the consumption of lime and the output of BOF slag under the condition of maintaining dephosphorization efficiency, the dephosphorization period blowing model and dephosphorization slag property are adjusted during the dephosphorization period. At the end of the dephosphorization period, the temperature, the basicity and the ingredient of the slag were evaluated to confirm the effect of the dephosphorization capacity in the double-slag process. The hot-metal temperature and composition during production are shown in Table 1.

Table 1. The compositions and temperature of liquid iron

Temperature / K	The molten steel composition /mass%				
	[C]	[Si]	[Mn]	[S]	P
1523-1597	4.12	0.37	0.21	0.07	0.13

In order to reduce the lime consumption of the converter, it is necessary to improve the dephosphorization efficiency during the dephosphorization period of the double-slag process. Dephosphorization depends on changes in oxidation state of the slag and is driven by slag-metal droplet reaction in slag/steel interface, where they react with the metal droplets ejected due to the impact of the oxygen jet. Oxygen partial pressures drive the stability of phosphorus in the slag as phosphateions, (PO_4^{3-}) [1]. The ionic reaction is given in Eq. (1):

$$[P] + 2.5(FeO) + 1.5(O^{2-}) = (PO_4^{3-}) + 2.5[Fe] \qquad (1)$$
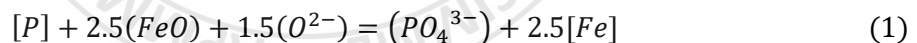
Here it should be reminded that the round brackets (_) indicate concentrations in slag while square brackets [_] indicate molten steel concentration. A low oxygen lance height was adjusted in the dephosphorization period for the double-slag process to decrease the interface energy. As increasing in the interface fluid velocity, causing disruption of the slag/steel interface, interface area increases and that promote the dephosphorization capacity [2,3]. In order to identify the endpoint of the dephosphorization period with the efficient dephosphorization ratio. The dephosphorization ratio (η_P) is defined as Eq. (2):

$$\eta_p = \frac{w[p]_0 - w[p]_e}{w[p]_0} \qquad (2)$$

where $W[P]_0$ is the initial phosphorus content in liquid iron before the start of dephosphorization and $W[P]_e$ is the endpoint phosphorus content in molten steel. Fig. 2 shows the change principles of the dephosphorization ratio versus temperature. As increasing in temperature, the dephosphorization ratio increased to achieve the max dephosphorization ratio, 70%, in period Temperature < 1675 K. When

temperature above 1675 K, the dephosphorization ratio dropped with increasing in temperature. The desired temperature operated in dephosphorization stage was between 1665 ± 10K and the average dephosphorization ratio reached average 59.5%.
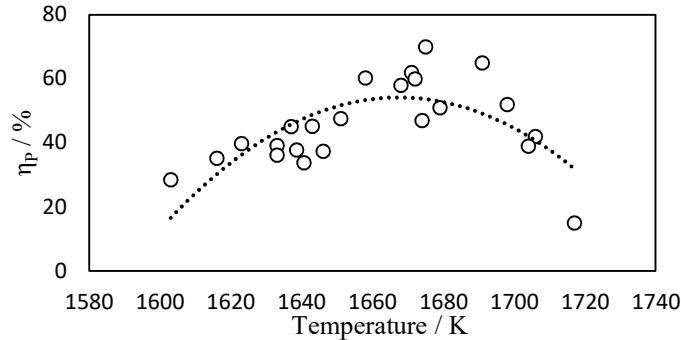

Figure 2. The relation between the dephosphorization ratio and temperature at the end of dephosphorization period

RESULTS AND DISCUSSION

The study of dephosphorization in the European Union Research Fund for Coal and Steel project [4] illustrates the order of oxidation of impurity elements, including the content of silicon, phosphorus and carbon in molten steel during the oxygen blowing process. To improve the efficiency of dephosphorization, it is necessary to remove a large property of silicon rather than carbon, because the decarbonization reaction will cause a rapid rise in temperature, which is unfavorable of dephosphorization [5]. In this case, the blowing pattern operated in low oxygen lance control mode and stabilized the temperature in 1665 ± 10K in the dephosphorization period of the double-slag process. Fig. 3 shows that the desiliconization ratio (η_{Si}) and decarburization ratio (η_C) dispersed among 70-90% and 25-45%, respectively, in the conventional single-slag process. After adopting the double-slag process, the desiliconization ratio (η_{Si}) was concentrated in 85~95% and decarburization ratio (η_C) was mostly lower than 35%. As shown in Fig. 4, in the dephosphorization period, the dephosphorization ratio (η_P) for the double-slag process, mostly above 37%, was higher than single-slag process,20-40%.
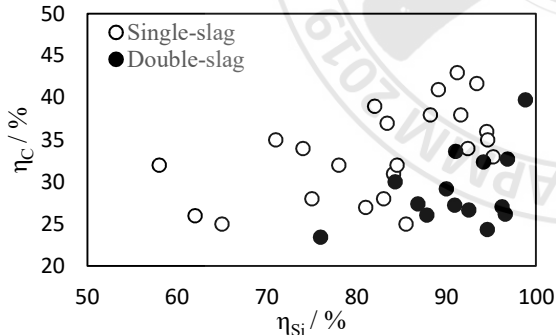
Figure 3. The relation between η_C and η_{Si} in the endpoint of the dephosphorization period
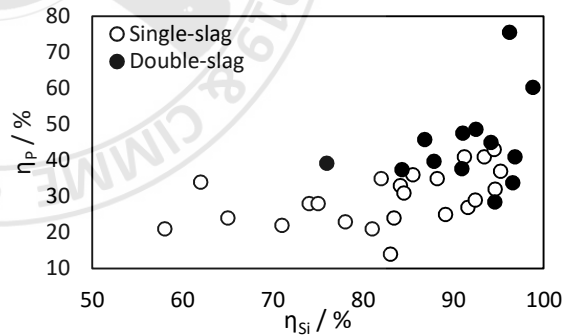
Figure 4. The relation between η_P and η_{Si} in the endpoint of the dephosphorization period

Phosphorus distribution ratio (Lp = (%P)$_{slag}$/[%P]$_{steel}$), which is often used to analyze the dephosphorization capacity calculated by Suito's and Inoui's equations [6] as Eq. (3):

$$\log Lp = 2.5 \times \log W_{TFe} + 0.072 \times \left(W_{CaO} + 0.3 \times W_{MgO} + 0.6 \times W_{P_2O_5} + 0.6 \times W_{MnO} \right) + \frac{11570}{T} - 10.52 \tag{3}$$

As shown in Fig. 5, the slag discharged by the double-slag process has a lower salt basicity than the slag discharged by the single slag method, but has a higher dephosphorization efficiency.As the result,

the advantages in the dephosphorization capacity and lime efficiency were achieved in the double-slag process compared with the single-slag process. A comparison of the lime consumption between the single-slag process and the double-slag process is shown in Fig. 6. After adopting the double-slag process, the lime costs decreased by an average of 14 kg per metric ton steel; the amount of BOF slag output average decreased by 9.4 kg per metric ton of steel and the dephosphorization ratio (η_P) was both around 87% in BOF endpoint.
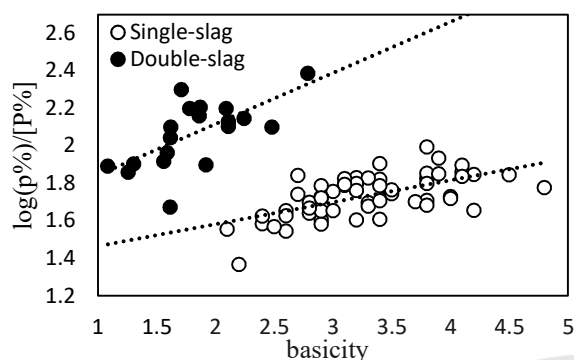

Figure 5. Comparison of logLp and slag basicity between sinle- and double-slag process
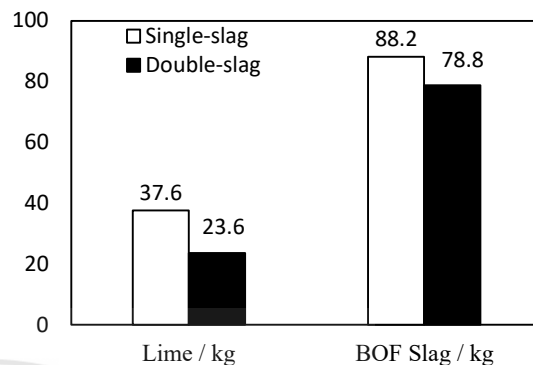

Figure 6. Comparison of lime and slag volume between single- and double-slag process

SUMMARY AND CONCLUSIONS

1. The double-slag process was employed to reduce lime consumption and the BOF slag volume without influencing the dephosphorization capacity at China steel corporation. During the dephospharisation period, the blowing pattern operated in low oxygen lance control mode and the temperature was controled in 1665±10K.

2. In endpoint of the dephosphorization period, the dephosphorization ratio (η_P) was boosted by increasing the desiliconization ratio (η_{Si}) and decreasing the decarburization ratio (η_c). The desiliconization ratio (η_{Si}), the decarburization ratio (η_c) and the dephosphorization ratio (η_P) were $90 \pm 5\%$, $\leq 35\%$ and $\geq 37\%$, respectively.

3. The advantage in lime efficiency was achieved in the double-slag process; as the result, the lime consumption decreased by an average of 14 kg per metric ton steel and the BOF slag increased by 9.4 kg per metric ton of steel. The dephosphorization ratio (η_P) in both single-slag and double-slag process were kept at 87%.

REFERENCES

[1] N. Sano (1997). Advanced physical chemistry for process metallurgy. Academic Press.

[2] C.P. Manning and R.J. Fruehan (2013). The rate of the phosphorous reaction between liquid iron and slag. Metallurgical and materials transactions B, 44(1), 37-44.

[3] S. Spooner, J.M. Warnett, R. Bhagat, M.A. Williams and S. Sridhar (2016). Calculating the Macroscopic Dynamics of Gas/Metal/Slag Emulsion during Steelmaking. ISIJ International, 56(12), 2171-2180.

[4]European Commission: Research Fund for Coal and Steel. Imphos: improving phosphorus refining. (2011)

[5] C.G. Zhou, J. Li, C.B. Shi, W.T. Yu, Z.M. Zhang, Z.M. Liu and C.F. Deng (2016). Dependence of Temperature and Slag Composition on Dephosphorization at the First Deslagging in BOF Steelmaking Process. High Temperature Materials and Processes, 35(4), 433-440.

[6] H. Suito and R. Inoue (1995). Thermodynamic assessment of hot metal and steel dephosphorization with MnO-containing BOF slags. ISIJ international, 35(3), 258-265.

International Conference on Asia Pacific Mining and Metallurgy
Tainan, Taiwan, November 17-20, 2019

Section 1：Materials Science

13：00 – 14：50　　　2nd Lecture Room

13:00-14:50	Session Chair:	Prof. **Kuei-Chih Feng** Ming Chi University of Technology
13:00-13:30	CIMME108110	**Prof. Chia-Cheng Lin** National Taipei University of Technology *Water Oxidation with Cobalt Oxide Based Materials*
13:30-13:50	CIMME108006	**Tsung-Hsien Wang** China Steel Corporation, Taiwan *The Development of Ultra High Strength Steel- JSC980YH* *with Superior Hole Expansibility and Bendability*
13:50-14:10	CIMME108028	**Yen-Nan Lin** China Steel Corporation, Taiwan *The Development of Abrasion Resistant Steel Plates by Direct-Quench Process*
14:10-14:30	CIMME108160	**Dhayanantha Prabu Jaihindh** National Dong Hwa University Deep Eutectic Solvents Assisted Synthesized Bismuth Based NanoMicro Structured Materials for Environmental Applications

Water oxidation with cobalt oxide based materials

Chia-Cheng (John) Lin

Department of Materials and Mineral Resources Engineering, Institute of Materials Science and Engineering, National Taipei University of Technology, Taiwan
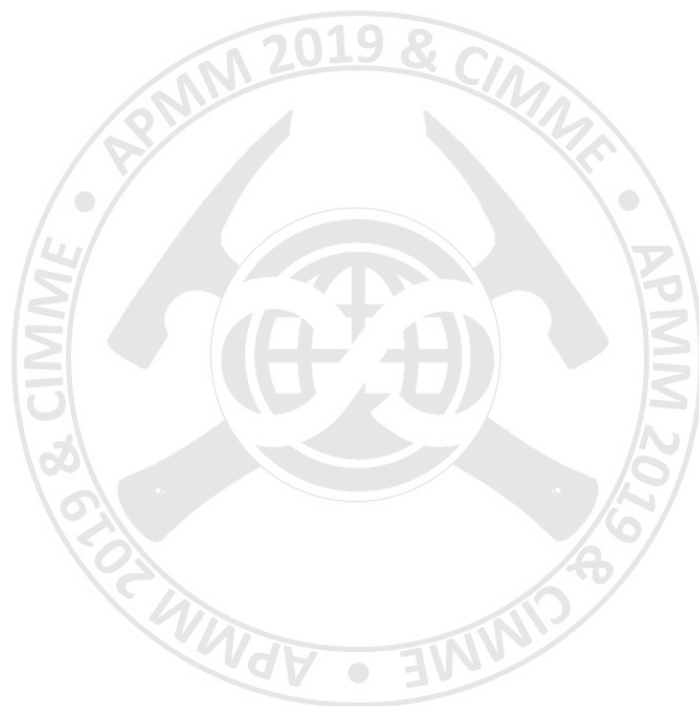*johncclin@ntut.edu.tw*

ABSTRACT

Electrochemical and photochemical water splitting are ways to produce hydrogen gas, H_2, a potentially valuable and clean-burning fuel. Water oxidation is the more difficult half-reaction in water splitting, involving the transfer of four electrons and the formation of oxygen–oxygen bonds. After many studies devoted to developing more efficient and economic water oxidation catalysts, cobalt-based materials have been identified as one of the most promising candidates due to their relative abundance, high activity, and stability.

We first investigate the effect of microstructuring on the photochemical water oxidation (oxygen evolution) activity of two types of Co_3O_4/porous silica composites: Co_3O_4/porous SiO_2 core/shell nanoparticles with varying shell thicknesses and surface areas, and Co_3O_4/mesoporous silica nanocomposites with various surface functionalities. Catalytic tests in the presence of $Ru(bpy)_3^{2+}$ as a photosensitizer and $S_2O_8^{2-}$ as a sacrificial electron acceptor show that porous silica shells of up to ~20 nm in thickness lead to increased water oxidation activity. We attribute this effect to either (1) a combination of an effective increase in catalyst active area or consequent higher local concentration of $Ru(bpy)_3^{2+}$; (2) a decrease in the permittivity of the medium surrounding the catalyst surface and a consequent increase in the rate of charge transfer; or both. Functionalized Co_3O_4/mesoporous silica nanocomposites show lower water oxidation activity compared with the parent nonfunctionalized catalyst, likely because of partial pore blocking of the silica support upon surface grafting. A more thorough understanding of the effects of microstructure and permittivity on water oxidation ability will enable the construction of next generation catalysts possessing optimal configuration and better efficiency for water splitting.

We then synthesized a series of $Co_{3-x}Cr_xO_4$ ($0 < x < 2$) catalysts via thermal decomposition and explored how the composition difference affect their intrinsic activity for the electrochemical oxygen evolution reaction (OER). By changing the Cr content, we were able to modify the overall OER activity. Among the compositions investigated, $Co_{2.25}Cr_{0.75}O_4$ is the most active, which achieves 10 mA cm^{-2} current density per geometric area and a mass activity of 10.5 A/g at 0.35 V overpotential. We hypothesize that this enhanced OER activity is due to the increase of the adsorption energy of the intermediates (*O, *OH, and *OOH) resulting from the increased electrophilicity of Co^{2+} sites in the material after the introduction of the electron-deficient Cr. This systematic doping strategy enables the investigation of the correlation between the doping and OER activity and allows for the rational design of future catalysts with higher activity and efficiency.

REFERENCES
1. **Lin, C.-C.**; McCrory, C. C. L.* "Effect of Chromium Doping on Electrochemical Water Oxidation Activity by $Co_{3-x}Cr_xO_4$ spinel catalysts." *ACS Catalysis* **2017**, *7*, 443–451.
2. **Lin, C.-C.**; Guo, Y.; Vela, J.* "Microstructure Effects on the Water Oxidation Activity of Co_3O_4 Porous Silica Nanocomposites." *ACS Catalysis* **2015**, *5*, 1037–1044.

The Development of Ultra High Strength Steel – JSC980YH with Superior Hole Expansibility and Bendability

Tsung-Hsien Wang
Metallurgical Department, China Steel Corporation, Kaohsiung
175448@mail.csc.com.tw

Kuo-Cheng Yang
Iron and Steel Research & Development Department, China Steel Corporation, Kaohsiung
152423@mail.csc.com.tw

ABSTRACT

With the rise of energy conservation and safety requirements for the automotive industry, the newest material currently used for vehicle seat slide tracks is 980MPa cold-rolled steel. This research introduced the development of cold-rolled steel grade with high yield ratio– JSC980YH used for automotive structure application. The microstructure of this steel mainly consists of nearly full bainite which provided material strength, through appropriate design of chemical composition and heat treatment to inhibit ferrite and martensite-austenite volume fraction. Considering the heating pattern design and cooling capacity of continuous annealing line (CAL), the composition of the steel is based on low carbon with addition of Mn, Cr and Mo element which contribute to hardenability and retard the transformation of the ferrite and pearlite phase, as well as the addition of Si for the solid solution strengthening, good ductility and ferrite stabilizing. With the appropriate metallurgical design of hot rolling, cold rolling and continuous annealing, China Steel Co. (CSC) has successfully developed 980MPa grade ultra high strength steel (UHSS) with high yield strength, superior hole expansibility and bendability.

INTRODUCTION

Recent years, with the rise of energy conservation and safety requirements for automotive industry, the advantage of advanced high strength steels (AHSS) for mass reduction and climate change are shown in the previous study by Shaw *et al*. One of these applications is vehicle seat tracks, which combines the seats with vehicle itself, and most importantly, it secures the safety of driver and passengers. The vehicle seat assembly and the vehicle seat slide tracks are shown in figure 1, the tracks had experienced punching, forming, bending, hole-expanding and sizing during multiple production process.

Normally, the dual phase steel with superior formability and high tensile strength was first considered for ultra high strength steel used in automotive application, but when referring to the vehicle seat tracks, its poor hole expansibility and lower yield strength had become disadvantages for forming and the seat safety testing. This is because the microstructure of the dual phase steel are the soft ferrite phase and the hard martensite phase, which are easily prone to crack and propagate along the interfaces during hole expanding as shown in the work by Hasegawa *et al.* (2004). According to the

previous by Hasegawa *et al.* (2004), one of the best ways to improve the hole expansibility of dual phase steel is to modify the microstructure from the dual phase (ferrite & martensite) to full or nearly full bainite or martensite, which could eliminate the difference of hardness between the two phase and resist the micro cracks propagating during hole-expanding. In this study, the development of the ultra high strength steel grade - JSC980YH with superior hole expansibility and bendability was revealed.
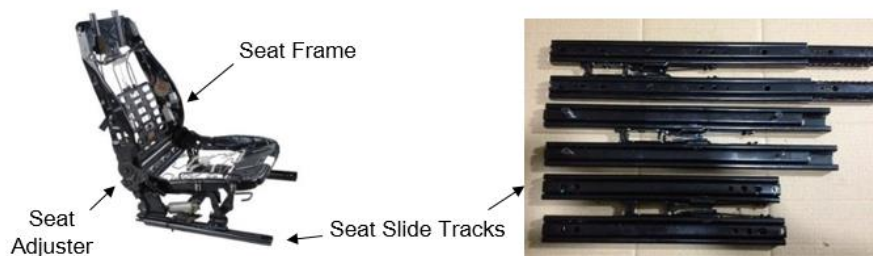

Figure 1. The vehicle seat assembly and seat slide tracks

METALLURGICAL DESIGN AND EXPERIMENTAL METHOD

The manufacturing process of JSC980YH developed by CSC is shown in figure 2. The chemical composition is strictly controlled during the steel making, and then the slab would be reheated after continuous casting and be hot-rolled to the hot roll band (HRB). Table 1 shows the chemical composition based on the heat analysis of JSC980YH and DP980Y manufactured by CSC, the carbon and silicon addition of JSC980YH are higher than DP980Y. The hot roll band was pickled and cold-rolled to achieve desired thickness. Finally, the cold-rolled steel sheets were heated to 860℃ which was higher than A_3 temperature, soaked for about 250 to 350 seconds and then rapidly cooled to a temperature below the Bs temperature (bainite start temperature) and kept for at least 500 seconds.
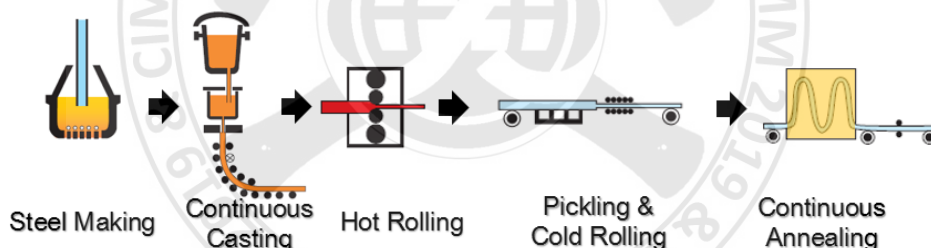
Figure 2. The manufacturing process of JSC980YH

Table 1. Chemical composition of JSC980YH and DP980Y (in wt%)

Grade	C	Mn	Si	others
JSC980YH	0.16	2.0	0.5	Cr, Mo $\leqq$ 0.80
DP980Y	0.09	2.0	0.08	Cr, Mo $\leqq$ 0.80

The tensile test of the cold-rolled steel sheets was conducted in accordance with JIS Z 2241 and the test piece was the No.5 test piece perpendicular to the rolling direction. The test method and test piece for the hole expanding test was as specified in JIS Z 2256. The test method and test piece for V-bending test was as specified in TSG2385G. The steel sheets were sampled along the rolling direction, and the samples were etched by 3% nital and analyzed by OM (Optical Microscope), SEM (Scanning Electron Microscope) to observe the microstructure.

RESULTS AND DISSCUSION

The mechanical properties of DP980Y and JSC980YH manufactured by CSC are shown in table 2. The tensile strengths of both grade were greater than 980 MPa, but the yield strength of JSC980YH was greater than DP980Y, moreover, the yield ratio (yield strength/tensile strength ratio) of JSC980YH was 0.80, which was also greater than that of DP980Y. Another obvious difference between JSC980YH and DP980Y was the hole expansion ratio, the hole expansion ratio of JSC980YH had reached 56%, which was 26% higher than DP980Y. The microstructure of DP980Y and JSC980YH are shown in figure 3 and figure 4. The microstructure of DP980Y mainly consists of ferrite and martensite. The ferrite phase provided excellent formability and the martensite phase distributed over the ferrite matrix provided the desired strength. Compared to DP980Y, the microstructure of JSC980YH was nearly full bainite, which provided great crack-resistance. On the contrary, the dual phase microstructure of DP980Y was prone to crack during hole expanding, and the micro-cracks were easily to propagate.

Table 2. Mechanical Properties of JSC980YH and DP980Y (in wt%)

Grade	YS (MPa)	TS (MPa)	EL (%)	Y/T Ratio	Hole Expansion Ratio (%)
JSC980YH	855	1068	11.8	0.80	56
DP980Y	635	1016	14.5	0.63	30

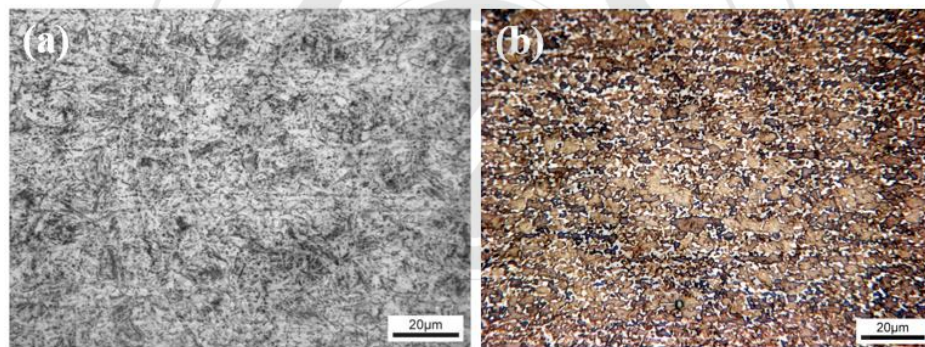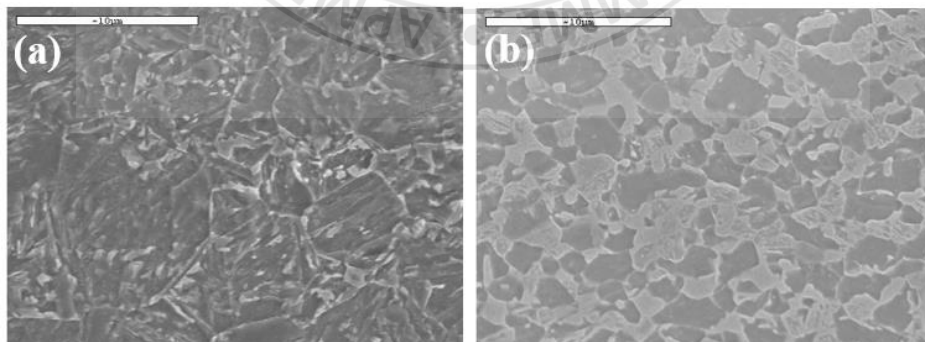Figure 3. Optical microstructures of (a) JSC980YH and (b) DP980Y

Figure 4. SEM microstructures of (a) JSC980YH and (b) DP980Y

Due to the main application of JSC980YH grade developed by CSC is vehicle seat slide tracks, the bendability of the material had also been studied. According to TSG2385G standard, the test piece was placed on a V-shaped block, and an upper die with different bending radius was placed on the central

part of the test piece as shown in figure 5. After the load had been given to the test piece, the outer bending ridge line of the test piece had been observed to judge whether the cracks were presented of not. The R/t value was considered as V-bending characteristic value, where R refers to bending radius and t refers to plate thickness of the test piece. Table 3 shows the results of the bending test, where the thickness of test pieces was 1.4 and 1.6 mm respectively. The specified R/t value and the corresponding bending radius were shown in table 3 according to TSG3100G standard. The test results revealed the R/t values at each steel sheets thickness were 0.36 and 0.31 respectively, which were much lower than the specified values. And the lower R/t value is, the better bendability the steel sheets has. Therefore, compared to DP980Y, JSC980YH is more suitable for the application of higher hole expansibility and bendability demands, for example, the vehicle seat slide tracks.
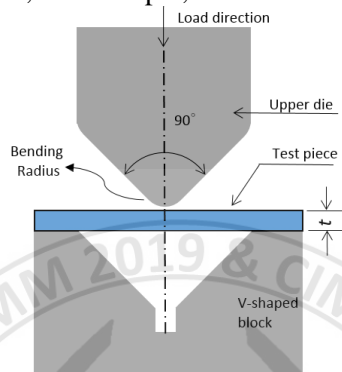

Figure 5. The V-bending test method specified in TSG2385G

Table 3. The results of V-bending test of JSC980YH

Thickness, t (mm)	Specified Bending Radius (mm)	Specified R/t Value	Results of V-bending test of JSC980YH	
			R=0.5(mm)	R/t
1.4	2.0	1.43	○○○	0.36
1.6	2.0	1.25	○○○	0.31

(The bending ridge line is perpendicular to the rolling direction)

CONCLUSIONS

With the highly demands of energy conservation and safety requirements for the automotive industry, the newest material currently used for vehicle seat slide tracks is 980MPa cold-rolled steel sheets. Compared to traditional dual phase steel-DP980Y, the JSC980YH grade developed by CSC with proper chemical composition and heat treatment design had higher yield strength, superior hole expansibility and bendability, which were achieved by modifying the microstructure from the dual phase to nearly full bainite.

REFERENCES

Jody Shaw and George Coates. "Automotive Steel Performance Advantages for Mass Reduction and Climate Change," www.autosteel.org.

K. Hasegawa, K. Kawamura, T. Urabe and Y. Hosoya. "Effects of Microstructure on Stretch-flange-formability of 980 MPa Grade Cold-rolled Ultra High Strength Steel Sheets," ISIJ International, Vol. 44 (2004), No. 3, 603–609

The Development of
Abrasion Resistant Steel Plates By Direct-Quench Process

Yen-Nan Lin

Metallurgical Department, China Steel Corporation, Kaohsiung

181800@mail.csc.com.tw

Delphic Chen

Iron and Steel Research & Development Department, China Steel Corporation, Kaohsiung

185108@mail.csc.com.tw

ABSTRACT

Abrasion is the determining factor of mechanical equipment life. High-performance abrasion resistant steel plate not only extends service life and reduces equipment maintenance frequency. Conventional abrasion resistant steel plates are produced by reheating-quenching & tempering process (RQ-T). In this study, abrasion resistant steel plate was quenched immediately after control rolling by direct-quenching technology, and auto-tempered by the heat dissipated from the center of the plate. Off-line Tempering process is removed by Direct-quenching and Auto-tempering (DQAT) technology that reduce costs and shorten delivery time. Hardness of 400 HBW series abrasion resistant steel plates was development such as CSC AR400F by DQAT technology. The hardness of the CSC AR400F reached 400HBW and longitudinal Charpy absorption energy at -40°C also exceeded 50J. It shows that the DQAT process is well-suited for producing abrasion resistant plate and reduces the energy consumption during plate fabrication.

INTRODUCTION

Abrasion resistant steel has been widely used in mining machinery, agricultural machinery, transportation equipment, construction machinery and raw material conveying equipment. In recent years, the heavy equipment in industries demands for steel plates with higher strength, abrasion resistance, low temperature toughness, and formability. Two processes, RQT(Reheating-Quenching & Tempering) and DQT(Direct-Quenching & Tempering) , are often used to manufacture abrasion resistant steels. In RQT process, the rolled steel plates are normalized and quenched rapidly. After quenching, the steel plates are tempered to acquire proper microstructure and mechanical properties. RQT process is capable to produce the abrasion steel plates with excellent flatness and uniform microstructure. These advantages make RQT the primary process in manufacturing abrasion resistant steels. On the other hand, steel plates are rolled and quenched directly with DQ equipment before tempering in DQT process. The combination of rolling and quenching in DQT process is beneficial to energy saving but the flatness is also compromised[2,3].

In this study, CSC AR400F is developed by the integration of auto-tempering[5] alloy design and DQ equipment in CSC. The heat dissipates during quenching promotes the self-tempering[4] of the steel plates. The offline tempering in DQT process can be replaced by the auto-tempering during quenching.

Therefore, DQAT process reduces the energy consumption and makes the production of CSC AR400F steel plates more eco-friendly.

RESEARCH METHOD

Table 1 lists the requirements for mechanical properties of CSC AR400F abrasion resistant steel plate. The composition of CSC AR400F is listed in Table 2. The CSC AR400F is a low carbon martensitic steel microalloyed with Mn, Cr, Mo, Ti, Nb, and B. The addition of niobium refines the grain size during controlled-rolling, hence the low temperature is greatly improved. Besides microalloying, the alloy is also calcium-treated. Calcium treatment turns the deleterious MnS into harmless CaS and enhances the elongation. In order to produce AR400F in CSC plate mill, the CC-casted slab was reheated to 1150°C and controlled-rolled to obtain fine pancake-shaped austenite grains. After rolling, the defects in pancake-shaped austenite grains provide lots of nucleation sites for phase transformation and carbide precipitation during quenching and auto-tempering process. After quenching, the microstructure of the steel plate is composed of auto-tempered martensite which provides sufficient hardness and excellent low temperature toughness.

Table 1. Mechanical property specification of CSC AR400F

Grade	Hardness (HBW)	YS (MPa)	TS (MPa)	EL (%)	Absorbed energy[1] @-40°C (J)
AR400F	370 430	1030 min.	1270 min.	11 min.	34 min.

Note: (1) Test direction parallel to rolling direction.

Table 2. Chemical composition of CSC AR400F (wt%)

Grade	C (wt%)	Mn (wt%)	Si (wt%)	B (wt%)	Ca (wt%)	Others (wt%)
AR400F	0.13	1.17	0.32	15 ppm	19 ppm	≦0.80

Results and discussion

Figure 1 shows the optical metallography of CSC AR400F steel plate which is produced by the controlled-rolling and DQAT process. The pancake-shaped prior austenite in microstructure indicates that the controlled-rolling refined the microstructure and increase the grain boundary density. With higher grain boundary density, the low temperature toughness can be greatly improved. Figure 2 shows the SEM micrograph image of CSC AR400F. The evenly dispersed sub-micron carbides in martensite matrix after DQAT also improve the low temperature toughness of the steel plate. The presence of auto-tempered martensite in SEM micrograph image suggests the steel plate can be tempered properly during quenching through appropriate cooling control without additional offline quenching process. Therefore, the DQAT process could save the precious energy and time during plate production.
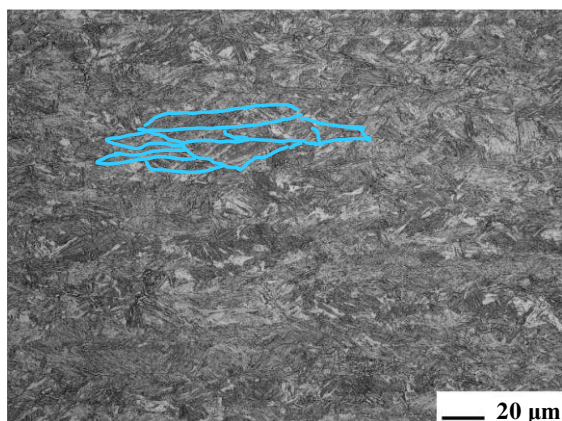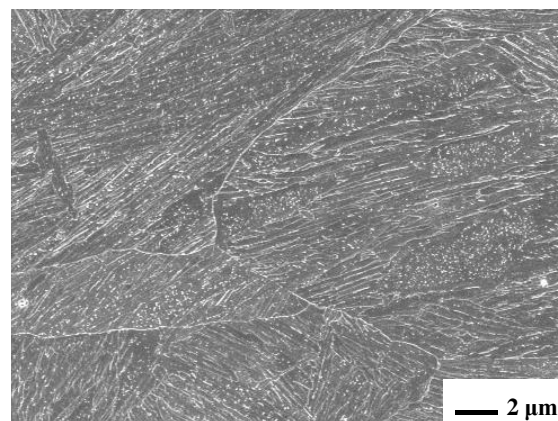
Figure 1. Microstructure of CSC AR400F

Figure 2. Microstructure of CSC AR400F by SEM

Table 3 lists the mechanical properties of CSC AR400F made by DQAT process. The average hardness is 397HBW while the elongation is 13.1%. The average low temperature Charpy absorption energy also reach 70J. Therefore, CSC AR400F is capable to provide high hardness, good elongation, and excellent low temperature toughness. As for the formability, Table 4 shows that CSC AR400F can be bent to 90 degree without the appearance of cracks under the severe bending condition of R/t$\geq$2. From the above results, CSC AR400F is suitable to be adopted in quarrying vehicles in high latitude regions.

Table 3. Average mechanical properties of CSC AR400F

Plate thickness	Hardness (HBW)	YS (MPa)	TS (MPa)	EL (%)	Absorbed energy[1] @-40°C (J)
12.70	387	1143	1293	13.8	80
15.88	406	1238	1327	13.9	78
19.05	401	1181	1369	12.3	63
25.40	394	1131	1322	12.4	62
Total	**397**	**1176**	**1330**	**13.1**	**70**

Note: (1) Test direction parallel to rolling direction.

Table 4. Bending test of CSC AR400F

Plate thickness t (mm)	Bending angle	R/t	Bending radius R (mm)	Result
12.7	90°	1.7	21.5	Crack
		2	25	OK
		3	38	OK
		4	51	OK
25.4	90°	1.7	43	Crack
		2	51	OK
		3	76	OK
		4	102	OK

Note: Test direction perpendicular to rolling direction.

Conclusion

CSC AR400F is produced by the combination of controlled-rolling and DQAT processes. The process yields a microstructure of fine-martensite matrix with submicron carbide embedded evenly. The microstructure of CSC AR400F is sufficient to provide high hardness, elongation , formability, and good low temperature toughness. Therefore, CSC AR400F is capable to fulfill the requirements of quarrying vehicles in high-latitude region.
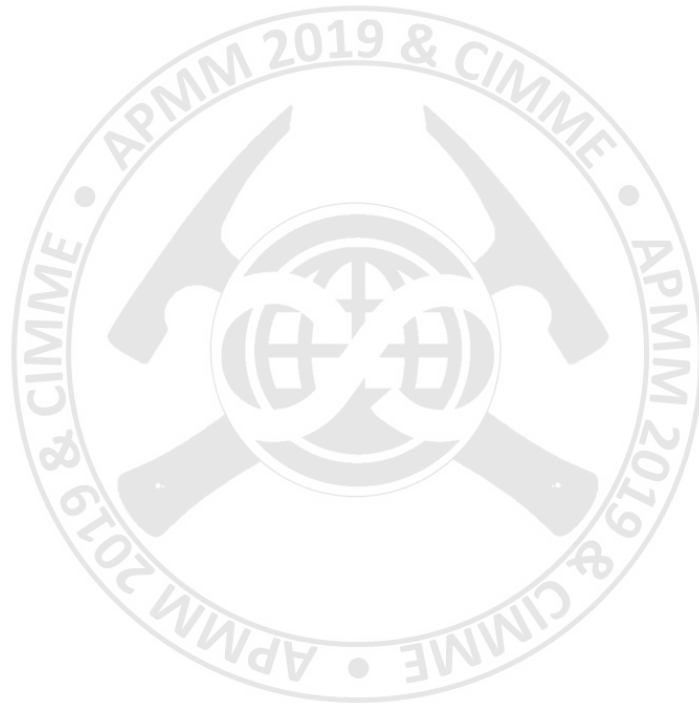
Deep Eutectic Solvents Assisted Synthesized Bismuth Based Nano/Micro Structured Materials for Environmental Applications

**Dhayanantha Prabu Jaihindh**[1] and Yen-Pei Fu[1, *]

[1]*Department of Materials Science and Engineering, National Dong Hwa University, Hualien-97401, Taiwan*
dhayanandhaprabu@gmail.com, ypfu@gms.ndhu.edu.tw

ABSTRACT

Heterostructured nanomaterials can paid more significant attention in environmental safety for the detection and degradation/removal of hazardous toxic chemicals over a decay. Here, we report the preparation of hierarchically nano/micro structured bismuth based visible light photocatalysts for photocatalytic degradation methylene blue, rhodamine B dye molecules and highly toxic hexavalent chromium (Cr(VI)) using the green deep eutectic solvent reline, which allows morphology control in one of the less energy-intensive routes. In this talk, the preparation photocatalytic transition metal-oxide semiconductor materials are investigated, namely bismuth-based heterogeneous photocatalysts using Deep eutectic solvents (DESs) as green solvents. This work is focused on the design of visible-light-active metal-oxide photocatalysts to increase the absorption of visible light and to decrease the rates of electron-hole recombination, resulting in a high photocatalytic efficiency in regards to the degradation of organic pollutants. In First study deals synthesis of $BiOCl/BiVO_4$ p-n heterojunction photocatalysts was synthesized using DESs reline (Choline chloride: Urea, 1:2) *via* simple one-pot sol-gel method at room temperature. $BiOCl/BiVO_4$ sheet like structure was characterized and experimentally investigated for the degradation of Methylene blue, rhodamine B under visible light irradiation and also the mechanism was investigated using scavenger experiment. To improve the photocatalytic activity and electron-hole pair recombination time, the silver nanowires combined with $BiOCl/BiVO_4$. Here, we report a one dimensional (1D) AgNWs combined with $BiOCl/BiVO_4$ photocatalysts. The appearance of elemental AgNWs during the photocatalytic reaction would be in favor to enhanced visible light absorption, the facilitated photoinduced electrons transfer, and the enhanced separation of photoinduced electron−hole pairs contributed to the improvement of photocatalytic activities. The second study proposed, the preparation of hierarchically nanostructured shuriken like bismuth vanadate ($BiVO_4$) as a bifunctional catalyst for photocatalytic degradation of highly toxic hexavalent chromium (Cr(VI)) and the electrochemical detection of Cr(VI). The reline solvents leads the role of a latent supramolecular catalysts where the enhance in reaction rate from solvent driven pre-organization of the reactant is most remarkable. The SEM results showed a good dispersion of $BiVO_4$ catalyst and the HR-TEM revealed an average particle size of ca. 5–10 nm. As a result, the $BiVO_4$ exhibited good photocatalytic activity under UV-light about 95% reduction of Cr(VI) to Cr(III) was observed in 160 min. The recyclability of $BiVO_4$ catalyst exhibited an appreciable reusability and stability of the catalyst towards the photocatalytic reduction of Cr(VI). Also, the $BiVO_4$-modified screen printed carbon electrode ($BiVO_4$/SPCE) displayed an excellent electrochemical performance towards the electrochemical detection of Cr(VI). Besides, the $BiVO_4$/SPCE demonstrated tremendous electrocatalytic activity, lower linear range (0.01–264.5 μM), detection limit (0.0035 μM) and good storage stability towards the detection of Cr(VI). Importantly, the $BiVO_4$ modified electrode was also found to be a good recovery in water samples for practical applications. The shape dependent nanostructured $BiVO_4$ catalyst could also be used an effective electrode material for energy storage and hybrid capacitor in future.
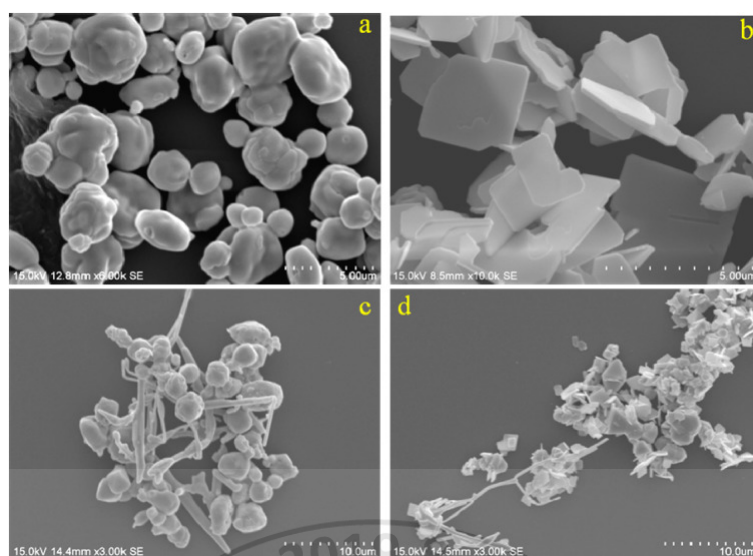
Figure 1. SEM images: (a) $BiVO_4$ prepared via sol-gel method at room temperature without DES; (b) $BiOCl/BiVO_4$, (c) 5% AgNWs@ $BiVO_4$ and (d) 5% AgNWs @ $BiOCl/BiVO_4$ prepared via sol-gel method at room temperature with DES.
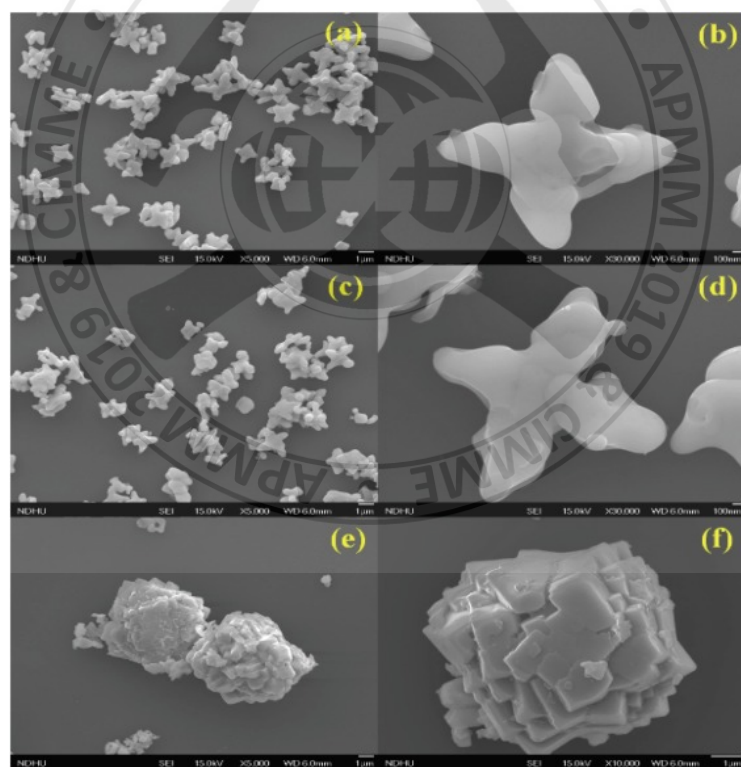
Figure 2. Scanning electron microscopy image: (a–b) $BiVO_4$-5 h, (c–d) $BiVO_4$-10 h and (e–f) $BiVO_4$-15 h.
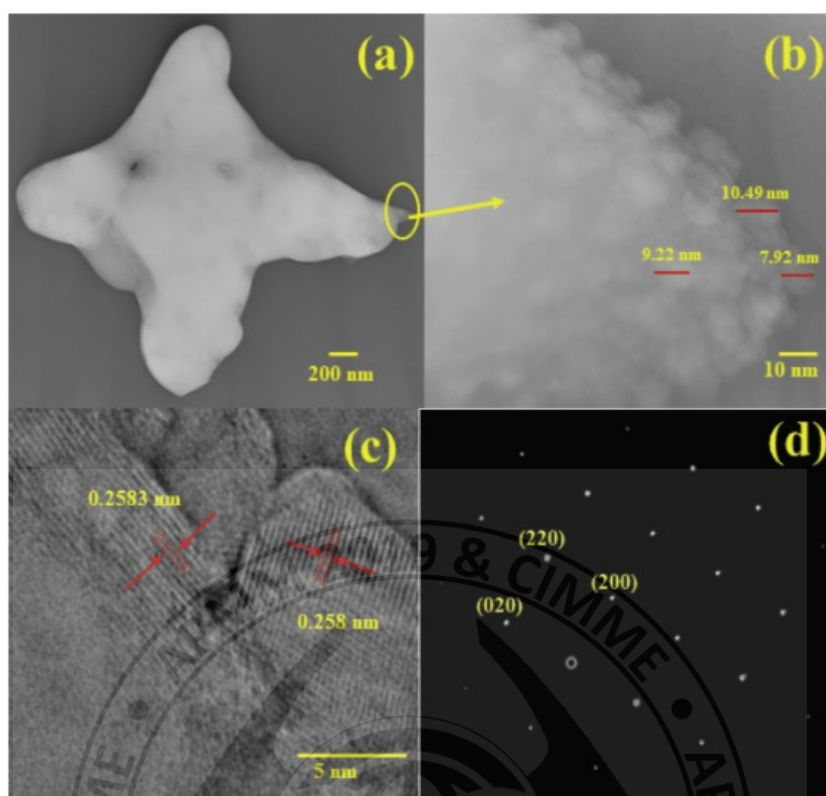
Figure 3. $BiVO_4$-10 h specimen: (a) TEM image, (b) Magnified TEM image, (c) HR-TEM image, and (d) SAED pattern.

REFERENCES

Jaihindh, D.P., Fu, Y.P. (2017). "Facile synthesis of deep eutectic solvents assisted BiOCl/BiVO4@AgNWs plasmonic photocatalysts under visible light enhanced catalytic performance", Catalysis Today 297: 246-254.

Jaihindh, D.P., Balamurugan, T., Chen, S.M., Paramasivam, B., and Fu, Y.P. (2019). "Facile synthesis of hierarchically nanostructured bismuth vanadate: An efficient photocatalysts for degradation and detection of hexavalent chromium", Journal of Hazardous Materials 367: 647-657.

International Conference on Asia Pacific Mining and Metallurgy
Tainan, Taiwan, November 17-20, 2019

Section 1：Circular Economy and Sustainable Resources

13：00 – 14：50　　　　3rd Lecture Room

13:00-14:50	Session Chair:	Prof. **Yun-Hsun Huang** National Cheng Kung University
13:00-13:30	CIMME108175	**Prof. Keiko Sasaki** Kyushu University, Japan *Challenges to Gold Recovery from Carbonaceous Gold Ores Using Biotechnology*
13:30-14:00	CIMME108069	**Prof. Hsing-I Hsiang** National Cheng Kung University *Development of Novel Lithium Recovery Technology from Brine Water by Using Spent LiFePO$_4$ Battery*
14:00-14:20	CIMME108185	**Yu-Jie Xie** National Taipei University of Technology *A Study on Solidification of Simulated Radioactive Cationic Exchange Resins Using Geopolymer*
14:20-14:40	CIMME108184	**Yung-Ting Lin** National Taipei University of Technology *A Study on Improvement Geopolymer Fabrication Process*

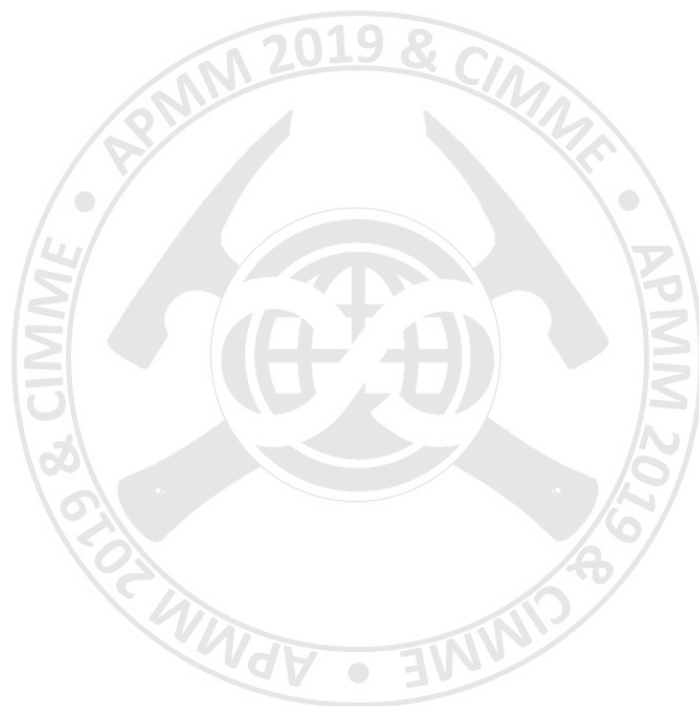# Challenges to gold recovery from carbonaceous gold ores using biotechnology

Kojo Twum Konadu and **Keiko Sasaki**

Department of Earth Resources Engineering, Kyushu University, Japan
keikos@mine.kyushu-u.ac.jp, kojo@ mine.kyushu-u.ac.jp

ABSTRACT

The cyanidation is a royal road of gold hydrometallurgy. However, in case of carbonaceous gold ores, very fine graphitic carbon particles act to sorb $Au(CN)_2^-$ causing up to 30% recovery loss, so-called as "preg-robbing". In addition, tiny gold grains are locked in sulfide minerals, such as pyrite and arsenopyrite. So graphitic carbon-bearing sulfidic gold ores are classified as double refractory gold ore (DRGO), which are generally difficult to develop despite this type of gold ore corresponding to around 1/3 of the global gold production. Recovering gold from DRGO necessitates the use of some ore pretreatment techniques prior to cyanidation to remove or minimize the effects of the sulfides and carbonaceous matter. Methods like bio-oxidation or pressure oxidation of sulfides and blanking followed by Resin in-leach have already been used to treat these refractory components, but sufficient recovery has not yet been obtained. In the present work, challenges to improving gold recovery from 24% to 92% are introduced using biotechnology, which is environmentally friendly without using high temperatures and high pressures. Graphitic refractory gold ore was sequentially pretreated to oxidize sulfides by thermophilic archaeon *Acidianus brierleyi* and then to decompose carbonaceous matters using the cell-free spent medium (CFSM) from white-rot fungus *Phanerochaete chrysosporium*. The pretreatment by *A. brierleyi* significantly improved the gold recovery from 24% to 77%. Additionally, the crude lignin-degrading enzymes in the CFSM converted the carbonaceous matters into more easily degradable substances, which were removed by alkaline washing, leading to a final gold recovery of 92%. These mineralogical alterations were confirmed by differential thermogravimetric analysis, Raman spectroscopy and quantitative evaluation of minerals with scanning electron microscopy (QEMSCAN). Based on the results, gold grains were mostly liberated after bio-oxidation of sulfides, and in the following CFSM treatment, large particles of carbonaceous aluminosilicate were formed from the aggregation of clay minerals, gold grains and with partially decomposed carbonaceous matters acting as binders, which are easily dissolved in alkaline solutions.

Development of Novel Lithium Recovery Technology from Brine Water by Using Spent LiFePO$_4$ Battery

T.H. Chen, L.Y. Lee, H.I Hsiang

Department of Resources Engineering, National Cheng Kung University, Taiwan
hsingi@mail.ncku.edu.tw

ABSTRACT

In nature, the reserve of lithium in brine and seawater is much larger than that in ore. Therefore, lithium extraction from brine and seawater is the most important way in the present and future. Lithium ion sieve adsorbent is currently used to extract lithium from brine and seawater, which is the most environmentally friendly and economic value. Although it has the advantages of high stability and high selectivity, there are still some disadvantages in operation such as low actual adsorption amount, short life, high dissolution rate of adsorbent, and slow exchange rate. In this study we first develop the technology of recycling waste lithium iron phosphate battery to recycle the spent lithium phosphate which is cheap and has no recycling benefit. Then the recycled lithium iron phosphate powder was electrophoretic deposited on the surface of the metal foam, which was used as an electrode to recover lithium ions from brine and seawater. A novel lithium recovering process with the benefits of low cost, environmentally friendly, high selectivity, high cycle efficiency and a long life cycle was successfully demonstrated.

INTRODUCTION

The properties of lithium and the properties of its main compounds, such as a lithium carbonate, chloride, or hydroxide are essential to many technologies, such as "green" low-carbon technologies, especially for electric vehicle (EVs) batteries, with very important economic and environmental issues at stake. The production of lithium has increased rapidly over recent years due to its high demand in the manufacture of lithium-ion batteries (LiBs) used for portable electronic devices, electric tools, electric vehicles, and grid storage applications. Lithium and its chemicals have been produced on an industrial scale around the world using brines and ores as principal feedstock. However, according to the US Geological Survey in 2015, the global lithium resource is about 39.5 million metric tons, while reserves of lithium with commercial exploitation value is only 13.5 million tonnes, which is far from the needs of the market for lithium resources [1]. In addition, lithium resources are unevenly distributed, mainly in Bolivia, Chile and China. The total storage capacity of lithium resources in these countries accounts for over 80% of the world and the salt lake brine lithium resources is about 70-80% of the total storage capacity. Thus, up to now, high-grade lithium compounds have been processed mostly from salar brines due to low operation costs.

At present, a wide variety of lithium technologies, such as evaporation crystallization, precipitation, solvent extraction, ion exchange, adsorption, calcination and leaching have been developed according to climate, environmental conditions to meet their needs [2]. Among these methods, the ion exchange method is the most green and great economic value. Lithium ion sieve adsorbent has many advantages, such as high stability and selectivity etc., but there are also some disadvantages, such as a small amount of the actual adsorption, high adsorbent loss rate is high, short life and slow exchange rate [3-5].

Olivine-type LiFePO$_4$ has many superior properties, such as high capacity, chemical stability and good

cycle performance, non-toxic, low cost etc., which has been widely used as cathode material in lithium ion batteries [6-7]. The organic electrolyte Li^+ ions constantly intercalate/de-intercalate in the positive electrode material accompanied by the occurrence of Fe^{3+}/Fe^{2+} in the oxidation/reduction reactions during the $LiFePO_4$ battery charge-discharge process. Previous studies investigated the electrochemical properties of an $LiFePO_4$ battery aqueous solution consisting of $LiNO_3$, Li_2SO_4 instead of the organic electrolyte and found that it exhibited good cycle performance (1000 cycles capacity can be maintained at more than 90%) [8]. Therefore, if brine can substitute for aqueous lithium compounds as the electrolyte, the lithium ions in the brine should intercalate/de-intercalate into the electrode via the oxidation- reduction process, which could be used to extract lithium from brines.

In this study we first develop the technology of recycling waste lithium iron phosphate battery to recycle the spent lithium phosphate which is cheap and has no recycling benefit. Then the recycled lithium iron phosphate powder was electrophoretic deposited on the surface of the metal foam, which was used as an electrode to recover lithium ions from brine and seawater. A novel lithium recovering process with the benefits of low cost, environmentally friendly, high selectivity, high cycle efficiency and a long life cycle was successfully demonstrated.

RESULTS

Figure 1 shows the zeta potential of the spent $LiFePO_4$ slurry with solid content of 1wt%. It can be clearly seen that when the dispersant is added at 0.5 mg/m^2, the zeta potential reaches 38 mV when the pH is about 8.5, indicating the $LiFePO_4$ powder is well dispersed and hence can be electrophoretic deposited onto the surface of the Ni foam.
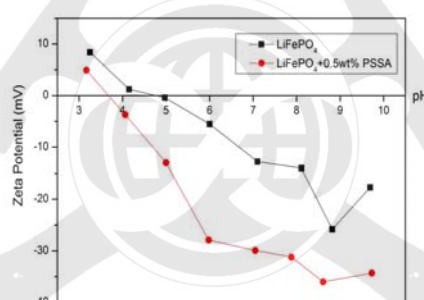
Fig. 1 zeta potential of the spent $LiFePO_4$ slurry with solid content of 1wt%.

Figure 2 is the microstructure of the nickel foam after electrophoresis at 4 V for 2 min. It indicates that the thickness of the electrophoretic deposited $LiFePO_4$ is about 10 μ m to 40 μ m.

Fig. 2 microstructure of the nickel foam after electrophoresis at 4 V for 2 min.

Figure 3 is the ion adsorption selectivity in the simulated brine at 0.3 volt, showing that lithium can be selectively recovered from salt water which contains various cations at the voltage of 0.3 volts.

Fig. 3 Ion adsorption selectivity in the simulated brine at 0.3 volt.

CONCLUSIONS

1. This lithium recovery system successfully demonstrated that lithium can be selectively recovered from salt water which contains various cations.
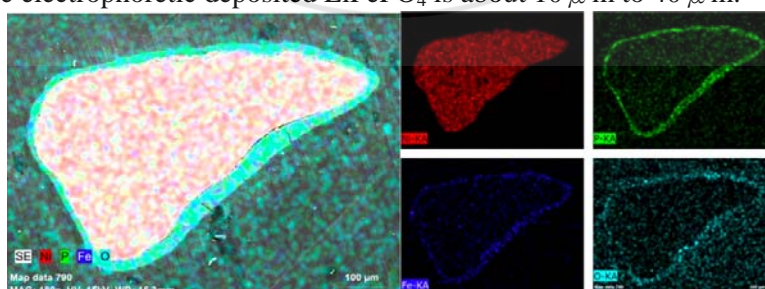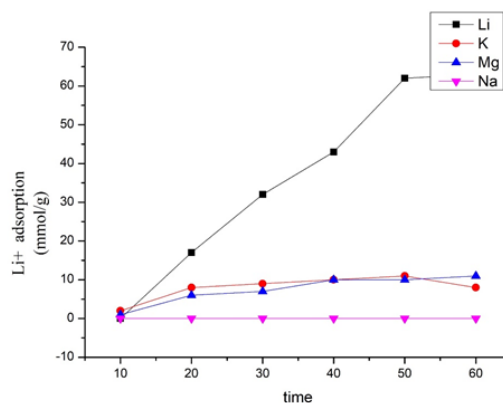2. The Li^+ adsorption efficiency of the nanostructured lithium ion sieve and electroadsorption is better than the traditional ion sieves.
3. Novel lithium recovery technology from brine water by using spent $LiFePO_4$ battery was successfully developed.

REFERENCES

[1] U. S. Geological Survey, Mineral Commodity Summaries, 2015.

[2] A. Chagnes, J. Swiatowska, Lithium Process Chemistry, Elsevier Inc., 2015.

[3] L. Chen, X. Xu, J. Song, X. Zhu and Z. Qi, Microwave assisted hydrothermal synthesis of $MnO_2 \cdot 0.5H_2O$ ion-sieve for lithium ion selective adsorption, Sep. Sci. Tech., 51 (2016) 874-882.

[4] R. Chitrakar, Y. Makita, K. Ooi, A. Sonoda, Selective uptake of lithium ion from brine by $H_{1.33}Mn_{1.67}O_4$ and $H_{1.6}Mn_{1.6}O_4$, Chem. Lett., 41 (2012) 1647–1649.

[5] X.J. Yang, H. Kanoh, W.P. Tang, K. Ooi, Synthesis of $Li_{1.33}Mn_{1.67}O_4$ spinels with different morphologies and their ion adsorptivities after delithiation, J. Mater. Chem., 10 (2000) 1903–1909.

[6] C.L. Gong, Z.G. Xue, S. Wen, Y.S. Ye, X.L. Xie, Advanced carbon materials/olivine $LiFePO_4$ composites cathode for lithium ion batteries, J. Power Sources, 318 (2016) 93-112.

[7] A.M. Haregewoin, A.S. Wotango, B.J. Hwang, Electrolyte additives for lithium ion battery electrodes: progress and perspectives, Energy Environ. Sci., 9 (2016) 1955-1988.

[8] T.V.S.L. Satyavania, A.S. Kumara, P.S.V.S. Rao, Methods of synthesis and performance improvement of lithium iron phosphate for high rate Li-ion batteries: A review, Eng. Sci. Tech., 19 (2016)178-188.

A Study on Solidification of Simulated Radioactive Cationic Exchange Resins using Geopolymer Technology

Yu-Jie Xie, Wei-Hao Lee and Ta-Wui Cheng

Institute of Mineral Resources Engineering, National Taipei University of Technology, Taiwan
kuankuan1234567@gmail.com, glowing955146@hotmail.com, twcheng@ntut.edu.tw


Chun-Ping Huang and Jia-Ying Wu

Institute of Nuclear Energy Research, Atomic Energy Council, Executive Yuan, Taiwan
chunping@iner.gov.tw, sai761030@iner.gov.tw

ABSTRACT

The volume reduction and stabilization of radioactive ion-exchange resins waste produced by the nuclear industry are international problems and need to be solved. Radioactive ion exchange resins waste are low- radioactive wastes, which are usually solidify by cement, asphalt or polymer materials, each method has its own shortcomings needs to be overcome. The development of new solidification technique is still an important issue.

In recent years, there is a new material called Geopolymer. It has been gradually attracting world attention. Geopolymer, similar to natural zeolite minerals, is a class of three-dimensionally networked aluminosilicate materials. Due to its superior mechanical and physical properties, such as non-combustible, heat resistant, fire/acid resistant, easily making, and forming at room temperature. Therefore, it has great potential as the new generation materials for radioactive waste treatment.

This study developed a new form material for solidify radioactive waste by geopolymer technology. According to the experiment results, after the cation-exchange resins solidify by geopolymer technology, the mechanical strength and durability are in compliance with the standards. The same solidification ratio was used to a single batch test of 60 liter, and it was found that the test samples can still meet the standard. This can be proved that solidification of ion-exchange resins using geopolymer technology is effectively meets the low-radioactive waste form standard, and increasing the amount of solidification by volume for the ion-exchange resins, thereby helping to store more ion exchange in the effective space.
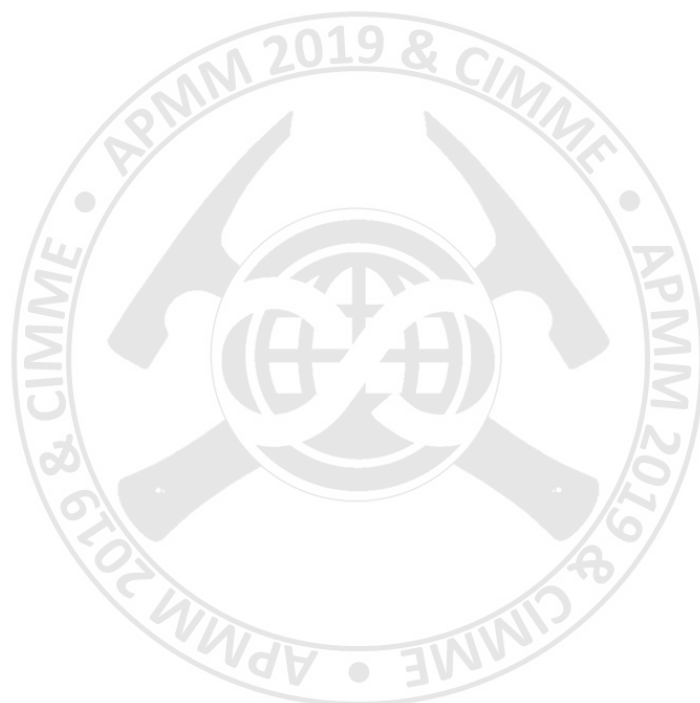
A Study on Improvement Geopolymer Fabrication Process

Yung-Ting Lin and Ta-Wui Cheng

Institute of Mineral Resources Engineering, National Taipei University of Technology,
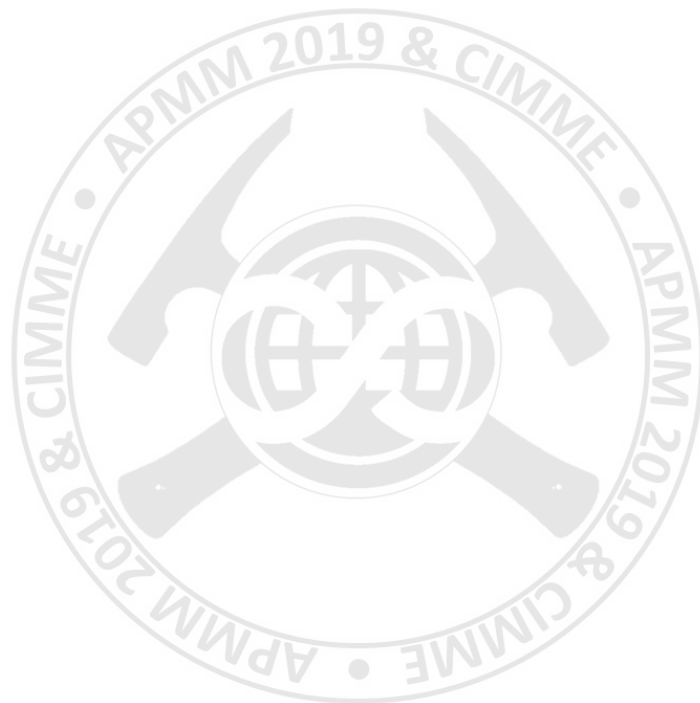*Taiwan*
t104332042@gmail.com, twcheng@mail.ntut.edu.tw

ABSTRACT

Geopolymer material mainly uses industrial waste as bonding material. When bonding material mixing with alkali solution, the abundant of silicon ion and aluminum ion are dissolved from the waste surface. After polymerization, dehydration and hardening, Si-O-Si and Si-O-Al structure of three-dimensional framework was formed, which similar to the zeolite phase. It provides great properties such as high compressive strength, fire resistant performance and durability. Therefore, geopolymer material have great potential on replacing traditional Portland cement in the future. Generally, to form geopolymer need to mix reaction powder and alkali solution. It is not very convenient while operation geopolymer in real case. The purpose of this study is improving the process of geopolymer as similar as utilization of traditional Portland cement, directly adding water to occur the reaction. Starting with slurry, the concentration of sodium hydroxide came from calcium hydroxide and sodium carbonate reaction. According to the experiment results, glass powder replacing partial bonding material can increase the compressive strength up to 72.2 MPa after 28-day curing at room temperature. In the follow-up test, the geopolymer mortar was made with a molar concentration of 6M, liquid-solid ratio of 0.8, and glass powder replacing 10% for bonding material. Compared with Portland cement mortar after 28-day curing at room temperature, the results show: geopolymeric mortar can reach 37.5 MPa higher than 33.4 MPa in Portland cement mortar; the compressive strength of geopolymeric mortar in long-term curing has continuous rising, and it's invariable in Portland cement mortar. Hence, adding glass powder instead of partial boding material is highly feasible on improvement geopolymer fabrication process.

Keywords
Geopolymer technology; calcium hydroxide; sodium carbonate; glass powder

International Conference on Asia Pacific Mining and Metallurgy

Tainan, Taiwan, November 17-20, 2019

Section 1：Geo-resource Exploitation

13：00 – 14：50   International Conference Hall

13:00-14:50	Session Chair:	Prof. **Yung-Chin Ding** National Taipei University of Technology

13:00-13:30	CIMME108158	**Prof. Sangki Kwon** Inha University, Korea

Influence of Excavation Damaged Zone around an Underground Excavation on Thermal, Hydraulic, and Mechanical Behaviors of Rock

13:30-14:00	CIMME108088	**Cheng-Wen Chu** CPC Corporation, Taiwan

Application of James Lip Pressure Method for Geothermal Wells in North-Eastern Taiwan

14:00-14:30	CIMME108100	**Yuan-Ming Li** CPC Corporation, Taiwan

The Application of Machine Learning to Gamma Ray Prediction of Well Logging

14:30-14:50	CIMME108061	**Yi-Lung Huang** CPC Corporation, Taiwan

From Reservoir to Tanks - the Practical Experience of the Field Operation in Chad

Influence of Excavation Damaged Zone Around an Underground Excavation on Thermal, Hydraulic, and Mechanical Behaviors of Rock

Sangki Kwon

Department of Energy Resources Engineering, Inha University, Korea
kwonsk@inha.ac.kr

ABSTRACT

It is inevitable to have an excavation damaged zone(EDZ), in which the original rock properties are changed due to the blasting impact or stress redistribution around underground facilities In order to predict the performance of underground facilities, the understanding of the characteristics of EDZ and its influence on the thermal, hydraulic, and mechanical behaviors are important. In this study, the characteristics of an EDZ were investigated from in situ experiments and laboratory tests. Using computer simulation, the influence of the EDZ on the thermal, hydraulic, and mechanical behaviors was evaluated.

INTRODUCTION

There are two possible causes of EDZ development.
1) Blasting impact: In a crystalline rock mass, a large part of the EDZ develops due to the blasting impact. With the ignition of explosives in blast holes, extremely high pressures can be developed. Because of the high pressure, the rock surrounding the blast hole is crushed and radial cracks spreading from the hole with the expansion of fume gas at high temperatures. The cracks generated from the explosion can increase the hydraulic conductivity in the EDZ significantly. A previous study reported that the degree of rock damage was reducing gradually with increasing distance from the tunnel wall (Kwon et al., 2009).
  2) Stress redistribution: After a tunnel excavation, the original stress is redistributed and reoriented depending on the tunnel geometry, rock properties and in situ stress condition. When the induced stress around a tunnel is higher than the rock strength, the rock can be damaged. Because the crack initiation stress is much lower than the rock strength, the rock surrounding an underground tunnel can be spalled with time even under relatively low stresses. Other effects, such as relaxation of failed material, pore pressure change and thermal stress related to decay heat generation, can also be involved in the time dependent evolution of an EDZ. The change in stress expected after excavation can also affect the aperture of discontinuities and the hydraulic conductivity of rock mass.

CHARACTERISTICS OF EDZ

The Excavation Damaged Zone (EDZ) is a zone with hydro-mechanical and geochemical modifications inducing significant changes in flow and transport properties. The size of EDZ and the variation of rock properties in the zone were investigated at an underground research tunnel, KURT(Kwon et al., 2006). Various thermal, hydraulic, and mechanical properties were extensively measured using in situ and laboratory tests at KURT. Fig.1 shows the variation of deformation
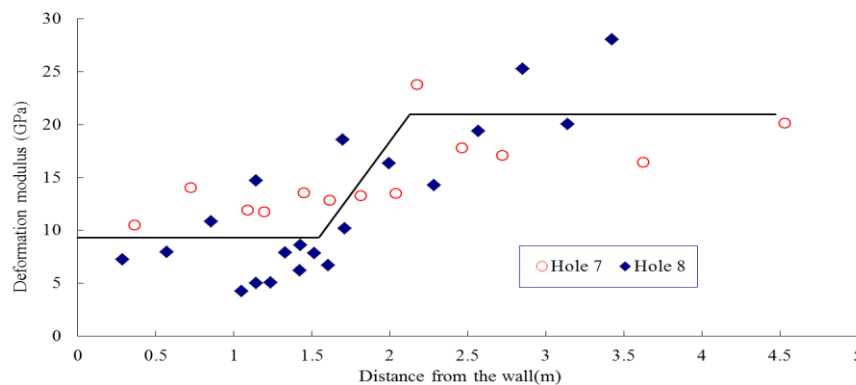
modulus with distance from the tunnel wall.

Figure 1. Variation of the deformation modulus measured at KURT

SIMULATION OF THE INFLUENCE OF EDZ

Several computer simulations were carried out to examine the influence of the EDZ on various aspects. Initially, mechanical analysis of KURT rock was performed to determine the influence of the EDZ itself and the non-uniform rock properties in the EDZ. The displacement and factor of safety can be influenced significantly by the EDZ and its properties Secondly, hydro-mechanical analysis was carried out for KURT(Fig.2(a)). Finally, thermo-mechanical analysis was carried out for an in situ experiment(Andersson, 2007) for determining the spalling strength(Fig.2(b)). When a 0.5m thick EDZ was considered in modeling, the stress condition and possible failure zone changed, particularly in the zone near the floor.
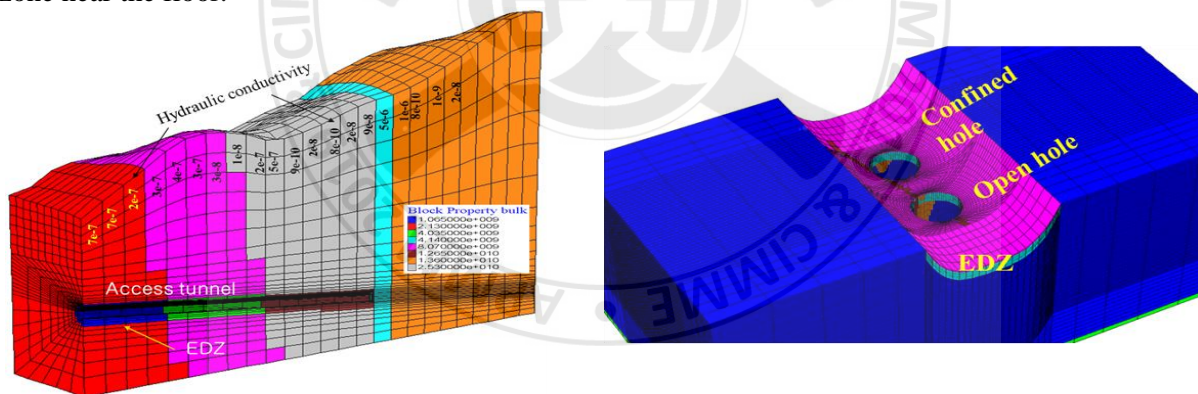
(a) Hydarulic-Mechanical analysis for KURT   (b) Thermal-Mechanical analysis for APSE

Figure 2. Comuter simulations for investigatin the influence of EDZ
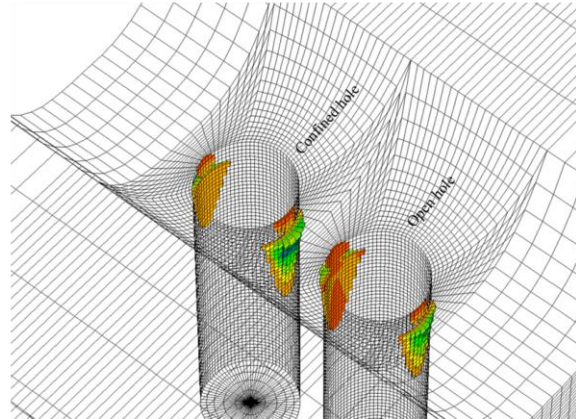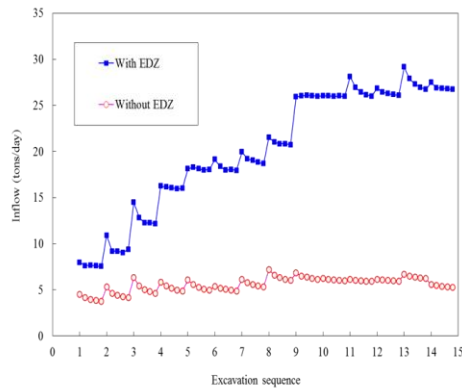
(a) Inflow from HM analysis for KURT   (b) Failed zone from TM analysis for APSE

Figure 3. Results of computer simulation with a consideration of EDZ

CONCLUSIONS

According to the laboratory tests using the rock cores from KURT, it was possible to determine that the rock properties were damaged during excavation. For example, the elastic modulus in an EDZ was approximately 50% of the undisturbed rock. From the in situ tests, it was possible to conclude that an EDZ would develop up to 2m from the tunnel wall. A transition zone was observed in the range, 1.5~2m.   From the different modeling, it was concluded that the EDZ around an underground opening can affect the various behaviors of rock mass.   Therefore, it is strongly recommended to minimize the development of EDZ by careful blasting.

REFERENCES

Andersson, J.C.(2007). Aspo Pillar stability experiment. Final report, SKB TR-07-01.

Kwon, S., Cho, W.J., Han, P.S.(2006). "Concept development of an underground research tunnel for validating the Korean reference HLW disposal system," Tunnelling and Underground Space Technology 21: 203~217

Kwon,S., Lee.C.S., Cho,S.J.,Jeon,S.W.,Cho,W.J.(2009). "An investigation of the excavation damaged zone at the KAERI underground research tunnel," Tunnelling and Underground Space Technology 24:1~13

Application of James Lip Pressure Method for Geothermal Wells in North-Eastern Taiwan

Cheng-wen Chu, Te-Kun Huang, Jin-Fa Chen and Wei-Jr Wu
Exploration and Development Research Institute, CPC Corporation, Taiwan.
155934@cpc.com.tw, 155314@cpc.com.tw, 155438@cpc.com.tw, and 155331@cpc.com.tw.

Bing-Cheng Chen
Exploration and Production Business Division, CPC Corporation, Taiwan.
050881@cpc.com.tw

ABSTRACT

According to the white paper on energy planning from the ministry of economic affairs in 2017, it is planned that building 150 MWe geothermal power plant in 2020 in Taiwan. To finish the government's policy, in 2019, CPC has drilled 2 new geothermal wells at northeastern Taiwan and look forward to high-temperature geothermal fluids through two new geothermal well. Then, cooperating with Taipower company builds new geothermal power plants. To know the production capacity of geothermal wells, the two new wells are planned to have a production test. The enthalpy of geothermal fluid is measured by using the method of horizontal discharge test with James lip pressure method. This study collated the publicly available data of the James Lip Pressure Method in the geothermal wells in northeastern Taiwan and matched the discharge test data of the two new geothermal wells in this year. The James Lip Pressure method was applied to the two new geothermal processes. The results of the discharge test of these wells were collected and analyzed. The sensitivity analysis of James lip pressure method was also analyzed. The information is necessary as parameters for calculating power generation in the future and as an important reference for construction planning of geothermal power plant in the future.

INTRODUCTION

To build Taiwan geothermal power plant smoothly, it is necessary to know the production capacity of geothermal wells. Among them, the horizontal discharge test is the most direct method to know the enthalpy (kJ/kg) of production capacity of geothermal wells, and the James lip pressure method is the main method to measure the enthalpy of geothermal fluid in the world. This paper shows how James lip pressure method applied to the geothermal discharge test in northeast Taiwan and analyzes the test data to understand the production capacity of geothermal wells in northeast Taiwan.

The purpose of this study is to use the James lip pressure method to measure the pressure (Lip pressure) of the geothermal fluid ejected from the lip pipe, and to measure the flow rate of the geothermal liquid by weir measurement method. Then, we would calculate the enthalpy(kJ/kg) of the geothermal well, and use the formula to calculate the gas content (%) and the total enthalpy (kJ/s), and use the data obtained by this method to carry out important reference data for the selection of geothermal power plant generator design. Therefore, this study collected both the geothermal wells in Qingshui geothermal area which has publicly available data in the past and the qualitative data currently of new geothermal wells drilled by CPC this year. The method of measuring enthalpy is James lip pressure

method. However, since the geothermal wells drilled this year have not completed the complete capacity test, only the currently collected qualitative data is analyzed and sorted.

METHOD

By testing and recording lip pressure at different pipe diameters, wellhead temperature, separated liquid flow rate and using the James lip pressure method to calculate the enthalpy (kJ/kg) of unit weight of the geothermal fluid. The test process of James Lips Pressure is that (1) Build up horizontal pipes in the horizontal ground (2) To erect a nozzle in the exit of horizontal lip pipe (3) To measure the lip pressure at the place where the geothermal fluid is sprayed through the lip pipe and the nozzle. (4) The geothermal fluid is led to the silencer to separate liquid and gas. (5) The separated water is led to the rectangle weir and measuring the flow rate. Therefore, the nozzle diameter is measured at step (2), the lip pressure is measured at step (3) and the flow rate is measured at step (5). Horizontal discharge test equipment schematic is shown in Figure 1.
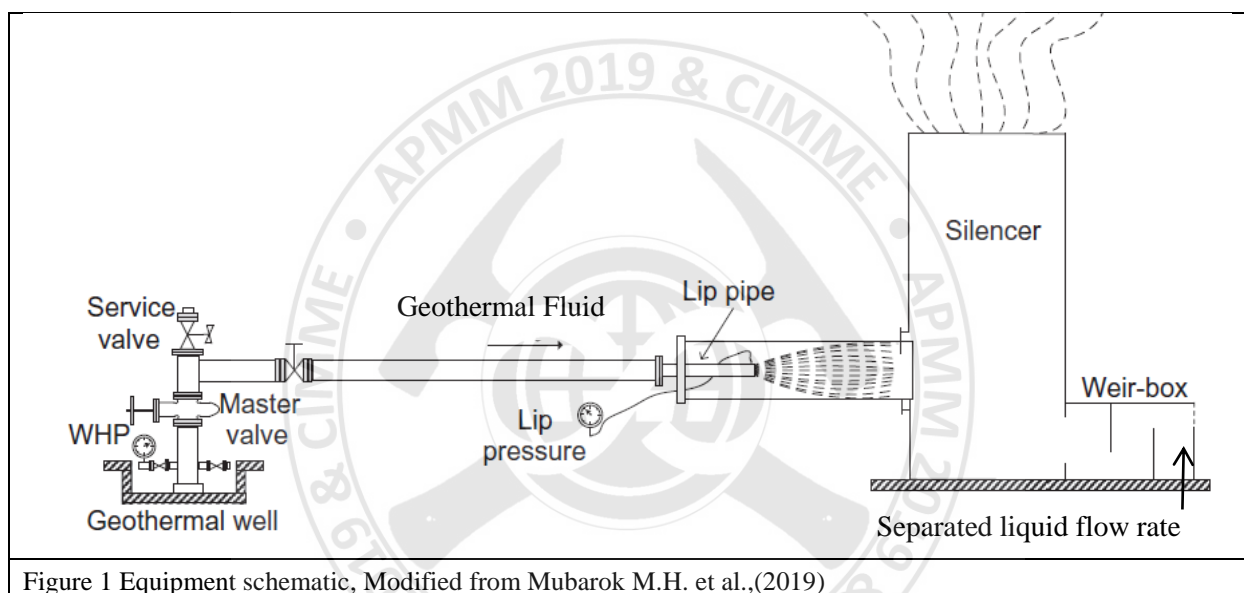

Figure 1 Equipment schematic, Modified from Mubarok M.H. et al.,(2019)

To carry out the calculation of the discharge test, only 3 parameters are measured. First one is the cross-section area of horizontal lip pipe (cm^2). Second one is absolute lip pressure (kg/cm^2) (absolute pressure = table pressure + atmospheric pressure). The last one is separated liquid flow rate (tph). According to that 3 parameters and the formulas from James Lip Pressure Method can calculate the enthalpy (kJ/kg), total enthalpy (kJ/s), steam flow rate (tph), total flow rate (tph) and gas content (%).Otherwise, a study showed that this method gives the results with about 8% error margin. (Grant M.A. et al.,2011)

RESULT AND DISCUSSION

1. Qualitative data of two new geothermal wells have been drilled by CPC in northeast Taiwan this year

According to figure 2 and figure 3, because of the unstable situation of opening well, data from first 250 seconds has a significantly different character than data after 250 seconds, so the reliable data from four-inches pipe discharge is only taken after 250 seconds. In four-inches pipe flow, lip pressure

values are slightly unstable. The total enthalpy is also slightly unstable. Separated liquid flow rate is relatively stable, and the enthalpy is also relatively stable.
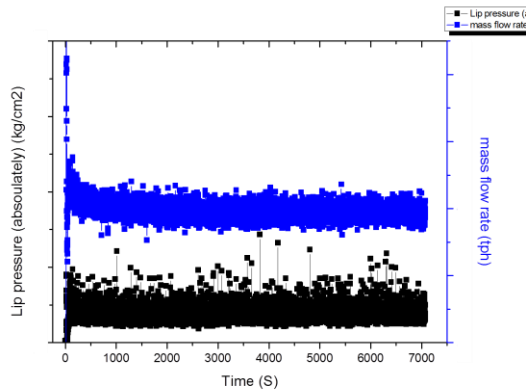

Figure 2 Linear diagram of lip pressure and separated liquid (mass) flow rate over time in a new well with a four-inch lip pipe.
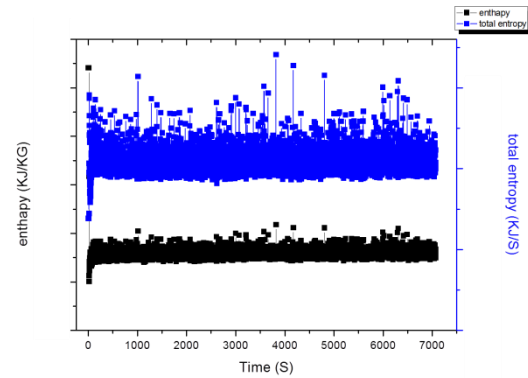

Figure 3 Linear diagram of the change of enthalpy and total enthalpy over time in a new well with a four-inch lip pipe
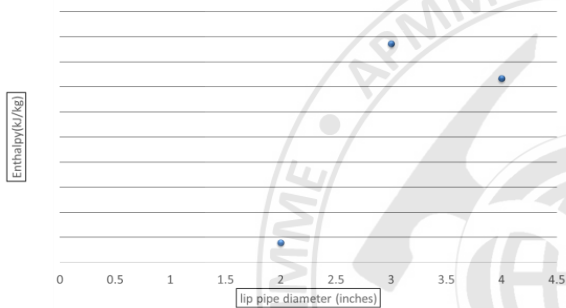

Figure 4 The larger lip pipe diameter size, the more separated liquid flow rate in a new geothermal well.
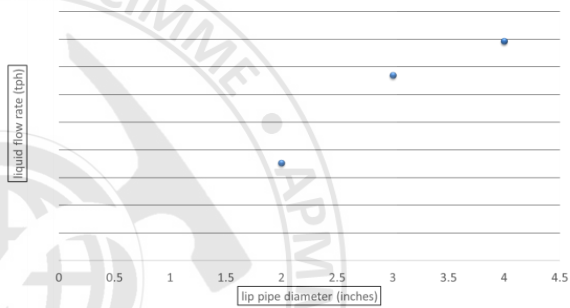

Figure 5 The larger lip pipe diameter size, the higher the trend of enthalpy, but the linear relationship is bad.

According to figure 2 and figure 3, the larger lip pipe diameter size is, the more separated liquid flow rate will be. However, according to figure 4 and figure 5, in the value of enthalpy, although the trend is the larger the lip pipe diameter size is, the linear relationship is not good. Therefore, although the larger lip pipe diameter size is, the more hot water flow will be, but the enthalpy will not necessarily be higher, and the overall domain will not be too large. In addition, according to the data of Qingshui geothermal wells, the larger lip pipe diameter size is, the more separated liquid flow rate is. On the other hand, in the valve of enthalpy, the larger lip pipe diameter size is, the higher the trend of ic-9 and ic-21 are, but in the ic-19, ic-13 and a new well are not the same.

2. Sensitivity analysis of James lip pressure method of new geothermal wells drilled by CPC

According to figure 6 and figure 7, if the error of lip pressure (gauge) is +10%, it will only cause an impact of about +2% on enthalpy, but if the error of hot water flow is +2.5%, it will cause an error of +2% on enthalpy. When the same error is caused by +2% on enthalpy, the influence degree of hot water flow is about four times that of lip pressure (gauge). In addition, it can be found that both the negative error of lip pressure (gauge) and the negative error of hot water flow have less impact on enthalpy than the positive error. Among them, the error of lip pressure (gauge) -100% results in the

error of enthalpy of about -16%. The error of lip pressure (gauge) +100% results in the error of enthalpy about +18.5%. The error of separated liquid flow rate -12.5% results in the error of enthalpy -8%, while the error of separated liquid flow rate +12.5% results in the error of enthalpy +11%.
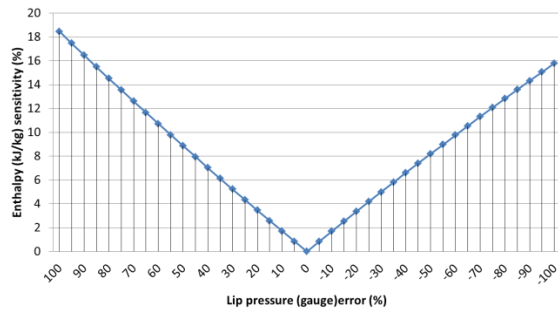

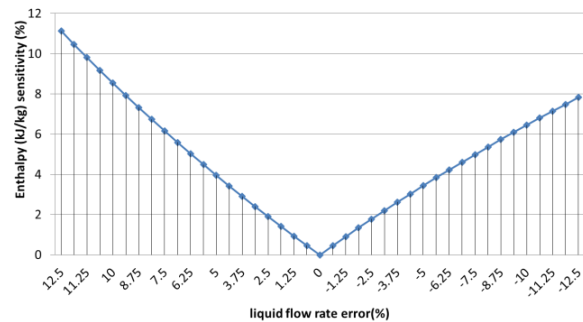Figure 6 Diagram of a sensitivity analysis of lip pressure to enthalpy

Figure 7 Diagram of a sensitivity analysis of separated liquid flow rate to enthalpy

CONCLUSION

1. Regarding the correlation between enthalpy and lip pipe diameter size, the trend is that the larger the size is, the higher the enthalpy will be. However, it can be further explored whether there is a linear relationship or no obvious correlation, or whether the linear relationship will decrease after a certain size.
2. The larger lip pipe diameter size is, the more hot water flow will be. The value needs some time to reach a stable balance.
3. In the sensitivity analysis, the positive errors of both lip pressure (gauge) and separated liquid flow rate have greater influences on enthalpy than the negative errors. When the same effect is +2% on enthalpy, the influence degree of hot water flow is about four times that of lip pressure (gauge).
4. The separated liquid flow rate is stable, and there is no intermittent fountain phenomenon, which means the flow data shows a high fluctuation over time. It is speculated that due to the new drilling, pollution is not big, and the well is in good condition.
5. The discharge test is only part of the productivity test. Downhole pressure and temperature measurements, water injection tests, and build-up tests must be performed to achieve full well or geothermal field productivity. Interference test is also necessary to know whether the new two geothermal wells connect each other and affect the capacity with each other.
6. A pressure gauge can be installed in the wellbore to measure wellbore flow pressure (IPRs). Productivity index (PI) can also be calculated from this data as a quantitative method to determine the relationship between pressure loss per unit of production well and production flow. As a benchmark comparison of different production wells.

REFERENCES

1. 經濟部-宜蘭縣清水地熱區 IC-9、IC-13、IC-19 地熱井修井後產能測試成果摘要。(2015)
2. Bixley P.F. and Grant M.A. (2011)。Geothermal Reservoir Engineering。P147-150。
3. Zarrouk S. and Mclean K. (2019)。Geothermal Well Test Analysis。P135-154。
4. Ireamukhti R. et al., (2015)。Evaluation of James Lip Pressure Method for Low Flow Rate Geothermal Well: ML-5 Case Study.
5. Mubarok M.H., Zarrouk S.J., Cater, J.E., (2019). Two-phase flow measurement of geothermal fluid using orifice plate:field testing and CFD validation. Renew. Energy 134, 927-946.

The Application of Machine Learning to Gamma Ray Prediction of Well Logging

Yuan-Ming Li

Geologist, EDRI, CPC Corporation, Taiwan
155837@cpc.com.tw

ABSTRACT

Recently lots of disciplines are integrated by Machine Learning (ML) to form an effective data processing tool to address the problems, particularly those with huge, sophisticated, diverse and nonlinear data, namely the Big Data. The conventional software of data processing or artificial approach gradually fails to copy with them. Big data is a feature of the well logging data. In order to obtain the subsurface geological data around in an area around a given concession where lacks precise geological model, a Gamma Ray (GR) model is established by ML to predict the GR value of the virtual well. Making a comparison between virtual and real helps to understand how big the error is. Based on the data of six wells from A to F, the study aims to predict the GR value of Well A through a well-trained ML model with Well A as testing data and Well B-F as training data. The predicting model established by ML can be divided into two types: Regression and Classification. There are five types of algorithms of ML used in this study including four Regressions: Random Forest Regression (RF), Gradient Boosting Regression (GBR), Support Vector Regression (SVR), and Multi-layer Perception Regression (MLPR), and finally one Classification: Decision Trees (CART). To summarize, the comparison among all five algorithms shows that the RF is the best to predict the GR value of well logging.

INTRODUCTION

With great improvement of computer hardware facility and algorithm, for the diverse and sophisticated big data the application of ML in image recognition, voice recognition, automatic translation, medical diagnosis, virtual individual assistant, recommendation by search engine, internet fraud detection, etc. is increasingly popular. Huge data will be produced every day in operation of upstream including exploration and production, midstream storage and transportation, downstream refining and marketing. The accumulated data over the years could shed light on where the reserve is, where the unstable formation is, where the unperceived damage is and where the prospective oil area is.

Engineer and geoscientist spend over half of their time in searching and assembling data before multidisciplinary analysis is even begun (Brulé, 2015). It was not until 2012 that among all oil and gas companies there are about 70% haven't perceived yet the emerging issue related to both big data and ML (Feblowitz, 2012). However, during 2012 to 2018, it was gradually gathering momentum and about 81% of senior management in 2018 took it as one of the year's top three issues (Mehta, 2016). Besides, in 2019 the AAPG annual convention that has been demonstrating the latest knowledge, state-of-the-art technology, and global achievement in exploration put the issue related to big data exclusively as one of the convention several major theme sessions and set up three theme sessions for

the discussion of the issue combining the big data and the exploration (Fig. 1), compared to previous ones whereby there was no sessions for the issue. Therefore, the application of big data, AI and ML in oil and gas exploration has become a trend. The study about the issue is the important job that global oil companies are undertaking.
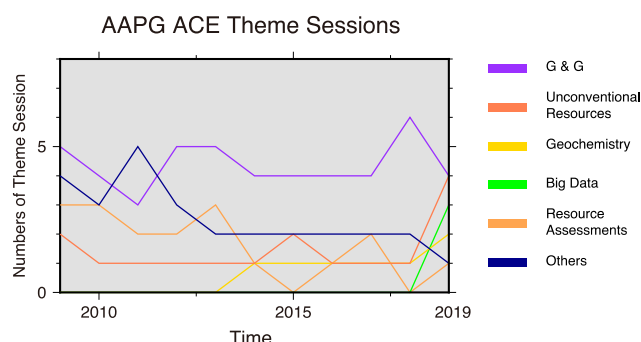

Figure 1. The distribution of the theme sessions demonstrated by AAPG annual convention. From top to down are G&G (geology and geophysics), unconventional resources, geochemistry, big data, resource assessments, and others (climate change, renewable energy and exploration of the Mar)

The study aims to establish a GR prediction model with six wells from A to F by the application of algorithm, widely used in ML in both academia and industry, which include RF, GBR, SVR, MLPR and CART. A comparison between the outcomes resulted from different algorithms and the real figure will show the error and imply its suitability. The real GR value of six wells A-F is shown in Fig. 2.
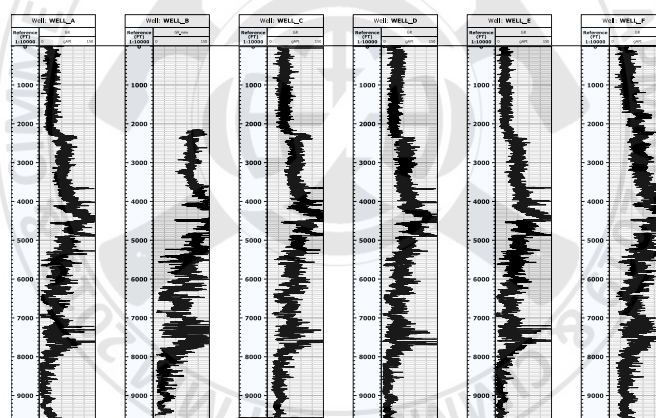
Figure 2. The GR value of wells A to F, the unit: gAPI

Study Method

The ML uses the software Python 3.6 with the input libraries/packages os, numpy, pandas, math, mathplotlib.pyplot, sklearn.neural_network, sklearn.ensemble, sklearn.metrics, sklearn.tree, sklearn.svm, and pydot to establish a GR prediction model. After going through data preprocessing, the data is reorganized to be a data structure in the form of Dataframe table. The parameters include depth, GR value, longitude and latitude with the GR values taken as label and other three items as features of the data. Then the data is separately input into the various algorithms of ML with Well A as the data of the testing well, Wells B-F as the data of training wells to predict the GR value of Well A through a well-trained model. An error will be found by comparison between the value obtained by prediction and the real one. It helps to understand the accuracy and efficiency of various algorithms of ML and also test the reliability of the prediction model in the prospective area.

The Process of the study is as follow. (Fig. 3)

| State the question and determine required data |
| Question: can we predict the well's GR value around a prospect? |

| Acquire the data in an accessible format |

| Identify and correct missing data or anomalies |

| Data preprocessing |

| Machine Learning | | | | |
| RF | GBR | SVR | MLPR | CART |

| Results visualization and interpretaion |

Figure 3. The process of prediction model established by ML

Results and Discussion

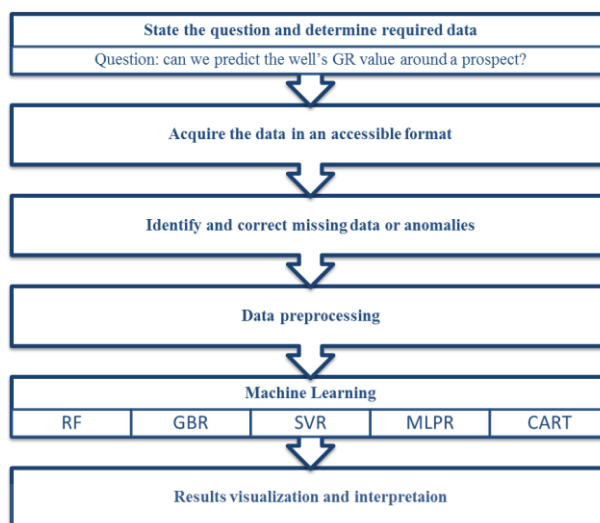The comparison between GR prediction value and real one is shown in Fig. 4. The error caused by statistically calculation is shown by MAE (Mean Absolute Error), RMSE (Root Mean Square Error), and R^2 (Coefficient of Determination) (Table 1). The results obtained by five different algorithms of ML show that the MAE is 14.29 to 17.51, the RMSE is 20.04 to 23.55, and R^2 is -0.12 to 0.49. The prediction indicates that the error of the RF is the lowest in terms of MAES and RMSE, while the GBR value is the highest in terms of R^2, compared to the algorithm of other ML.

With regard to GR prediction value, the algorithms of RF, CART and GBR are most suitable, although calculation is different. The error produced by calculation of CART is substantial in particular, which could be ascribed to the reason that the CART belongs to the Classification Mode, in contrast, other four belong to the Regression one. The CART cannot be conducted until the data type is transformed from floating point number to integer when the GR value is input as the label of the data. This method is able to process both numerical data and categorical on simultaneously, but the RF, one kind of Decision Trees, has some advantages such as higher speed of processing, smaller error of the repeated calculation, and better accuracy of prediction.

Based on the prediction result of the Well A through prediction model into which the data of the trained Wells B-F is put, the GR prediction value of the GBR is better than that of the RF in terms of R^2. However, the better result obtained by the GBR through gradient rise to repeatedly input weakens the change of lithology which is presented by the real GR value. One segment of GR value around the 8,000 feet is abnormally high and the GBR here also weakens the feature caused by its high GR value. In the GR value prediction model established by the study, the RF performs better and produces the result that corresponds much better to the real one.

As the GR value prediction model is established in a prospect with multi-wells that are not far from one another, similar geological conditions without faulting activities, the predicted value much more correspond to the real one. Although the GR value can be obtained quickly from the nearby well, with assistance of characteristic figure from well data and seismic data the ML will improve its prediction

quality by more study of the feature.

Since there is a plethora of data in oil and gas exploration sector, much time consumed in searching and organization can be saved if the previous data is effectively organized and structured. Consequently, if a problem is raised and solved by ML, we will be able to strengthen efficiency, increase success rate of exploration, lower cost of risk and then pass down the expertise and experience to the future.
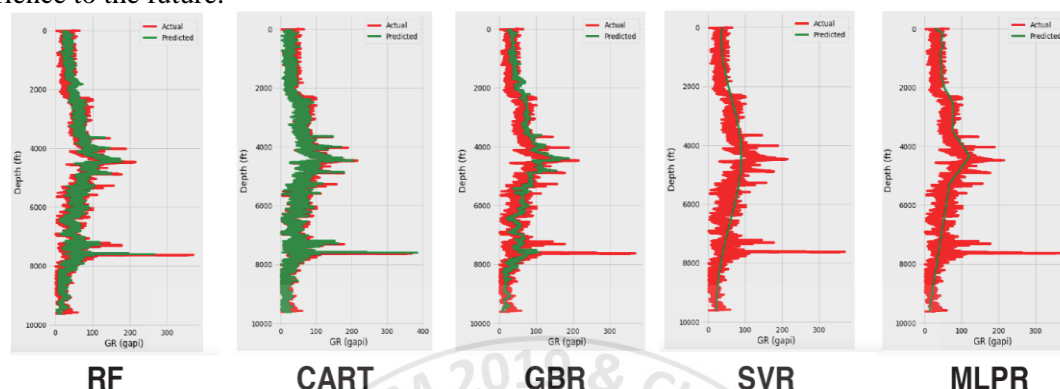
Figure 4. The comparison of the predicted GR values obtained by five algorithms of ML. The predicted GR value is line in green, the real on is in red

Table 1. The statistics of errors caused by five different algorithms of ML

	RF	CART	GBR	SVR	MLPR
MAE	14.29	14.80	16.16	17.51	16.68
RMSE	20.04	21.50	21.73	23.55	21.93
R^2	0.45	0.43	0.49	-0.12	0.26

CONCLUSIONS

1. In the GR value prediction model, the RF has the advantage of prediction, as it can provide more effective and quality results, compared to other algorithms of ML.
2. The growing trend toward the application of big data, AI and ML in exploration, improve efficiency, lower cost and pass down the expertise and experience.

ACKNOWLEDGEMENTS

REFERENCES

Brulé, M.R. (2015). The Data Reservoir: How Big Data Technologies Advance Data Management and Analytics in E&P. Society of Petroleum Engineers (SPE). Doi: 10.2118/173445-MS.

Feblowitz, J. (2012). The Big Deal About Big Data in Upstream Oil and Gas. IDC Energy Insights, 1-11.

Mehta, A. (2016). Tapping the Value from Big Data Analytics. Journal of Petroleum Technology, 68, 40-41.

From Reservoir to Tanks - the Practical Experience of the Field Operation in Chad

Yi-Lung Huang, Jin-Fa Chen, Hong-Sen Liang, Wei-Jr Wu, and Ta-Lin Chen
Exploration and Development Research Institute, CPC Corporation, Taiwan.
155497@cpc.com.tw, 155438@cpc.com.tw, 155446@cpc.com.tw, 155331@cpc.com.tw, and
049298@cpc.com.tw.

Chen-Hui Fan
Exploration and Production Business Division, CPC Corporation, Taiwan.
155322@cpc.com.tw

ABSTRACT

Among all projects that CPC involves abroad, the Oryx field in Chad is the only one operated by OPIC, a subsidiary of CPC Corporation, Taiwan, and go through from the exploration phase into the development phase. This field is expected to be put into production by the end of 2019, and the field development is currently on its last mile towards the first oil. The success of this oil field is a result of cross-departments cooperation, and a successful patent has been set up for future cooperation. This study describes the works and the challenges of the field operation in different phases in Chad, and how we conquer the challenges.

INTRODUCTION

OPIC Africa Chad Branch (OPIC), a wholly-owned subsidiary of CPC Corporation, Taiwan (CPC) has been awarded the exploration permit of the BCOIII block in Chad since 2006 (Figure 1). Meanwhile, Exploration and Production Business Division (EPBD) and Exploration and Development Research Institute (EDRI) organized a task force to conduct the in-house study supporting the exploration from Taiwan. The 2D seismic data collection was completed in 2007. After seismic interpretation and petroleum system research, several structures with high hydrocarbon-bearing potential were identified. The first well, Benoy-1 was spudded in November 2010, and completed in January 2011 with remarkable success. The production rate is as high as 9,800 bbl/d, which encouraged and enabled further explanation to continue. The 3D seismic data collection was completed in 2011, and the interpretation indicates the hydrocarbon-bearing structures more accurately. After Benoy-1 OPIC had another three discoveries in Benoy West, Mbaikoro and Mouromar in the following years. Four hydrocarbon-bearing structures are identified in the Oryx oil field (Figure 2), and the preliminary study indicates that it has the potential to be commercialized. The Field Development Plan (FDP) was composed by the task force in Taiwan in 2016 and submitted to the Chad government with the Environmental Impact Assessment (EIA) and other essential documents. The Exploitation Permit (EP) were granted to OPIC in July 2017. The development is currently at its final stage, targeting the goal of first oil by the end of 2019.

2006	2007	2008	2009	2010	2011	2012	2013	2014	2015	2016	2017/7
• Blocks Awarded	• 2D Seismic				• Benoy • 3D Seismic		• Benoy West	• Mbaikoro	• Mouroumar	• FDP	• EIA • EP

2017/7	2018	2019/12
• FEED	• EPCIC	• First Oil

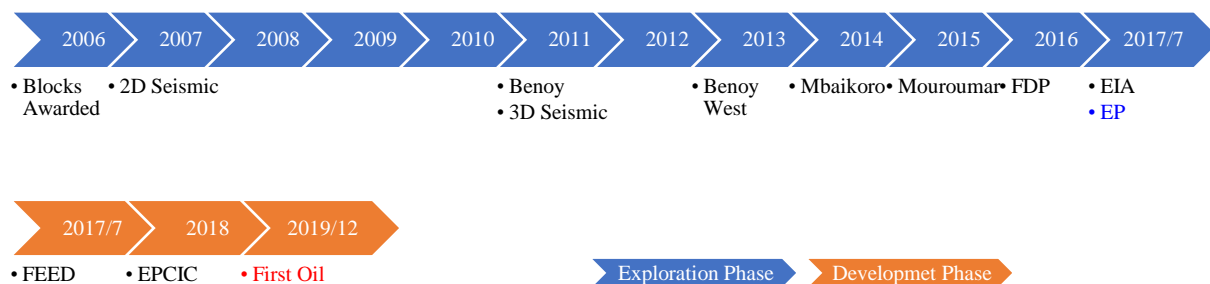Exploration Phase   Developmet Phase

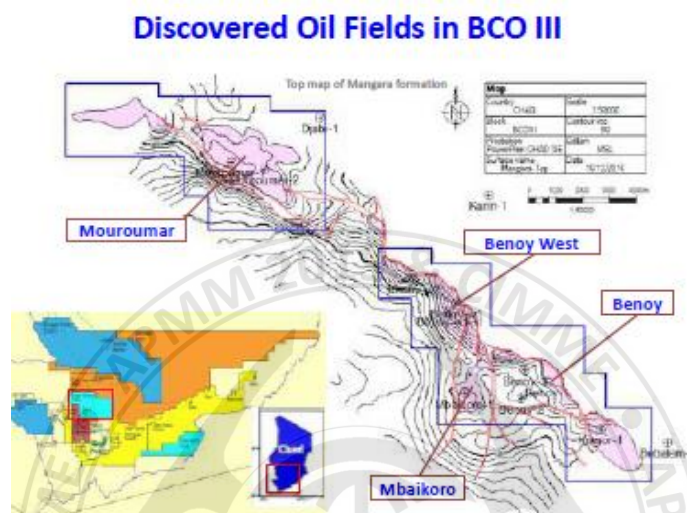Figure 1 The chronicle of CPC's field operation in Chad

Figure 2 Oil Fields in BCOIII

Source: Wen-Lu Shen et al. (2018)

EXPLORATION PHASE (2006/1-2017/5)

The main objective of the exploration phase is to find enough hydrocarbon and to verify its commercialization potential. To fulfill the objective above, geologists, geophysicists, and geochemists have to do a lot of researches to find the well location with the highest hydrocarbon-bearing potential to drill. Figure 3 shows the works been done in the exploration phase. Several data were collected and some tests conducted while the exploration or appraisal wells were drilling, such as cutting, logging, mud logging, fluid sampling, drill stem test (DST) and modular formation dynamic test (MDT) etc.. The test data and the samples were sent back to EDRI for laboratory analysis and computer simulation, and the results were then fed back to modify the geology model and to decide the location for the next well. It's a reinforcing loop for optimizing the drilling decision. The development concept is provided based on the reservoir simulation, and the feasibility of commercialization are evaluated through economic analysis. The task force starts to compose the FDP since four major structures were confirmed, and Figure 4 shows the workflow. On top of the FDP, OPIC also completed the EIA to file for the EP.

The major challenges of the exploration phase are time, the rainy season and approach the operator of the export pipeline. The hydrocarbon with commercialized potential must be found before the end of the exploration phase or Chad government will revoke the exploration permit. So, the task force spent a lot of efforts to find the best spot to drill and continued to optimize the decision through the reinforcing loop (Figure 3). The rainy season causes huge trouble for logistics and the fieldwork, such as seismic

data collection and drilling, due to the road and wellsite condition. Therefore, all the field works should be done before or after the rainy season. There is only one crude oil export pipeline in Chad which transports the crude oil from Chad to Cameroon and sales to the international market. OPIC starts the transportation negotiation with the pipeline operator in 2015 to know what requirements needs to be fulfilled before the crude oil from the Oryx field to be pumped into the export pipeline. OPIC also launch the pipeline route survey project to investigate the route to tie-in the export pipeline.
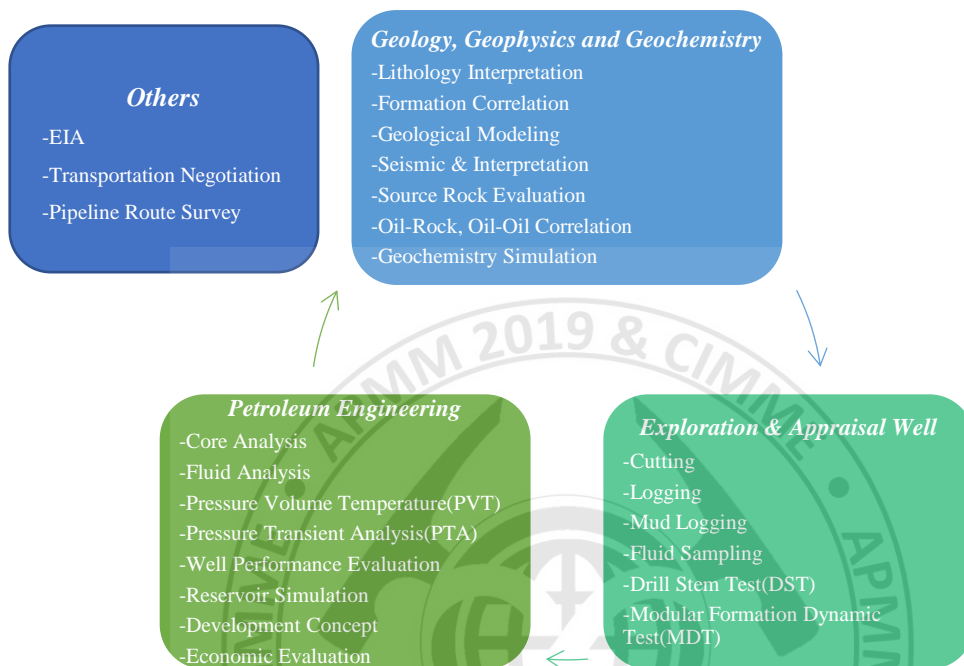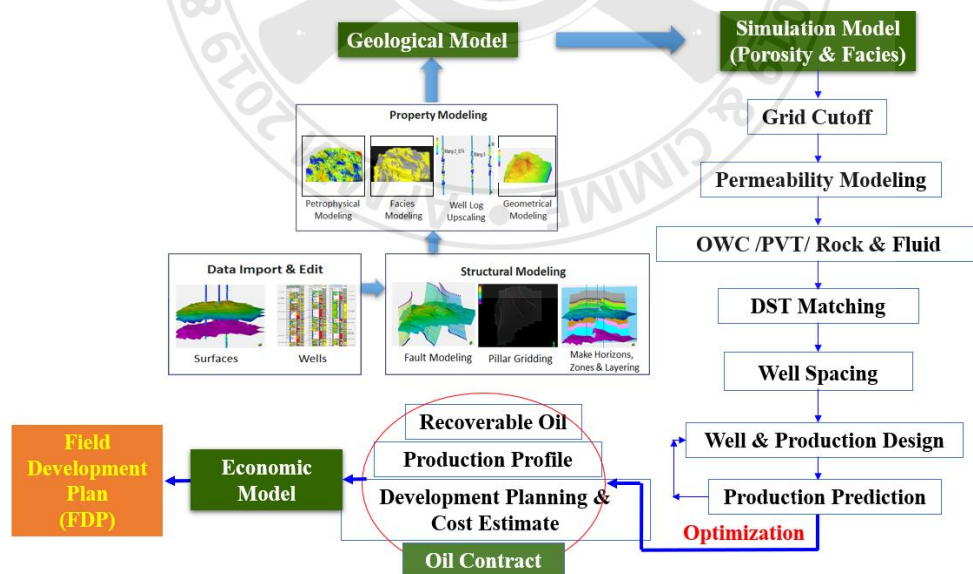

Figure 3 Works in the exploration phase

Figure 4 Field development plan workflow

DEVELOPMENT PHASE (2017/7~)

The main objective of the development phase is to construct the essential facilities, such as development wells, surface facility, pipeline, etc., and to settle the agreements, such as crossing, transportation, export, etc., to make sure that the crude can be produced and transported to the market on schedule. As soon the crude flows into the pipeline, as quickly the income can be generated. Figure 5 shows the major works of this phase. OPIC contracted the service company to conduct the Front-End Engineering Design (FEED) in 2018 based on the FDP which is composed by EPBD and EDRI. The facility specification, the crude process flow, and all auxiliary design were completed in the FEED. Then, OPIC contracted the engineering company to execute the Engineering, Procurement, Construction, Installation, and Commission (EPCIC) based on the FEED. The EPCIC includes detail design and engineering works in the field. Several development wells have been drilled during the development phase, and all the data and samples were sent back to Taiwan for the task force to improve the geology and reservoir model to optimize the drilling decision for the next well.

The rainy season is still the major challenge for the development phase, and OPIC constructs the new road and the base camp to smooth the logistics and improve the wellsite condition to overcome this challenge.

The development works are still carrying on to assure all the facilities could be commissioned by the end of this year.
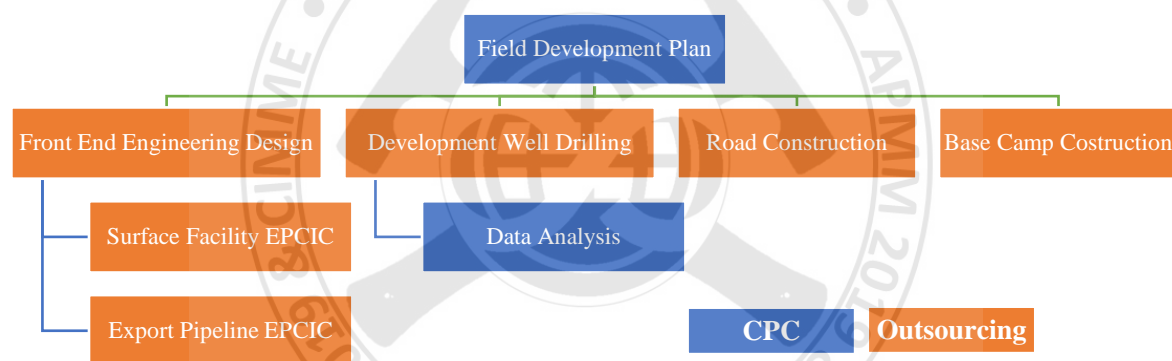
Figure 5 Works in the development phase

CONCLUSION

The Oryx field in Chad is the only field operated by OPIC abroad and go through from the exploration phase into the development phase. The success of this oil field is a result of cross-departments cooperation, such as the task force in charge of in-house technical support from Taiwan and OPIC take care of the operation in Chad. It set up a successful patent for future cooperation. The FDP which is composed by the task force helps OPIC to be granted the EP smoothly. It means that CPC can propose an integrated FDP, and CPC is ready to provide this service for other oil company.

REFERENCES

Wen-Lu Shen et al. (2018). "Milestone of CPC Abroad Exploration – the First Oil in Chad (中油海外 探勘新里程碑-查德礦區第一桶油就在明年)", CPC Monthly, 805: 5-7.

International Conference on Asia Pacific Mining and Metallurgy

Tainan, Taiwan, November 17-20, 2019

Section 2：Metallurgical Engineering

15：10 – 17：00　　　1st Lecture Room

15:10-17:00	Session Chair:	Dr. **Muh-Jung Lu** China Steel Corp., Taiwan

---

15:10-15:40	CIMME108187	**Prof. Jian-Xun Fu** Shanghai University, China

Study of Control of Mg for Inclusions in Fine Dispersion in Steel

---

15:40-16:00	CIMME108014	**Hui-Jan Lin** China Steel Corporation, Taiwan

Development of Batch Charging Process
in Hot Metal Desulfurization with Mechanical Stirring

16:00-16:20	CIMME108029	**Kuo-Pen Chen** China Steel Corporation, Taiwan

Improvement of Slab Central Quality For High-Performance Heavy Plates

---

16:20-16:40	CIMME108022	**Dr. Chiung-Wen Hsu** National Sun Yat-sen University

Effect of Morphology of Slab Grains
on the Hot-Rolled Microstructure and Texture of a High-Silicon Steel

---

Study of Control of Mg for Inclusions in Fine Dispersion in Steel

Weng-sheng Fu, Jian-bo Xie, Ping Shen, and **Jian-xun Fu**[*]

Center for Advanced Solidification Technology (CAST), School of Materials Science and Engineering, Shanghai University, Shanghai 200072, P.R. China
Corresponding Author: Jian-xun Fu; E-mail: fujianxun@shu.edu.cn.

ABSTRACT

The effect of Mg on the morphologies of inclusions in 49MnVS3 steel was investigated with various Mg additions to steel with a high-temperature heating furnace and pilot trials in this paper. Results show that more fine dispersed inclusions were obtained and the complex inclusions of MnS around $MgO \cdot Al_2O_3$ and MgO inclusions in spherical or ellipsoid state appeared after Mg addition. Mg addition increased the ratio and diameter of complex inclusions. With raising Mg content from 0 to 22 ppm, the ratio of MnS inclusion reduced from 89.2% to 45.7%, whereas the ratio of complex inclusions increased from 10.8% to 54.3%. After pilot trials, the Mg content of 5 ppm in steel showed a better effect for modification of Al_2O_3 and $CaO \cdot Al_2O_3$ inclusions into complex inclusions. Mg modified the morphology and size of sulfide inclusions in steel significantly.

Keywords: Mg, 49MnVS3 steel, sulfide, distribution, morphology

INTRODUCTION

With the great requirements of clean steel, the control level of non-metallic inclusions in steel is therefore vital for worldwide steel plants[1]. Of all useful methods, Mg treatment is a promising manner in control of inclusions in fine dispersion in steels, greatly fostering the properties of steel. Mg element has superiority towards the S and O, with better metallurgical thermodynamics state. Upon the addition of Mg to liquid steel, Mg-vapor bubble generated strongly stirs the molten bath. Besides, the advantages of Mg treatment are that: (1) Strong de-oxidation, e.g., a Mg content of 10 ppm can deduce the [O] to 1 ppm in steel; (2) MgO & $MgO \cdot Al_2O_3$ particles (0.1~3 μm) generated are regarded as heterogeneous nucleation cores of sulfides and oxides during solidification of steel, resulting in more dispersed distribution of inclusions, and further contributing to the nucleation of the ferrite in the grain of austenite, grain refinement, and higher strength and toughness of steel.

In the 1990s, Saxena, et al. [1] firstly proposed that small amounts of Mg addition to liquid steel could enhance the property of steel. However, at that time, a low requirement for cleanliness in steel restricted the development of technology. In recent years, the technology of Mg treatment has made great progresses. Jiang, et al. [2] studied the Mg-Al alloy treating inclusions in liquid steel during refining phase, with a result showing that after alloy addition, large quantities of clustered or rod-like inclusions were avoided so as to contribute to the refinement of grain size. Wang, et al. [3] studied the feed process of Mg-cored wire, and found that the type, shape, and

size of inclusions greatly changed. Xiao, et al. [4] discussed the as-cast steel with Mg treatment, with results showing that the type of inclusions changed from II-type to I, III-types and improved the distribution of sulfide with a larger size. Tian, et al. [5] believed that Mg treatment resulted in more small-sized particles of Mg-Al-O oxides as nucleation cores during solidification of liquid steel to reduce the precipitation amount of MnS in the grain boundary. Luo, et al. [7] discussed the Mg-treated SS400 steel, and found that with Mg content of 2 ppm in steel, Al_2O_3 and Al_2O_3-MnS were transformed into $MgO·Al_2O_3$ and $MgO·Al_2O_3$-MnS, respectively. Kim, et al. [8] studied the effect of Mg on the inclusions in the Mn/Si/Ti de-oxidized steels, with results showing that with raising Mg content to steel, the size of inclusions reduced, while the number of inclusions increased. The evolution of core oxides in complex inclusions was that: $Ti_2O_3 \rightarrow (Ti-Mg-O) \rightarrow MgTiO_3 \rightarrow MgO$.

This paper aims to further investigate the evolution of inclusions in 49MnVS3 steel with Mg treatment in the laboratory. Although the Mg has a low yield in actual production, it still exists a bright prospect for application [9]. In this work, we systematically investigated the effect of Mg on the fine dispersion and formation mechanism of sulfide, alumina inclusions, laying foundations for the production of high-quality special steel.

MATERIALS AND METHODS

The experimental materials include 49MnVS3 steel, Ni–Mg alloys, and highly pure argon gas (99.999%). The chemical compositions of the materials used are listed in **Table 1**.

Table 1 Chemical composition of the materials (wt.%)

Composition	Fe	C	Si	Mn	P	S	Al$_t$	Cr	V	Ti	Ni	Mg	Ca	O
49MnVS3	97.33	0.47	0.35	0.92	0.013	0.047	0.012	0.02	0.01	0.025	—	<0.0005	0.0006	0.0015
Ni-Mg alloy	0.85	0.56	0.11	—	—	—	—	—	—	—	74.19	24.29	—	—

When the pure Mg is added to liquid steel directly, a serious splash occurs during smelting. Thus, Ni–Mg alloy was adopted to conduct the experiments. The experimental procedures were described here: a steel sample of 700~900 g was polished and then placed to a corundum crucible (diameter of 53 mm, height of 120 mm). Then the corundum crucible was placed in the graphite crucible, located on the supporting platform inside the high-temperature tube electric resistance furnace shown in **Fig. 1(a)**. Thereafter, the high-purity Ar gas flow at 1 L/min was ventilated into the tube to prevent oxidation of liquid steel during smelting. Next, the electricity supply started, and the temperature control curve was shown in **Fig. 1(b)**. Upon heating to 1600°C for 20 min, the Ni–Mg alloy wrapped by pure iron sheet (thickness, 0.03 mm) was thrown into liquid steel. After 5 min, the melt was stirred for 15 s by using a quartz pipe. Afterwards, the tube electric resistance furnace cooled with the manner of 'cooling with furnace' to room temperature.

After the smelting, the Mg content in the steel ingot was measured by an inductively coupled plasma-optical emission spectrometry (ICP-OES), as shown in **Table 2**. Scheme *a* was the
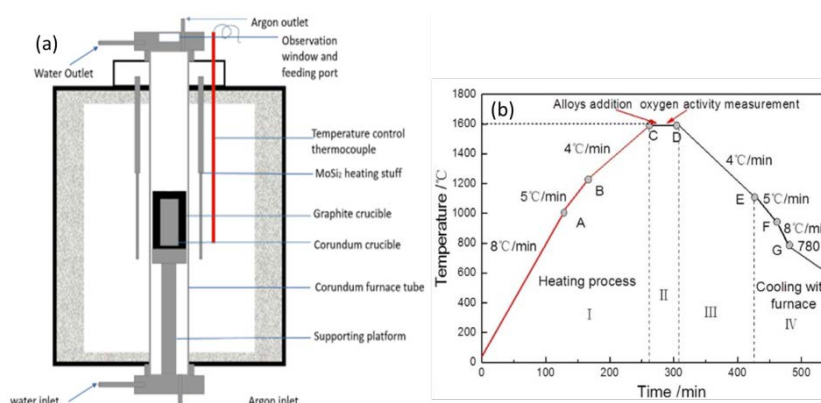
original sample, with Mg content below 5 ppm.

Fig. 1 Schematic of high-temperature tube heating furnace (a)[11], and alloying process (b)[9]

Table 2 Mg content in each Mg-treated 49MnVS3 steel (ppm)

Scheme	*a*	*b*	*c*	*d*	*f*
Content	<5	7	10	19	22

In the center of each ingot, a steel sample with area of 10 mm×10 mm was machined. Apart from the observation of two-dimensional morphologies of inclusions in samples, the non-aqueous solution electrolytic etching method was also adopted to observe the stereoscopic morphologies of the inclusions with SEM.

INCLUSION STATISTICS AND ANALYSIS

Using the methods of SEM+EDS, the compositions of inclusions in steels were shown in **Fig. 2**. **Fig. 2** shows that the main compositions of inclusions in original steel were MnS distributing in the grain boundary, and small amounts of complex Al_2O_3-MnS inclusions in irregular shape. With increasing the Mg content to 7~10 ppm, the complex inclusions of MnS around the $MgO·Al_2O_3$ inclusions appeared. With Mg addition further increasing to 19~22 ppm, the complex inclusions of MnS around the $MgO·Al_2O_3$ and MgO inclusions appeared in spherical or ellipsoid state. And it was also found that MnS inclusions contained small amounts of MgO, attributed to the diffusion of MgO into MnS. Besides, the ratio and diameter of complex inclusions increased with increasing Mg content to steel.

Mg bubbles in liquid steel can strongly adhere to the dissolved [O]. Therefore, upon the Mg alloy into liquid steel, Mg bubbles are bound to first react with [Al] and [O] to form $MgO·Al_2O_3$. With more addition to steel, $MgO·Al_2O_3$ reacts with Mg to generate MgO. At end-solidification, the $MgO·Al_2O_3$, MgO particles induced the encapsulation of sulfide to form complex inclusions.
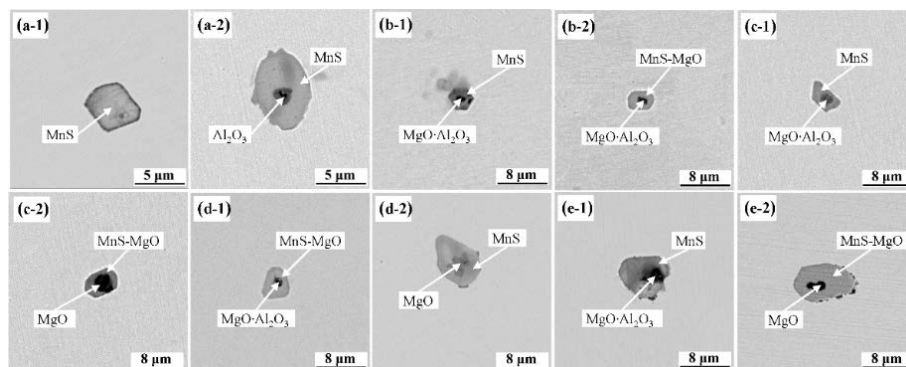
Fig. 2 Morphologies of inclusions in Mg-treated 49MnVS3 steel

After statistics with SEM photos, the ratios of various inclusions in 5 schemes were shown in **Fig. 3**. **Fig. 3** shows that with increasing the Mg content to steel, the ratio of single MnS inclusion was reduced. With raising the Mg content from 0 to 22 ppm, the ratio of single MnS inclusion was reduced from 89.2% to 45.7%, whereas the ratio of complex inclusions increased from 10.8% to 54.3%. Besides, the cores of complex inclusions also changed. So Mg addition to steel enhanced the number of precipitation nucleation cores of inclusions greatly.
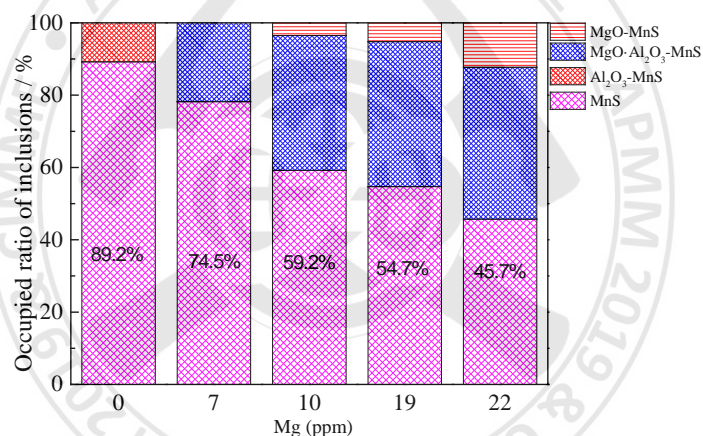
Fig. 3 Variation of MnS and its composite sulfide with Mg addition after experiments

To observe the tri-dimensional morphologies of inclusions in steel, the non-aqueous solution electrolytic etching method was adopted with SEM shown in **Fig. 4**. After analyses of SEM+EDS, the morphology of sulfide in original steel was in arborized or rod-like shape in the grain boundary, which belongs to II-type sulfide. However, for the Mg-treated steels, the sulfide distributed in steel uniformly, and the morphology of sulfide changed from II-type to III- and I-type. It was illustrated that Mg modified the morphology of the sulfide in the steel significantly. Besides, small contents of [O]+[Mg] in steel contributed to the precipitation of type-III sulfide. Fine and dispersed MgO particles as the nucleation cores for MnS reduced the generated probability of III-type sulfide.

Fig. 4 Tri-dimensional morphologies of inclusions in 49MnVS3 steels: (a)a; (b)b; (c)c; (d)d; (e)e
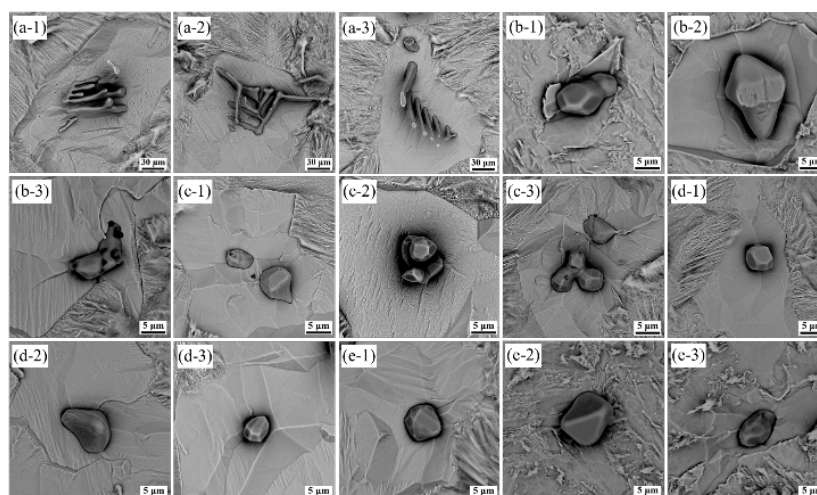
APPLICATION OF Mg IN INDUSTRY

Based on the laboratory study, the Mg modification technique was applied in the manufacture of re-sulfurized 49MnVS3 steel in a steel plant, with a production of being treated with Mg shown in **Fig. 6**. The production procedures are as follows: EAF→LF→VD→CC.

Fig. 5 Industrial trials with Mg treatment: (a) Mg-containing core wire; (b) Pilot trials of 49MnVS3[11]

The analyses of industrial trials of 49MnVS3 steel were discussed with various Mg additions to steel below. **Table 3** shows the target composition of the steel during the tests.

Table 3 Target composition of 49MnVS3 steel(wt. %)

C	Si	Mn	P	S	Cr	V	Ni	Ti	Al	N
0.47	0.35	0.9	≤0.020	0.05	0.2	0.1	≤0.20	0.025	0.01	0.015

Mg in the form of cored wire was added to a ladle after VD refining. The steel samples were taken. The typical morphologies of sulfide in steel with a Mg content of 5 ppm were shown in **Fig. 6**, showing that after Mg treatment, the morphologies of MnS tended to be in spherical or spindle shape.
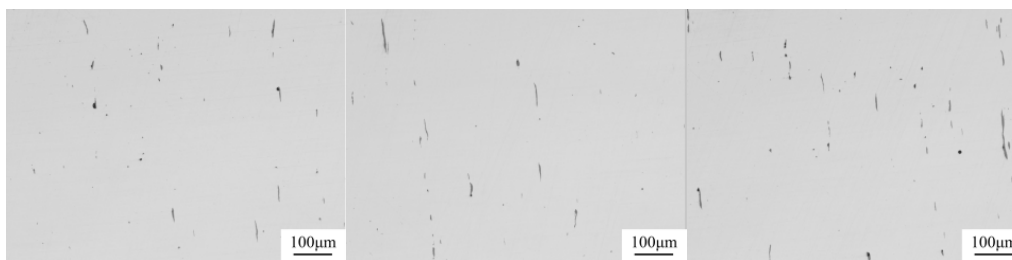
Fig. 6 OM morphologies of inclusions in 49MnVS3 steel after Mg treatment

Fig. 7 shows the inclusions in the steel with Mg content of 5 ppm. Few Al_2O_3 and $CaO \cdot Al_2O_3$ were observed, and most inclusions have been transformed to $MgO \cdot Al_2O_3$. Considering the actual situation, the Mg content of 5 ppm can fully modify Al_2O_3. To sum up, the shape of sulfide in steel was greatly transformed to spindle shape after Mg treatment compared to non-treatment.
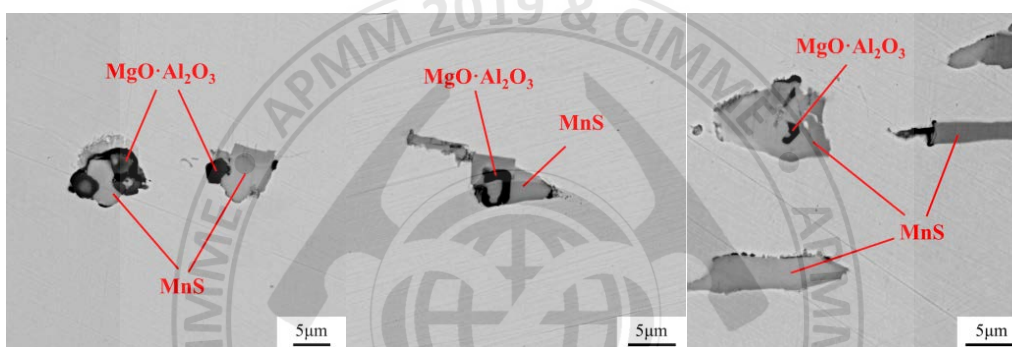

Fig. 7 EDS result of inclusions in the steel after Mg treatment

Based on the discussions above, Mg modified the Al_2O_3 and MnS inclusions. The small-sized inclusions and the ratio of complex inclusions increased. A larger number of inclusions unchanged in terms of their morphologies after hot rolling, attributed to the effective restriction of Mg to the deformation of inclusions, improving the quality of final product.

CONCLUSIONS

The effect of Mg on the morphologies of inclusions in 49MnVS3 steel was investigated with various Mg additions to steel using a high-temperature electric resistance furnace and pilot trials. The following conclusions were obtained.

(1) Mg addition to steel contributed to more fine dispersed distribution of inclusions. With addition of Mg to steel, the complex inclusions of MnS around $MgO \cdot Al_2O_3$ and MgO inclusions appeared in spherical or ellipsoid state.

(2) Mg addition increased the ratio and diameter of complex inclusions. With raising the Mg content from 0 to 22 ppm, the ratio of MnS inclusion reduced from 89.2% to 45.7%, whereas the ratio of complex inclusions increased from 10.8% to 54.3%.

(3) After pilot trials, the Mg content of 5 ppm in steel owned a better effect for modification of Al_2O_3 and $CaO \cdot Al_2O_3$ inclusions into complex inclusions.

ACKNOWLEDGEMENTS

REFERENCES

1. Wang DY, Qu TP, Deng LQ, et al. Development and practice of Mg clean technology. Proceedings of the Refining Outside Furnace, 2019, 324-336.

2. Jiang Z H, Zhuang Y, Li Y, et al. Effect of modification treatment on inclusions in 430 stainless steel by Mg-Al alloys. Journal of Iron and Steel Research International, 2013, 20 (5):6-10.

3. Wang J S, Xu J G, Sun W, et al. Experimental study on inclusion modification in the steel by Mg cored wire feeding process. Journal of University of Science and Technology Beijing, 2007, 29(Suppl 1):22-25. *In Chinese*.

4. Xiao G H, Dong H, Wang M Q, et al. Effect of Mg/Ca-treatment on morphology of sulfide in non-quenched and tempered steel. Iron and Steel, 2011, 46(4):65-69. *In Chinese*.

5. Tian J, Wang D Y, Qu T P, et al. Role and distinction of Ca and Mg to sulfide modification for sulfur steel. Iron and Steel, 2017, 52(11):27-31.) *In Chinese*.

6. Luo S, Su Y F, Lu M, et al. EBSD analysis of magnesium addition on inclusion formation in SS400 structural steel. Materials Characterization, 2013, 82(5):103-112.

7. Zhang T S, Wang D Y, Liu C J, et al. Mechanism of modifying oxide and sulfide by Mg in liquid iron at 1873 K. Journal of University of Science and Technology Beijing, 2014, 36: 189-193. *In Chinese*.

8. Kim H S, Chang C H, Lee H G. Evolution of inclusions and resultant microstructural change with Mg addition in Mn/Si/Ti deoxidized steels. Scripta Materialia, 2005, 53(11):1253- 1258.

9. Wang H, Li J, Wang L L, et al. Inclusion modification of magnesium treatment in H13 die steel. China Science paper, 2014, (9)2:175-177. *In Chinese*.

10. Xie J B, Zhang D, Yang Q K, et al. Exploration of morphology evolution of the inclusions in Mg-treated 16MnCrS5 steel. Ironmaking & Steelmaking, 2019, 46(6):564-573,

11. Shen P, Fu J X. Application of Mg-Ca modification in the manufacture of resulfurized special steel. Materials, 2019. Accepted

12. Ai KN, Xie J B, Zeng Z Q, et al. Effect of Mg on microstructure and sulfide in non-quenched and tempered Steel. Journal of Iron and Steel Research International, 2019, 31(4):361-367. *In Chinese*.

Development of Batch Charging Process in Hot Metal Desulfurization with Mechanical Stirring

Hui-Jan Lin and Yung-Chang Liu, Kuan-Ju Lin
Iron & Steel Research & Development Department, China Steel Corporation, Taiwan
209791@mail.csc.com.tw, 150185@mail.csc.com.tw, t120@mail.csc.com.tw,

Ching-Tsung Tseng
Steel-Making Department, China Steel Corporation, Taiwan
170217@mail.csc.com.tw

ABSTRACT

In steelmaking industry, the commonly used desulfurization method in KR desulfurization process is one-batch charging method, by which sulfur level in hot metal can be reduced to less than 20 ppm. However, one-batch charging method will cause the desulfurization agent to spread unevenly during the stirring process. To improve the distribution of desulfurization agent in the hot metal ladle, two-batch charging method was tested to evaluate the desulfurization efficiency and the dispersion of desulfurization agents in hot metal during KR desulfurization process.

From the test results, it was found that the desulfurization rate of two-batch charging was faster than one-batch charging.

Furthermore, from the desulfurization mass transfer calculation model, the product of the mass transfer rate constant (k) and the contact area (A) of the hot metal was examined as well. Under the condition of 2000 and 1800 kg as the total weight of desulfurization agent, the absolute values of product kA of two-batch charging were around 4% and 21% respectively, higher than that of one-batch charging method.

INTRODUCTION

In recent years, the demand on high-quality steel with low sulfur content has been increasing drastically. If sulfur content in the steel exceeds 0.05%, it tends to cause brittleness and reduce weldability. Therefore, many desulfurization methods have been developed to meet performance requirements. Among them, desulfurization by mechanical stirring method was found to be a simple and effective technique. (Nakai, Y. *et al*, 2017)

Many researches have focused on various aspects of the process to increase the desulfurization efficiency. For example, water model experiments are used to evaluate dispersion, (Nakai, Y. *et al*, 2015) eccentric rotors are used to enhance dispersion, or optimize the composition of desulfurization agent. (Lindström, D. 2014) Moreover, it has been shown that the influence of the kinetic condition is huge. (Nakai, Y. *et al*, 2013) When the molten iron is fully rotated, a good metallurgical kinetic condition can be obtained, and the desulfurization agent can be fully reacted. Therefore, the desulfurization efficiency can reach as high as 95% or even more.

In this work, different batch charging methods during KR desulfurization process were examined and desulfurization efficiencies were also evaluated.

EXPERIMENTAL METHOD

In the batch charging test of the KR desulfurization process, 2000 and 1800 kg were selected as the total weight of the charging lime, and the time interval between two batches was 3 minutes. Besides, different portions of lime distributed in the first and second batches were also conducted. The detail of charging amount of lime was shown in Table 1.

Table 1. Batch-Charging Experimental Condition

Desulfurizer Total Wt.(kg)		First Charging	Time Inteval	Second Charging
1800 & 2000		CaO + Fluorite	(mins)	CaO + Fluorite
Test Number	#1	60%		40%
	#2	70%	3	30%
	#3	80%		20%

Based on the sulfur content in the hot metal before and after the experiment, the desulfurization efficiency was evaluated by Eq.1.

$$Desulfurization\ efficiency(\%) = \frac{[S]_{ini} - [S]_t}{[S]_{ini}} * 100\% \tag{1}$$

Where $[S]_{ini}$ is the concentration of sulfur in the molten iron at the beginning; $[S]_t$ is the concentration of sulfur in the molten iron after the desulfurization process. Besides, in this work, 1point represents 10 ppm of HM[S].

Additionally, according to the law of mass transfer and mass conservation, the variation of sulfur in molten iron during the desulfurization process will be the same as the amount of sulfur removed from the interface between the molten iron and the desulfurizer, expressed as Eq.2.

$$W_t * (S_1 - S_0) = k * A * (S_0 - S_{eq}^*) * dt \tag{2}$$

Where W_t is the weight of molten iron (ton), S_1 is the concentration of sulfur at time t, S_0 is the concentration of sulfur at time (t-1), k is the mass transfer rate constant (ton/min· m^2), A is the contact area (m^2) between hot metal and desulfurization agent, S_{eq}^* is the ideal equilibrium concentration of the hot metal, and dt is the time interval (min).

In this study, the product value of the mass transfer rate constant (k) and the contact area (A) of the hot metal was monitored to evaluate the dispersion of the desulfurization agent and the desulfurization efficiency, which was changed by different charging methods.

RESULTS AND DISCUSSION

In terms of desulfurization efficiency, the value of one-batch charging of 2000 kg lime is as high as 99.26%. Whereas in two-batch charging, the desulfurization efficiency is close to or over 99%, except for the test 3, which might have slightly poor impeller mixing due to larger tonnage of hot metal. Under the condition of 1800 kg as the total weight of desulfurization agent, the desulfurization efficiencies of both one- and two-batch charging are over 99%, it indicates that the desulfurization effect under all conditions is very satisfying, shown in Table 2.

The changes of HM[S] of one- and two-batch charging desulfurization, before and after KR process, are shown in Figure 1. When the total weight of desulfurization agent is 2000 kg, HM[S] before and after desulfurization was 20.6, 0.2 points respectively for one-batch charging. For two-batch charging,

HM[S] before desulfurization was 22.1~26.3 points, and HM[S] after desulfurization was between 0.2~0.8 points. Moreover, as the weight of the first charging lime is higher, the desulfurization efficiency is getting worse. Similar phenomenon was found in the case of desulfurizer of 1800 kg, shown in Figure 1(b).

Table 2. Process Parameters during KR Desulfurization Process.

KR Desurfurization		Before KR HM [S] (pts)		After KR HM [S] (pts)		De-S Efficiency (%)	
CaO 2000 kg		Median	S.D.	Median	S.D.	Median	S.D.
One-Batch		20.60	7.16	0.20	0.34	99.26	2.32
Two-Batch	#1	26.30	4.82	0.20	0.56	98.99	2.57
	#2	22.20	3.26	0.20	0.09	99.06	0.43
	#3	22.10	2.73	0.80	0.77	96.02	3.35

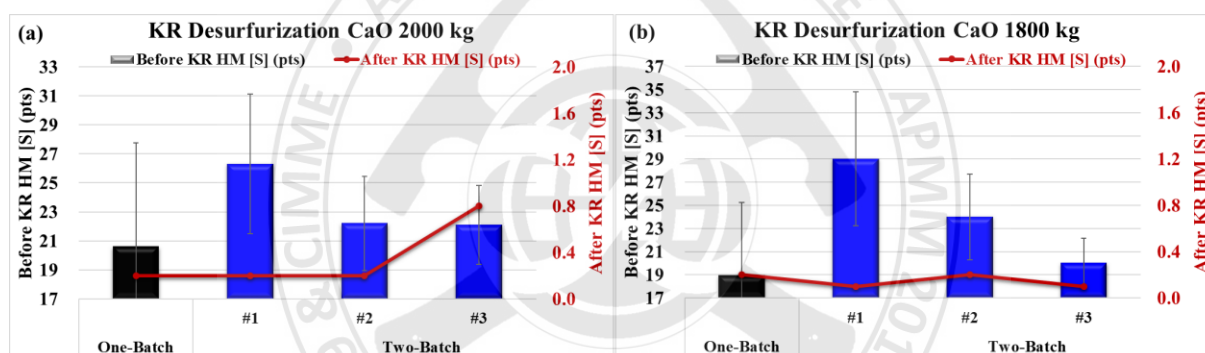| CaO 1800 kg		Median	S.D.	Median	S.D.	Median	S.D.
One-Batch		18.95	6.29	0.20	0.22	98.92	1.47
Two-Batch	#1	29.00	5.79	0.10	0.00	99.66	0.07
	#2	24.00	3.70	0.20	0.05	99.31	0.29
	#3	20.00	2.17	0.10	0.94	99.50	4.06

Figure 1. Before and After KR Process, Change of HM[S] of One- and Two-Batch Charging Desulfurization. (a)CaO 2000 kg, (b) CaO 1800 kg.

Desulfurization mass transfer calculation model shows the prediction of HM[S] with time, shown in Figure 2. When the total weight of desulfurizer is 2000 kg, it can be seen that in one-batch charging test, the product of the mass transfer rate constant (k) and the contact area (A) of the hot metal is about -77 (ton/min), and that of two-batch charging is about -80 (ton/min). The desulfurization effect of the two-batch charging is slightly better performance than the one-batch method, which is about 4% faster. However, in the charging condition of desulfurization agent of 1800 kg, the kA value is about -75 (ton/min) for a one-batch charging, and that of two-batch charging is increased to about -91 (ton/min), which is 21% faster than sing-batch one.

In the same way of two-batch charging, the kA value of 1800 kg as the total charging desulfurizer is about 13% faster than that of 2000 kg, which means that the dispersion is better under the condition of 1800 kg, which makes the product of the mass transfer rate constant (k) and the contact area (A) of molten iron higher and beneficial to remove sulfur from the hot metal.
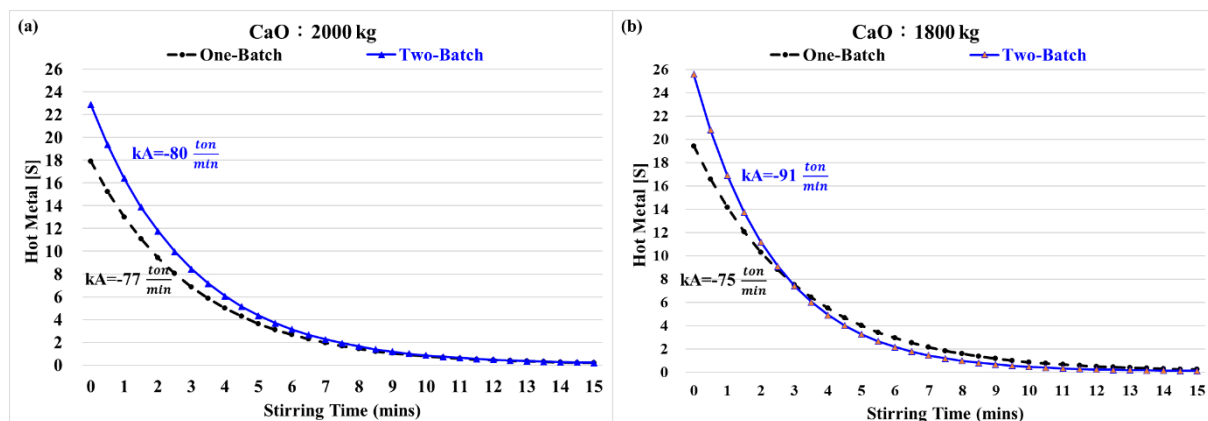
Figure 2. HM[S]-Time Prediction Model of One- and Two-Batch Charging Desulfurization Process. (a) CaO 2000kg, (b) CaO 1800 kg.

CONCLUSIONS

The results from both one-batch and two-batch charging test in the KR desulfurization process show that the desulfurization efficiency is close to or over 99% when the total amount of desulfurizer is 2000 or 1800 kg. It indicates that the desulfurization effect perform well in these tests.

The test data with different total charging amounts showed that the desulfurization rate of two-batch charging test was faster than that of one-batch. Moreover, as the weight of the first-batch charging desulfurization agent is higher, the desulfurization efficiency is slower.

The kA value obtained by the desulfurization mass transfer calculation model shows that larger amount of desulfurizing agent may cause worse dispersion of desulfurization agent in the hot metal, and it may also cause difficulty in stirring and affect the mass transfer rate. However, the higher absolute value of kA can be obtained by two-batch charging method, which leads to better desulfurization efficiency.

REFERENCES

Nakai, Y., Matsui, A., Kikuchi, N. (2017). "High Efficiency Hot Metal Desulfurization by Enhancing Flux Dispersion in Mechanical Stirring Process," JFE Technical Report, No.22, Mar. 2017

Nakai, Y., Hino, Y., Sumi, I., Kikuchi, N., Uchida, Y., Miki, Y. (2015). "Effect of Flux Addition Method on Hot Metal Desulfurization by Mechanical Stirring Process," ISIJ International, 55(7): 1398-1407

Lindström, D. (2014). " A Study on Desulfurization of Hot Metal Using Different Agents," PhD Dissertation, Royal Institution of Technology, Sweden.

Nakai, Y., Sumi, I, Hino, Kikuchi, N., Kishimoto, Y., Miki, Y. (2013). "Aggregation Behavior of Desulfurization Flux in Hot Metal Desulfurization with Mechinical Stirring," ISIJ International, 53(8): 1411-1419

Improvement of Slab Central Quality
For High-Performance Heavy Plates

Kuo-Pen Chen and Ming-Hung Chen
Continuous Casting Steelmaking Department, Iron & Steel Research & Development Department
China Steel Corporation, Taiwan, R.O.C
151241@mail.csc.com.tw, 150326@mail.csc.com.tw

ABSTRACT

With the increasing demand for high-performance heavy plates in wind power structures and large container ships, China Steel Corporation (CSC) has started to develop the related technologies since 2010. Such high-performance heavy plates are usually in 60~115 mm thickness and applied in a extremely severe environment. Therefore, the more rigid mechanical properties are required, including high central (t/2) impact toughness in extreme low temperature and sufficient reduction of area in the thickness direction (ZRA).

The determining factor of central impact toughness in extremely low temperature is decided by the degree of the micro-porosity in the center of a heavy plate. The less micro-porosity, the better toughness can be achieved. The porosity existing in the center of the slab is hardly eradicated during the rolling process due to insufficient reduction.

The heavy reduction technology has been developed in CSC to eliminate the micro-porosity of slabs during casting. The reduction of 4~10 mm in thickness at fs 0.7~1.0 is effective for the elimination of micro-porosity, which is proved by radiation inspection, porosity index, and UT examination. The heavy reduction technology have significantly improved the central impact toughness of heavy plate in low temperature.

Keywords
Continuous casting, heavy reduction, soft reduction, heavy plate, slab

INTRODUCTION

In recent years, CSC has been actively developing the high-performance heavy plates with critical demands of central impact toughness in low-temperature for marine and wind-power industry. Some literature points out that the micro-porosity in the center of the heavy plates will result in the insufficient central impact toughness under low-temperature. The traditional soft reduction technology in continuous casting can effectively improve the macro-porosity and central segregation, but it cannot improve the visually undetectable micro-porosity.

Technical literatures indicated that it can only be improved by heavy reduction technology [1-3], forging [4-5], and reduction at strand exit[6] . So a heavy reduction technology was also developed in our company in order to eliminate micro-porosity.

TECHNOLOGY DEVELOPMENT

The process of heavy reduction at the crater end of strand will be more effective than the rolling process of the steel plate to eliminate the central micro-porosity. The key factor is the temperature distribution characteristics of the slab, as shown in Fig1. When the steel is completely solidified in

casting, the center temperature is as high as 1480 °C, which is much higher than the temperature of the plate for rolling process, i.e., 1250 °C. The temperature difference between the surface and the center is about 450 °C for the slab, which is also much higher than the temperature difference for the rolling process, i.e., 150 °C. Therefore, the compressive strain of heavy reduction can concentrate on the center of the slab and achieve the effect of eliminating the micro-porosities. In Figure 1 (b), it shows the model under heavy reduction. The numerical simulation also confirmed that the strain concentration effect on the center of the steel under heavy reduction, as shown in Fig 2. It has significant improvement on elimination of the micro-porosity at the center of slab and the impact toughness in low-temperature of the heavy plate. After evaluation, CSC has revamped the existing #1 caster to maximize pressing force of the roller, so that it can achieve a reduction of 10 mm in thickness for the casting of 1880 mm width slab.
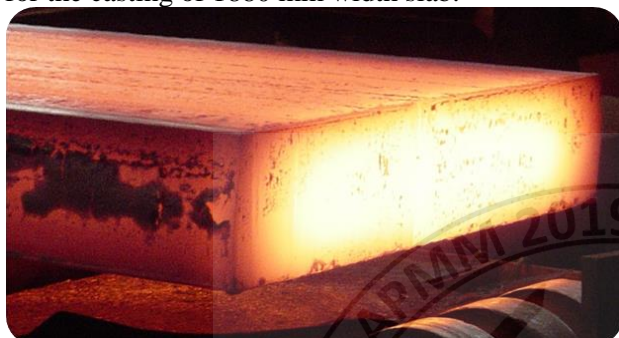

Fig. 1 (a) The temperature distribution characteristics of the slab.

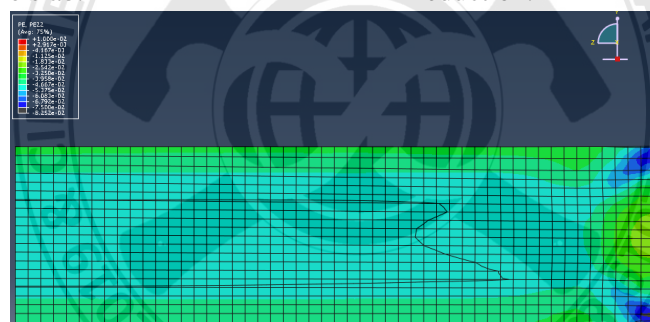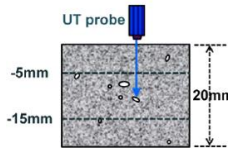Fig. 1 (b) The simulation model of heavy reduction.
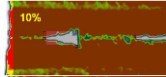
Fig. 2 The. The strain concentration effect of heavy reduction in numerical simulation model

MICRO-POROSITY DETECTION

The current sulfur print and pickling test used to evaluate the macro-porosity in CSC is unable to detect visually defects less than 1mm after pickling. Therefore, CSC has established further technique for inspection of micro-porosities and building-up quality indicator for the assessment of heavy reduction. The related inspection methods are as follows:

No.	Description of detection methods	Photos of detection
1	Penetration Test (PT) after pickling enables to detect and compare the micro pore defects, as shown in the right figure. Pickling + PT has the better effect on the distribution of the micro-porosity. However, it cannot meet the demands of quantitative information including the size and quantity, which is the most important characteristics for the production of heavy plates.	

2	By reducing the thickness of the pickling sample piece less than 10 mm with X-ray observation can obtain a clearer image. As shown in the right Fig. The distribution and shape of the micro-porosity can be clearly displayed.	
3	Detecting the defect by focused-type of UT detection, which can improve the detection sensitivity of small defects due to the increase of ultrasonic energy per unit area, and has a layer-by-layer scanning to enlarge the detection range. The result of UT detection can be efficiently obtained in two weeks after slab sampling. The software also can analyze the size and numbers of defects for a given area. The UT test shows that micro-porosity is concentrated near the triple point of slab from this sample. The characteristic between UT and X-ray is very consistent. The detection index can be established accordingly.	

THE TRIALS AND RESULTS

Under several tests of heavy reduction, the results demonstrate that when the reduction in thickness with single roller exceeded 4 mm, the compression strain is sufficient to improve the center quality on the slabs. As shown in Fig.3 and Fig.4, there is no segregation in the macroscopic and micro-porosities under heavy reduction. In contrast, without the heavy reduction process, the slab has obvious segregation and micro-porosities. This proves that the process under heavy reduction can effectively improve the segregation and micro-porosity defects at the center of slab, which is one of the key factors for the production of the high performance heavy plates.

The pickling test piece and the sulfur print have obvious characteristics of the squeeze zone in the center, and the thickness of the squeeze zone is proportional to the amount of reduction. The larger the reduction, the thicker the squeeze zone, as shown in Fig.5. The UT detecting result by different continuous casting process shows different characteristics, as shown in Fig.6.
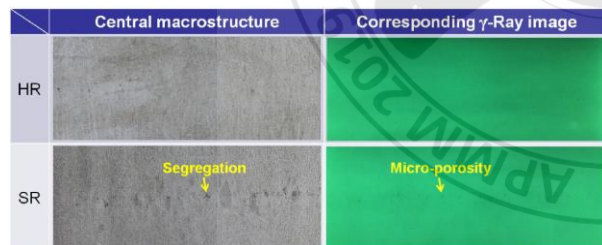

Fig.3 The macrostructure of slab adopting heavy reduction and soft reduction.
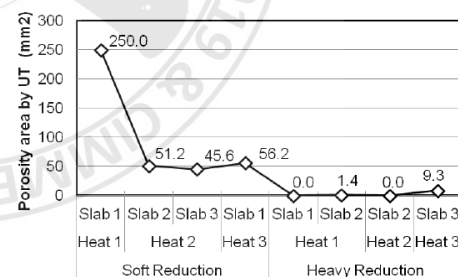

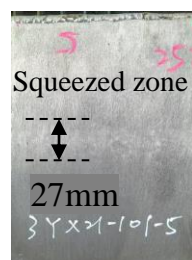Fig.4 The porosity area of slab adopting heavy reduction and soft reduction.

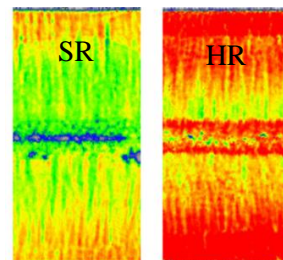Fig.5 Squeezed zone of slab adopting heavy reduction.

Fig.6 The UT detecting result of slab adopting soft reduction and heavy reduction.

CONCLUSIONS

To achieve a sufficient reduction of slab thickness, CSC has modified the steel structure and electrical control system to enlarge the pressing force at the crater end section of the existing casting machine. With continuous trials, the new pressing system proved to be able to achieve 10 mm reduction in thickness for the 1880mm width of slab.

The consequences of the trials demonstrate that more than 4 mm reduction with single-roller can eliminate the micro-porosities and improve the segregation. For heavy plate of 110~120 mm in thickness, the ZRA and the low-temperature impact toughness are also obviously improved with heavy reduction process.

To evaluate the micro-porosities, the new detection process was developed by incorporating different methods of pickling + PT, pickling +X-ray or focused-type of UT. However, focused-type of UT detection is proved to be the most efficient method.

The insufficient rolling ratio in rolling mill can't eliminate the micro-porosities in the plate center effectively, which will result in loose central structure and insufficient low-temperature impact toughness. During continuous casting, the solidification crater end of slab center temperature is 450 °C higher than the surface temperature, the micro-porosities can be effectively eradicated with heavy reduction process.

The heavy reduction technology has been developed in CSC to eliminate the micro-porosity of slabs during casting. The reduction of 4~10 mm in thickness at fs 0.7~1.0 is effective for the elimination of micro-porosity, which is proved by radiation inspection, porosity index, and UT examination. The heavy reduction technology have significantly improved the central impact toughness of heavy plate in low temperature.

REFERENCES

1. Sei Hiraki, Akihiro Yamanaka, Yoshihisa Shirai, Yasuhiro Satou, Seiji Kumakura (2009). "Development of New Continuous Casting Technology (PCCS) for Very Thick Plate," Material Japan, 48(1): 20-22.

2. Kazuhiko Hasegawa, Nobufumi Kasai, Seiji Kumakura, Yoshihisa Shirai, Akihiro Yamanaka (2005). "Continuous Casting Method and Extra-thick Steel Plate Excellent in Inner Quality and Producing Method Therefor", Japan patent, JPA2005305516.

3. Tadashi Hirashiro, Yasuhiro Sato, Akihiro Yamanaka (2008). "Continuous Casting Method of Cast Ingot for Very Thick Steel Plate", Japan patent, JPA2008173647.

4. D. Shinichi and, Takahashi Kazuhide, Endo Shigeru, Hasunuma Junichi, Saka Kei, Nagahama (2004). "Steel for Production, Transportation, and Storage of Energy", JFE Technical Report, (2): 55-67.

5. K. Araki, T. Kohriyama, M. Nakamura(1998). "Development of Heavy Section Steel Plates with Improved Internal Properties through Forging and Plate Rolling Process Using Continuous Casting Slabs," Kawasaki Steel Giho, 30(3): 181-185.

6. Tetsuo Kikutake, Masaji Nakao(1979). "Production of continuous steel plate,", Japan patent, JPS55114404

Effect of morphology of slab grains on the hot-rolled microstructure and texture of a high-silicon steel

Chun-Chieh Wang, Po-Chun Liao, **<u>Chiung-Wen Hsu</u>**, YuYuan Zheng, and Liuwen Chang

Department of Materials and Optoelectronic Science, National Sun Yat-Sen University, Kaohsiung 80424, Taiwan, R. O. C.

boy840301@gmail.com,gary12900@gmail.com,zosul307@gmail.com,zhyy@outlook.com,lwchang@mail.nsysu.edu.tw

ABSTRACT

This study aims at clarifying the evolution of microstructure and texture for slab grains having a columnar and equiaxed shape, respectively, during hot rolling. The microstructure and texture of a continuously cast slab and the inherited hot bands were characterized by electron backscatter diffraction (EBSD) technique. Thick plates, 50 mm in thickness, consisting of either columnar grains (CG) or equiaxed grains (EG) were prepared from an industrially produced slab containing 3 wt% Si. The plates were hot rolled to approximately 4.5 mm thick at a finishing temperature of 860 °C. A portion of them were annealed afterwards at 950 °C for 60 s. Results indicated that the hot band rolled from an EG plate contained rolled grains of 100-300 μm thick and nearly equiaxed grains of 50-200 μm is size. The latter were presumably formed by dynamic recrystallization during hot rolling. On the other hand, the hot band of the CG plate contained mainly the rolled grains of 400-1500 μm in thickness. The dynamically recrystallized grains were seldom observed. In addition to the grain microstructure, both the rolled and dynamically recrystallized grains in the EG hot band contain high densities of low angle boundaries, indicating that the strain energy in it is high. Oppositely, the rolled grains in the CG hot band contain much less low angle boundaries. EBSD analyses showed that some rolled grains exhibited orientations which are usually observed in the recrystallized state, such as Goss ({110}<001>) and Cube ({100}<001>).

INTRODUCTION

The motors of current electric vehicles are produced from non-oriented electrical steel (NOES) laminations having high strength, high magnetic flus density and low core loss. Addition of high amount of silicon in NOES is preferred due to its strong effect on solution strengthening and increasing electric resistivity which is beneficial for reducing the eddy current loss. Low carbon steels containing silicon of 2.5 wt% or higher are in absence of the $\delta-\gamma-\alpha$ phase transformations on cooling. In other words, the cast slab usually contains coarse columnar grains of millimeters to centimeters in size[1]. It has been reported that these grains are difficult to recrystallize after hot rolling, which might indirectly affect the microstructure and properties of the final NOES products [2-3]. In order to clarify the effect of the slab grain morphology on the evolution of microstructure and texture during hot rolling, a series of experiments were carried out for plates containing columnar grains (CG) and equiaxed grains (EG), respectively.

EXPERIMENTAL

Two slabs, 170 mm (w) x 200 mm (l) x 50 mm (t) in size, consisting of either columnar or equiaxed grains were prepared from a continuous-casting slab containing 3wt% Si. The slabs were heated to 1100 °C for 3600 s and hot rolled in five passes to a thickness of 4.5 mm and cooled rapidly to temperatures below 100 °C by water spraying. The finish rolling temperature was 840 °C. The hot rolled bands were cut transversely to thin slices of 5 mm wide. Each slice was further cut in every 10 mm to 20 samples. Each one is 5 mm wide along the rolling direction (RD) and 10 mm wide along the transverse direction (TD). Three samples were then electropolished and analyzed by electron backscatter diffraction (EBSD) with an Oxford Symmetry detector attached to a Zeiss Supra 55 scanning electron microscope (SEM) on the plane perpendicular to RD (the RD plane). Another three samples were annealed at 950 °C for 60 s in an infrared furnace at a pressure below 1×10^{-1} torr and followed by EBSD analyses. In addition, the slabs containing either columnar grains or equiaxed grains were also analyzed by EBSD on their normal planes (NDs). A Cartesian sample coordinates consisting of three orthogonal directions RD, TD and ND are used for orientation analysis.

RESULTS AND DISCUSSION

Fig. 1 shows the montaged EBSD ND and RD orientation image maps (OIMs) and inverse pole figures (IPFs) taken from the normal plane for CG and EG slabs before hot rolling. The OIMs for the CG sample (see Fig. 1(a) and 1(b)) reveal that the columnar grains are 2-5 mm in diameter and possess a strong <100>//ND fiber texture. These grains indeed grew along ND to lengths of 20-60 mm as observing the slab from RD. The equiaxed ones exhibit similar sizes according to the OIMs in Fig. 1(c) and 1(d) with random orientations as demonstrated clearly by the IPFs.
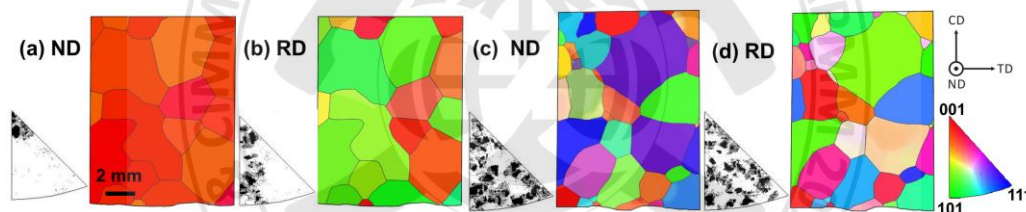

Figure 1. The orientation image maps (OIMs) and inverse pole figures (IPFs) for (a)~(b) the CG sample and (c)~(d)the EG sample.

More than three areas with distances of more than 30 mm between each other were analyzed by EBSD to reveal the through-thickness microstructure and texture characteristics of the hot bands. Fig. 2 shows the ND/RD OIMs and the corresponding boundary map for both samples as examples. Each map is montaged from four maps acquired in a step size of 2.25 μm. Fig. 2(a) shows the EBSD results for the EG hot band, revealing that the top and bottom surfaces (~500 μm thick) contain equiaxed or slightly elongated grains with a bimodal size distribution. The fine, equiaxed grains are 10-30 μm in size and are free from low angle boundaries, whereas the slightly elongated ones are 50-200 μm in size and contain high population of low angle boundaries. The former do not distribute homogeneously throughout the surface layer. Instead, they concentrate in the central region of the surface layer. Both types of grains were probably formed by dynamic recrystallization during deformation or static recrystallization between rolling passes. The slightly elongated grains were formed in the early few passes, grew larger in sizes, but were deformed later. The fine, equiaxed ones were formed in the last pass and were fine and reserve a deformation-free state. On the other hand, thick rolled grains are observed in the center region associated with many equiaxed grains which are slightly elongated. Most of the rolled grains are too large to be covered by the analytical area (1200

μm wide). The thicknesses of these grains, estimated from the distances between high angle boundaries, are in a region of 100-300 μm according to which the original grain sizes is estimated to be 1000-3000 μm, coinciding well with the grain sizes of the equiaxed grains described above. In other words, the original grains have not been partitioned by hot reduction up to 90%. The slightly elongated grains with sizes up to 150 μm distributed at the original high angle grain boundaries are also formed by a dynamic recrystallization process.

For the CG hot band shown in Fig. 2(b), surface layers consisting of fine, equiaxed grains are also observed. However, much less high angle boundaries are observed in the center region. Accordingly, only three rolled grains are observed and are as thick as 400-1500 μm. Dynamically recrystallized grains are only observed on one original high angle boundary. In addition, the density of low angle boundaries in the rolled grains are low, though a few medium angle boundaries are found inside them. The result indicates that the accumulation of plastic strain is a slow process during hot rolling in the columnar slab grains.
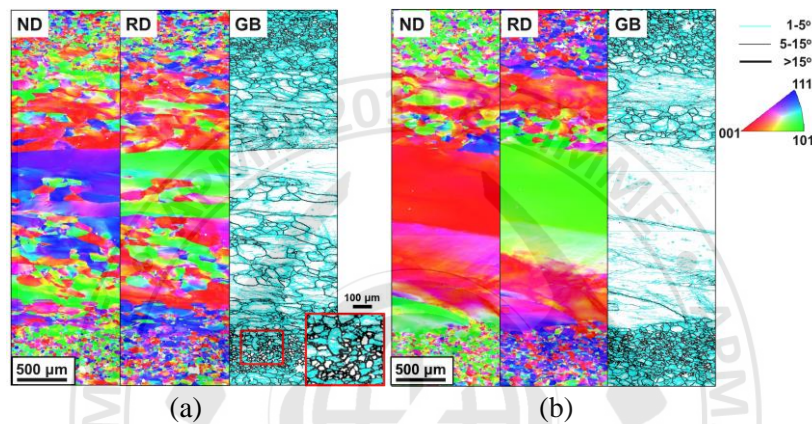
Figure 2. The ND and RD OIMs and boundary maps (with low angle boundaries (LABs, 1°-5°), medium angle boundaries (MABs, 5°-15°), and high angle boundaries (HABs, >15°) highlighted) for the (a) EG and (b) CG hot bands.
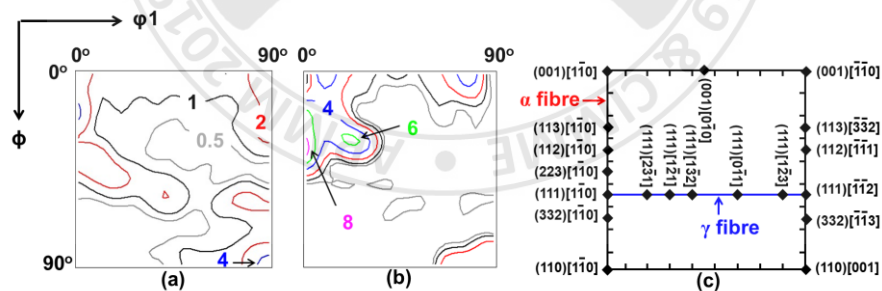
Figure 3. φ2=45° sections showing the orientation distribution function (ODF) obtained from EBSD analyses of three areas for the (a) CG and (b) EG hot bands.

Fig 3(a) shows the orientation distribution of the EG hot band. In addition to the well-known rolling components of the <110>//RD (α) fiber and <111>//ND (γ) fiber, components of Goss ({110}<001>), cube({100}<001>) and {100}<120>, which are usually present in recrystallized samples, are also observed. With the assistance of the OIMs in Fig. (2), it is clear that the α- and γ-fiber grains are mainly distributed in the central area, while the non-conventional ones are distributed in the 1/4 and 3/4 thickness regions. Fig.3 (b) shows the orientations distribution of the CG hot band. The intensity of the γ-fiber is low whereas the non-conventional ones are still exists.

After the hot bands were annealed at 950 °C for 60 s (Fig.4), the rolled grains are mostly replaced by the recrystallized ones, which contain no low angle boundaries, in EG hot band. There are, however, still about 40% of rolled grains remaining unrecrystallized in CG hot band. The recrystallized grains in the CG sample are larger than those in the EG one.

Figure 4. The ND and RD OIMs and boundary maps for the annealed (a) EG and (b) CG hot bands.

CONCLUSION

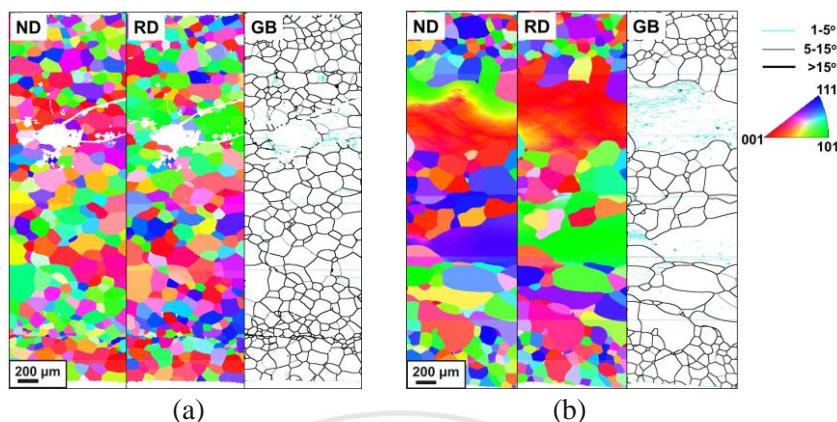This study demonstrates that the columnar grains in a continuous-casting slab evolved into thick rolled grains during hot rolling which contained relatively low density of low angle boundaries. A few equiaxed grains were formed at selected original grain boundaries through a dynamic recrystallization process. The hot band rolled from a slab consisting of equiaxed grains contains more dynamically recrystallized grains at the original grain boundaries. High density of low angle boundaries were observed inside both the rolled and the dynamically recrystallized grains. Accordingly, the rolled grains in the EG hot band recrystallized to equiaxed grains on subsequent annealing, whereas only half of the rolled grains in the CG hot band could recrystallize successfully. In addition, EBSD analyses showed that some rolled grains exhibited orientations which are usually observed in the recrystallized steels, such as Goss ({110}<001>) and Cube ({100}<001>).

ACKNOWLEDGEMENTS

REFERENCE

1. H.T. Liu, Z.Y. Liu, Y.Q. Qiu, G.M. Cao, C.G. Li, and G.D. Wang. (2009). Characterization of the solidification structure and texture development of ferritic stainless steel produced by twin-roll strip casting. Materials Characterization. 60:79-82.
2. D. Raabe and K. Lucke. (1992). Texture and microstructure of hot rolled steel. Scripta Metallurgica et Materialia. 26(8): 1221-1226.
3. E. Gomes, J. Schneider, K. Verbeken, H. Hermann and Y. Houbaert. (2010). Effect of Hot and Cold Rolling on Grain Size and Texture in Fe-Si Strips with Si-Content Larger than 2 wt%. Materials Science Forum. 637-642: 3561-3566.

International Conference on Asia Pacific Mining and Metallurgy

Tainan, Taiwan, November 17-20, 2019

Section 2：Materials Science

15：10 – 17：00　　　　2nd Lecture Room

| 15:10-17:00 | Session Chair: | Dr. **Dhayanantha Prabu Jaihindh** |
| | | National Dong Hwa University |

| 15:10-15:40 | CIMME108053 | **Prof. Chun-Hong Kuo** |
| | | Academia Sinica |

Fabrication of Bimetallic Nanoicosahedra Building Strain Surfaces
by Twinning Boundaries toward Catalytic Energy Conversion

| 15:40-16:10 | CIMME108192 | **Prof. Kuei-Chih Feng** |
| | | Ming Chi University of Technology |

Development of Low-K and Mid-K co-fired LTCC Materials and Silver-diffused
Mechanism for Millimeter-wave Properties

| 16:10-16:30 | CIMME108065 | **Atul Verma** |
| | | National Dong Hwa University |

Ag-Cu_xO_g-C_3N_4 Composite Systems Synthesized via Facile Hydrothermal Route
from HMT Mediated Reaction for Catalytic 4-Nitrophenol Reduction

| 16:30-16:50 | CIMME108066 | **Sanath Kumar** |
| | | National Dong Hwa University |

Ni Doped Iron Pyrite Embedded over rGO as an Efficient Catalyst
for Reducing Tri-Iodide in Dye Sensitized Solar Cell

Fabrication of Bimetallic Nanoicosahedra: Building Strain Surfaces by Twinning Boundaries toward Catalytic Energy Conversion

Chun-Hong Kuo,[1,2,*] Ming-Yen Lu,[3] Yu-Chun Chuang,[4] and David A. Cullen[5]

[1]*Institute of Chemistry, Academia Sinica, Taipei 11529, Taiwan*

[2]*Department of Materials Science and Engineering, National Central University, Taoyuan 32001, Taiwan*

[3]*Department of Materials Science and Engineering, National Tsing Hua University, Hsinchu 30013, Taiwan*

[4]*National Synchrotron Radiation Research Center, Hsinchu 30076, Taiwan*

[5]*Materials Science and Technology Division, Oak Ridge National Laboratory, Oak Ridge, Tennessee 37831-6496, United States*

Building strain surfaces on bimetallic nanocrystals renders them superior catalysts for energy-conversion reactions. In the common types of alloy, core-shell, and Janus structures, the alloy forms in atom-level blending of elements while the latter two form with interfaces by contacts of different components in the structures where specific strain is generated due to lattice mismatch. The strain varies the surface states in the vicinities of interfaces and hence leads to further alterations in the catalytic behaviors of bimetallic nanocrystals. Recently, an icosahedron is known a structure with 30 twinned boundaries that induce large tensile strain on its 20 facets, significantly improving the surface reactivity of the nanoicosahedron in a catalytic reaction. In this talk, two stories about bimetallic AuPd nanoicosahedra and icosahedral PdRu nanoframes for liquid fuel oxidation, photoreduction of nitro-compounds, and anthropogenic chemical carbon cycle will be introduced. In the first part, we will demonstrate how monodispersed AuPd nanoicosahedra with photoactivity were fabricated in one-step aqueous synthesis. Figure 1 shows the selected data of structural information about the AuPd (a-c) alloy and (d-e) core-shell nanoicosahedra. These results indicate their well-defined yet different structures. In Figure 1g and 1h, the atom-resolved HAADF-STEM images tell the difference clearly, where the shell of the AuPd core-shell nanoicosahedra is composed by 3 to 4 atomic layers of Pd. With these AuPd nanoicosahedra, the performances by their variable yet controlled surface compositions in ethanol oxidation via electrocatalysis and photoreduction of 4-nitrophenol aided by visible energy had been explored and will be presented. Moreover, we will discuss about the technique in surface modulation of the AuPd core-shell nanoicosahedra at atomic scale, by which the shell merely varies in the thickness of 2-3 atomic layers but largely changes in the surface activity. In the final part, we will further introduce the work where unique icosahedral PdRu nanoframes were also prepared in one-step strategy and water phase. The novel nanoframes grow via evolution from solid nanoicosahedra followed by vertex-etching and interior excavating. Figure 2 collects some structural information of icosahedral PdRu nanoframes where clearly display the excavated structures and conversed twinned boundaries. Apart from the synthesis, we had explored the growth kinetics of the nanoframes and looked into their performances in a mimicking anthropogenic carbon cycle by running electrocatalytic ethanol oxidation and CO_2 reduction.
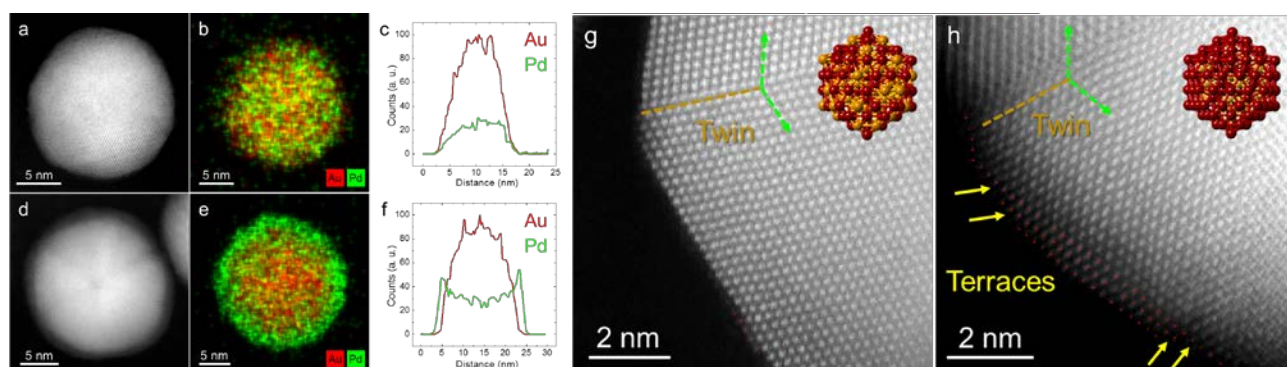
Figure 1. HAADF-STEM images and EDS analytic results of AuPd (a-c) alloy and (d-f) core-shell nanoicosahedra. (g,h) Atom-resolved HAADF-STEM images at a twinned corner of AuPd (g) alloy, and (h) core-shell nanoicosahedra.
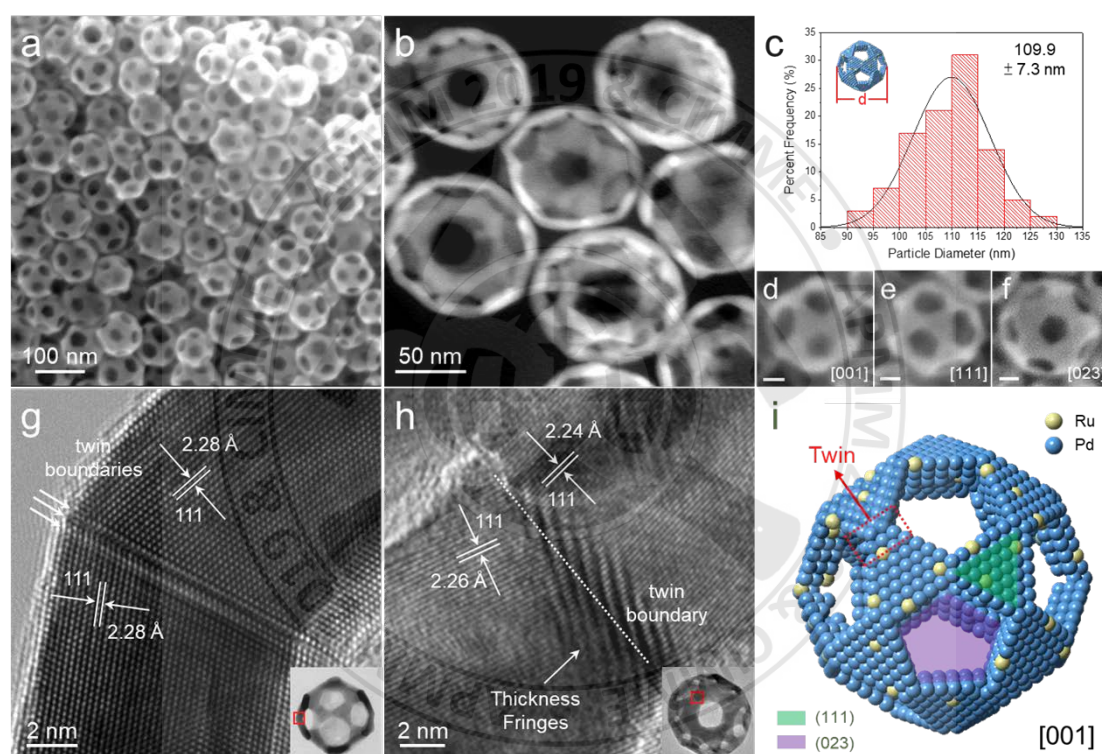
Figure 2. (a) SEM image, (b) HAADF-STEM image, (c) histogram of particle sizes, (d-f) SEM images of a single particle viewed along different axes, (g,h) bright-field HRTEM image at twinned sites, and (i) structural model of icosahedral PdRu nanofrmaes.

Development of low-K and mid-K co-fired LTCC materials and silver-diffused mechanism for millimeter-wave properties

Kuei-Chih Feng

Department of Mechanical Engineering, Ming Chi University of Technology,
New Taipei City 24301, Taiwan

Abstract

The low-K and mid-K co-fired microwave dielectric materials for the development of low temperature co-fired ceramics (LTCC) were investigated. The mid-K material is $Ba_5Nb_4O_{15}$ ceramic added with <10% glass (BN-40). The low-K materials include $BaWO_4$ ceramic added with <10% glass (BW-10), $CaMgSi_2O_6$ glass-ceramics (CMS-7), and CaO -Al_2O_3-B_2O_3-SiO_2 glass added with Al_2O_3 ceramic-filler (CABS-7). BN-40 and BW-10 contain less than 3% silicate oxide addition, and CMS-7 and CABS-7 contain high concentrations of silicate oxide up to above 50%. In order to develop the heterogeneous co-firing of low-K and mid-K materials, four materials were prepared by tape casting and then low/mid-K materials co-fired at 900^oC for 30 mins with Ag electrode.

The BN-40 co-fired with both CMS-7 and CABS-7 shows high Si diffusion in the heterogeneous boundary. CMS-7 and CABS-7 co-fired with silver inner-electrode also exhibit high silver diffusion in the matrix. It was suggested that the liquid phase sintering easily induces interaction and silver diffusion due to the high silicate concentration. Moreover, the BN-40 co-fired with BW-10 exhibits clearly heterogeneous boundary and no Ag diffusion due to a few silicate existence in the BN-40 and BW-10. BN-40 and BW-10 can be considered as candidates for low-K and mid-K co-fired materials for LTCC development.

Furthermore, the silver diffusion of CMS-7 and CABS-7 was analyzed. In the CABS-7 system, the higher sintering temperature and the longer soaking time increase silver diffusion distance to comply with the Fick's second law. In the glass-ceramics of CMS-7, silver obviously diffused into matrix while nucleation took place. Ag diffusion and elemental inter-diffusion occur during the endothermic-exothermic process near nucleation temperatures (~820 ^{o}C), where Ag diffused into the glass-ceramic matrix and resided around the diopside-phase grain boundaries while other metal elements (Zn, Mg, and Al) diffused into the Ag layer. Oxygen ions can flee from the glass-ceramic network above glass transition temperature (Tg~780 ^{o}C) during the endothermic process and react with the Ag ions to form the Ag-O bonds. The low dielectric dissipation in the millimeter-wave range remains after Ag diffused into the matrix. However, conductivity of Ag-electrode layer decreases at a GHz frequency due to the inter-diffusion elements with lower electric conductivities.

In order to inhibit silver diffusion, 0-2.0 wt% SiO_2 added CMS-7 glass-ceramics co-fired with silver electrode were studied. SiO_2-added $CaMgSi_2O_6$ exhibits a reduction of inter-diffusion and Ag-O phase in the diffusive layer, indicating that SiO_2 addition in the $CaMgSi_2O_6$ can inhibit inter-diffusions. 2 wt% SiO_2-added in CMS-7 glass-ceramics were prepared to fabric the patch antenna. The patch antenna exhibits a return loss of S_{11} = -23 dB at frequency = 28GHz, which is better than ~S_{11} = -18 dB in specimens without SiO_2 addition.

Keywords: LTCC, Glass + ceramic-filler, Glass-ceramics, silver diffusion, millimeter-wave

∗ **Corresponding author**: kwechin@mail.mcut.edu.tw

Ag-Cu$_x$O/g-C$_3$N$_4$ composite systems synthesized via facile hydrothermal route from HMT mediated reaction for catalytic 4-Nitrophenol reduction

Atul Verma*, Zong-Hsiang Hseih, Yen-Pei Fu

Department of Materials Science and Engineering, National Dong Hwa University,
Shoufeng, Hualien-97401, Taiwan.

atulverma1992@gmail.com

The immense need to build highly efficient catalysts has always been on the forefront of environmental remediation based research. Herein we have synthesized a dual phase copper oxide containing Cu$_2$O and CuO originating from the same reaction using hexamethyltetramine (HMT) and simultaneously coupled it with g-C$_3$N$_4$ (g-CN) constructing a p-n-p type heterojunction which have been reported very less often in the literature. The hydrothermal reactions led to the formation of various catalysts namely Ag-Cu$_2$O-CuO-gCN (ACCG), Ag-CuO-gCN (ACG), Ag-Cu$_2$O-CuO (ACC) and Ag-CuO (AC). The catalyst were thoroughly characterized via XRD and FESEM to gain the structural, crystallographic and morphological insights of the catalyst leading to the conclusion of pure phase formation of the catalyst and development of sheet like CuO and truncated octahedrons of Cu$_2$O fused together within the g-CN framework. Also XPS studies revealed the presence of copper in two different oxidation states namely Cu^{2+} and Cu$^+$. BET analysis was performed to analyze the surface area and pore volume of the catalysts which plays a very significant role in catalytic reduction. The catalytic efficiency of the catalysts was evaluated via the reduction of 100 ppm 4-Nitrophenol (4-NP) to 4-Aminophenol (4-AP) in the presence of excess NaBH$_4$. The most efficient catalyst was ACCG revealing that, both Cu$_2$O and g-CN played a significant role in the reduction of 4-NP which occurred in 4 minutes following a zero order kinetics unlike most often reported in literature. We also evaluated the catalytic reduction with different concentrations of 4-NP and tuning the catalyst amount as well.

Keywords: Ag-Cu$_2$O-CuO-gCN (ACCG), 4-Nitrophenol (4-NP), Catalytic reduction, Dye degradation

1. INTRODUCTION

4-Nitrophenol (4-NP) is considered to be major environmental contaminant and is also called as stubborn pollutant in industrialized wastewater. Environmental protection agency (EPA) of the United States considers nitrophenols as "priority pollutants" due to their toxic and hazardous nature [1]. Commonly employed materials for the reduction of 4-NP are noble metals namely Au, Ag, Pt, Pd. The fact that these materials are rare and expensive limits their extensive use [2]. Copper oxide which is inexpensive can be a viable alternative to such noble metals. CuO is a versatile material used in various applications such as solar energy conversion, solar cells, lithium ion batteries, gas sensors, supercapacitors, magnetic storage etc.Cu$_2$O, an alternate phase of copper oxide also is explored by researchers due to its narrow bandgap, it possesses well distinguished optical, electronic and catalytic properties. Cu$_2$O has been used more often than CuO for reduction of nitrophenol according to earlier research [3]. g-C$_3$N$_4$ is a cheap, metal free and non-toxic material which can be prepared via simple technique though it does not possess the ability to work alone without hybridization with other semiconductors [4] Here we have synthesized a unique ternary composite material comprising of CuO, Cu$_2$O and g-C$_3$N$_4$ via a very facile hydrothermal technique. We used this Ag-Cu$_2$O-CuO-gC$_3$N$_4$ material for the catalytic reduction of 4-Nitrophenol. In order to study the effect of 4-NP and catalyst dose, we performed the reduction experiments at different concentrations of 4-NP, varying catalyst dose. Surprisingly, it took about only 4 minutes to completely reduce 100 ppm 4-NP.

2. EXPERIMENTAL

2.1 Synthesis of Ag-Cu$_2$O-CuO-gCN(ACCG), Ag-CuO-gCN(ACG), Ag-Cu$_2$O-CuO(ACC), Ag-CuO(AC)

0.1 g of as prepared g-C$_3$N$_4$ was ultrasonically dispersed in 20 ml DI water for 40 minutes (Solution A). 0.5 g

of Hexamethyltetramine (HMT) was dissolved in 10 ml DI water in a separate beaker (solution B). 1.207 g and 17 mg of $AgNO_3$ were dissolved in 10 ml DI water in another beaker (solution C). Also 1M NaOH solution was prepared by dissolving 0.46 g in 10 ml DI water (Solution D). Sol. B is poured into sol. C and the mixture is vigorously stirred for 30 minutes to form a creamy blue solution. Later sol. A and 10 ml ethanol were added to the above mixture and stirred for 10 minutes. Finally sol D was added drop wise to the above reaction mixture and was left for stirring for 30 minutes. This final solution was placed in a Teflon lined stainless steel autoclave and loaded in a furnace at 130°C for 3 hours. A greyish black powder was obtained which was then washed with DI water and ethanol several times and dried in an oven for 6 hours at 65°C. A final annealing was performed at 160°C for 6 hours. The obtained powder sample was labelled as ACCG. ACG was synthesized via the same procedure as above only with the exception that HMT was not added into the reaction mixture. In the synthesis of $Ag-Cu_2O-CuO$, addition of $g-C_3N_4$ was eliminated with rest of the procedure being identical. Finally Ag-CuO was synthesized by skipping the steps of addition of $g-C_3N_4$ and HMT.

3. RESULT AND DISCUSSION

3.1. XRD characterization

XRD patterns comprises of highly crystalline peaks corresponding to Cu_2O, CuO and $g-C_3N_4$. No other impurity peaks were found implicating that the materials were highly pure in nature. The peaks of Cu_2O were matched to the standard JCPDS 77-0199, CuO matched to 89-5895 and $g-C_3N_4$ matched to 85-1526. $g-C_3N_4$ was identified with the peak at 27.3° corresponding to the plane (002) attributed to the stacking of aromatic conjugated system.
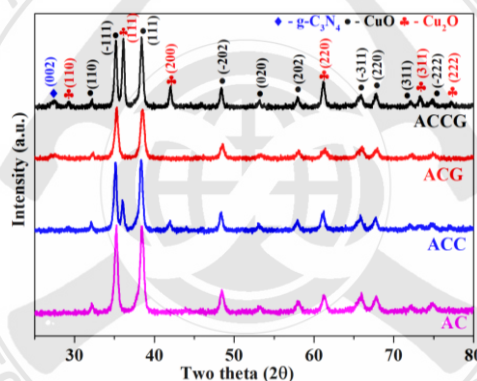
Fig. 1. XRD pattern of the synthesized composite materials

3.2 FESEM images

The morphology and microstructure of the composite catalysts are depicted in figure 2. ACCG shows the presence of bright Cu_2O octahedrons formed due to the influence of HMTA along with elongated leaf like structure of CuO and sheets of $g-C_3N_4$ enfolded around both CuO and Cu_2O. ACG image only shows the presence of CuO and $g-C_3N_4$. ACC depicts only CuO and Cu_2O. AC represents only CuO.
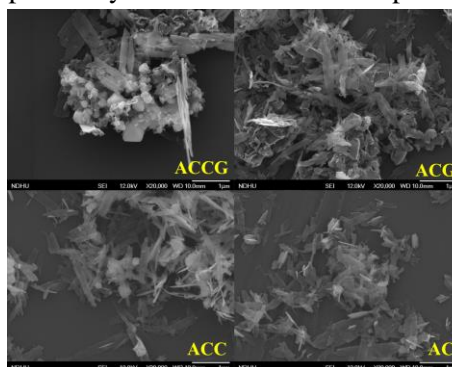
Fig. 2. FESEM images of the synthesized catalysts

3.3 X-ray Photoelectron spectroscopy (XPS)

Cu 2p displays that copper is present in oxidation states namely 2+ at binding energy value of 936.1 eV and 1+ at 934.2 eV belonging to the Cu $2p_{3/2}$ with Cu^{2+} being the majority component. The O1s spectra peaks at

531.4 eV, 532.9 eV, 533.9 eV and 536.1 eV can be assigned to the lattice oxygen in CuO, Cu_2O, adsorbed oxygen molecules and oxygen in chemisorbed water molecules respectively.
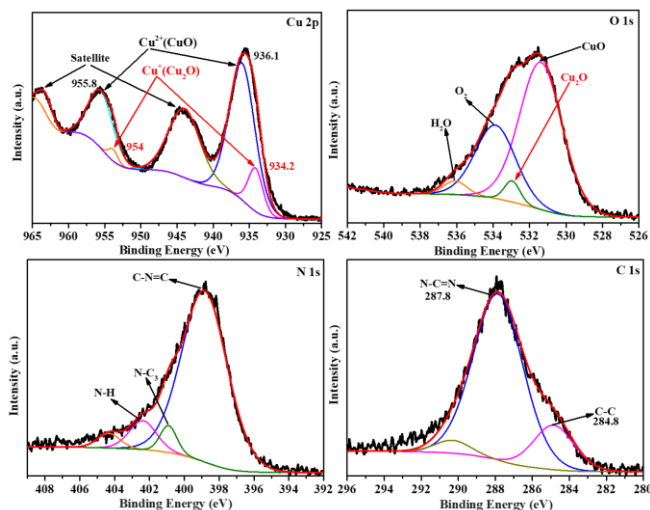
Fig. 3. XPS spectra of ACCG catalyst

N 1s spectra indicate the presence of nitrogen in different chemical environments at 398.9 eV which belong to the C-N=C triazine bonds predominantly present in g-C_3N_4, peak centered at 400.9 eV originates from the N-C_3 bridges in g-C_3N_4 and peak at 402.4 eV may be attributed to the uncondensed N-H bonds emerging from the synthesis process with urea [56] Peak at binding energy 284.8 eV belongs to the C-C bond of the adventitious sp^2 carbon and the peak at 287.8 can be corroborated with the N-C=N bonds in the g-C_3N_4.

3.4. Catalytic reduction of 4-Nitrophenol
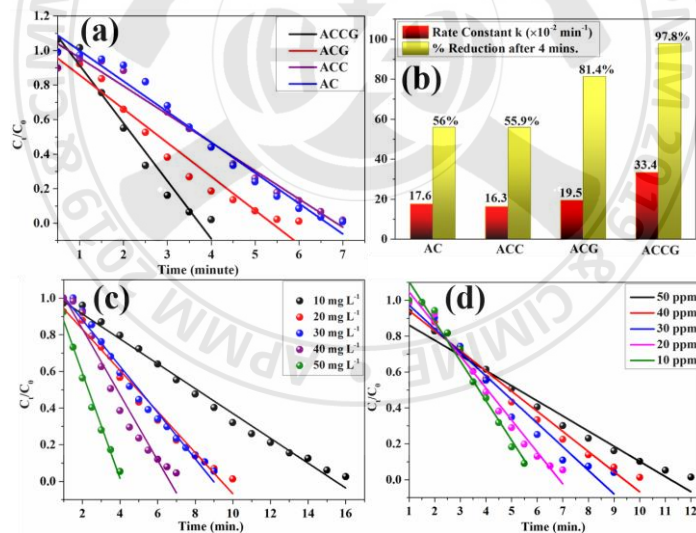
Fig. 4. Catalytic reduction of 4-NP with various catalysts [4-NP=100 ppm (1.5 ml), $NaBH_4$=0.1M (1.5 ml) & Catalyst=100 mgL^{-1}], (b) rate constant and percentage of catalytic reduction by various catalysts, (c) Effect of catalyst loading (4NP=40 ppm, $NaBH_4$=0.1M) and (d) Effect of 4-NP initial concentration (Catalyst=20 mgL^{-1}, $NaBH_4$ = 0.1M).

Figure 4 (a) depicts the ability of the catalysts to reduce the 4-NP pollutant. The time taken for ACCG, ACG, ACC and AC is 4, 6, 7 and 7 minutes respectively. C_t/C_0 vs time plot indicates that a constant amount of 4-NP is eliminated per unit time and the reduction followed pseudo zero order kinetics. Figure 4(b) portrays the percentage reduction and its corresponding rate constants by various catalysts in 4 minutes. It is easily perceivable that ACCG material is by far the best catalyst amongst the synthesized materials. These results suggest that C_3N_4 and Cu_2O play an important role to significantly enhance the catalytic efficiency of the material. Even after the addition of Cu_2O in the pristine CuO i.e; in the ACC composite, the reduction ability was not improved. Enhancement occurs only with the addition of C_3N_4. C_3N_4 has a sheet like structure and

can help in adsorption of 4-NP species and also drawing them towards the active sites. Cu_2O octahedrons have an exposed (111) planes which are rich in Cu (I) sites possessing the ability to efficiently adsorb nitroarenes [7]. Figure 4(c) and (d) illustrate the effect of catalyst loading and 4-NP concentration on the catalytic reduction. The reduction rate is rapid as the catalyst amount is increased and the concentration of 4-NP is decreased. High amount of catalyst gives rise to more adsorption of the reacting species and active sites for the reduction to occur. Even after changing the catalyst amount and initial concentration, the reaction still followed a pseudo zero order kinetics.
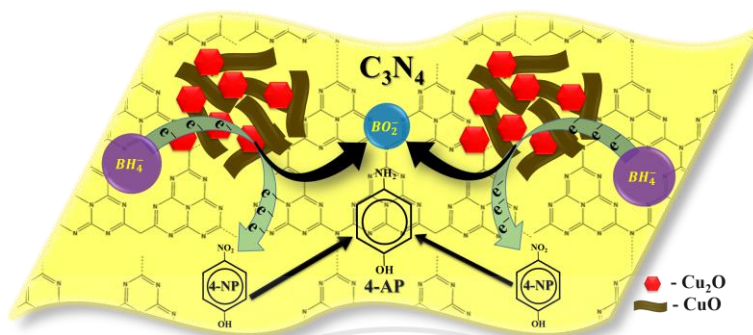
Fig. 5 Mechanism of 4-NP catalytic reduction by ACCG catalyst

Figure 5 illustrates the mechanism of electron transfer from BH_4 ions to the 4-NP species through the catalyst material. This transfer of electron is thermodynamically possible but kinetically restricted in the absence of catalyst. The main steps in the reduction process are (i) adsorption of 4-NP to the catalyst and its diffusion into the active sites (ii) electron transfer to form products and (iii) desorption of product 4-AP from the surface of the catalyst.

CONCLUSION:
ACCG composites were successfully synthesized via HMT mediated reaction in order to obtain dual phase copper oxide from the same precursor via a simple hydrothermal technique. The materials were thoroughly investigated with XRD in order to differentiate between the materials formed during synthesis and confirm the purity and crystallinity of the material. FESEM images were used to determine the morphology, attachment of the materials to each other and also to learn about their dimensions. It was found that Cu_2O had formed octahedrons in contrast with CuO which formed leaf like structures. XPS analysis was performed to learn about the oxidation states of the elements present and also to realize the types of bonds. It was evidently demonstrated that the material contained copper in 1+ and 2+ states. Finally the materials were subjected to catalytic reduction of 4-Nitrophenol which is a highly toxic and stable pollutant in water. It was found that ACCG catalyst was able to reduce 4-NP upto 97% in 4 minutes which was very high compared to other synthesized materials. We also evaluated the effect of catalyst loading and initial 4-NP concentration on the catalytic reduction.

References
1. D. Choi and D. J. Jang, *New J. Chem.*, 2017, **41**, 2964–2972.
2. Z. Jin, C. Liu, K. Qi and X. Cui, *Sci. Rep.*, 2017, **7**, 1–9.
3. L. Chen, M. Liu, Y. Zhao, Q. Kou, Y. Wang, Y. Liu, Y. Zhang, J. Yang and Y. M. Jung, *Appl. Surf. Sci.*, 2018, **435**, 72–78.
4. R. Abazari, A. R. Mahjoub and G. Salehi, *J. Hazard. Mater.*, 2019, **365**, 921–931.
5. P. Zhang, T. Wang and H. Zeng, *Appl. Surf. Sci.*, 2017, **391**, 404–414.
6. D. P. Sahoo, S. Patnaik, D. Rath, B. Nanda and K. Parida, 2016, 112602–112613.
7. T. Aditya, J. Jana, N. K. Singh, A. Pal and T. Pal, *ACS Omega*, 2017, **2**, 1968–1984.

Ni doped iron pyrite embedded over rGO as an efficient catalyst for reducing tri-iodide in dye sensitized solar cell

Sanath Kumar*, Shao-Ping Chiang, Yen-Pei Fu,
Department of Material science and Engineering, National Dong Hwa University
Shoufeng, Hualien-97401, Taiwan.
skumarchilimbi@gmail.com,

ABSTRACT

In this work, Ni doped iron pyrite/reduced graphene oxide (rGO) was prepared in one step hydrothermal process and the material was used as alternative for platinum counter electrode in Dye sensitized solar cells(DSSCs). Crystallinity and purity of the material was analyzed using X-ray diffractometer and Raman spectroscopy. Morphology of the prepared material was studied using Field emission scanning electron microscopy. Further, counter electrode was prepared and electrochemical characterizations was studied. Finally, DSSCs was fabricated which exhibited better performance than platinum based DSSCs.

1. INTRODUCTION

Dye Sensitized solar cells (DSSCs), which is categorized under third generation solar cells has the competitive performance using low cost environmental friendly materials [1] and has simple fabrication technique. DSSCs made of platinum counter electrode has excellent catalytic activity and showed the efficiency over 11%. But the issue of CEs stands with using noble metal but lags in large scale application due to its cost and scarcity. Hence it is very necessary to find an alternate for platinum.

In this paper Ni doped FeS_2/rGO composite material was prepared via one step hydrothermal process. The reason for keeping the doping concentration as 10 % to the Iron pyrite as the p-type nature of the material was kept intact and Graphene oxide with 1 mg/mL at 200oC in autoclave will have an exfoliated layers of graphene to exhibit few layers of graphene. The synthesized material morphology showed the spheres with rough, porous surface, which helps in efficient reduction of tri-iodide and also could replace the platinum based DSSCs.

2. SYNTHESIS PROCEDURE

Graphene Oxide was prepared using hummers method as reported previously[2]. 1 mg/mL of GO was dispersed in DI water (80 mL) and 2 mmol of ferrous sulfate heptahydrate, 8 mmol of sodium thiosulfate pentahydrate and 0.2 mmol of nickel nitrate hexahydrate was dissolved in the GO dispersed solution by stirring it for 30 min. Then the solution was transferred to Teflon lined autoclave and placed inside muffle furnace at the temperature of 200ºC for 24 h. Further the autoclave is naturally cooled till room temperature and obtained composite was washed with hot distilled water and ethanol for several times and dried at 80oC for 12 h to obtain Ni-FeS_2/rGO composite.

2.1. COUNTER ELECTRODE PREPARATION AND DSSC FABRICATION

Counter electrode was prepared via doctor blade method with a slurry prepared via mortaring 8:1:1 ratio of material: carbon black and PVDF dissolved in NMP, prepared slurry was coated and dried at 100ºC for 10 hrs. Photo-anode was prepared as per previous report [3] and DSSCs was fabricated by sealing surlyn spacer. The liquid electrolyte EL-200 was injected via drill hole made in counter electrode.

3. RESULTS AND DISCUSSION
3.1. XRD AND RAMAN SPECTROSCOPY
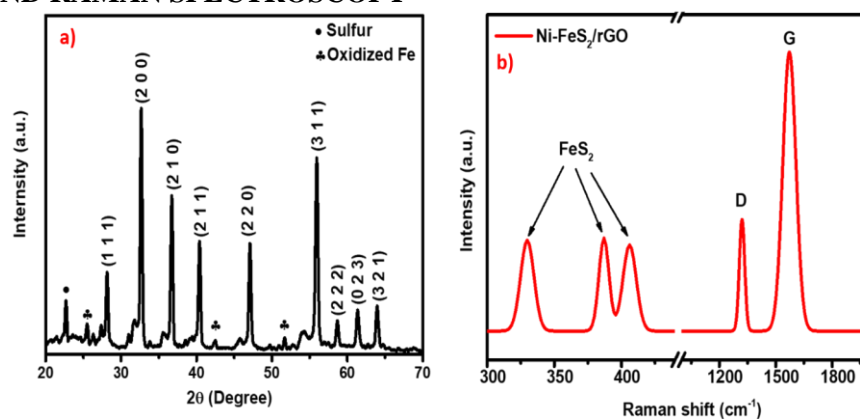
Fig 1 XRD pattern and Raman spectra if Ni-FeS2/rGO

Fig. 1(a) is the XRD pattern of Ni-FeS$_2$/rGO has the phase purity consisting of dominant pyrite matching with the JCPDS card no 42-1340[4]. In Fig, 2(b), is the Raman spectra is revealed where D and G and of the few layers' graphene is observed in 1330 and 1575 cm-1 respectively. The I$_D$/I$_G$ was calculated to be 0.47. Apart of these the peaks of FeS$_2$ microcrystal are observed at 330, 385, and 405 cm^{-1}. These are the characteristic peaks of active modes for bulk pyrite corresponding to vibration of S2 (Eg), phase stretch of S-S (Ag), and coupled vibration and stretch (Tg$_{(3)}$)[5] modes, respectively.

3.2. FIELD EMISSION SCANNING ELECTRON MICROSCOPY
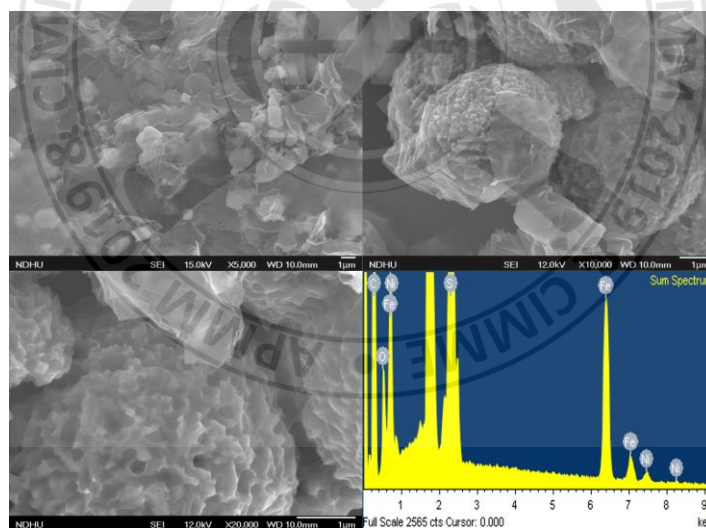
Fig 2. FESEM-EDS of Ni-FeS$_2$/rGO

The specific structure with Ni-FeS$_2$/rGO composite exhibits much higher specific conductivity and better electron transfer ability. It is assumed that combined contribution of several features gives the excellent electrochemical properties. First, the contact of the Ni ions on FeS$_2$ particles and embedding of those particles with rGO. Finally, the integral conductive rGO networks facilitates the facile electron transport pathway, which ensures the higher performance. The EDS shows the presence of Ni, Fe, S and C in the synthesized material.

3.3. CYCLIC VOLTAMMETRY STUDIES

To examine the cyclic ability of the prepared electrodes cyclic voltammetry (CV) test was conducted in a three electrode electro-chemical cell setup with a potential window of -0.4 V to 1.2 V at the scan

rate of 50 mV/sec. The CV shown in Fig 3a exhibits two pair of oxidation and reduction peaks corresponding to the following equation.
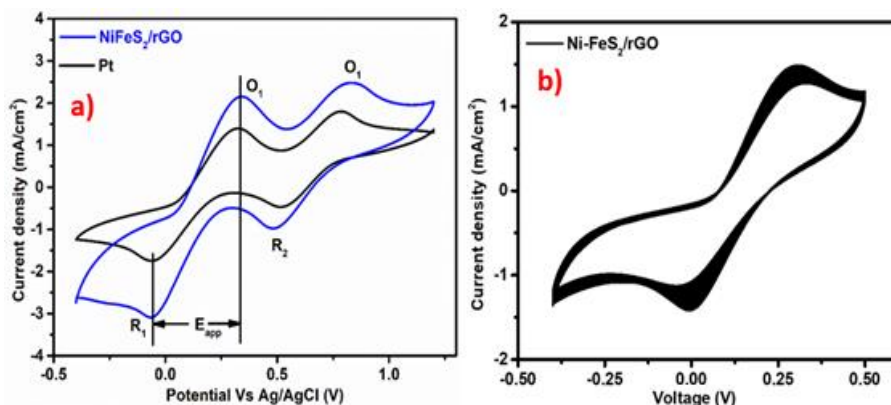
Fig 3. CV of Pt and Ni-FeS$_2$/rGO and multiple scan CV of Ni-FeS$_2$/ rGO

$$3I^- - 2e^- = I_3^- \ldots\ldots\ldots (1)$$
$$I_3^- + 2e^- = 3I^- \ldots\ldots\ldots (2)$$
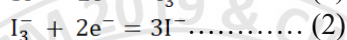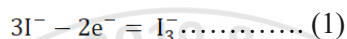
The peaks current density is important in signifying the electrochemical parameters of the prepared counter electrode, the higher peak current density and lower potential difference in the redox peak exhibits a good electro-catalytic performance. The parameters describing the electrochemical properties are shown below.

Table-1 Electrochemical parameters of counter electrode.

Counter electrodes	E_{app} (mV)	J_{red} (mA cm^{-2})	D_n (cm^{-2} s^{-1})
Ni-FeS$_2$/rGO	0.31	2.61	$8.35*10^{-6}$
Pt	0.34	1.82	$5.82*10^{-6}$

Further multiple scan voltammetry shown in Fig 3b was carried out to study the stability of the prepared counter electrode, where the counter electrode surface was in contact with the electrolyte for 50 cycles at the scan rate of 25 mV/secs and it was able to hold 90 % of the redox properties, this explains the good stability of the developed electrode.

3.4. EFFICIENCY OF FABRICATED DSSCs
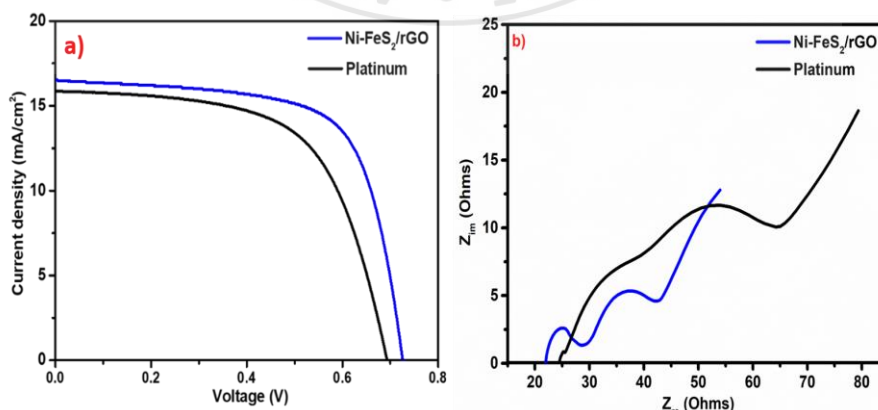
Fig.4 J-V plot (a) and EIS(b) of fabricated DSSCs

DSSCs was fabricated with the photo-anode active area of 0.25 cm^2 and characterized under solar simulator with the light intensity of 100 mW/cm^2 and the photocurrent density vs voltage plot (J-V) is shown in Fig 4a and photovoltaic properties of the fabricated cells are shown in the Table-2 and from the table is clear that the synthesized material could outperform the platinum based DSSCs.

Fig 4b is the electrochemical impedance spectroscopy (EIS) of the fabricated DSSCs and the test was done in the frequency range from 1 MHz to 1 mHz which exhibits a nyquist plot which explains the interfacial resistance of the DSSCs. In the obtained plot with two semi-circles, the first semicircle is resistance occurring at the interface of counter electrode/electrolyte is important in signifying the charge transfer resistance of prepared counter electrode. The EIS of the platinum free DSSCs exhibited the lesser charge transfer resistance than platinum based DSSCs, which could efficiently transfer electrons. The EIS properties are shown in Table-2.

Table-2 Photovoltaic properties of fabricated DSSCs

Counter electrode	V_{oc} (V)	J_{sc} (mA/cm^2)	FF	Eff (%)	R_{ct} (Ohms.cm^{-2})
Ni-FeS$_2$/rGO	0.726	16.53	0.64	7.60	6.49
Pt	0.695	15.8	0.61	6.69	15.8

4. CONCLUSION

The one pot synthesized materials has dominant pyrite phase with Nickel ions doping and Nickel doped Pyrite was embedded over rGO to exhibit a good interconnecting morphology with helps in electron transfer. The prepared counter electrode has good electrochemical and photovoltaic properties that could outlast the existing standard platinum based DSSCs.

5. REFERENCES

1] Grätzel, M. Recent Advances in Sensitized Mesoscopic Solar Cells. Acc. Chem. Res. (2009) 42 (11), 1788–1798

2] Shahriary, L., Athawale, A. A. Graphene oxide synthesized by using modified hummers approach. Int. J. Renew. Energy Environ. Eng, (2014) 2(01), 58-63.

3] Kumar, S., Manikandan, V. S., Palai, A. K., Mohanty, S., & Nayak, S. K. Fe$_2$O$_3$ as an efficient filler in PVDF-HFP based polymeric electrolyte for dye sensitized solar cell application. Solid State Ionics, (2019) 332, 10-15.

4] Liu, Z., Lu, T., Song, T., Yu, X. Y., Lou, X. W, Paik, U. Structure-Designed Synthesis of FeS$_2$@C Yolk-Shell Nanoboxes as a High-Performance Anode for Sodium-Ion Batteries. Energy Environ. Sci. (2017) 10 (7), 1576–1580

5] Cabán-Acevedo, M., Liang, D., Chew, K. S., Degrave, J. P., Kaiser, N. S., Jin, S., Synthesis, Characterization, and Variable Range Hopping Transport of Pyrite (FeS$_2$) Nanorods, Nanobelts, and Nanoplates. ACS Nano (2013), 7 (2) 1731–1739

International Conference on Asia Pacific Mining and Metallurgy
Tainan, Taiwan, November 17-20, 2019

Section 2：Circular Economy and Sustainable Resources

15：10 – 17：00　　　3rd Lecture Room

15:10-17:00	Session Chair:	Prof. **Hsing-I Hsiang** National Cheng Kung University
15:10-15:40	CIMME108074	**Prof. Yun-Hsun Huang** National Cheng Kung University
		Changes in Energy Consumption and CO2 Emissions among Taiwan, Japan and Korea Using International Input-Output Decomposition Analysis
15:40-16:00	CIMME108011	**Chun-Hsiu Wang** China Steel Corparation, Taiwan
		Performance Testing for Solid Oxide Fuel Cell with Simulated By-Product Gases in Steel Industry
16:00-16:20	CIMME108148	**Yang-Rong Chen** National Cheng Kung University
		Techno-economic Analysis of Large-scale Energy Storage System in Taiwan
16:20-16:40	CIMME108149	**Yi-Ya Yang** National Cheng Kung University
		The Impact of Taiwan's Energy Transformation Policy on Power Supply Planning

Changes in energy consumption and CO₂ emissions among Taiwan, Japan and Korea using international input–output decomposition analysis

Yun-Hsun Huang, Jung-Hua Wu and Hao-Syuan Huang
Department of Resources Engineering, National Cheng Kung University, Taiwan
z10808014@email.ncku.edu.tw, hwaa@mail.ncku.edu.tw, haoshang.huang@gmail.com

ABSTRACT

Identifying the driving forces behind CO_2 emissions changes in various countries and conducting comparisons throughout the cross-country could be a valuable and effective strategy for the reduction of CO_2. This study combined the world input-output database with the two-tier KLEM input-output structural decomposition analysis to analyze the factors that led to the change of CO_2 emissions in Taiwan, Japan, and Korea between 1999 and 2009. Empirical results revealed that the change of exports was the most important factor to increased CO_2 emissions in Taiwan and Korea, whereas the technological change contributed significantly to the decrease of CO_2 in Japan. To decouple the economic growth from CO_2 emissions, proponents of technology upgrading policy in Taiwan and Korea should focus on encouraging research and development in energy efficient technologies, promoting industrial upgrading, encouraging the development of high energy-efficiency and high value-added products, and providing incentives for enterprises in the purchase of energy-saving technologies.

INTRODUCTION

In response to the climate change, countries around the world have successively planned actions to reduce greenhouse gas emissions. Taiwan actively participated in international affairs and proposed its specific targets to reduce the CO_2 emissions. In June 2015, the Greenhouse Gas Reduction and Management Act (GGRMA) had passed in Taiwan, setting the long-term goal of reducing greenhouse gas emissions to less than 50% of the 2005 level by the year 2050. In September 2015, Taiwan put forward the Intended Nationally Determined Contributions (INDCs) which, as a periodical target, promised to reduce the emissions by 50% compared to the business as usual (BAU) in 2030. CO_2 comprises approximately 70% of the greenhouse gases. It mainly originates from the burning of fossil energy, which is a crucial factor input for economic growth. Moreover, the reduction in CO_2 emissions cannot be significantly achieved by a single country alone; hence it needs to depend on international cooperation in order to strike a balance between economic growth, energy consumption and CO_2 emissions.

The changes in CO_2 emissions are influenced by many factors. The driving forces affecting CO_2 emission changes should be identified to better understand CO_2 mitigation strategies. According to the world input-output database (WIOD) released by the statistical office of the European Communities (Eurostat), the structures of energy consumption in Taiwan, Japan, and Korea were similar. Coal consumption accounted for approximately 10%, oil around 20~30%, gas less than 10%, and electricity approximately 50~60%. Hence, this study aims to analyze the factors influencing the changes of CO_2 emissions in Taiwan, Japan, and Korea during 1999-2009, and to conduct a cross-country comparison between the main factors.

Performance testing for solid oxide fuel cell with simulated by-product gases in steel industry

Chun-Hsiu Wang

Energy Development and Application Section, New Materials Research & Development Department,
China Steel Corporation, Kaohsiung, Taiwan.
175695@mail.csc.com.tw

ABSTRACT

The coke oven gas (COG) and blast furnace gas (BFG) are by-product gases during the iron and steel making process. The purpose of this study is to assess the adaptability of the by-product gases as a fuel in the steel industry for a SOFC power system. Performance testing was conducted on a 60-cell stack fueled with the simulated gases from gas cylinders. The results indicate: (1) the high voltage and fuel utilization is the key condition for high efficiency output. (2) the electrical efficiency of COG is 52.8% at full load of 1kW output and 59.6% at part load of 0.5kW. (3) the electrical efficiency of BFG is 40.3% at full load of 1kW output and 45.2% at part load of 0.5kW. (4) it is experimentally proved that SOFC can be fueled with well purified by-product gases with high efficiency.

INTRODUCTION

The COG and BFG are by-product gases during the iron and steel making process. COG contain 60% hydrogen, 25% CH4, and 6% CO, which has higher heating value of 4100 kcal/Nm^3. BFG contain 4% hydrogen and 23% CO, which has lower heating value of 781 kcal/Nm^3. All these fuel are applied as energy source of heat or power in the steel industry. However, the efficiency is lower due to lower heating value. SOFC is an energy conversion unit that converts a gaseous fuel to electricity by electrochemical reaction. It is able to convert hydrocarbon fuel with high efficiency, and to produce high quality heat for energy conversion. Theoretically, COG and BFG can be fuel sources for SOFC. However, there is no literature about the testing.

Since SOFC offers a wide range of operating possibilities, identifying the influence of operation conditions on the efficiency and power density is critical for optimal operation of SOFC. The performance of SOFC strongly depends on the operating conditions and the inlet fuel composition. Operating in the region of high efficiency may result in a very low power density requiring large cell volume to deliver the required power output, while operating at high power density can lead to low efficiency. Hence, the SOFC has to be operated in a reasonable region compromised between efficiency and power density.

This study is to assess the adaptability of the by-product gases for a SOFC power system, and a reasonable operating region is also developed.

EXPERIMENTAL METHOD

The SOFC test rig for 1kW system is supplied via sunfire. The performance test was operated with an external DC load, and the simulated fuels was supplied by gas cylinders. Various current loads were set here to measure the relative power output and efficiency. The definition of efficiency here is shown as Eq. (1), where η is DC efficiency, P is power, and H is low heating value (LHV) of gases.

$$\eta = \frac{P}{H}$$

(1)

RESULTS AND DISCUSSION

Due to polarization, SOFC stack produces heat during electric generation. The heat will be managed very carefully to prevent thermal shock or over temperature limited. The quantity of heat output during electrochemical reaction is proportion to the voltage drop. The material of SOFC anode is Ni based material, which is a promising catalyst for hydrocarbon internal reforming with endothermal reaction. The 100% internal reforming is possible to obtain the high efficiency and manage the heat output. Fig.1 is the I-V test result of dilute 10% natural gas (NG) with 100% internal reforming. The result shows that the power is increased with decreasing operating voltage, but efficiency is decreased. At 10 A load, the power is around 500W and the electrical efficiency is 64.2%. At 22.5A, the full load is obtained with 1kW output, and the electrical efficiency is 57%. During the test, there is no significant effect of NG concentration between 5% ~ 30%.
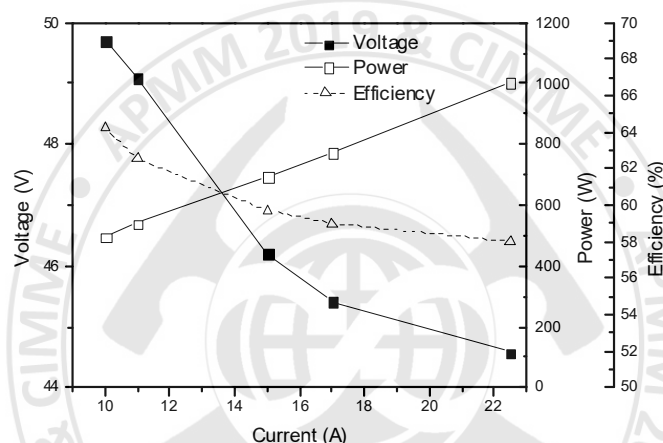
Figure.1 Performance test with natural gas

Table 1 and Table 2 are the summary of COG and BFG testing results. The electrical efficiency of COG is 52.8% at full load of 1017 W output and 59.6% at part load of 504 W. The electrical efficiency of BFG is 40.3% at full load of 1003 W output and 45.2% at part load of 504 W. Due to the chemical potential of composition, performance ranking is highest for NG, followed by COG, and BFG is the worst. However, the efficiency is still higher than the traditional steam turbine, especially for lower heating value gas of BFG.

Table 1. Performance test result of COG

Current (A)	Power (W)	Efficiency (%)
10	504	59.6
15	717	57.2
20	909	53.8
22	983	53.5
23	1017	52.8

Table 2. Performance test result of BFG

Current (A)	Power (W)	Efficiency (%)
10	503	45.2
13	610	44.2
15	696	43.7
23	1003	40.3

CONCLUSIONS

1. The electrical efficiency of COG is 52.8% at full load of 1kW output and 59.6% at part load of 0.5kW.
2. The electrical efficiency of BFG is 40.3% at full load of 1kW output and 45.2% at part load of 0.5kW.
3. Performance ranking is highest for NG, followed by COG, and BFG is the worst due to the chemical potential of composition.
4. It is experimentally proved that SOFC can be fueled with well purified by-product gases.

REFERENCES

N. Laosiripojana, W. Wiyaratn, W. Kiatkittipong, A. Arpornwichanop, A. Soottitantawat, and S. Assabumrungrat. (20009). " Reviews on solid oxide fuel cell technology," Engineering Journal, 13: 65-83 .

V. M. Janardhanan, V. Heuveline, and O. Deutschmann. (2007). " Performance analysis of a SOFC under direct internal reforming conditions," Journal of Power Sources 172: 296-307.

S.H. Chan, C.F. Low, and O.L. Ding. (2002). " Energy and exergy analysis of simple solid-oxide fuel cell (SOFC) power systems," Journal of Power Sources 103: 188–200.

S. Douvartzide, F. Coutelieris, and P. Tsiakaras. (2004). "Exergy analysis of a solid oxide fuel cell power plant fed by either ethanol or methane," Journal of Power Sources 131: 224–230.

Techno-economic Analysis of Large-scale Energy Storage System in Taiwan

Tsu-Chun Chang[1], Yan-Rong Chen[1], Jung-Hua Wu[1], Chang-Chung Yang[2]
, Chien-Chung Huang[2] and Yun-Hsun Huan[3]

[1]Department of Resources Engineering, National Cheng Kung University, Taiwan
kk71337984@gmail.com, alison850804@gmail.com, hwaa@mail.ncku.edu.tw,
abshung@hotmail.com

[2]Energy Storage Technology Division, Green Energy and Environment Research Laboratories,
Industrial Technology Research Institute, Taiwan
ccyang@itri.org.tw, middle@itri.org.tw

ABSTRACT

In response to the rising of environmental awareness, countries around the world have been making energy transformations, such as promoting renewable energy to reduce greenhouse gas emissions and to increase local energy supply. Taiwan government set the policy goal of reaching 20 % of renewable energy generation in total power generation by 2025. Renewable energies (e.g. solar and wind) are unstable and intermittent. Solar irradiance and wind speed could change drastically in hours or days and thus influence the rate of power generation. One of the application of energy storage system (ESS) is to eliminate the intermittence of renewable energy and to stabilize the power supply.

This study established a techno-economic analysis module for energy storage system. Access 2016 was used to build the energy storage system database, and Excel 2016 was utilized to create the technical and economic analysis module and user interface. Visual Basic for Applications (VBA) was applied to connect the database, technical and economic analysis module and user interface. Monte Carlo Simulation method will be introduced so as to enhance the accuracy of the techno-economic analysis.

The results show that the discount rate affects the value of levilized cost but does not affect the sequence. The levelized cost of energy storage system from low to high are sodium-ion battery(NaNiCl2), sodium-ion battery (NaS), lithium-ion battery (NCA), lithium-ion battery (NMC/LMO), lithium-ion battery (LFP), flow battery (V), lithium-ion battery (LTO), flow battery (ZnBr) and flywheel. The benefit of storage including bulk energy services, ancillary services, social benefit…etc. This study tries to estimate the benefit of energy storage system in Taiwan, including arbitrage, uninterruptable power system and carbon emissions. This study set three scenarios to execute techno-economic analysis. The cost-benefit for building the energy storage system is significantly affected by the methods applied when quantifying the benefit, the discount rate, and service life.

Keywords: Energy Storage System, Techno-economic Analysis, Monte Carlo Simulation Method

The Impact of Taiwan's Energy Transformation Policy on Power Supply Planning

Hsin Lee[1], Yi-Ya Yang[2] , Jung-Hua Wu[3] and Yun-Hsun Huan[4]

Department of Resources Engineering, National Cheng Kung University, Taiwan
d840512@yahoo.com.tw, yiyayang2030@gmail.com, hwaa@mail.ncku.edu.tw,
abshung@hotmail.com

ABSTRACT

In order to achieve Taiwan's Intended Nationally Determined Contribution (INDC) goal, the government has created an Energy Transformation Plan. Under these goals, gas-fired power generation will make up 50% of total energy usage, coal-fired power generation 30% and Renewable Energy 20% by 2025. This study analyzes the feasibilities and cost implication of meeting these goals by using "Simulation Model for Aggregate Generation Expansion Planning (SMAGE-II)" to simulate the transition to Taiwan's proposed 2025 energy portfolio under different scenarios.

Because of the growing of Renewable Energy penetration, intermittence would be a problem on power supply planning. Consequently, this study introduces the Energy Storage Systems in order to stabilize the intermittence of renewable energy and to analyze costs variation on power supply planning. In addition, health concerns over air pollution have grown recently, leading to reduction in burning of coal under local governments' request. For the purpose of analyzing the effects on power supply planning from the above issues, a total of four different scenarios were formulated under the prerequisite of meeting the 2025 goals. The first is a basic scenario of the costs and outcomes and is used to compare against the other simulation results. The second scenario consists of incorporating energy storage into the mix. The third scenario is composed of derating of coal power plants in order to further reduce coal consumption. The final scenario includes meeting the 2018 referendum requirements of decreasing total fossil fuel usage by 1% annually.

Analytical results show that, on the basis of decommissioning and renewing of the current power units, the reserve margin of Taiwan from 2019 to 2024 is about 15%, which meet the authorized standard. But, it declines to 13.7% in 2025 due to decommissioning of Maanshan nuclear power plant and the other fossil fuel power plants. If the Energy Transformation goals can be reached in 2025, the total amount of CO_2 emission will be reduced from 124.8 (million metric tons) to 112.9 (million metric tons). Meanwhile, the cost of power generation per unit will increase from 2.79 (NTD/kWh) to 2.90 (NTD/kWh).

In the introducing Energy Storage scenario, implementing Energy Storage Systems while meeting 2025 goals, the cost of using lithium-ion batteries to store every 10% of electricity will increase by around 0.25 (NTD/kWh) per unit. In the derating of coal power plants scenario, reducing coal usage through increasing restrictions, the total amount of annual CO_2 emission from 2019 to 2025 decreases by about 10 (million metric tons), and unit costs increase by about 0.1 (NTD/kWh) each year, when compared to the basic scenario. In the 2018 referendum requirements scenario, an annual 1% decrease in fossil fuels is found to be feasible from 2019 to 2021, but it is difficult to continue to be met after 2022.

Our results indicated that SMAGE-II is a flexible model which can be used for formulating various scenarios for addressing energy issues and making referable recommendation for government on power supply planning.

Keywords: Energy Transformation Plan, power supply planning, energy storage system

METHODS

This study adopted the two-tier KLEM input-output structural decomposition analysis (KLEM I-O SDA), with the advantage of decomposing factors from the perspective of inter-industry economic activities. Changes in energy and CO_2 emission are distinguished by six main effects, namely change of exports, change of domestic autonomous final demand, change of household induced consumption, imports substitution, factors substitution, and technological change, all of which are collated in Table 1. Please refer to Rose and Chen (1991), Wu et al. (2007) for detailed formula derivations.

Table 1. Factors decomposition of changes in CO_2 emissions

Determinants	Formula
Change of exports	$c_{t-1}B_{t-1}(I - R_{t-1}A_{t-1}^C)^{-1}(Ex_t - Ex_{t-1})$
Change of domestic autonomous final demand	$c_{t-1}B_{t-1}(I - R_{t-1}A_{t-1}^C)^{-1}[R_{t-1}(Y_t^A - Y_{t-1}^A) + Ex_t - Ex_{t-1}]$
Change of household induced consumption	$c_{t-1}B_{t-1}\{[I - R_{t-1}(A_{t-1}^P|b_t)]^{-1} - [I - R_{t-1}(A_{t-1}^P|b_t)]^{-1}\}[R_{t-1}Y_t^{Ad} + Ex_t]$
Imports substitution	$c_tB_t[(I - R_tA_t^C)^{-1} - (I - R_{t-1}A_t^C)^{-1}][(R_t - R_{t-1})Y_t^{Ad} + Ex_t]$
Factors substitution	$\{c_tB_t[I - R_{t-1}(A_t^P|b_t)]^{-1} - B_{t(t-1)}[I - R_{t-1}(A_{t(t-1)}^P|b_t)]^{-1}\}[R_{t-1}Y_t^{Ad} + Ex_t]$
Technological change	$\{c_{t-1}B_{t(t-1)}[I - R_{t-1}(A_{t(t-1)}^P|b_t)]^{-1} - B_{t-1}[I - R_{t-1}(A_{t-1}^P|b_t)]^{-1}\}[R_{t-1}Y_t^{Ad} + Ex_t]$

Note: The denotations of the symbols are as follows. c: the matrix of CO_2 emission factors related to various forms of energy; B: the matrix of energy consumption per unit of outputs; I: unit matrix; R = I-M, where M denotes the diagnose matrix of import coefficients; A^C: the matrix of induced demand coefficients, $A^C = [A^P | b]$; A^P: the matrix of industry production functions. b: household induced consumption; Y^{Ad}: the matrix of autonomous final demand; Ex: the column vector of exports; t: year t.

DATA

This study adopted the WIOD compiled by Eurostat which includes the datasets of input-output table, socio economic accounts and environmental accounts. The first edition of these datasets was released in 2013. Based on the System of National Accounts 1993 (SNA 1993) published by the United Nations (UN), it covered 40 countries and was classified into 35 sectors in accordance with the International Standard Industrial Classification Revision 3 (ISIC Rev. 3); the data period varied from 1995 to 2009 or to 2011. In 2016, a new edition of the input-output tables was released and its data was from 2000 to 2014, while the remaining energy and environmental data tables have not yet been updated. Because the Energy Use Emission Relevant (EM) in WIOD covers the data of 2009 as the latest, this study selected data covering the period 1999~2009, including the following: National Input-Output Tables (NIOT), Energy Use Emission Relevant (EM), as well as the labour compensation, capital compensation, nominal gross fixed capital formation, price levels of gross output, price levels of intermediate inputs, price levels of gross value added, and price levels of gross fixed capital formation in Socio Economic Accounts (SEA). Additionally, the coefficients of CO_2 emissions for energy were from IPCC guidelines.

RESULTS AND DISCUSSION

Fig. 1. illustrates how these determinants influence CO_2 emissions. The total CO_2 emissions in Taiwan grew by 25% and the main reason was export growth, which increased CO_2 emissions by 29%. The main sectors of export growth were electrical and optical equipment, and chemicals and chemical products; the former pushed up electricity consumption, and the latter increased electricity and coal consumptions. The total CO_2 emissions in Japan declined by 7% due primarily to the technological

progress, leading to a decline in CO_2 emissions by 42%. The main sectors that reduced CO_2 emissions were because of the technological advances in basic metals and fabricated metals, and chemicals and chemical products. The former reduced coal consumption and the latter decreased oil consumption. The total CO_2 emissions in Korea grew by 46% and the main reason was export growth, leading to an increase in CO_2 emissions by 47%. Moreover, the main sectors with export growth were basic metals and fabricated metals, and electrical and optical equipment; the former increased gas and electricity consumption, and the latter raised electricity consumption.
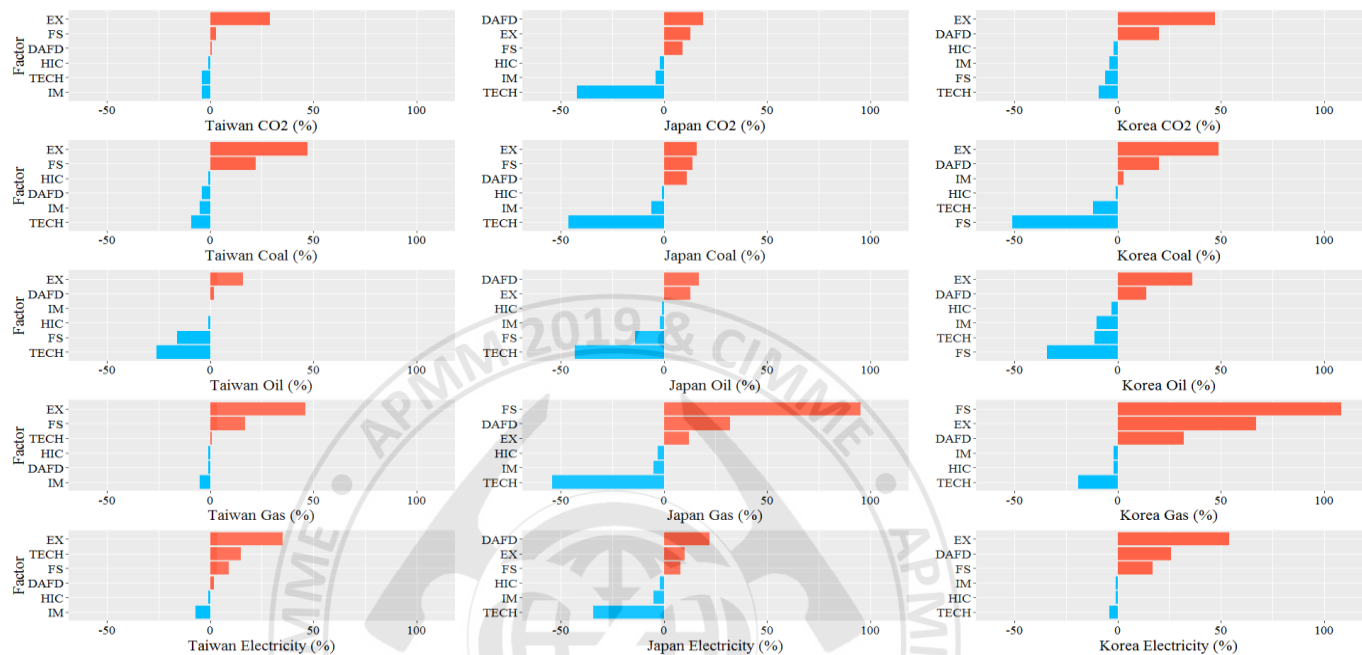
Note: The denotations of the symbols are as follows. Change of exports (EX); Change of domestic autonomous final demand (DAFD); Change of household induced consumption (HIC); Factors substitution (FS); Imports substitution (IM); Technological change (TECH).

Figure 1. Sources of changes in CO_2 emissions in Taiwan, Japan and Korea

Among the main factors for the cross-country comparison of CO_2 emissions, the change of exports in Taiwan and Korea pushed up the growth of CO_2 emissions but their industries and sources of energy consumption were different. In Taiwan, the increase in electricity consumption in the electrical and optical equipment sector as well as the increase in electricity and coal consumption in the chemicals and chemical products sector resulted in the growth of CO_2 emissions. However, in Korea, the increase in gas and electricity consumption in the basic metals and fabricated metals sector as well as the increase in electricity consumption in the electrical and optical equipment sector contributed to the growth in CO_2 emissions. On the other hand, the growth in the consumption of energy sources (e.g. coal and oil) with higher CO_2 emission coefficients was insignificant in Japan due to the slow expansion in export-oriented industries.

Regarding to the technological change, the technological change in coal and oil in Taiwan, Japan, and Korea all led to the decline in CO_2 emissions. However, the technological change in gas led to different degrees of CO_2 emission changes among Taiwan, Japan, and Korea (1%, -54%, and -19%, respectively). In addition, the technological change in electricity led to a 15% increase in Taiwan's CO_2 emissions, whereas this effect decreased CO_2 emissions by 34% and 4% in Japan and Korea, respectively. This

illustrated the difference in industrial technology advances between various countries has different influence on energy requirements of production, thus affecting the variation of CO_2 emissions.

CONCLUSIONS

Empirical results obtained in this study revealed that strong exports demand was the main reasons for increases in CO_2 emissions in Taiwan and Korea. The result also reflected the export-oriented and continued growth characteristic of the Taiwanese and Korean economy even though main export industries and sources of energy consumption may be different. Hence, if the strategy for reducing export expansion is employed for decreasing CO_2 emissions, it is crucial to evaluate the impact on export-oriented industries to ensure that it does not hamper a country's economic development. In addition, reducing export expansion may need more comprehensive evaluation, considering their significant impact on economic growth. Therefore, other strategies for reducing CO_2 emissions should be required. As indicated in our study, the technological change in various energy forms in Japan had a significant positive contribution to CO_2 emissions decrease. This demonstrated that technological advances can effectively decrease the energy requirements of production materials, thus contributing significantly to emission decrease. Consequently, relevant strategies of technology upgrading for Taiwan and Korea should aim at encouraging research and development in energy efficient technologies, promoting industrial upgrading, encouraging the development of high energy-efficiency and high value-added products, and providing incentives for enterprises in the purchase of energy-saving technologies.

REFERENCES

Albrecht, J., François, D. and Schoors, K. (2002). "A Shapley decomposition of carbon emissions without residuals," Energy Policy 30(9): 727-736.

Cansino, J. M., Román, R. and Ordóñez, M. (2016). "Main drivers of changes in CO_2 emissions in the Spanish economy: A structural decomposition analysis," Energy Policy 89: 150-159.

Hoekstra, R., Michel, B., and Suh, S. (2016). "The emission cost of international sourcing: using structural decomposition analysis to calculate the contribution of international sourcing to CO_2 emission growth," Economic Systems Research 28(2): 151-167.

Huang, Y.H. and Wu, J.H. (2013). "Analyzing the driving forces behind CO_2 emissions and reduction strategies for energy-intensive sectors in Taiwan, 1996–2006," Energy 57: 402-411.

Jiang, X., and Guan, D. (2016). "Determinants of global CO2 emissions growth," Applied energy 184: 1132-1141.

Plank, B., Eisenmenger, N., Schaffartzik, A. and Wiedenhofer, D. (2018). "International trade drives global resource use: A structural decomposition analysis of raw material consumption from 1990–2010, " Environmental science & technology 52(7): 4190-4198.

Rose, A. and Chen, C.Y. (1991). "Sources of change in energy use in the US economy, 1972–1982: a structural decomposition analysis, " Resource Energy 13 (1): 1-21.

World Input–Output Database (2013). National Input–Output Tables. Available from ⟨www.wiod.org⟩.

Wu, J.H., Chen, Y.Y. and Huang, Y.H. (2007). "Trade pattern change impact on industrial CO_2 emissions in Taiwan," Energy Policy 35 (11): 5436-5446.

Xu, Y., and Dietzenbacher, E. (2014). "A structural decomposition analysis of the emissions embodied in trade," Ecological Economics 101: 10-20.

Zhu, B., Su, B. and Li, Y. (2018). "Input-output and structural decomposition analysis of India's carbon emissions and intensity, 2007/08–2013/14," Applied energy 230: 1545-1556.

International Conference on Asia Pacific Mining and Metallurgy

Tainan, Taiwan, November 17-20, 2019

Section 3：Metallurgical Engineering

10：10 – 12：00　　　　1st Lecture Room

10:10-12:00	Session Chair:	**Jian-Xun Fu** Shanghai University, CHINA
10:10-10:30	CIMME108010	**Cheng-Chuan Tsai** China Steel Corporation, Taiwan
		Comparison between Stopper Control System and Slide Gate Control System
10:30-10:50	CIMME108008	**Chang-Sheng Lin** China Steel Corporation, Taiwan
		Development of RH Vacuum Vessel Condition Monitoring System *Using Thermography Technology*
10:50-11:10	CIMME108037	**Dr. Ming-Hung Chen** China Steel Corporation, Taiwan
		Development of Rapid Micro-porosity Detection Technology Used for Slab Casting
11:10-11:30	CIMME108009	**Yung-Hsiang Chuang** China Steel Corporation, Taiwan
		Development of Automotive Steel SAPH 440 *with High Dimension-Accuracy after Heat Treatment*

Comparison between Stopper Control System and Slide Gate Control System

Cheng-Chuan Tsai

No.2 B.O.F. & Continuous Casting Plant, Steel Making Department, China Steel Corporation, Taiwan
164327@mail.csc.com.tw, maxcop.csc@ gmail.com

ABSTRACT

To further improve the quality of slabs, China Steel Corporation (CSC) has started to assess the transformation of mold level control system from the existing slide gate (S/G) system to the stopper system since 2016. Comparing between these two systems practically, one strand of one tundish car in No.7 slab continuous caster was revamped to install stopper system with one-piece submerged entry nozzle (SEN) for better air tightness. The experiment for two control systems in one thundish has been progressed from Oct. 2017 to Sept. 2018, and there were 1183 heats in cast during this test period. The results of experiment for these two systems were evaluated in different aspects of operation, safety and quality. The Stopper system was relevantly equal to S/G system in aspect of safety. But the stopper system is far behind the S/G system in aspects of quality and operation. The quality of first slabs in hot rolled process for all steel grades in stopper system is worse than in S/G system, especially in ultra-low carbon steel with rejection ratio in stopper system is 2.2 times higher than in S/G.

Keywords: slab continuous casting, stopper control system, slide gate control system

INTRODUCTION

The mold level control systems in continuous casting machine can be basically divided into two types. One is stopper system and the other is S/G system. The characteristics of these two systems are reviewed as shown in Table 1. Comprehensively speaking, stopper system has reliable start of cast, better air tightness and less bias flow in the mold. S/G system has precise of mold level control and easy set-up work. For upgrading products quality, the investigation was made to find out the optimal control system.

Table 1: Review of two systems

Items	Stopper	Slide Gate
Casting start	• More reliable due to stopper open with tundish filled.	• Starting tube used to delay the start: low tundish level as start. • Gas open: high risk of freezing steel as start.
Mold level control	• Complicated calculation(3D), small stopper rod movement leads to large flow different.	• More easy regulation(2D), small plate movement leads to small flow different.
Maintenance	• More skill needed to keep clearance of guides to minimum. • Electromechanical actuator doesn't need preventive maintenance.	• No clearance in mechanism due to direct connection between hydraulic cylinder and middle plate. • Need to more maintenance for hydraulic units.

Items	Stopper	Slide Gate
Set-up work	• Difficulties to align the stopper nose with the nozzle seat. • Goose neck must be protected from heat.	• Casting bore alignment through slide gate dimensions. No risk of mistakes. • Need spring arrangements to apply pressure between the plates. Additional cooling is needed for these springs.
Quality issue	• Delay the vortex effect at low tundish level. • Low residual steel height in the tundish at the end of cast. • Easy for steel grade change.	• The vortex at low tundish level. • More residual steel in the tundish at the end of cast. • Very difficult for steel grade change. • Easily to induce bias flow in mold.
Anti-clogging	• Stopper vibration can reduce sticking. • Clogging in the well nozzle area can be washed by automatic stopper pumping.	• Automatic program for fast middle plate movement can prevent clogging. • Argon supply through the inner nozzle can reduce clogging.
Air tightness	• One-piece SEN design has no refractory joint. • Tube changer design only has one joint. • Less air suction problem.	• Classic three-plate slide gate has two to five refractory joints sealed through additional inert gas. • More air suction problem.

At present, China Steel Corporation (CSC) has ten continuous casting machines (three bloom casters and seven slab casters) using S/G control systems. In early time (more than thirty years ago), stopper control system was applied in some machines, but poor manual control led to worse quality and safety issues due to immature automation system at that time. After that, all newly added casters and existed caster have selected slide gate control system to control steel flow. With the advancement of automation technology, now the control precision of stopper system can keep up with the S/G system. Therefore, since 2016, CSC has started to assess the revamping of the stopper system. Finally, we decided to revamp one strand to stopper system with one piece SEN to achieve better air tightness. In the meantime, the dual control systems can be evaluated under the same conditions (molten steel, superheat, cooling practice …etc.).

EXPERIMENTAL METHOD

The experiment was progressed in No.7 slab continuous caster of CSC. The new stopper control system was only installed in strand No.3 of tundish car No.3 and original S/G system was reserved for flexibly switching dual systems. The S/G control system in strand No.4 was kept. The stopper system is designed as one piece type with one argon bubbling place at stopper nose, as shown in Fig.1. However, S/G system is designed as typical three plate type with three argon bubbling places at upper nozzle, upper plate and SEN, as shown in Fig.1. As parallel using dual systems, experimental data could be collected and compared on the same base. From Oct. 2017 to Sept. 2018, a total of 290 tundishes and 1183 heats were cast during this test period. The two systems were evaluated in different aspects of operation, safety and quality. This experiment equipped with different dams and weirs design was divided into three stages: A, B, and C (see Table 3 and Fig. 4).
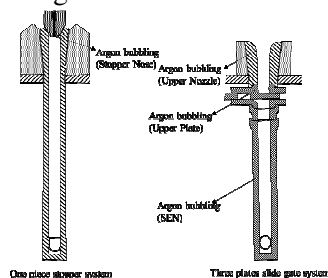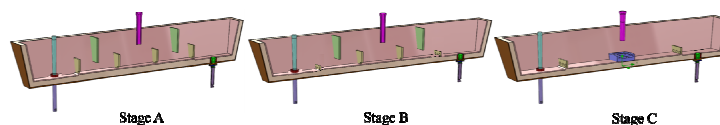

Figure 1: Stopper and slide gate in SCC No.7

Figure 2: Tundish furniture for three stages

Table 3: Test period for three stages

Stages	Test period	Tundish furniture
A	Oct. 2017 ~ Jan. 2018	See left picture in Fig. 2(typical dams and weirs)
B	Feb. 2018 ~ Jun. 2018	See middle picture in Fig. 2(modified dams and weirs)
C	July 2018 ~ Sept. 2018	See right picture in Fig. 2(turbostop and modified dams)

RESULT AND DISCUSSION

From the comparison between stopper and S/G system in aspect of operation (see Table 4), it has shown that stopper system can control the start of mold filling exactly, but both ratios of successful auto cast start and failed cast start are worse than S/G system due to improper auto start patterns and freezing steel between the stopper nose and the nozzle seat. Owing to accurate control by servo actuator, mold level of high silicon steel (silicon concentration larger than 3%) in stopper strand is more stable than S/G strand, as shown in upper part of Fig. 3. Slabs bulging between rollers of segments in high silicon steel often leads to mold level fluctuation, but stopper system could still keep mold level stable while anti-bulging function activated. Lower part of Fig. 3 shows that stopper opening becoming worse (large opening means clogging occurred) during 4th heat and stopped casting during 5th heat due to overall clogging in SEN (Reaching the max. opening 100 mm). Instead, S/G opening is more stable (small opening means clogging occurred). This result means argon bubbling is an efficient method to prevent clogging. In stage A, the slight steel infiltration from the gap of the SEN and the nozzle seat occurred four times due to improper surface coating of nozzle seats at S/G system. According to our past experience, if the steel leaking occurs, the problems are mostly from worse maintenance and set-up work. Anyhow these two systems can equivalently meet our safety requirement.

Table 4: Comparison in aspect of operation

| Items	Stopper	Slide Gate
Tundish weight as start to fill mold	• Cast start with dummy bar : 30 tons • Cast start as tundish change : 20 tons	• 12~15 tons with starting tube
Ratio of successful auto cast start	• About 90%	• About 99%
Ratio of failed cast start	• About 0.92%	• About 0.61%.
Stability of mold level	• Better	• Worse
Clogging	• Anti-clogging function activated, clogging phenomena still worse.	• Efficiently delay clogging phenomena by purging argon.
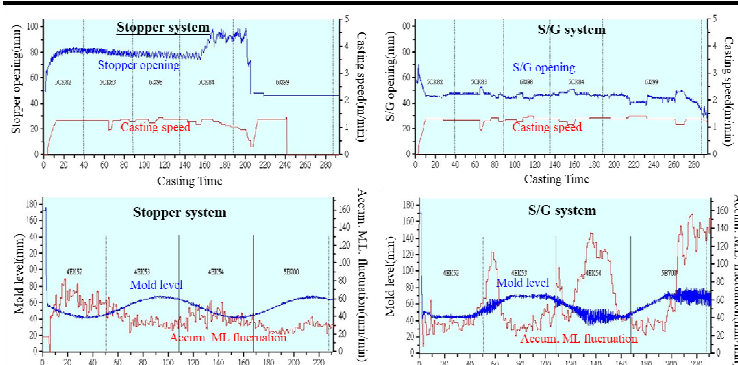
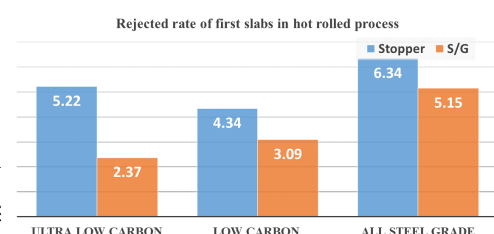Figure 3: Trend of Stopper and S/G

Figure 4: Rejection ratio of first slabs in hot rolled process

In the aspect of quality, Fig. 4 shows the rejection ratio of first slabs in hot rolled process for different steel grades in two systems. Stopper's performance in all steel grades are worse than S/G's, especially in ultra-low carbon steel with rejection ratio in stopper system is 2.2 times higher than in S/G. The throttle in stopper system is much narrow than S/G while the stopper rod initially open to fill the mold. As a result, the inclusions of molten steel in tundish may be easily sucked into the mold during casting starts. The quality of each stage is compared as shown in Table 5. Except for the stage C, the stopper strand rejection rate of first slabs is better than S/G strand, and the others are worse than S/G. The molten steel near stopper side in the tundish has 40% of the dead zone more than S/G side according to the analysis. The phenomena would inhibit the inclusion floating in tundish and induce to reoxidation of the molten steel, which may cause the quality in hot and cold rolled process to be inferior to S/G system. According to the data of stage C, it was also found that the turbostop in the tundish could improve the quality in both system.

Table 5. Quality feedback from rolling mill

Stage	Ctrl. system	RJ Ratio of first slabs		RJ Ratio of all slabs	
		Hot rolled process (%)	Cold rolled process (%)	sliver defects in hot rolled process (%)	inclusion defects in cold rolled process (%)
A	Stopper	7.30	10.03	0.93	0.56
	Slide gate	7.00	9.20	0.52	0.38
B	Stopper	5.17	11.04	0.46	0.81
	Slide gate	3.48	5.80	0.32	0.69
C	Stopper	3.95	5.81	0.60	0.64
	Slide gate	4.64	7.43	0.11	0.37
Total	Stopper	6.34	11.43	0.66	0.70
	Slide gate	5.15	7.33	0.39	0.54

CONCLUSIONS

In the beginning, we expected that stopper control system via more stable mold level control, better air tightness in SEN and controllable steel level of starting to fill the mold can achieve further quality improvement. But after the assessment in aspects of quality, it is found that the rejection ratio of first slabs or all slabs in stopper system is higher than in S/G system, no matter what in hot rolled process or cold rolled process. Even as we compare the clogging index, the S/G system also surpassed the stopper system. In this experiment, it can be concluded that S/G system in CSC with thirty-year operation experience can overcome its disadvantage and even has better performance than stopper system.

REFERENCES

Chih-Hung Li (2017). "煉鋼廠七號連鑄機模液面塞棒控流試驗結果期中報告," , No.2 B.O.F. & Continuous Casting Plant, Steel Making Department, China Steel Corporation, Taiwan.
Cheng-Chuan Tsai (2018). "煉鋼廠七號連鑄機模液面塞棒控流試驗總結報告," , No.2 B.O.F. & Continuous Casting Plant, Steel Making Department, China Steel Corporation, Taiwan.

Development of RH Vacuum Vessel Condition Monitoring System Using Thermography Technology

Chang-Sheng Lin, Yung-Chang Liu and Yu-Te Su

Iron and steel Research & Development Department, China Steel Corporation, Taiwan
180703@mail.csc.com.tw, 150185@ mail.csc.com.tw, 185074@ mail.csc.com.tw

ABSTRACT

RH (Ruhrstahl-Heraeus) is a widely used vacuum decarburization/degassing way in secondary refining steelmaking processes. Vacuum treatment of the molten steel is carried out in a refractory-lined vessel equipped with two snorkels immersed in the steel bath. When refractories of the vacuum vessel hit by the melt are worn to the outside steel shell, molten steel breakout may occur. It will cause downtime and need more time and cost to repair the vacuum vessel. Thermography technology is applied in China Steel Corporation (CSC) to monitor the RH vacuum vessel condition. The vessel refractory monitoring system combines thermal image camera with refractory thickness model, can give users not only an early warning but also the information of remaining refractory thickness.

INTRODUCTION

In steelmaking processes, excess carbon and impurities such as nitrogen, oxygen, silicon, phosphorus and sulfur are removed from the hot metal. Furthermore, alloy elements such as nickel, chromium, titanium and etc. are added to produce different grades of steel. After primary steelmaking, such as BOF (Basic oxygen steelmaking) and EAF (Electric arc furnace), molten steel was poured into a ladle for further processing. The RH (Ruhrstahl-Heraeus) is one of secondary refining steelmaking processes that using vacuum decarburization/degassing way. A schematic diagram of RH unit is shown in Fig. 1. The main part of a RH unit is a vessel with two snorkels immersed in the molten steel in the ladle. As vessel pressure is reduced, the molten steel rises into the vessel, and Argon lifting gas is injected into the up-leg snorkel at the same time to circulate the molten steel. The refractories of vessel and snorkel are worn away by circulating molten steel. When the refractory of the vacuum vessel are worn out as fig. 2 shown, the high temperature molten steel will melt the outside steel shell, and breakout may occur. Once the vessel is broken, the vacuum can't be maintained and the steel may fail of refining. Besides, if the vessel is broken, it spend more time and cost to repair the vessel than when just the refractory was worn. These indicate that knowing when to change the vessel to prevent the refractory worn out is important. The temperature of vessel outside shell rises when the refractory is worn. Therefore, if the outside vessel temperature can be observed, the refractory thickness can be monitored. Thermography technology is chosen because it's a non-contact temperature measuring method and very suitable in high temperature environment.

MONITORING SYSTEM

The main part of the monitoring system is the thermography camera from FLIR and a computer as human machine interface (HMI). The installation of CSC RH monitoring system is shown in the illustration fig. 3. The camera is put in a stainless cylinder with air purge to keep away from dust and

installed at a distance of about 10 meters from the RH vessel as fig. 4 shown. The digital thermal images data is connected via Ethernet to the HMI computer. The HMI displays thermal images as fig. 5 shown, and provides camera control functions. Users can adjust the camera parameters and choose regions of interest (ROI). When the shell temperature rises to specific value or sudden increases, the system will give an alarm. The system also collects temperature data as a time-lapse photography for future analysis.
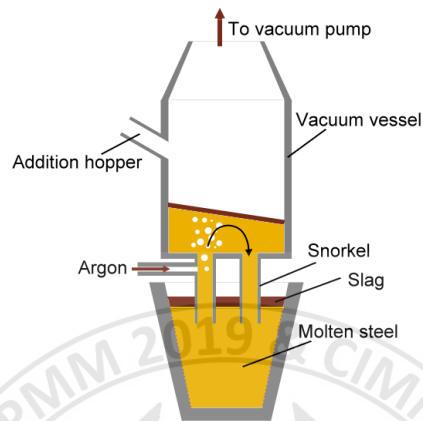

Figure 1. RH (Ruhrstahl-Heraeus) vacuum degasser
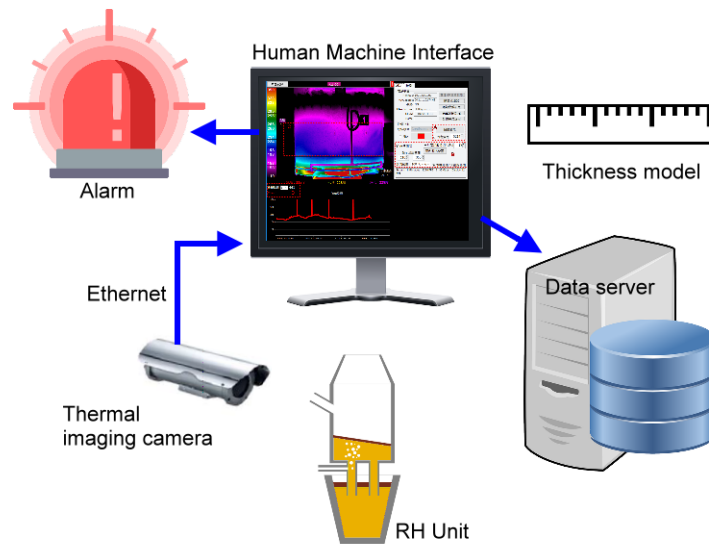

Figure 2. Worn out refractory of the vessel

Figure 3. Installation of CSC RH monitoring system
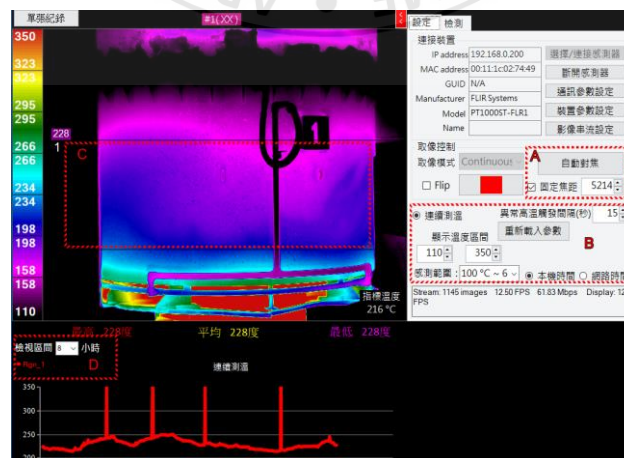

Figure 4. Thermography camera set up

Figure 5. RH Monitoring system HMI

REFRACTORY THICKNESS MODEL

The original system can give alarm and collects temperature data and it works well for normal production usage. However, it is not enough for improving processes schedule because the remaining refractory thickness is unknown. Every different vessel, even the same vessel after revamping, has different thermal properties and therefore the same outside shell temperature doesn't mean the same remaining refractory thickness. The remaining refractory thickness model was developed to solve this problem. In this model, the temperature of vessel outside shell after first 5 heats is set as initial temperature, and the molten steel temperature is set as $1600℃$. The initial temperature is used to calibrate the thermal properties and the thickness can be estimated. By comparing estimate and measuring thickness, several results are shown in Table. 1. If the initial temperature are the same, when the temperature of outside shell is higher, the remaining refractory thickness is thinner. From the other point of view, if the temperature of outside shell are the same, when the initial temperature is lower, the remaining refractory thickness is thinner. The errors of the estimate thickness at these last heats are less than 20mm, and comparing with original refractory thickness of 300mm, the errors are usually less than 5%. In the case of vessel C, the estimate refractory thickness is 15mm, but actually it is too thin and surely fall off and therefore the error is larger.

Table 1. Estimate and measuring thickness comparison

Vessel	Initial temp. (℃)	Temp. (℃) before maintenance	Estimate thickness (mm)	Measuring thickness (mm)	Error (mm)	Error (%)
A	220	257	64	75	11	3.7
B	220	262	38	45	7	2.3
C	212	257	15	0 (worn out)	-15	5

CONCLUSIONS

RH vacuum vessel condition monitoring system using thermography technology has been successfully developed in China Steel Corporation. The monitoring system combines thermal imaging camera with refractory thickness model, can give users not only an early warning but also the information of remaining refractory thickness. The monitoring system was on line at #2 RH site of CSC from 2018 January and the vessel breakout doesn't occur so far (2019 June) while 4 vessels breakout occurred per year before.

REFERENCES

Vert, T (2016). Refractory Material Selection for Steelmaking, Wiley.

Edward H. Smith (1994). Mechanical Engineer's Reference Book, Society of Automotive Engineers.

Bagavathiappan, S., Lahiri, B., Saravanan, T., Philip, J., Jayakumar, T (2013). "Infrared thermography for condition monitoring-A review," Infrared Phys. Technol. 60: 35-55.

Osterholtz, C.E., Baab, K.A., Morog, M. (1967). "Design considerations for vacuum vessel refractories," Journal of Metals 19(9): 65-68

Development of Rapid Micro-porosity Detection Technology Used for Slab Casting

Ming-Hung Chen

Iron & Steel R&D Department, China Steel Corporation, Taiwan
150326@mail.csc.com.tw

Chao-Yun Wang

Metallurgical Department, China Steel Corporation, Taiwan
175455@mail.csc.com.tw

Te-Fu Weng

Intellectual Property & Testing Technology Department, China Steel Corporation, Taiwan
139386@mail.csc.com.tw

ABSTRACT

For heavy plates with thickness between 50mm to 120mm and used in a severe environment such as large container ships and off-shore wind power engineering, heavy reduction technology is used to eliminate central micro-porosities within slabs to ensure the mechanical performance of heavy plates when serving in extreme low temperature. However, central micro-porosities within the slab are usually hundreds μm in dimension and not detectable by conventional visual inspection even after etching. Some technologies were therefore developed for slab quality control as well as process improvement. Some technologies are quick but rough, for example RT (Radiographic Testing) and PT (Penetrant Testing). Some are very accurate but both time and labor consuming, for example specific weight method and ultrasonic testing (UT). As to provide fast and reliable inspection results, China Steel Corporation has developed a rapid UT technology. 10MHz transducers and attenuation principle are used for micro-porosity detection. Samples are collected directly from existing sampling and quality control procedures without extra material loss and labor.

INTRODUCTION

There always exists central porosity structure in continuous casting due to solidification contraction and insufficient compensation of molten steel. Conventional central porosities in slab centralline are usually several mm in dimension and can be easily found by conventional visual inspection, which are usually improved by mean of soft reduction or S-EMS technology. However the central porosity structure are not eliminated completely, the so-called micro-porosities with size small than 1mm are still existing and cannot be found by visual inspection. Central micro-porosities are usually not harmful for most steel products because they are closed up during rolling process. But for heavy plates with thickness between 50mm to 120mm and served in extreme low temperature, they become a big problem because the micro-porosities cannot be closed up due to insufficient reduction rate and act like micro-cracks to decrease the mechanical properties of heavy plates, especially for central toughness and elongation. Many steelmaker developed technologies to eliminate central

micro-porosities, the most important and effective technology was heavy reduction.

As to produce high class heavy plates with thickness between 50mm to 120mm, such as those used for large container ships and off-shore wind power engineering, heavy reduction technology was developed (Chen *et al*. 2018) at China Steel Corporation since 2014. And the rapid central micro-porosity detection technology as a supporting technology for heavy reduction was also developed in 2017. Below describe how it works and some results.

EQUIPMENT AND SPECIFICATIONS

Some technologies were developed for detection of central micro-porosities existing in slab centralline, such as conventional RT (Radiographic Testing) and PT (Penetrant Testing) technologies as well as density measurement (Morris and *et al.*, 1994), specific weight method (Hiraki and *et al.*, 2009) and ultrasonic testing (Preßlinger and *et al.*, 2006). Some technologies are quick but rough, for example RT (Radiographic Testing) and PT (Penetrant Testing). Some are very accurate but both time and labor consuming, for example specific weight method, density measurement and ultrasonic testing (UT). As to provide fast and reliable inspection results, China steel developed a rapid UT technology. Sampling, ultrasonic incidence with respect to the centralplane in thickness direction and also detection principle are completely different from Preßlinger 2006, which contributes to substantially improve inspection efficiency.

10MHz focused transducers were used for micro-porosities detection and the water tank were 1500mm×1500mm as shown in Fig.1. Samples were obtained from existing sampling procedures used for routine quality check, i.e. used for sulfur prints and macro-etchings, no extra materials were consumed. Ultrasonic incidence was normal to the cross-section of slab, i.e. parallel to the centralplane in thickness direction. Both defect and backwall echoes were used to characterize the central micro-porosities depending on the application.

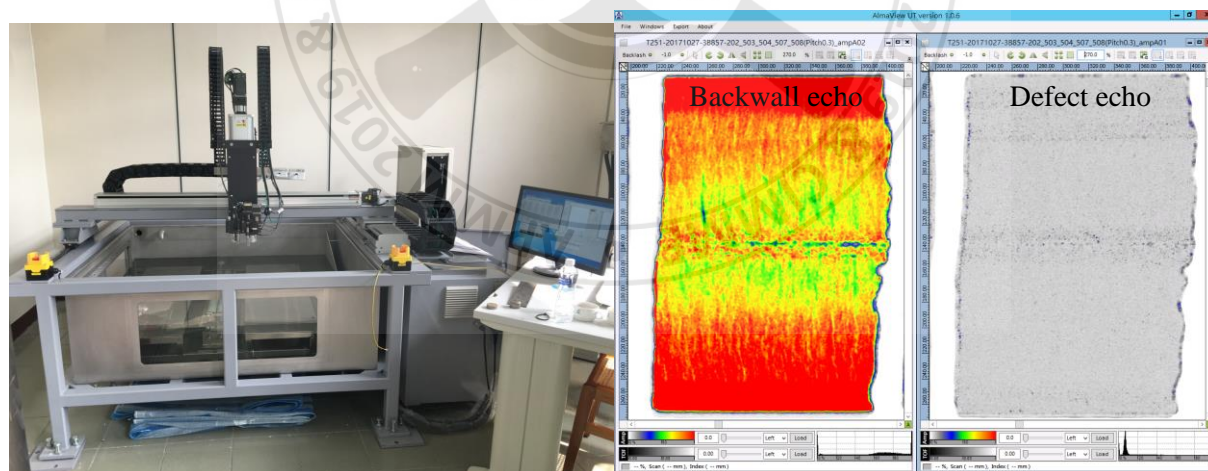Fig.1   Self-developed UT equipment and C-scan images constructed by backwall and defect echoes.

EXPERIMENTAL RESULTS

Ultrasonic incidence was normal to the cross-section of slab, which means the distribution of central micro-porosities in whole slab cross-section could be obtained. However the slabs were always cut into several pieces due to operational consideration and re-assembled together after UT detection.

C-scan images constructed by defect echo were used to qualitative analysis due to its high spatial resolution. As illustrated in Fig.2, the central micro-porosities were widely distributed in S-EMS condition while they were concentrated in the central line for conventional process.

C-scan images constructed by backwall echo were used to quantitative analysis instead of defect echo because of shadow effect. As indicated in Fig.3, defect echo detected more defects as compared to backwall echo, however defect echo could not detected micro-porosities under other micro-porosities with similar or bigger size and resulted in considerable deviation. Although spatial resolution of backwall echo was lower than defect echo, but it was still sufficient for micro-porosities detection as shown in Fig.3. Metallurgical function of heavy reduction technology was evaluated by backwall echo as shown in Fig.4, the central micro-porosities were substantially eliminated by heavy deduction technology.

Fig.2　Micro-porosity distributions caused by different continuous casting processes, C-scan images were constructed by defect echo.
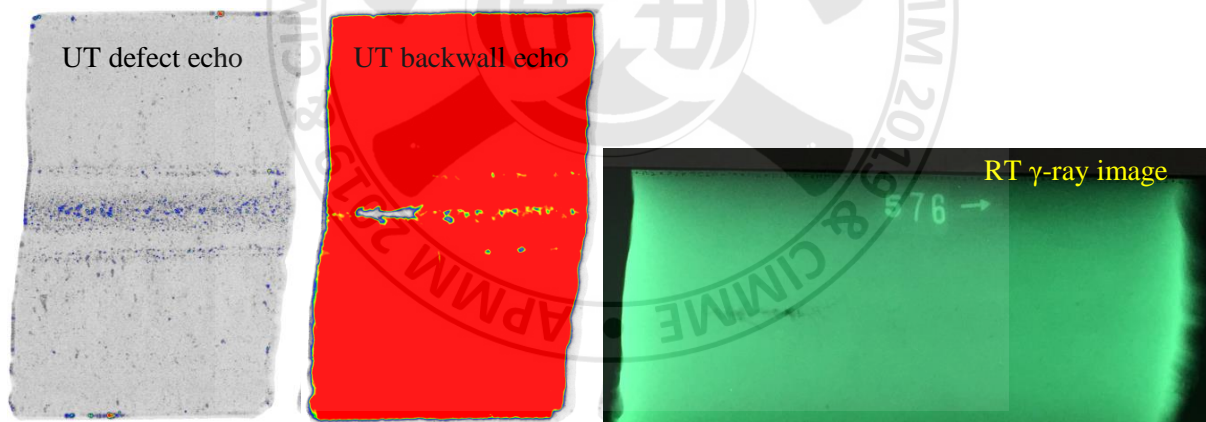

Fig.3　Comparison of central micro-porosity images made by UT and RT.
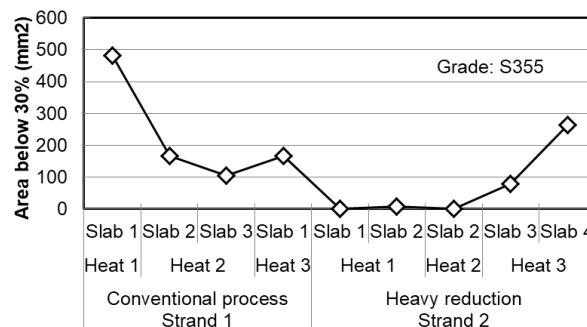

Fig.4　UT inspection results for central micro-porosity from different continuous casting processes.
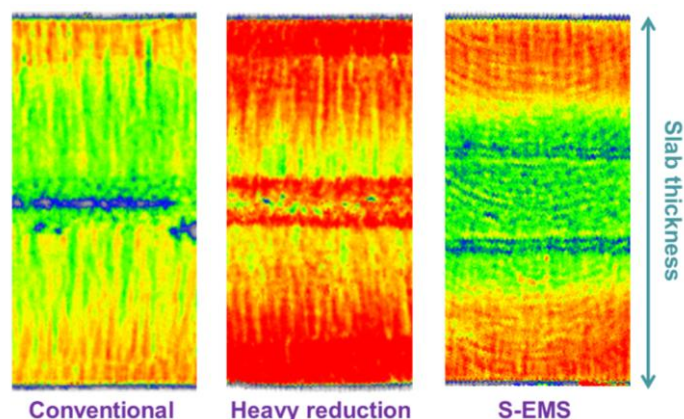
Fig.5   Different slab macrostructures characterised by UT backwall echo.

In addition to quantitative analysis, backwall echo could also be applied to characterize different macrostructures resulted from different processes due to the variety in slab macrostructure as shown in Fig.5.

CONCLUSIONS

As a supporting technology for heavy reduction process, the method of rapid central micro-porosity detection was developed by means of ultrasonic inspection. Slab samples were obtained from existing sampling procedures used for routine quality check, i.e. used for sulfur prints and macro-etchings, no extra materials were consumed. Ultrasonic incidence was normal to the cross-section of slab, i.e. parallel to the centralplane in thickness direction, which provide micro-porosity distribution in whole slab cross-section.   Both defect and backwall echoes were used to evaluate the central micro-porosities, where defect echo was used to qualitative analysis and backwall echo was used for quantitative analysis. Backwall echo could also be used for characterizing macrostructures of slabs.

REFERENCES

Ming-Hung Chen, Chao-Yun Wang, Kuo-Pen Chen, Ching-Chien Chang, Jee-Chao Lin, Cheng-Hsie Peng, "Improvement of Slab Central Micro-porosity to Produce High Performance Heavy Plates,"CSST2018, China Symposim on Sustainable Steelmaking Technology 2018, Tianjin, China, Oct 24-26, 2018

P.W. Morris, S.P. Ryalls and B.A. Wade, "Optimization of the Deformation Process for Continuously Cast Billets to Provide the Most Appropriate Material Properties," Final Report, Contract No.7210.EB/804 (Dl-D5.5/88), European Commission, 1994, ISSN: 1018-5593, A1094

Hubert Preßlinger, Sergiu Ilie, Peter Reisinger, Andreas Schiefermüller, Andreas Pissenberger, Erik Parteder and Christian Bernhard, "Methods for Assessment of Slab Centre Segregation as a Tool to Control Slab Continuous Casting with Soft Reduction," ISIJ International, Vol.46, No.12, 2006, pp1845-1851, A277

Sei Hiraki, Akihiro Yamanaka, Yoshihisa Shirai, Yasuhiro Satou, Seiji Kumakura, "Development of New Continuous Casting Technology (PCCS) for Very Thick Plate," Materia Japan, Vol.48, No.1, 2009, pp20-22, A1048

Development of automotive steel SAPH 440 with high dimension-accuracy after heat treatment

Yung-Hsiang Chuang

Metallurgical Department, China Steel Corporation, Kaohsiung
167098@mail.csc.com.tw

Hsiao-Hung HSU

Green energy & system integration research & development department, China Steel Corporation, Kaohsiung
175877@mail.csc.com.tw

ABSTRACT

JIS G3113 SAPH440 was a wildly used steel grade with good performance of formability and strength for automotive application. Without adding micro-alloy element like Nb, the content of C and Mn is higher to achieve high strength. When materials heated between A1 and A3 temperature and then quenched and tempered, the materials deformed obviously due to the higher content of C and Mn. In order to achieve customer's requirement, China Steel Co. (CSC) has successfully developed a new product of SAPH440 with lower amount of deformation after heat treatment by optimizing the content of C and Mn and adjusting the appropriate process of hot rolling.

INTRODUCTION

Among the hot-rolled automotive products in CSC, SAPH440 is the largest production more than 100,000 tons per year. SAPH440 is used in wheel discs, structure members, clutches, seat tracks, bumpers, motorcycle parts and other various application. Figure 1 shows a clutches part called retaining plate made of SAPH440. Although the dimensional accuracy can be maintained during pressing and forming, but the deformation in ID and OD occurs obviously after special heat treatment of heating, quenching and tempering.

In this study, the effects of the heat treatment temperature and composition were investigated, and the new component design suitable for heat treatment were developed and also had similar formability and strength by adjusting hot rolling process.

Figure 1. The (a) inside diameter (ID) and (b) outer diameter (OD) of retaining plate after pressing

METALLURGICAL DESIGN AND EXPERIMENTAL METHOD

Table 1 shows the chemical compositions based on the heat analysis, and the carbon and manganese contents of modified steel grade are less than normal SAPH440.

Table 1. Chemical composition of normal SAPH440 and modified sample (in wt%)

Grade	C	Mn	Si	others
Spec. of JIS	-	-	-	P, S $\leq$ 0.040
Normal SAPH 440	0.09	1.41	$\leq$ 0.04	P, S $\leq$ 0.020
Modified steel grade	0.07	1.35	$\leq$ 0.04	P, S $\leq$ 0.020

The hot rolling process of SAPH440 is shown in figure 2. The experimental slabs were heated and soaked at 1150°C-1250°C, and then hot rolled. Reheated slabs were rolled to transfer bars by roughing mill and then rolled to strips by finishing mill. The finishing rolling temperature (FT) was within 800-950°C. After finishing rolling, coils were cooled by laminar flow. Coiling temperature (CT) was designed more than 550°C, depending on the chemical composition.

reheating and soaking 1140-1300 ℃

rough rolling

finish rolling, FT 800-950℃

laminar flow, CT >
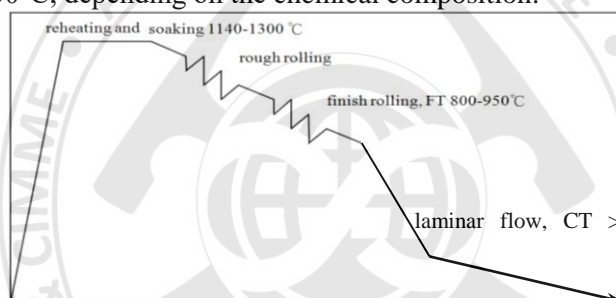
Fig. 2. The hot rolling process

The longitudinal tensile test of SAPH440 was according to JIS Z 2241, and the No.5 test piece was taken at the quarter position of strip width. The OM (Optical Microscope) test piece were also taken, and etched by 3% nital to observe the microstructure.

The phase transformation ratio of the different chemical composition and the heat treatment process in figure 3 were simulated by software JMatPro. (Ana Maria Yagüe Bermudez, 2008)

Heating to 810~825°C

Quenching

Temperature

Time
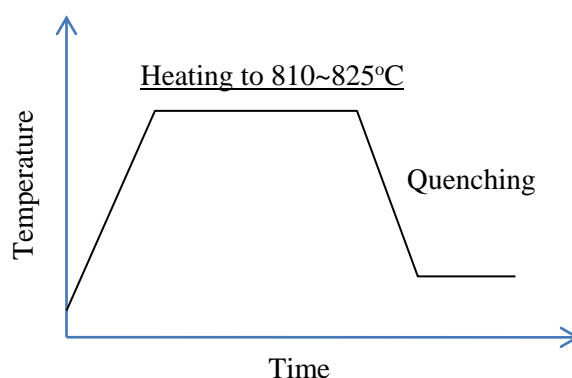
Figure 3. The heat treatment process of retaining plate

RESULTS AND DISSCUSION

The experiment results are shown in table 2. By adjusting FT and CT, the tensile strength of both grade were very similar and met spec requirement, but modified grade has higher yield strength and grain size. However, the most important was modified grade showed a better performance in dimension-accuracy after heat treatment.

Table 2. Tensile test and grain size of normal SAPH 440 and modified steel grade

Grade	YS (MPa)	TS (MPa)	EL (%)	ASTM GRAIN SIZE No.	Deformation in Dia. After heat treatment (mm)
Spec. of JIS	305 min	440 min	32 min	-	-
Normal SAPH 440	333	461	36.5	11.9	0.252
Modified steel grade	351	463	35.7	12.2	0.194

In generally, the main source of heat treatment deformation is the thermal stress and phase transformation during heat treatment. Thermal stress can be considered consistent under the same heat treatment process, and therefore the influence of phase transformation must be further studied (George E. Totten, 2006). Figure 4 shows the simulated results of normal SAPH 440 in different heating temperature. When SAPH440 heated over 600°C (A1), ferrite starts to transform to austenite, and higher heating temperature has higher austenite ratio. It means more austenite tranformed to martensite or bainite after quenching, and more deformation caused by phase transformation.
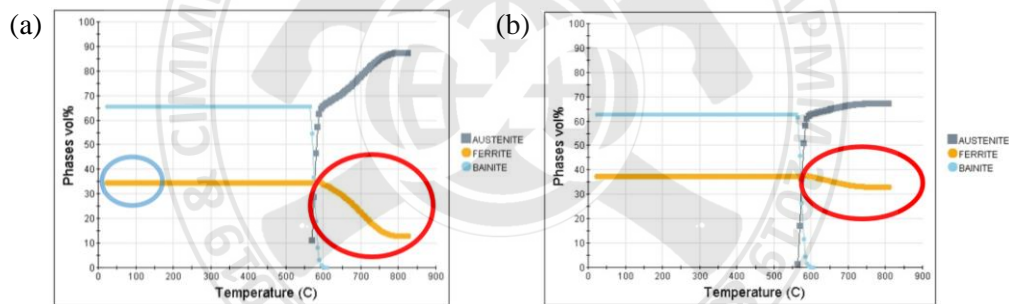
Figure 4. Normal SAPH440 phase trasformaion in different heating temperature (a) 825°C and (b) 810°C

Figure 5 shows the simulated results of normal SAPH 440 and modified steel grade in the same heating temperature 810°C. Modified steel grade with lower carbon and manganese content has higher ferrite ratio in as hot-rolled status and higher A3 temperature, it obviously reduces the ratio of ferrite transformed to austenite. Microstructure in Figure 6 shows phase transformation of normal SAPH440 and modified steel grade during heat treatment, also proves the simulated results and deformation results in table 2.
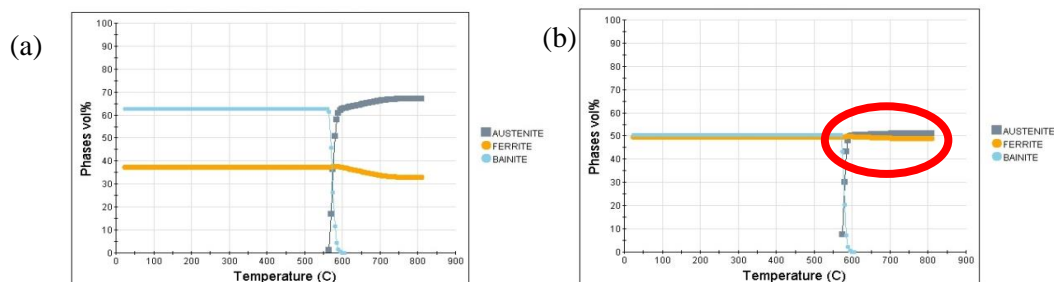
Figure 5. (a)Normal SAPH440 and (b) Modified steel grade phase trasformaion in same heating temperature 810°C
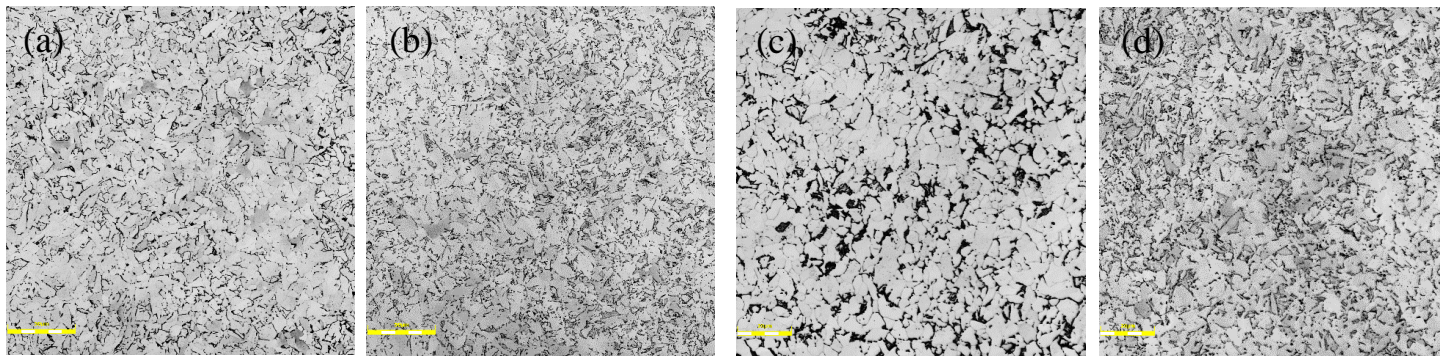
Figure 6. Microstructure of modified steel grade (a)before heating (b)after quench, and normal SAPH440 (c)before heating (d)after quench

CONCLUSIONS

The deformation of the heat treatment was derived from the thermal stress and the phase transformation during the heat treatment. In the same heat treatment process, the deformation after heat treatment mainly comes from the difference in the proportion of phase transformation. The difference in composition design causes different A3 temperature, also affects the phase transformation behavior and ratio.

A new design of SAPH440 by reducing the content of carbon and manganese with appropriate process of hot rolling increases the original ferrite ratio, and reduces the proportion of the second phase transformation, and thus improves dimension-accuracy during heat treatment.

REFERENCES

Ana Maria Yagüe Bermudez(2008). "Evaluation of JmatPro for General Steels"
George E. Totten(2006). " Steel Heat Treatment: Metallurgy and Technologies"

International Conference on Asia Pacific Mining and Metallurgy
Tainan, Taiwan, November 17-20, 2019

Section 3：Materials Science

10：10 – 12：00　　　2nd Lecture Room

10:10-12:00	Session Chair:	Prof. **Yen-Pei Fu** National Dong Hwa University
10:10-10:30	CIMME108135	**Gilang Baswara Anggara Putra** National Central University

Perovskite $La_{0.5}Sr_{0.5}Co_{0.2}Fe_{0.8-x}N_xO_{(3-\delta)}$ ($0 \leq x \leq 0.03$) Prepared
by Combustion Technique used for Cathode Materials of the Solid Oxide Fuel Cell

10:30-11:00	CIMME108077	**Yi-Cheng Lai** National Cheng Kung University

Synthesis of Sodium Titanate via
Hydrothermal Process and Its Adsorption Ability for Sr Ions

11:00-11:30	CIMME108105	**Lavinia Russell Clemente** National Central University

Fabrication of Three-Dimensional Nickel-Zinc alloying Micro-Features by
electroplating and study of their hydrogen evolution performance
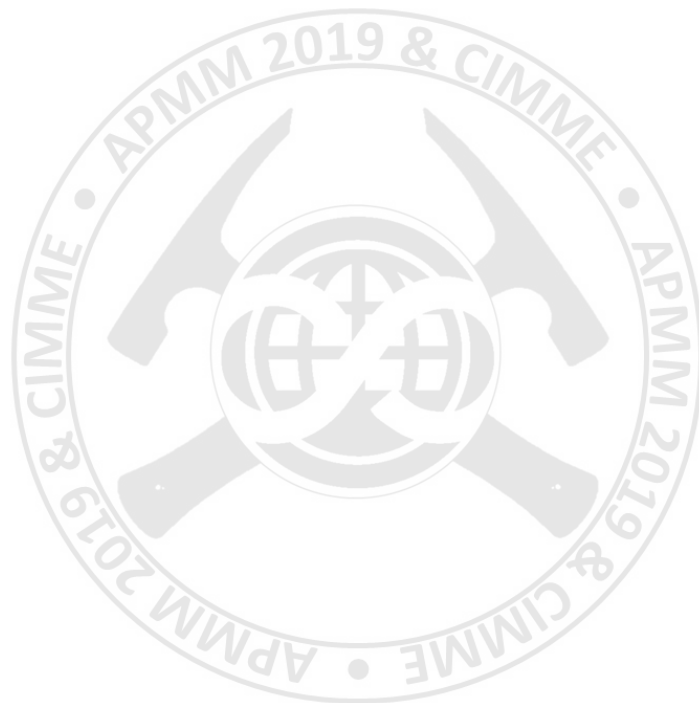
Perovskite $La_{0.5}Sr_{0.5}Co_{0.2}Fe_{0.8-x}Ni_xO_{3-\delta}$ $(0 \leq x \leq 0.03)$ Prepared by Combustion Technique used for Cathode Materials of the Solid Oxide Fuel Cell

Gilang Baswara Anggara Putra[1], Pan Ruey Jiun[1], Jing-Chie Lin[2, 3, *]

[1] *International Master Program in Applied Materials Science, National Central University*
[2] *Institute of Materials Science and Engineering, National Central University*
[3] *Department of Mechanical Engineering, National Central University*
*corresponding author: jclincom@cc.ncu.edu.tw

ABSTRACT

In a general form of ABO_3 with the perovskite structure, $La_{0.5}Sr_{0.5}Co_{0.2}Fe_{0.8}O_{3-\delta}$ (LSCF55) and its derivatives doped with nickel at 1, 2 and 3 at. % (denoted as LSCF55N1, LSCF55N2 and LSCF55N3) were successfully synthesized through combustion by means of glycine-nitrate process. Nascent powders were further calcined at elevated temperatures to form well crystalline forms for their formulation of the cathode material used in the solid oxide fuel cell (SOFC). The effect of Ni-doping on crystal structures, microstructural, and anisotropic oxygen vacancies was analyzed by XRD, SEM, and TGA. Resulted from TGA, LSCF55N3 (doped with 3 at. % Ni) reveals the highest anisotropic oxygen vacancies as compared to the other specimens. Resulted from station-testing, the single-cell assembled with the cathode from LSCF55N3 and the anode-supported O-SOFC based on YSZ-electrolyte displayed the highest power density at 151.4 mW/cm² at 800 °C. It has better performance in O-SOFC than P-SOFC (proton-conducting) type electrolyte due to its microstructure and vacancies offered. Overall the results show that offering micro-dose of Nickel doping in the Fe-site is one of an efficient way to be promising cathode materials for SOFCs.
Keywords: Cathode, Electrochemical Property, Ni-doped, Solid Oxide Fuel Cell.

INTRODUCTION

Perovskite oxides in a general form of ABO_3 are characterized as mixed ionic and electronic conductive (MIEC) material thus are extensively used in advanced applications, such as oxygen sensors and oxygen separation membranes [1]. Their good conductivity of electrons as well as of oxide ions make them a very popular choice as a cathode material in the solid oxide fuel cells (SOFCs). The present work focuses on developing new formulations in improved cathode performance for SOFCs.

$La_{0.5}Sr_{0.5}Co_{0.2}Fe_{0.8}O_{3-\delta}$ (LSCF55) is one of La-Sr-Co-Fe (LSCF) oxides categorized as MIEC perovskite to demonstrate good catalytic activity in the oxygen reduction reaction (ORR). It was reported that LSCF55 is an oxide with the ratio of (La/Sr) equal to (50/50) to reveal a superior level of conductivity to other oxides in different (La/Sr) ratios [2-3]. Recently, studies of the LSCF oxides have made a significant progress on their electro-catalytic reactivity by means of infiltration method, doping method, or fabrication of composites cathode materials [4-5]. Due to this improvement, LSCF is modified to a special structure of nanoparticles structures which result in extensive surface area for

three-phase boundaries (TPBs) among the electrode, electrolyte, and gas phases where catalytic reaction occurs [6].

As doping of impurities to ABO_3, the oxygen vacancy in the LSCF oxide could be improved either by Sr-doping to the A-site or impurity-doping to the B-site of the perovskite. In the present work, we focused the effect of B-site doping by substitution of iron with nickel in the LSCF55. According to theoretical viewpoint, a replacement of cationic sites with lower valence cations moves the B-site to a reducible trend. Therefore, this replacement facilitates the generation capability of oxygen vacancy. With respect to the studies of Ni-doping in the LSCF used for the cathode of SOFCs, it was found that the dilute Ni-dopant in the rage from 0.01 to 0.03 at. % results in a decrease of the activation energy for the cathodic reduction. This fact suggests that Ni-doping in the B-site of LSCF reveals higher catalytic reactivity than the monotonic LSCF [5]. Other studies show Ni dopant in B-site of perovskite structure give higher oxygen absorption in SOFCs operational temperature (800°-1000°C) compared by other aliovalent cations such as Zr and Al [7].

This works focused on a dilute Ni-doping ($0 \leq x \leq 0.03\ at.\%$) in LSCF55, which is a specific oxide among sequential LSCF oxides. All the oxides were prepared through combustion method by using the glycine-nitrate process (GNP). The adoption of this process is attributed to the advantages to obtain high purity of the product (containing the least carbon residue), homogenous distribution of nanoparticles, and porous pure perovskite structure [8].

EXPERIMENTAL METHODS

Powders varying in x values in the formula $La_{0.5}Sr_{0.5}Co_{0.2}Fe_{0.8-x}Ni_xO_{3-\delta}$ ($0 \leq x \leq 0.03$) were prepared by glycine-nitrate process. Chemical precursors $La(NO_3)_3$, $Sr(NO_3)_2$, $Co(NO_3)_2$, $Fe(NO_3)_3$, $Ni(NO_3)_2$ and Glycine were mixed in the stoichiometric amount to dissolve in the distilled water. The ratio of glycine to nitrate (G/N in molar ratio) was fixed in value 1.0/1.0 and the pH of the mixed solution then adjusted to 4 by using nitric acid or ammonia. The well mixed solution was then placed in an oven kept on 80°C until it became gel form. Then the beaker was transfer to a heating plate to continue heating and eventually up to 400°C to cause a spontaneous combustion. The nascent powder produced from the combustion was collected. They were then calcined at 1000°C for 4 hours. The calcined powders and zirconia balls were placed in a ball-mill jar at a ratio of 1:10, and an appropriate amount of isopropanol was added to complete cover the powder. The mixture was ground in a planetary ball mill at an angular rate of 200 rpm for 24 h. Then the solution was dried and sieved by 325-mesh screen used to prepare the cathode paste. Four dried powders such as LSCF55, LSCF55N1, LSCF55N2, and LSCF55N3 were kept in the desiccator for preparation the cathode paste.

Cathode paste was made by mixing a 60 wt.% cathode powder with a binder 40wt%. The binder consists of 97 wt. % α-Terpineol and 3 wt. % of ethyl cellulose. The precursor is mixed with high-speed mixer at an angular rate of 2000 rpm for 30 s and continued at 2200 rpm for 30 s. The cathode paste was then screen-printed on the electrolyte in a diameter of 3 cm and then sintered at 1100°C for 1 h.

Two kinds of the single-cell system were used in this works, oxygen-conducting SOFC (O-SOFC) and Proton-conducting SOFC (P-SOFC). O-SOFC were composed of dense and thin Yttria-stabilized zirconia (YSZ) electrolyte, with NiO-YSZ as the anode, and the cathode paste printed on the other side to result in the cell composition $NiO - YSZ\|YSZ\|GDC - Cathode$. P-SOFC cell consists of dense $BaCe_{0.6}Zr_{0.2}Y_{0.2}O_{3-\delta}$ (BCZY) as the electrolyte with Pt printed on one side (as the anode) and the cathode printed on the other side to accomplish a cell of $Pt\|BCZY\|Cathode$.

In this study, all the powders were examined by X-Ray Diffractometer (XRD, Bruker D8) to verify their crystal structure. The anisotropic oxygen vacancy content of the powders was evaluated by

means of thermogravimetric analysis (TGA). A dense bar (30 mm x 6.25 mm x 6.25 under a load of 4.0 metric ton.) of each kind of powders was subjected to electrical conductivity measurement with a four-point probe tester. All kind of single cell was set up and tested by the testing station to determine the I-V polarization and estimate the resistance and capacitance of the cell by using electrochemical impedance spectroscopy (EIS, Schlumberger, with a Z-view software).

RESULT AND DISCUSSION

The XRD pattern of the nascent powder LSCF55 resultant from GNP process revealed a less intensity of the characteristic perovskite peaks as compared to that of the corresponding calcined powders, even all the peaks were in phase with the typical ABO_3 in perovskite structure matching with the JCPDS Card No. 48-0122. For the Ni-doping powders (including LSCF55N1, LSCF55N2, and LSCF55N3), the main peak (i.e., with 2θ at 32.678°) of the perovskite indicated a slight shift to higher angle up to 33.412°). This result is consistent with the data reported previously [5].

The TGA of the powders performed under reducing condition could be used to estimate the oxygen non-stoichiometry (δ) in the oxide such as LSCF. The magnitude of δ is proportional to the oxygen vacancies by calculating the weight loss with increasing the temperature. The data of TGA display a weight loss around 650°C that is ascribed to a reduction of the transition metal elements such as Ni, Co, and Fe. The weight loss of the samples LSCF55, LSCF55N1, LSCF33N2, and LSCF55N3 was 0.293%, 0.374%, 0.4123%, and 0.505%, respectively. This result reflects higher Ni-dopant leading to higher weight-loss caused by higher oxygen vacancies. The measurement of the electrical conductivity depicted that the data for Ni-doped specimens are greater than LSCF55. At 700°C, the conductivity of LSCF55N3 is the highest (550 S/cm) as compared to that (325 S/cm) of the LSCF55.
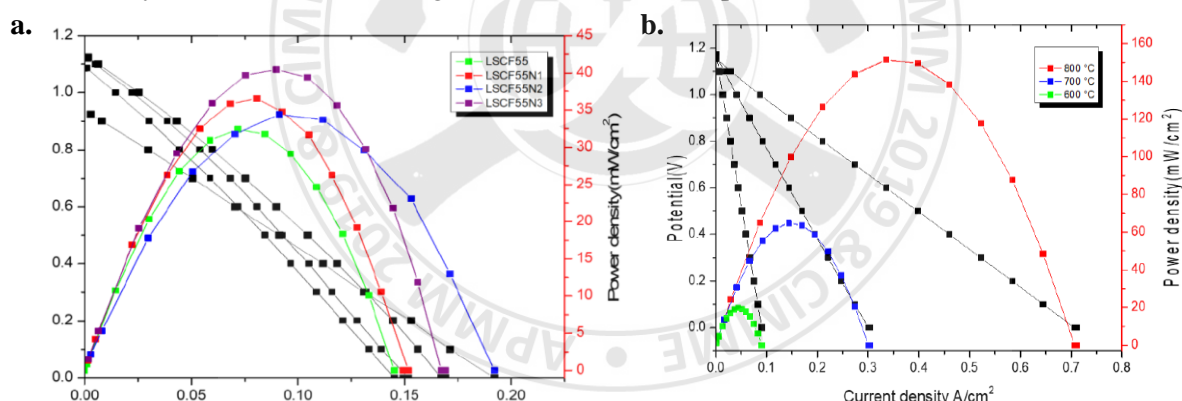
Figure 1. The voltage and power densities versus current density of (a) P-SOFC Cell with configuration $Pt\|BCZY\|Cathode$ with sample LSCF55, LSCF55N1, LSCF55N2, and LSCF55N3 in 800°C (b) of O-SOFC cell with configuration $Pt\|LSGM\|Cathode$ with sample LSCF55N3 in different temperature on the static air.

Figure 1(A) shows that the power density of the single cell based on P-SOFC, performed at 800 ℃, increases ($33 < 35 < 38 < 42$ mW/cm²) with increasing the Ni-dopant in the cathode. Consequently, Ni-doping resulted in an increase on the data of weight loss in TGA, conductivities and power density. Among all the powders, specimen of the powder LSCF55N3 is the best cathode material used in the SOFCs. Regarding the cathode made from LSCF55N3, when it was assembled to a single cell with an anode-supported of O-SOFC (with electrolyte of YSZ), the powder density at 800℃ is the highest (154 mW/cm²) as compared to other temperatures, as shown in Figure 1(B). The performance of the cathode

materials assembled to the O-SOFCs is superior to that P-SOFCs. In line with the results of SEM and TGA, the presence of numerous porosity and cavities in the cathode frame and the oxygen vacancies tend to facilitate ORR reaction.

Study through electrochemical impedance spectroscopy (EIS) is helpful to comprehend the polarization resistance in the performance of the single cell. The impedance data simulated by the Zview software, an equivalent electrical circuit is proposed to show the best fit. This circuit contains 4 types of resistance: contact resistance (R_{ohm}), electronic conduction resistance ($R_{electron}$), oxygen ion transfers resistance (R_{oxy}) and mass transfer resistance (R_{mass}). The summation of electronic conduction resistance, oxygen ion transfers resistance and mass transfer resistance is equal to polarization resistance, (i.e., $R_p = R_{electron} + R_{oxy} + R_{mass}$). The lower R_p value in the highest efficient operation of the cell. In this work, a single cell established with an anode-supported cell assembled to the cathode material of LSCF55N3 revealing the lest value of R_p (1.574 Ωcm^2) thus performs at 800ºC to show the highest current density.

CONCLUSION

In this study, a series perovskite powder of micro doped of nickel in $La_{0.5}Sr_{0.5}Co_{0.2}Fe_{0.8-x}Ni_xO_{3-\delta}$ ($0 \le x \le 0.03$) were synthesized. The structural and surface microstructure were checked and the effects of Ni doping also investigated via electrochemical properties. The best condition achieved in LSCF55N3 composition which contains 3% Nickel doping with pure perovskite structure and spongy microstructure. It also achieved power density 151.4 mW/cm^2 and lowest polarization resistance 1.574 Ωcm^2. This result show introducing micro doping of nickel in the LSCF system can enhance their electrochemical performance as a cathode of Solid Oxide Fuel Cell.

REFERENCE

[1] Vente, J.F., McIntosh, S., Haije, W.G., Bouwmeester, H.J.M. (2006): "Structure and oxygen stoichiometry of $Ba_{0.5}Sr_{0.5}Co_{0.8}Fe_{0.2}O_3$". Journal of the Electrochemistry Society 10, 581

[2] Mahato, N., Banerjee, A., Gupta, A., Omar, S., Balani, K. (2015): "Progress in material selection for solid oxide fuel cell technology: A review". Progress in Materials Science 72, 141–337.

[3] Vegar Øygarden and Tor Grande (2017): "The effect of Zr-Substitution in $La_{1-x}Sr_xCo_{0.2}M_{0.6}Zr_{0.2}O_{3-\delta}$, thermal expansion and electronic transport properties". Solid State Ionics, Solid State Ionics 301, 53–58.

[4] Jiang, S.P. (2012): "Nanoscale and nano-structured electrodes of solid oxide fuel cells by infiltration: advances and challenges". Int. J. Hydrogen Energy 37.

[5] Lakshminarayanan, N., Choi, H., Kuhn, J.N., Ozkan, U.S. (2015): "Effect of additional B-site transition metal doping on oxygen transport and activation characteristics in $La_{0.6}Sr_{0.4}(Co_{0.18}Fe_{0.72}X_{0.1})O_{3-\delta}$ (where X = Zn, Ni or Cu) perovskite oxides". Applied Catalysis B: Environmental, Volume 103, Issues 3-4, Pages 318-325.

[6] Hong, T., Zhang, L., Chen, F., Xia, C. (2012): "Oxygen surface exchange properties of $La_{0.6}Sr_{0.4}Co_{0.8}Fe_{0.2}O_3$ coated with $Sm_xCe_{1-x}O_2$". J. Power Sources 218.

[7] He, Y.J., Chang, X.F., Dong, X.L., Zhang, C., Jin, W.Q., Xu, N.P. (2008): "Effect of dopant valence on the oxygen desorption and oxygen permeability of $SrCo_{0.4}Fe_{0.5}M_{0.1}O_3$ (M =Ni, Al and Zr) mixed-conducting oxides". Chinese Chemical Letters 19, 725–729.

[8] Sun, C. (2014): "Cathode materials for solid oxide fuel cells: a review". Journal of Solid State Electrochemical 14, 1125-1144.

Synthesis of sodium titanate via hydrothermal process and its adsorption ability for Sr ions

Yi-Cheng Lai and Yu-Chun Wu

Department of Resources Engineering, National Cheng Kung University, Taiwan
N46074120@mail.ncku.edu.tw, yuchunwu@ mail.ncku.edu.tw

Abstract

Sodium titanate was prepared by hydrothermal method using three different starting materials, i.e., amorphous TiO_2, Degussa P25, and rutile TiO_2. The size of the precursor TiO_2 was found determining the morphology of sodium product, where fibrous, tubular and lamellar structure can be controlled. The sodium titanate in different forms are applied to remove Sr^{2+} ions from aqueous solution. The optimal adsorption efficiency up to 204 mg/g is achieved. The structural and elemental properties of sodium titanate in correlation to the adsorption mechanism are investigated and discussed in this work.

Introduction

Sr-90 ion is the one of the major radioactive ions in nuclear wastewater and its half-life is as long as 30 years. Leakage of Sr-90 containing wastewater into the environment may cause great damages to ecosystems and humans. Many wastewater treatments methods for removing metals ions from, such as chemical precipitation, membrane separation, electrochemistry, and ion-exchange. Among those methods, ion-exchange is a highly-efficient, cost-effective method. Synthetic ion-exchange resins are commonly used for removing metal ions, but its thermal and chemical stabilities are relatively poor which is less adaptive for the decontamination use of radioactive ions. Titanate exhibits layered structure where with Na ions intercalate between Ti-O-Ti composed layers[1], is considered as a good candidate as an ion-exchanger. Sodium tinanate has been reported for removing heavy metals ions (e.g. Pb^{2+} and Cd^{2+})[2]; transition metal ions (e.g. Ag^+, Cu^{2+}, Ni^{2+})[3][4], and dyes (e.g. methylene blue and basic dyes)[5][6]. In this work, sodium titanate was synthesized by hydrothermal process. Amorphous TiO_2, Degussa P25, and rutile TiO_2 were respectively used as the precursors, reacting in highly concentrated NaOH solution. The material properties of the as-obtained Na-titanate were investigated in correlation with the adsorption capability to Sr^{2+} ions.

Materials and Methods

2.1 Sodium titanate preparation

Amorphous TiO_2 precursor (5 nm) was obtained via the sol-gel process by dissolving Ti-isopropoxide (TIP) in isopropanol and hydrolyzed by deionized water in H_2O/Ti ratio = 3.3. 10 ml of 10 N NaOH solution was added into the previously prepared TiO_2 sol. In parallel, commercial Degussa P25 and rutile (US Nanomaterials、30 nm) powders were used readily as purchased. 1.316 g of commercial TiO_2 powders was dispersed in 17 ml of isopropanol and 10 ml of 10 N NaOH solution. The as-prepared solutions mentioned above were respectively transferred into 50 mL Teflon-lined autoclave and placed in an oven at 110 ℃ for 20 h. The as-obtained products were washed using 1 L D.I. water to remove the residual matters and then dried at 75 ℃ for 24 h. The samples prepared by amorphous TiO_2, P25 and rutile were labeled NA-11, NP-11 and NR-11, respectively.

2.2   Characterization and adsorption experiments

The hydrothermal derived products were analyzed by X-ray powder diffraction (XRD), transmission electron microscope (TEM), specific surface srea and porosimetry analyzer (BET), ^{23}Na-solid- state nuclear magnetic resonance spectroscopy (NMR), and energy-dispersive X-ray spectroscopy (EDXS) to characterize their structural properties and chemical composition. The batch adsorption experiments to of Sr^{2+} ions were carried out by placing 0.1 g of sodium titanate in 10 ml Sr^{2+} solution at different concentrations (10-3000 ppm) for 24 h. The residual concentration of Sr^{2+} was measured using Atomic Absorption spectrometer.

3. Result and discussion

3.1   Precursor effect

The XRD patterns and TEM images of NA-11, NP-11 and NR-11 are shown in Figure 1. Their diffraction peaks, located at approximately 10°, 28° and 48°, are generally in consistent with the reported sodium titanate.[7][8] The weak peak intensities imply that the crystallinity is low. As illustrated in Figure 1(b), NA-11 shows the fibrous morphology; NP-11 shows a lamellar structure and NR-11 shows a tubular structure. According to the literature[1][9], TiO_2 is stripped into sheet-like structure composed of TiO_6 units by the OH-groups at the hydrothermal reaction while Na^+ ions are intercalated in the interlayer spaces to neutralize the negative charge of the TiO_6 sheets and form multilayered structures. With a small precursor size, the dissolution and exfoliation processes are relatively easier and yielding a small titanate sheet unit, which is the case of NA-11 sample. As the epitaxial crystal growth occurs, the small titanate sheet units eventually grow into a fibrous structure. For NR-11 sample, the starting crystal size is about 30 nm that enables to form larger lamellar structure. A rolling action occurs to maintain crystal stability in order to lower the surface energy and form a tubular structure. Degussa P25 contains about 80% of anatase and the rest of rutile whereas the particle size is over 50 nm. Due to the mixed phase but also the large precursor size, the reaction rate was supposed to be slower than that occurred for NR-11 sample, thus the final product remained lamellar but not yet rolled into tubular.
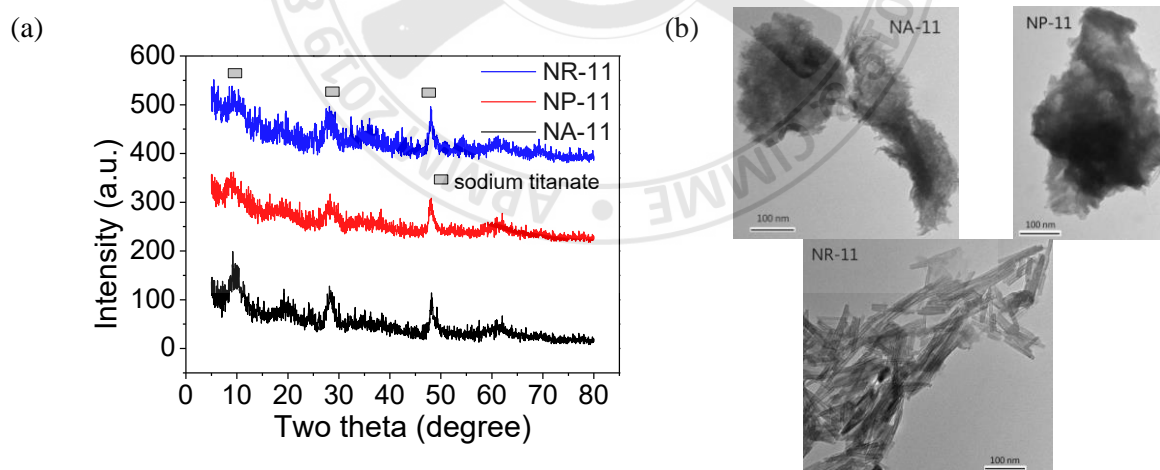
Figure 1 (a) XRD patterns and (b) TEM image of sodium titanate prepared by different TiO_2 precursors

3.2   Adsorption experiment of Sr^{2+}

The batch isothermal adsorption curves to Sr^{2+} is shown in Figure 2(a). To evaluate the adsorption model, the experimental data were analyzed by using Langmuir isotherm model (Equation 1). The fitting curves are presented in Figure 2(b). Since R^2 is close to 1, three samples are well described by the Langmuir isotherm model. The maximum adsorption capacities (q_{max}) of Sr^{2+} were 172 mg/g, 204 mg/g and 164

mg/g for NA-11, NP-11 and NR-11, respectively. These values indicate excellent uptake efficiency in comparison with conventional ion-exchange resin[10][11] and activated carbon [12][13]. The S^{BET} and elements compositions measured by EDXS analysis are shown Table 1. There is no positive correlation between the specific surface area and the adsorption capacity. This is generally in agreement with the reported literature that the specific surface area was found to have no definite relationship with adsorption capacity for the sodium titanate[14]. However, taking into account the Na content ratio, of seems not related to their adsorption capacities, either. There must exist other factors that determine the adsorption capacity.

$$\frac{C_e}{q_e} = \frac{C_e}{q_{max}} + \frac{1}{K_L * q_{max}}$$
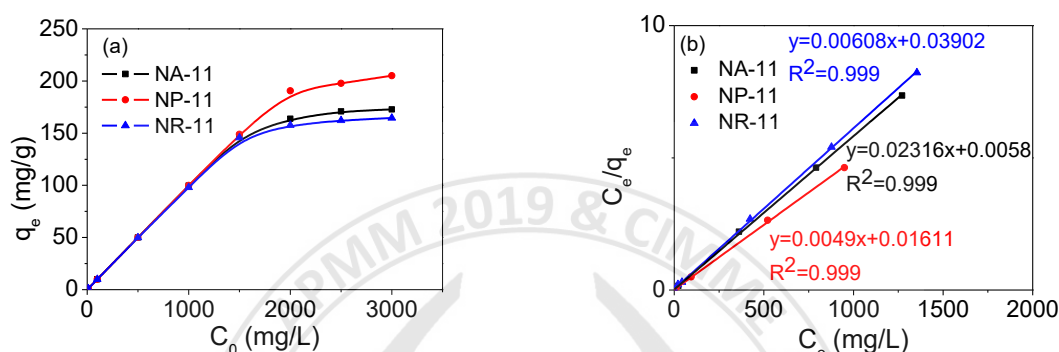
Equation 1

Figure 2 (a) Adsorption isotherms of sodium titanate and (b) Langmuir model fitting

Table 1 EDXS analysis and S^{BET} of sodium titanate

Sample	EDXS (At%)			Na content (meq/g)	S^{BET} (m²/g)	Q_{Sr-max}(meq/g)
	Ti	O	Na			
NA-11	19.86	70.5	9.64	4.18	139.8	3.92
NP-11	21.53	67.37	11.1	4.69	25.7	4.64
NR-11	23.25	64.99	11.76	4.84	76.2	3.74

3.3 Sorption mechanisms of Sr^{2+}

The coordination or ionicity of Na^+ in the structure has been found related to the ionic exchange efficiency with Sr^{2+}[15], ^{23}Na NMR analysis is employed to investigate the coordination state of Na^+ in sodium titanate and the fitting results are shown in Figure 3. According to the literatures,[16][17][18] the peak located at -12 ppm is assigned to Ti-O-Na^{IX}; -2 ppm is associated to the weakly attracted Na on the surface of sodium titanate; 4 ppm is Ti-O-Na^{VII}; 13 ppm is NaOH. Tsiamtsouri et al. [16] have suggested that the low coordinated Na^+ in sodium titanate tend to vanished after the acid-washing process while the high coordinated Na^+ remained. It implies that the lower coordinated Na^+ is easier to dissociate. According to the fitting results, the integral areas ratios of the NMR peaks corresponding to different structured Na^+ ions are listed in Table 2. In comparison with the three prepared samples, NR-11 contains the highest amount of Na^+ but presents the lowest uptake efficiency to Sr^{2+}. This is possibly due to its relatively lower proportion of Ti-O-Na^{VII} bondings. The ratios pf Ti-O-Na^{VII} for NA-11、NP-11, and NR-11 are 60%, 62%, and 49%, respectively. This is positively in agreement with their adsorption capacity to Sr^{2+}. Besides, the surface attached Na^+ (-2 ppm) may be dissociated in solution to form a negatively charged position, which has the opportunity to attract Sr^{2+} to form chemisorption. NR-11 presents high proportion of surface attached Na^+ and residual NaOH; however, is not beneficial for increasing its removing efficiency for Sr^{2+}. This indicates that the ion exchange is the major mechanism uptaking Sr^{2+} instead of chemisorption or chemical precipitation.
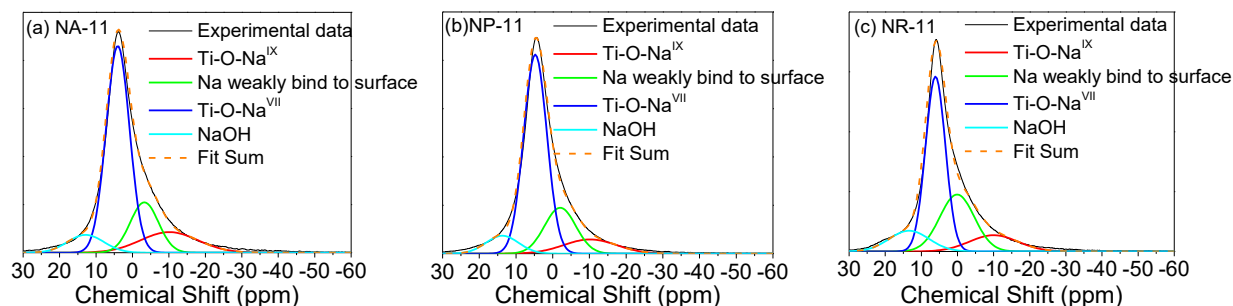
Figure 3 ^{23}Na spectra of sodium titanate

Table 2 ^{23}Na integral area ratio of sodium titanate and calculation of Na^{VII} content

	-12 ppm (%)	-2 ppm (%)	4 ppm (%)	13 ppm (%)
NA-11	15	18	60	8
NP-11	10	19	62	8
NR-11	11	28	49	12

Conclusion

The size of precursor TiO$_2$ determines the morphology of the hydrothermal derived sodium titanate. Small anatase (5 nm) results in fibrous structure and large rutile (30 nm) enables a formation of nanotubes. The reaction rate for commercial P25 is relatively low due to its large crystal size and finally showed lamellar structure, The sodium titanate synthesized prepared by using P25 powders demonstrates a highest adsorption capacity on Sr^{2+} of 204 mg/g due to its high Na content but also a high proportion of lower-coordinated Na$^+$ bonding state.

References

[1] Li, M. J., Chi, Z. Y., & Wu, Y. C. (2012). Morphology, chemical composition and phase transformation of hydrothermal derived sodium titanate. *Journal of the American Ceramic Society*, *95*(10), 3297-3304.

[2] Xiong, L., Chen, C., Chen, Q., & Ni, J. (2011). Adsorption of Pb (II) and Cd (II) from aqueous solutions using titanate nanotubes prepared via hydrothermal method. *Journal of hazardous materials*, *189*(3), 741-748.

[3] Li, N., Zhang, L., Chen, Y., Fang, M., Zhang, J., & Wang, H. (2012). Highly efficient, irreversible and selective ion exchange property of layered titanate nanostructures. *Advanced Functional Materials*, *22*(4), 835-841.

[4] Sheng, G., Yang, S., Sheng, J., Zhao, D., & Wang, X. (2011). Influence of solution chemistry on the removal of Ni (II) from aqueous solution to titanate nanotubes. *Chemical engineering journal*, *168*(1), 178-182.

[5] Lee, C. K., Lin, K. S., Wu, C. F., Lyu, M. D., & Lo, C. C. (2008). Effects of synthesis temperature on the microstructures and basic dyes adsorption of titanate nanotubes. *Journal of Hazardous Materials*, *150*(3), 494-503.

[6] Xiong, L., Yang, Y., Mai, J., Sun, W., Zhang, C., Wei, D., ... & Ni, J. (2010). Adsorption behavior of methylene blue onto titanate nanotubes. *Chemical Engineering Journal*, *156*(2), 313-320.

[7] Huang, J. Q., Huang, Z., Guo, W., Wang, M. L., Cao, Y. G., & Hong, M. C. (2008). Facile synthesis of titanate nanoflowers by a hydrothermal route. *Crystal Growth and Design*, *8*(7), 2444-2446.

[8] Yang, J., Jin, Z., Wang, X., Li, W., Zhang, J., Zhang, S., ... & Zhang, Z. (2003). Study on composition, structure and formation process of nanotube $Na_2Ti_2O_4(OH)_2$. *Dalton Transactions*, (20), 3898-3901.

[9] Bavykin, D. V., Kulak, A. N., & Walsh, F. C. (2010). Metastable nature of titanate nanotubes in an alkaline environment. *Crystal Growth & Design*, *10*(10), 4421-4427.

[10] Hafizi, M., Abolghasemi, H., Moradi, M., & Milani, S. A. (2011). Strontium adsorption from sulfuric acid solution by Dowex 50W-X resins. *Chinese Journal of Chemical Engineering*, *19*(2), 267-272.

[11] Rengaraj, S., & Moon, S. H. (2002). Kinetics of adsorption of Co (II) removal from water and wastewater by ion exchange resins. *Water research*, *36*(7), 1783-1793.

[12] Caccin, M., Giacobbo, F., Da Ros, M., Besozzi, L., & Mariani, M. (2013). Adsorption of uranium, cesium and strontium onto coconut shell activated carbon. *Journal of Radioanalytical and Nuclear Chemistry*, *297*(1), 9-18.

[13] Kasaini, H., Kekana, P. T., Saghti, A. A., & Bolton, K. (2013). Adsorption characteristics of cobalt and nickel on Oxalate-treated activated carbons in sulphate media.

[14] Liu, W., Sun, W., Han, Y., Ahmad, M., & Ni, J. (2014). Adsorption of Cu (II) and Cd (II) on titanate nanomaterials synthesized via hydrothermal method under different NaOH concentrations: role of sodium content. *Colloids and Surfaces A: Physicochemical and Engineering Aspects*, *452*, 138-147.

[15] 黃怡萱. (2019). 鹼活化高嶺土對 Sr2+及 Co2+離子之吸附特性研究. *成功大學資源工程研究所，碩士論文*, 1- 133.

[16] Tsiamtsouri, M. A., Allan, P. K., Pell, A. J., Stratford, J. M., Kim, G., Kerber, R. N., ... & Grey, C. P. (2018). Exfoliation of layered Na-ion anode material Na2Ti3O7 for enhanced capacity and cyclability. *Chemistry of Materials*, *30*(5), 1505-1516.

[17] Volgmann, K., Werth, V., Nakhal, S., Lerch, M., Bredow, T., & Heitjans, P. (2017). Solid-State NMR Spectroscopy Study of Cation Dynamics in Layered Na2Ti3O7 and Li2Ti3O7. *Zeitschrift für Physikalische Chemie, 231*(7-8), 1243-1262.

[18] Suetake, J., Nosaka, A. Y., Hodouchi, K., Matsubara, H., & Nosaka, Y. (2008). Characteristics of titanate nanotube and the states of the confined sodium ions. *The Journal of Physical Chemistry C*, *112*(47), 18474-18482.

Fabrication of Three-Dimensional Nickel-Zinc alloying Micro-Features by electroplating and study of their hydrogen evolution performance

*Lavinia Russell Clemente[1] and Jing-Chie Lin[2,3]

[1]International Master Program in Applied Materials Science, National Central University, Taiwan
[2]Institute of Materials Science and Engineering, National Central University, Taiwan
[3]Department of Mechanical Engineering, National Central University, Taiwan

ABSTRACT

The hydrogen evolution reaction (HER) of the nickel-zinc alloy was studied using alkaline water electrolysis, electrochemical impedance spectroscopy (EIS), and cathodic polarization techniques. Localized electrochemical deposition (LECD) process was used to fabricate Ni-Zn alloy micropillars. The process was carried out using a micro anode guided electrodeposition (MAGE) process in a chloride bath different in $NiCl_2$ concentrations (0.25 M – 1.00 M). The surface morphology, chemical composition, phase composition, and crystallography of the fabricated Ni-Zn alloy was characterized using SEM, EDS, XRD, and TEM, respectively. It was observed that micropillars with higher nickel content has a rougher surface and has a smaller diameter. With increasing the $NiCl_2$ concentration in the electrolyte, the amount of deposited nickel in the micropillar alloy also increases, as shown in the EDS results. XRD spectra revealed that the fabricated Ni-Zn alloy consists of γ-phase structure and for micropillar alloy with low nickel content it also showed a presence of Zn phase. One commercial software -i.e., COMSOL Multiphysics 5.2-was used to simulate the strength and distribution of the electric field in the electroplating process. Study of cathodic polarization provided useful information to realize the mechanism of anomalous Ni-Zn alloy electrodeposition.

Keywords: Hydrogen evolution, Electrolysis, Localized electrochemical deposition, Micro anode guided electrodeposition, Nickel-Zinc alloy

INTRODUCTION

Fossil fuels is the major energy source consumed in the world today, although CO_2 emissions from burning fossil fuels causes air pollution and contributes to global warming it still continues to be the major energy source for human activities. For the past years atmospheric carbon dioxide emissions has continued to rise rapidly. According to the CO_2 levels measured at Mauna Loa Observatory, Hawaii for the last decade, CO_2 ratio has peaked up to 411 ppm [1]. With the growing demand for energy and high consumption from industrialized nations, it is of great importance for scientists to seek and produce alternative energy sources that will not contribute to environmental pollution, could be easily produced, will be renewable and will be low cost. Considering all these criteria hydrogen gas could be an alternative source of energy.

Hydrogen gas was found to be an environmental friendly alternative to fossil fuels since one of the most

promising techniques to produce hydrogen on industrial scale for sustainable economy without CO_2 emissions is water electrolysis. However, this technique is expensive due to its high energy consumption. By choosing an appropriate electrode the energy consumption of this method could be reduced. The properties that a good electrode should have are large active surface area, good electrical conductivity, low overpotential and ease of use in order to reduce the method's cost [2,3].

In the past years, several nickel-based alloys have been developed to use as a catalyst for hydrogen production since it was found to be the best among all other alloys [4]. Nickel-Zinc based alloy was found to be a good catalyst for hydrogen production because of its dezincification during the process and forms a large active surface area [4-6]. In this study three-dimensional nickel-zinc alloy with varying nickel content was fabricated to investigate its hydrogen evolution reaction performance in alkaline water.

EXPERIMENTAL DETAILS

Localized electrochemical deposition(LECD) process was carried out by micro anode guided electroplating(MAGE) to fabricate nickel-zinc alloy micropillars. The anode was made of Pt wire with a diameter of 125um covered with an insulating glass. The cathode was made of copper wire and was wetly polished to reveal a flat surface where the alloy will be deposited. The electrolyte cell was made of polymethyl methacrylate (PMMA). The electrolyte bath composition is shown in Table 1. The anode was kept close to the cathode with a gap of 90um. The experimental set up was reported in a previous publication [7]. As the micropillar grows towards the anode, the gap between the electrodes was monitored by a charge-coupled device (CCD) microscope and the current was also measured to keep the separation constant.

Cathodic polarization curves was measured using Ag/AgCl as a reference electrode(RE), Pt as counter electrode(CE) and Cu as working electrode(WE) connected to a potentiostat(Princeton EG&G Model 273A). Before electrodeposition began the initial gap between the electrodes was set to 90um. As the micropillar grows towards the anode, almost in contact with it a sudden rise in the current will be detected and the electroplating will automatically stop.

Characterization of nickel-zinc alloy micropillar was carried out using scanning electron microscope (SEM), energy-dispersive x-ray spectroscopy (EDS) and x-ray diffraction(XRD) to study its surface morphology, chemical composition, phase composition and crystallography respectively. COMSOL multiphysics 5.2 was used to simulate the strength and distribution of electric field in the electroplating process and to observe its effect on the structure of the fabricated nickel-zinc micropillar.

Table 1: Electrolyte bath composition

Chemical composition	Concentration(M)
$NiCl-6H_2O$	0.25, 0.50, 0.75, 1.00
$ZnCl_2$	0.50
NH_4Cl	1.00
H_3BO_3	0.50
KCl	2.00

RESULTS AND DISUSSION

Scanning electron micrographs of fabricated nickel-zinc micropillar alloy deposited in chloride bath with different $NiCl_2$ concentrations (i.e., 0.25M, 0.50M, 0.75M, 1.00M) are shown in fig. 1. An electrodeposition potential of 4V was used and the micropillars are deposited with the same height of 3000um. It was observed in the EDS data shown in fig. 2 that as the $NiCl_2$ concentration is increased in the electrolyte bath the amount of deposited nickel in the micropillar also increases. This result is consistent to other studies because by increasing Ni^{2+} concentration in the bath it reduces the release of hydrogen, therefore adsorption of nickel to occupy active sites is increased [8,9]. For micropillars with lower nickel content a smooth surface morphology is obtained.
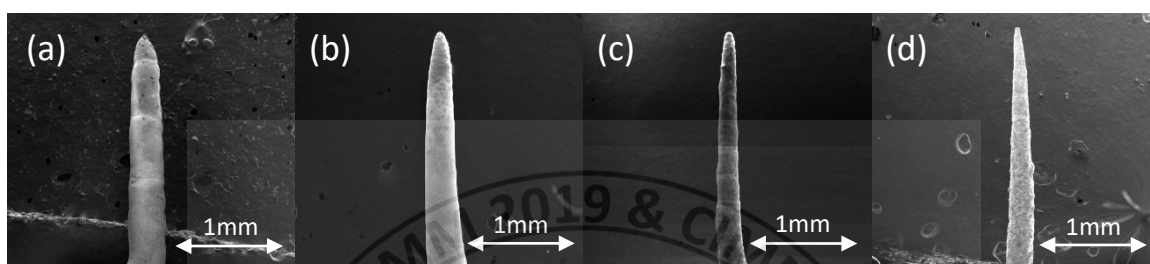
Figure 1. SEM micrographs of nickel-zinc micropillar alloys (a) 0.25M $NiCl_2$ (b) 0.50M $NiCl_2$ (c) 0.75M $NiCl_2$ (d) 1.00M $NiCl_2$
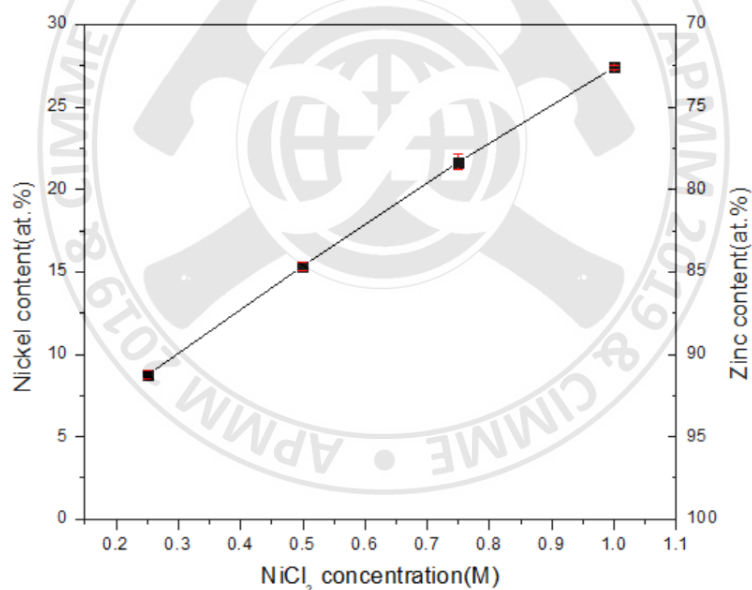
Figure 2. Effect of $NiCl_2$ concentration in the bath to the deposited Ni-Zn alloy

The XRD patterns of Ni-Zn micropillar deposited with different $NiCl_2$ concentration is shown in fig. 3. Results show that the fabricated micropillars with 15 - 27 at.% obtained a single γ-phase structure (Ni_2Zn_{21}). While micropillars with 8 at.% of nickel content obtained a γ-phase structure it also showed a presence of Zn phase and making it dual phased.
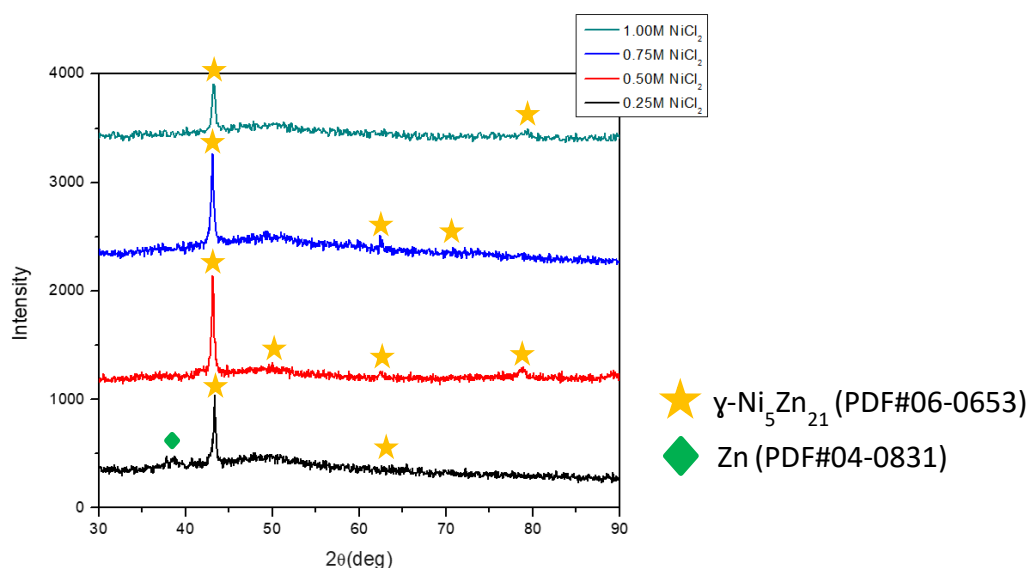
Figure 3. XRD patterns of Ni-Zn alloy produced at $NiCl_2$ concentrations of 0.25M, 0.50M, 0.75M and 1.00M

CONCLUSION

In the on-going research 3D Ni-Zn alloys was easily fabricated using LECD technique carried out by MAGE process. Results show that as the nickel ions in the bath is increased the nickel deposits also increase. All the XRD patterns showed the presence of ɣ-phase while for the alloy with low nickel content it also showed a presence of Zn phase. This is studied because one of the properties that affects the hydrogen production of a cathode is the chemical composition and structure of the material.

REFERENCES

[1] Global Climate Change. *Carbon dioxide* (Available from: https://climate.nasa.gov/vital-signs/carbon-dioxide/) (Accessed file July 2019)

[2] Yazici, B., Tatli, G., Galip, H., & Erbil, M. (1995). Investigation of suitable cathodes for the production of hydrogen gas by electrolysis. *International journal of hydrogen energy*, *20*(12), 957-965.

[3] Kronberger, H., Fabjan, C., & Frithum, G. (1991). Development of high performance cathodes for hydrogen production from alkaline solutions. *International journal of hydrogen energy*, *16*(3), 219-221.

[4] Raj, I. A., & Vasu, K. I. (1990). Transition metal-based hydrogen electrodes in alkaline solution—electrocatalysis on nickel based binary alloy coatings. *Journal of applied electrochemistry*, *20*(1), 32-38.

[5] Stevanović, J., Gojković, S., Despić, A., Obradović, M., & Nakić, V. (1998). Hydrogen evolution at Zn-Ni alloys. *Electrochimica acta*, *43*(7), 705-711.

[6] Hu, C. C., Tsay, C. H., & Bai, A. (2003). Optimization of the hydrogen evolution activity on zinc–nickel deposits using experimental strategies. *Electrochimica Acta*, *48*(7), 907-918

[7] Lin, J. C., Jang, S. B., Lee, D. L., Chen, C. C., Yeh, P. C., Chang, T. K., & Yang, J. H. (2005). Fabrication of micrometer Ni columns by continuous and intermittent microanode guided electroplating. *Journal of Micromechanics and Microengineering*, *15*(12), 2405.

[8] Abou-Krisha, M. M., Assaf, F. H., & Toghan, A. A. (2007). Electrodeposition of Zn–Ni alloys from sulfate bath. *Journal of Solid State Electrochemistry*, *11*(2), 244-252.

[9] Lee, H. Y., & Kim, S. G. (2000). Characteristics of Ni deposition in an alkaline bath for Zn–Ni alloy deposition on steel plates. *Surface and Coatings Technology*, *135*(1), 69-74.

International Conference on Asia Pacific Mining and Metallurgy
Tainan, Taiwan, November 17-20, 2019

Section 3：Geo-resource Exploration

10：10 – 12：00　　　　3rd Lecture Room

10:10-12:00	Session Chair:	Prof. **Wu-Cheng Chi** Acadima Sinica

10:10-10:30	CIMME108193	**Dr. Wei-Chung Han** Industrial Technology Research Institute, Taiwan

Seismic Analysis of the Gas Hydrate System at Pointer Ridge Offshore SW Taiwan

10:30-10:50	CIMME108194	**Dr. Liwen Chen** National Taiwan University

Marine Geothermal Studies Offshore SW & NE Taiwan

10:50-11:10	CIMME108039	**Prof. Chein-Lee Wang** National Cheng Kung University

A Study of the Basic Properties of API-G Cement with Different Weight Percent of Silicon Carbide Admixtures Exposed to the Supercritical CO_2 Environment

11:10-11:30	CIMME108079	**Eslam Mohammed Ali Mitwally** National Taipei University of Technology

Geochemistry of Magnetite from Sand, Beaches, Rivers and the Surrounding Rocks at North Taiwan

11:30-11:50	CIMME108128	**Yi-Wei Lin** CPC Corporation, Taiwan

Seismic Lithology Prediction in Depth Domain

Seismic Analysis of the Gas Hydrate System at Pointer Ridge Offshore SW Taiwan

Wei-Chung Han
Green Energy and Environment Research Laboratories, Industrial Technology Research Institute, Taiwan

Liwen Chen, Char-Shine Liu
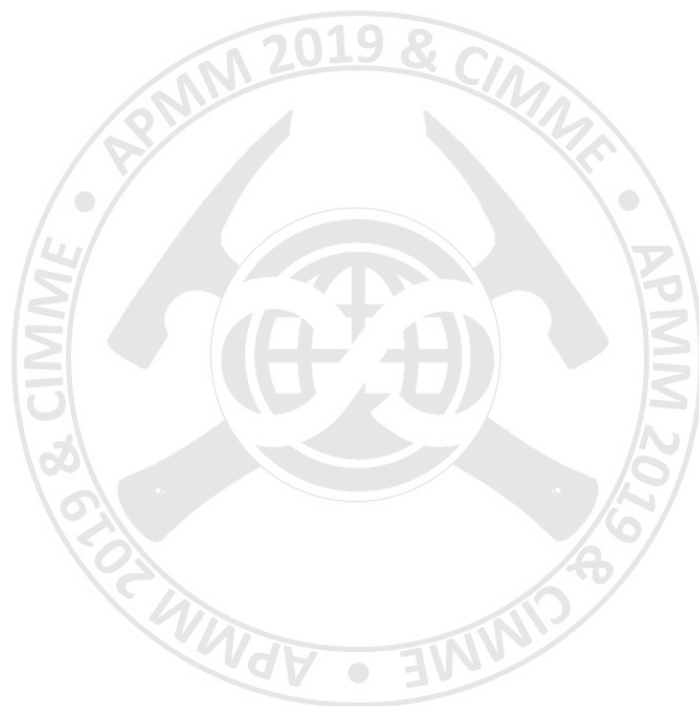*Ocean Center, National Taiwan University, Taiwan*

Christian Berndt
Helmholtz Centre for Ocean Research Kiel, Germany

Wu-Cheng Chi
Institute of Earth Sciences, Academia Sinica, Taiwan

Pointer Ridge is a gas hydrate prospect on the South China Sea continental slope offshore SW Taiwan. It is characterized by densely distributed bottom simulating reflections (BSRs), active gas seepage, and potential sandy gas hydrate reservoirs. To understand how the fluids have migrated toward the seafloor, and the role of geological processes in the gas hydrate system, we have collected and analyzed high-quality 2D and 3D reflection seismic data. We first mapped the spatial distribution of the BSRs, and interpreted a major normal fault, Pointer Ridge Fault (PR Fault). The NE-SW trending fault dips to the east, and separates the erosional regime to the west from the depositional regime to the east. One active vent site was identified directly above the PR Fault, while another is located on a topographic high to the west of the fault. On the hanging block of the fault we found at least one major unconformity. The seismic data indicate refilled channels with coarser-grained sediments in the hanging wall of the normal fault. Seismic attribute analysis shows subsurface fluid conduits and potential gas hydrate reservoirs. We propose two types of gas chimneys, which are separated by the fault. Gas plumes derived from hydroacoustic data are mostly from the footwall block of the fault. We infer that fluid flow is more active in the erosional environment compared to the depositional one, and that this is the result of reduced overburden. The methane-bearing fluids migrate upward along the PR Fault and chimneys and form hydrates above the base of the gas hydrate stability zone. Based on seismic interpretation and seismic attribute analysis, we postulate that the channel infill constitutes the most promising hydrate reservoirs in this geological setting. In the surveyed area of Pointer Ridge these channels occur mainly below the gas hydrate stability zone.

Marine Geothermal Studies Offshore SW & NE Taiwan

Liwen Chen, Jyun-Nai Wu and Char-Shine Liu
Ocean Center, National Taiwan University, Taiwan
mmammamma@gmail.com

Hsieh-Tang Chiang
National Ilan University, Taiwan

Ling-Yun Chiao and Chuen-Tien Shyu
National Ilan University, Taiwan

Yunshuen Wang
Central Geological Survey, MOEA, Taiwan

ABSTRACT

In the past decade, the marine geothermal surveys had been widely utilized in resource studies on offshore SW and NE Taiwan for gas hydrate and hydrothermal vents investigations. The measured heat flows provide the direct ground truths to approach the thermochronology in the subsurface, as well as the implications of possible thermal structure and fluid migration in subsurface. Therefore, the joint geophysical interpretations are necessary to help us to understand their reservoir potentials especially with some corresponding thermal effects induced by specifically some geological processes.

For gas hydrate research SW offshore Taiwan, we have collected 212 heat flow measurements conducted in 20 cruises from 2004 to 2014, meanwhile, we also accomplished some thermal modeling studies through integrating diverse geophysical investigations. The results show that the thermal gradient is between 0.008 °C/m and 0.388 °C/m, and 0.062 °C/m on average, while the bottom of the gas hydrate stability zone (BGHS) is about 301 mbsf in average while the water depth is between 1000 to 3000 m. Generally, the thrusted sediments on the east of the deformation front and the passive continental margin to the west were inferred that the cooling caused by the subduction and the thermal blanketing of the thickened sediments acted as dominant factors to cause unsteady-state heat transfer within the shallow 1 km sediments. Regionally, the diverse thermal effects also strongly dominated by near-surface geological processes in the active and continental margin, such as faulting, erosion, sedimentation, and diapirism. The information of heat flow measurements suggested very high potentials of gas hydrate here and it is helpful for planning our future investigation.

For investigating mineral resources NE offshore Taiwan, combing previous thermal studies and latest 53 heat flow measurements conducted in 4 cruises from 2015 to 2019, the enormous focus thermal effects caused a huge variation on thermal gradients from -0.3 to 27.3 K/m. Through dense sampling in small areas and time-dependent temperature records from CTD mooring, we are able to map the distribution of the hydrothermal fields and the volcanic structures to study different fluid migration patterns in the rifting basin of Southern Okinawa Trough. Besides, the time-dependent temperature records from CTD mooring also insinuate the heat flux information to support our interpretations. Combining with the geophysical and geochemistry investigations, we had located some high potentials mineral resources in this area.

A Study of the Basic Properties of API-G Cement with Different Weight Percent of Silicon Carbide Admixtures under the Supercritical CO₂ Environment

Chein-Lee Wang, Zhen-Hui Xu, Hui-Yu Huang

Department of Resources Engineering, National Cheng Kung University, Tainan

clwang@ mail.ncku.edu.tw

Chun-Chih Kuo

Department of Civil Engineering, National Taiwan University, Taipei

ABSTRACT

In the geological sequestration of carbon dioxide technology, carbonization of the sealing cement in the well at supercritical CO_2 environment could occur. This undesired effect reduces the mechanical properties of the cementing materials, thereby causes gas leakage problems. Previous studies have observed that the sealing cement with silicon carbide could prevent the severity of carbonization of supercritical CO_2 environment. This study proposes to add different weight percentages of silicon carbide to API-G cement and place them in a supercritical CO_2 reactor in order to determine the most appropriate proportions of silicon carbide for the better performance of sealing cement. The changes of these basic properties of cement with different proportions of silicon carbide were observed after reaction time up to 84 days. This study concludes that the API-G cement with 3 weight percent of silicon carbide provides the most favorable results in the proposed experiments.

INTRODUCTION

In order to determine the optimum proportions of silicon carbide, this study proposes to mix different weight percentages of silicon carbide (0.5%, 1%, 3%, 5%) to API-G cement, and place them in a supercritical CO_2 reactor at temperature of 45°C and pressure of 25 MPa. After different reaction durations (unreacted, 14, 28, 56, 84 days), this study carries out a series of tests including: uniaxial compressive strength, carbonation depth, permeability, pulse velocities, and microscopic material analysis (SEM, EDS, and XRD). The changes of these basic properties of cement with different

proportions of silicon carbide were observed.

CHEMICAL REACTIONS

There are three major chemical reactions governing the carbonation of cement (Onan et al., 1984, Kutchko et al., 2007, Duguid et al., 2008):

1. Dissolution of carbon dioxide:

$$CO_{2(g)} \leftrightarrow CO_{2(aq)} \tag{1}$$

$$CO_{2(aq)} + H_2O \leftrightarrow H_2CO_{3(aq)} \leftrightarrow H^+_{(aq)} + HCO_3^-{}_{(aq)} \tag{2}$$

2. Carbonation of calcium hydroxide:

$$Ca(OH)_{2(s)} + H^+_{(aq)} + HCO_3^-{}_{(aq)} \leftrightarrow CaCO_{3(s)} + 2H_2O \tag{3}$$

$$CSH_{(s)} + H^+_{(aq)} + HCO_3^-{}_{(aq)} \leftrightarrow CaCO_{3(s)} + H_2O + SiO_2 \tag{4}$$
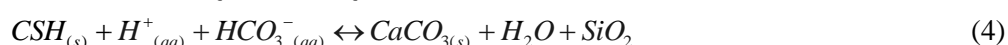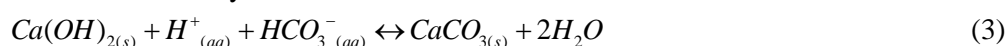
3. Dissolution of calcium carbonate:

$$CaCO_{3(s)} + CO_{2(aq)} + H_2O \leftrightarrow Ca(HCO_3)_2 \tag{5}$$

$$Ca(HCO_3)_2 + Ca(OH)_{2(s)} \leftrightarrow 2CaCO_{3(s)} + H_2O \tag{6}$$
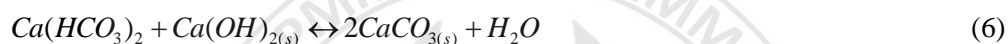
RESULTS

The experimental results in this study are shown from Figures 1 to 11:
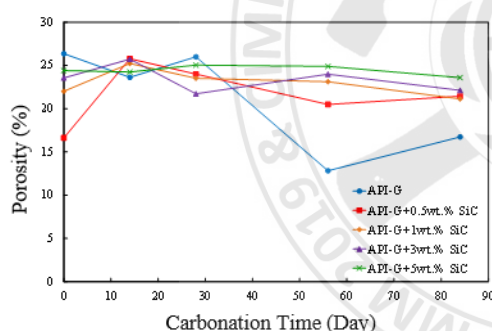
Figure 1. Porosity versus time
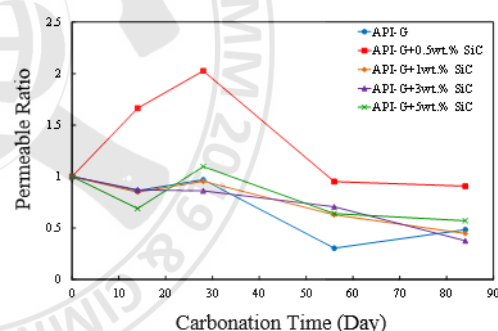
Figure 2. Water permeability ratio versus time
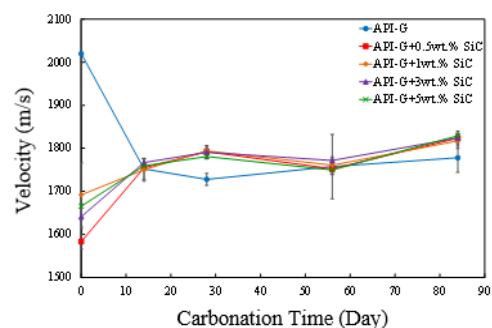
Figure 3. Longitudinal velocity versus time
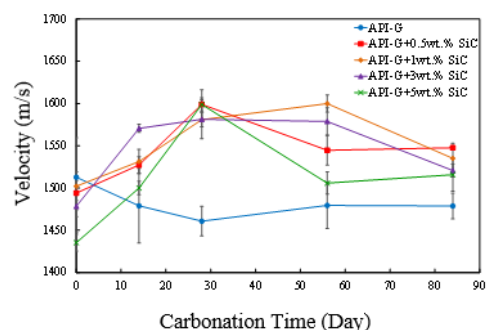
Figure 4. Transverse velocity versus time
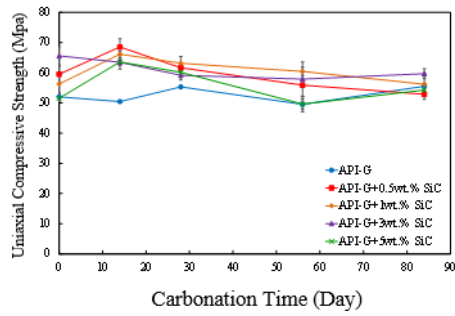
Figure 5. Uniaxial compressive strength versus time
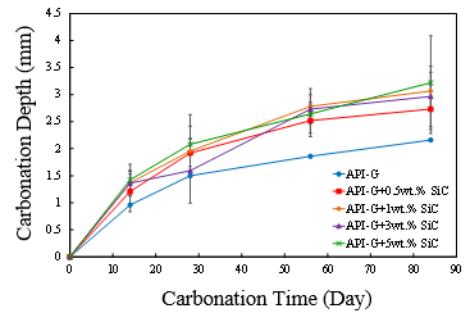
Figure 6. Carbonation depth versus time

(a) Before carbonation

(b) After carbonation

Carbonation zone
Transition zone
Non-carbonated zone
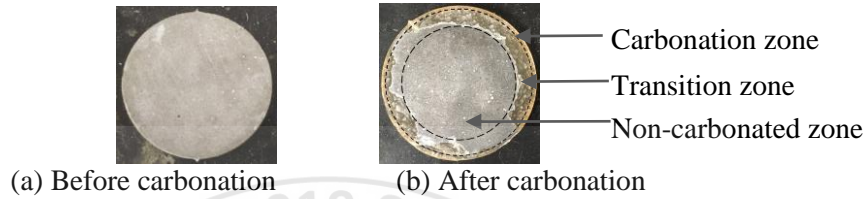
Figure 7. Three regions of cement section for analysis

(a) Before carbonation

(b) After carbonation

● Aragonite, $CaCO_3$ ■ Portlandite, $Ca(OH)_2$ ⊗ SiC
○ Calcite, $CaCO_3$ ▲ C-H-S

Figure 8.   XRD analysis

(a) Carbonation region

(b) Transition region

(c) Non-carbonation region
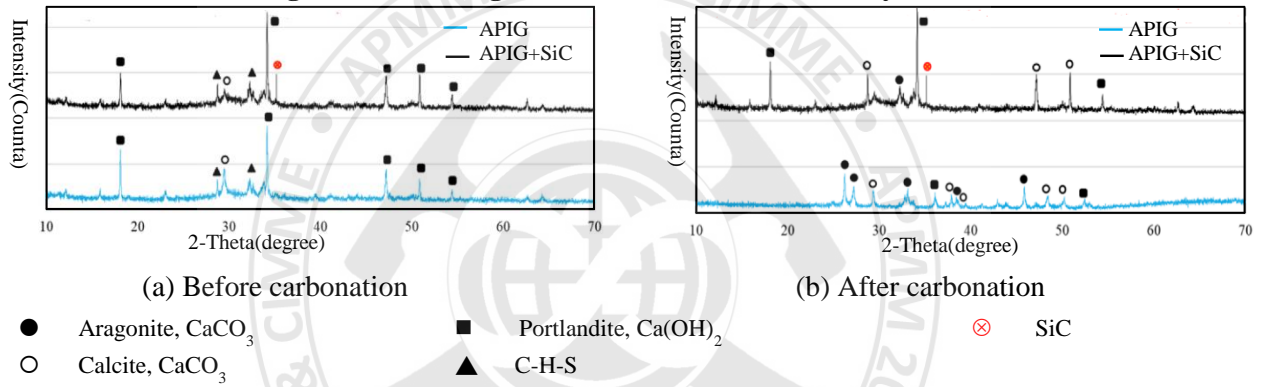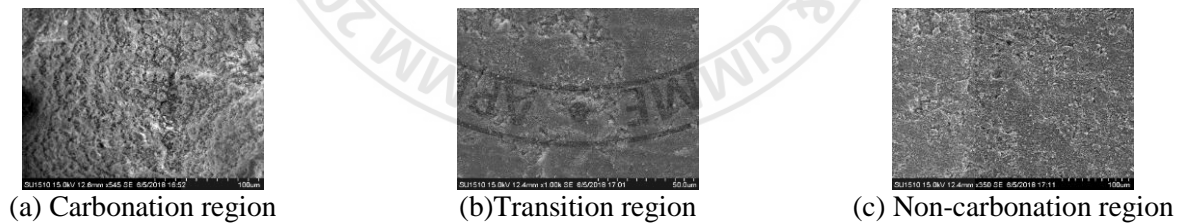
Figure 9. SEM analysis of API-G cement with 3 weight % SiC
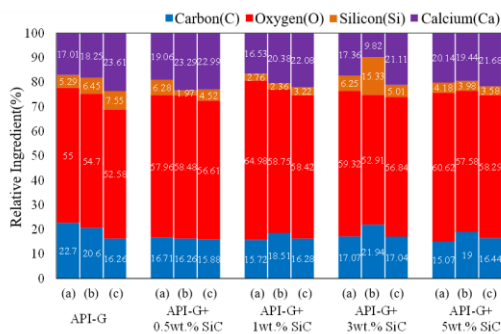
Figure 10. EDS analysis
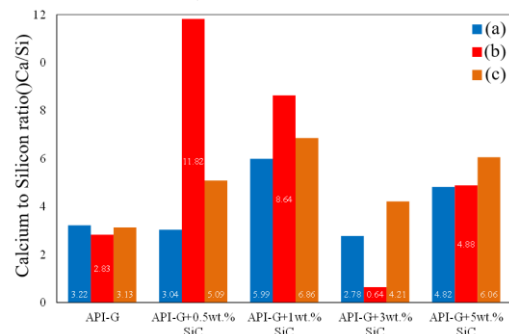
Figure 11. Calcium to silicon ratio

(a) Carbonation zone (b) Transition zone (c) Un-carbonated zone

CONCLUSIONS

1.   After 84 days of reaction, the permeable ratio of API-G cement+3wt.% SiC decreased most.

2.   After 84 days of reaction, the uniaxial compressive strength of API-G cement+3wt. % SiC is the most favorable and its value is higher than that of pure API-G cement by 7.51%.

3.   XRD analysis shows that before the reaction, the API-G cement is mainly composed of calcium hydroxide (Portlandite) and calcium citrate hydrate (C-H-S); after the reaction, a large amount of aragonite and calcite is observed in the specimen.

4.   From SEM analysis, the API-G cement with 3 weight % SiC or more has been able to sustain the crystal structure of calcium hydroxide and calcium citrate hydrate. The overall compactness of API-G cement with 3 weight % SiC is relatively high. It is presumed that the crystals of silicon carbide and calcium carbonate can effectively fill the voids in the cement matrices. As a result, the porosity decreases and the strength increases.

5.   Based upon EDS analysis, the ratio of calcium to silicon in cement with 3 weight % SiC significantly decreases because the voids are filled by more white tiny silicon crystals and calcium carbonates which make the material structure denser.

   This study concludes that the API-G cement with 3 weight percent of silicon carbide provides the most favorable results in the proposed experiments.

REFERENCES

Onan, D. D. (1984) ″Effects of supercritical carbon dioxide on well cements,″ Society of Petroleum Engineers ．SPE-12593-MS.

Kutchko, B. G., B. R. Strazisar, D. A. Dzombak, G. V. Lowry, N. Thaulow (2007). "Degradation of well cement by CO2 under geologic sequestration conditions," Environmental Science and Technology ,Volume 41 (13), Pages 4787-4792.

Duguid, A. (2008) "The effect of carbonic acid on well cements as identified through lab and field studies," Society of Petroleum Engineers, SPE-119504-MS.

Hsieh, H. T. (2016) A Study of the Mechanical, Physical and Chemical Properties of API G Well Cement with Silicon carbide Admixtures Exposed to Supercritical CO2 Environment, Master Dissertations, Department of Resources Engineering, National Cheng Kung University, Tainan, Taiwan.

Lin, T. Y. (2017) "A Study of the Mechanical, Physical and Chemical Properties of API G well Cement with CaO and Different SiO2 Admixtures Exposed to Supercritical CO2 Environment," Master Dissertations, Department of Resources Engineering, National Cheng Kung University, Tainan, Taiwan.

Xu, Z. H. (2018) "A Study of the Basic Properties of API-G Well Cement With Silicon Carbide Admixtures Exposed to Supercritical CO2 Environment," Master Dissertations, Department of Resources Engineering, National Cheng Kung University, Tainan, Taiwan.

Geochemistry of magnetite from sand beaches, rivers and the surrounding rocks at north Taiwan

Eslam Mohammed Ali Mitwally and Bing-Sheng Yu

Institute of Mineral Resources Engineering, National Taipei University of Technology, Taiwan.

Islam_mohammed4@yahoo.com or t107799401@ntut.org.tw, bing@ntut.edu.tw*)*

ABSTRACT

Magnetite forms under a wide variety of conditions, crystallizing at high temperature from silicate and sulfide melts or precipitating at lower temperatures from hydrothermal fluids. Due to a large number of minor and trace element substitutions into magnetite, these different conditions lead to distinctive trace element signatures in magnetite. Moreover, the compositional average of the studied magnetite beach and river samples is significantly similar to magnetite composition at andesite rocks of Dare et al. (2014), which reveal that these studied magnetite samples may have come from surrounding andesite rocks. According to high concentration of Ti and Al at magnetite attribute to the temperature of magnetite forming at this study is $700^{o}C$. According to Fe positive correlation with Ti, Cr and Ni, and a negative correlation with Mg, Mn and Zn. This may attribute to there is large verity at magnetite series at the study area. Due to a positive correlation of V, Co, Mo, Nb, Ga, Sn and Ta with Fe and a negative correlation with Al, this attribute to enrichment of these elements on magnetite series, and Ca, Li, Sc, Cu, As, Rb, Sr, Y, Cd, Sb, Sc, Ba, La, Ce, Pr, Nd, Sm, Eu, Gd, Dy, Ho, Er, Yb, Pb, U and Th show a negative correlation with Fe and a positive correlation with Al, this attribute to enrichment of these elements on spinel series. REEs as mentioned show a negative correlated with Fe and a positive correlated with Al, and enriched on spinel series.

This research has not been completed yet and there are other analyzes of rock and river samples we do it at this moment, and this paper is the first paper of magnetite at Taiwan.

INTRODUCTION

A number of elements commonly substitute into the spinel supergroup minerals: Fe, Al, Ti, Mg, Mn, Zn, Cr, V, Ni, Co, and Ga. We refer to these elements as spinel elements. Due to their common occurrence in spinel group minerals, these are often the most useful indicator elements to potentially distinguish magnetite from different sources (Rusk et al., 2009). Dupuis and Beaudoin (2011) demonstrate that Ni/(Cr + Mn) vs. Ti + V and Ca + Al + Al vs. Ti + V diagrams can be useful to discriminate magnetite from various mineral deposits. Dare et al. (2014) presented a coherent

explanation for the behavior of trace element partitioning in magnetite during crystallization from silicate melts and hydrothermal fluids in a variety of ore deposits. This new diagram could be applied to petrogenetic and provenance studies, in particular in the exploration of ore deposits as well as show how hydrothermal magnetite is distinct from that in igneous rocks based on the covariation of Ti, Ni and Cr. The study area extends over a length of 135 km and located at north Taiwan between longitude 120° 52' 24.1" and 122° 05' 51.88" E, and latitude 24° 45' 26.07" and 25° 22' 14.45" N (**Fig. 1**). Our primary purpose is to apply magnetite trace element chemistry by using ICP-Ms, ICP-AES and LA-ICP-MS to obtain trace elemental compositions of the magnetite from the various type magnetite sources such as sand beach, river deposits and rocks to provide a better understanding of the compositions of magnetite forming fluids and processes responsible for Fe. We also compare the composition of magnetite from the hard rocks with sand beach and river deposits, determine the provenance of magnetite by (1) different discrimination diagrams, and (2) detect the relationships between the different trace elements.

SAMPLING COLLECTION

The study samples were collected from different places in the northern part of Taiwan (Fig. 1A). About 23 samples were taken from different sites (8 samples from the river streams, 8 samples from the hard rocks around the river streams, and 7 samples from the beach sand), of the beach sand and river streams samples were collected by a hand high-magnet at the rate of metal attraction.

ANALYTICAL METHODS
MEASURING MICROSCOPE

A Measuring Microscope (Olympus STM7-SFA) with dimensions (W x D x H) mm (606 x 762 x 811), equipped with 100 mm x 100 mm stage, vertical movement range 175 mm, maximum measurable height 120 mm, LED illumination, LED unit white color (Reflected) (MM6-ILW) and green color (Transmitted) (MM6-ILG), observation tube (MM6-ETR-1-5 Erect image trinocular tube (100:0/0:100)), eyepiece (F.N.22) (MM6-OCC10X (with cross hairs) , MM6-OC10X), measuring range (X-axis 200 mm, Y-axis 200 mm), minimum resolution (0.1 um). This measuring microscope attached with PC, with these requirements, CPU Intel (Core i3 Processors 3 GHz or more), memory (4 GB or more), HD available space (100 GB or more hard disk space for installation SSD hard disk is recommended for high speed image acquisition), Graphic card available for resolution 1980 x 1080 and 32 bit color, Operating system (Microsoft Windows 10 Pro (32 bit / 64 bit) at National Taipei University of technology.

XRD DIFFRACTION

Also the purity of magnetite grains was tested by X-ray diffraction study (Fig. 2) (using Rigaku D/Max 2200, scintillation counter (scintillator Nal photomultiplier with preamp., rated output (2200v, 3kW), Cu-target tube and Ni filter at 40 kV and 30 mA, Start angle 5°, stope angle 70°, scan speed 2.00°/min. This instrument is connected to a computer system using X-40 diffraction program and ASTM cards for mineral identification in XRD laboratory at National Taipei University of technology.

ICP-MS

Trace element concentrations were determined by inductively coupled plasma mass spectrometer (ICP-MS) at Canada-Vancouver lab, Mineral laboratories, Bureau Veritas Commodities Canada Ltd. The samples subjected to extra wash with silica between each sample, pulverize to 85% passing 200 mesh, powdered splits (0.25 g) were dissolved by using 4 acid digestion ultra-trace ICP-MS analysis (A 0.25 g split is heated in HNO_3, $HClO_4$ and HF to fuming and taken to dryness) in tightly sealed 25 ml Teflon PFA screw-cap beakers, heated for 1 day on a hot plate at 130°C. The decomposed sample was progressively evaporated at 120°C for 24 hours, 160°C for 6 hours and 190°C until dryness. Subsequently, aqua regia was added to the residues, heated at 130°C for 12 hours and then evaporated. The residue was dissolved with 5 ml in HCl and the solution was diluted to 100 ml total volume.
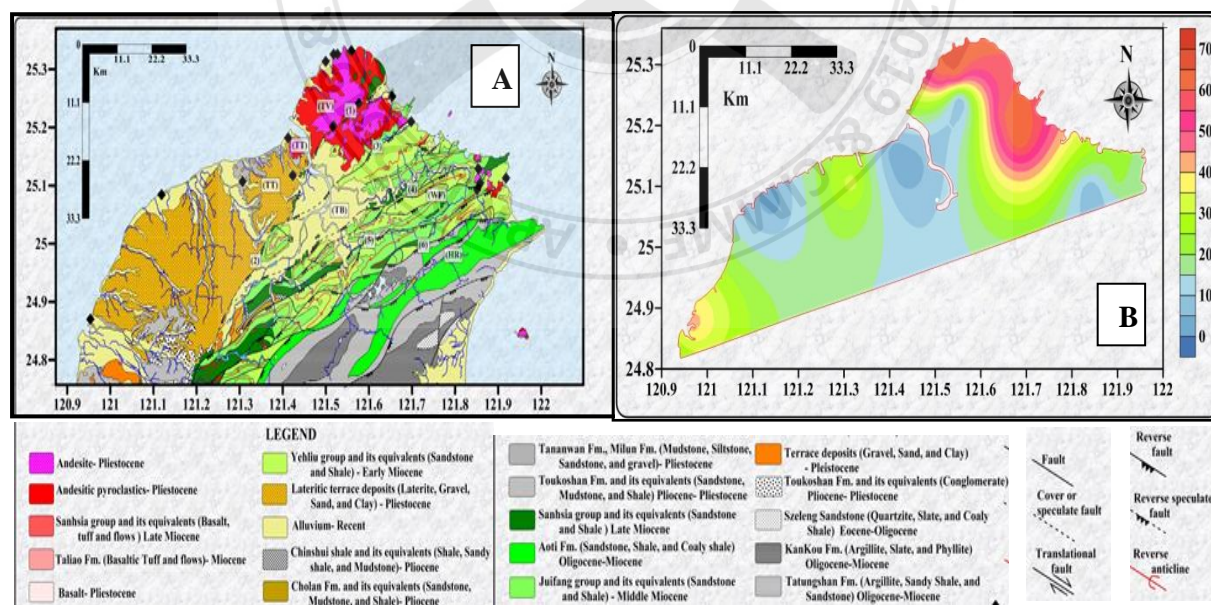

Figure 1. shows the geological and location map of the study area (A) and magnetite distribution map at north Taiwan (B).

RESULTS

By using the ratio of magnetite at beach and river samples, we made distribution map of magnetite at north Taiwan (Fig.1B). Magnetite concentrations are increasing in the far north of Taiwan, especially in each of the areas of Wanli, Fengyu, Laomei, White Sand Bay Creek, White Sand Bay beach and Xinzhuangzi, and decreasing in the north-east direction to become less concentrated in the region Longdong Bay, Keelung Mountain, Wudan shan and ChinKuashih Penshan Geological Park Creek, as well as decreases in the northwest direction towards the regions Near Qingshan Waterfall, Cai Gongkeng creek, Bianshan Fuan Palace creek and Shisan hun to become less concentrated in the region Bianshan Fuan Palace creek. Then gradually increases to become the average concentration in the region Linkou Creek, then decreases in the direction of the region Guanyin to become less concentrated, and then increase again to become relatively higher concentration in the region Crescent Beach.

The ICP-MS analysis of magnetite mineral from beach sand and some of river sample are presented in Table 1. The concentrations of elements in magnesites contain Fe ranging from >60 to 53.240 wt.%, Ti (5.873-3.633 wt.%), Al (2.220-1.330 wt.%), Mg (1.990-0.820 wt.%), V (4740-3162 ppm), Cr (1466-70 ppm), Mn (4277-3139 ppm), Zn (784.9-523.8 ppm), Ga (60.52-46.06 ppm), Sr (64-11 ppm), Zr (80.10-22.50 ppm), Nb (62.55-11.19 ppm), Mo (16.69-2.85 ppm), Sn (16.40-4.40 ppm), Ba (128-23 ppm), La (16.50-3.90 ppm), Ce (38.38-8.99 ppm), Pr (4.70-0.90 ppm), Nd (17.60-2.60 ppm), Sm (3.80-0.60 ppm), Eu (0.90-0.20 ppm), Gd (3.50-0.60 ppm), Tb (0.60-<0.1 ppm), Dy (2.70-0.50 ppm), Ho (0.50-0.10 ppm), Er (1.20-0.30 ppm), Yb (1.30-0.40 ppm), Hf (2.21-1.04 ppm), Ta (4.00-0.40 ppm), W (2.70-0.90 ppm), Pb (72.92-11.98 ppm), Th (5.20-1.10 ppm) and U (1.70-0.80 ppm). Moreover, the compositional average of the studied magnetite beach and river samples is compared with the world's average (Table 2), and we noted that these samples are significantly similar in Ti, Al, Mg, Sc, V, Cr, Mn, Co, Ga, Nb, Hf and Ni/Cr of magnetite at andesite rocks of Dare et al. (2014), which reveal that these studied magnetite samples may have come from surrounding andesite rocks.

Plot of Ti (ppm) versus Ni/Cr ratio (un-normalized) in magnetite to distinguish magmatic and hydrothermal setting (Fig. 3A), show that all samples plot in the magmatic field. In the Ni/(Cr+Mn) vs Ti+V and Ca+Al+Mn vs. Ti+V discriminant diagrams of Dupuis and Beaudoin (2011) as shown in (Fig. 3B and C) which detect type of the magnetite environments; Kiruna, IOCG, porphyry Cu, Fe-Ti-V, and BIF. Figures (3B and C) show that all samples plot in the Fe-Ti, V field.
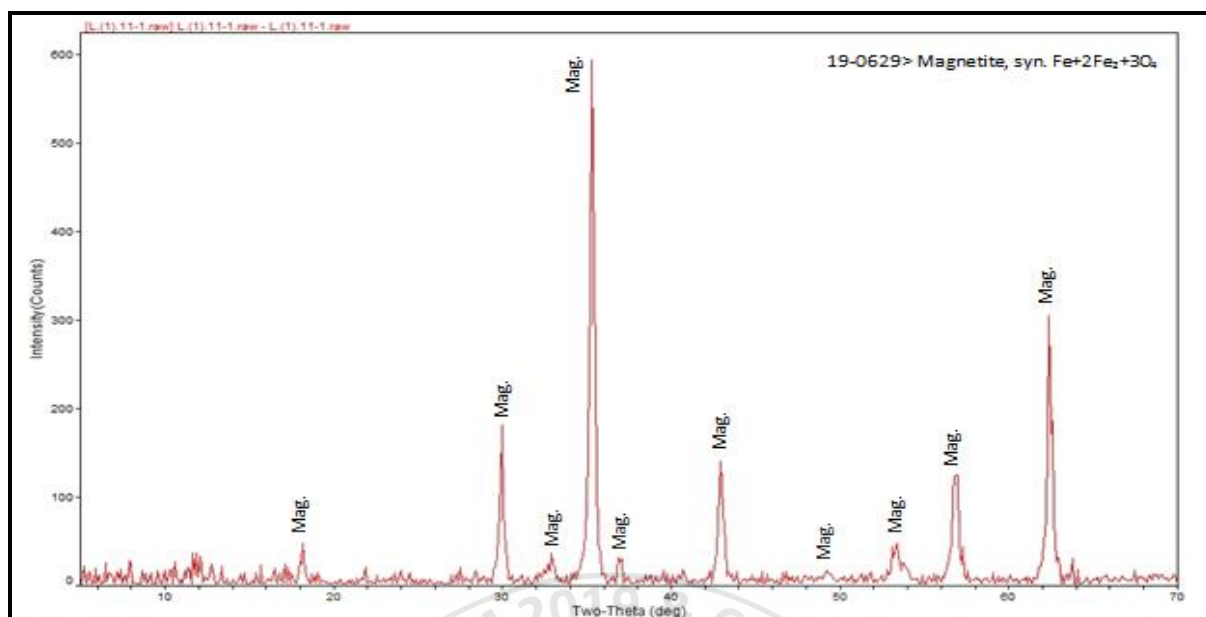
Figure 2. showing XRD patterns of magnetite at beach sand and some rivers.

Of most the trace elements, Al, Ti, V and Mn are consistently in highest concentrations in magmatic magnetite. The high standard deviations of the mean of analyses show that there is considerable variation within samples for many trace elements (Table 1). Al shows a negative correlation with Fe. Fe shows a positive correlation with Ti, Ni, Cr, V, Co, Mo, Nb, Ga, Sn and Ta, and these elements show a negative correlation with Al. On the other hand, Mg, Ca, Li, Sc, Mn, Cu, Zn, As, Rb, Sr, Y, Cd, Sb, Cs, Ba, La, Ce, Pr, Nd, Sm, Eu, Gd, Dy, Ho, Er, Yb, Pb, U and Th show a negative with Fe and a positive correlation with Al (Table 3). Elements that show significant variation in magmatic magnetite within and between localities are summarized in plots of medians and quartiles (Figs. 3D,E,F,G and H). The Ti level at the study samples (Table 5 and Fig. 3D) is 36330 ppm as minimum value and 58730 ppm as maximum value with median value 40695 ppm, lower quartile 39377.5 ppm and upper quartile 42787.5 ppm, and most Ti at this study of samples confine between lower and upper quartile approach to minimum value. The Al level at the study samples (Table 5 and Fig. 3D) is 13300 ppm as minimum value and 22200 ppm as maximum value with median value 17450 ppm, lower quartile 16700 ppm and upper quartile 19500 ppm, and Al confine between lower and upper quartile and mediates the minimum and the maximum value. Mg and Ca as Al mediate the minimum and the maximum value and there is no large variation between the study samples (Fig. 3D). Other elements (Table 4) arranged at 6 groups depending on the variation range; (1) V, Cr and Mn (variation range between 1138-1578 ppm), (2) Ni and Cu (variation range between 124-140.4 ppm), (3) Ce, Co and Nb (variation range between 29.39-51.36 ppm), (4) Ga, Mo, La, Sn and Nd (variation range between 12.6-18.4 ppm), (5) Pr, Sm, Gd, and Dy (variation range between 2.2-3.8 ppm), and (6) Eu, Tb, Ho, Er, Tm and Yb (variation range between 0.1-0.9 ppm) (Fig. 3E,F,G and H).

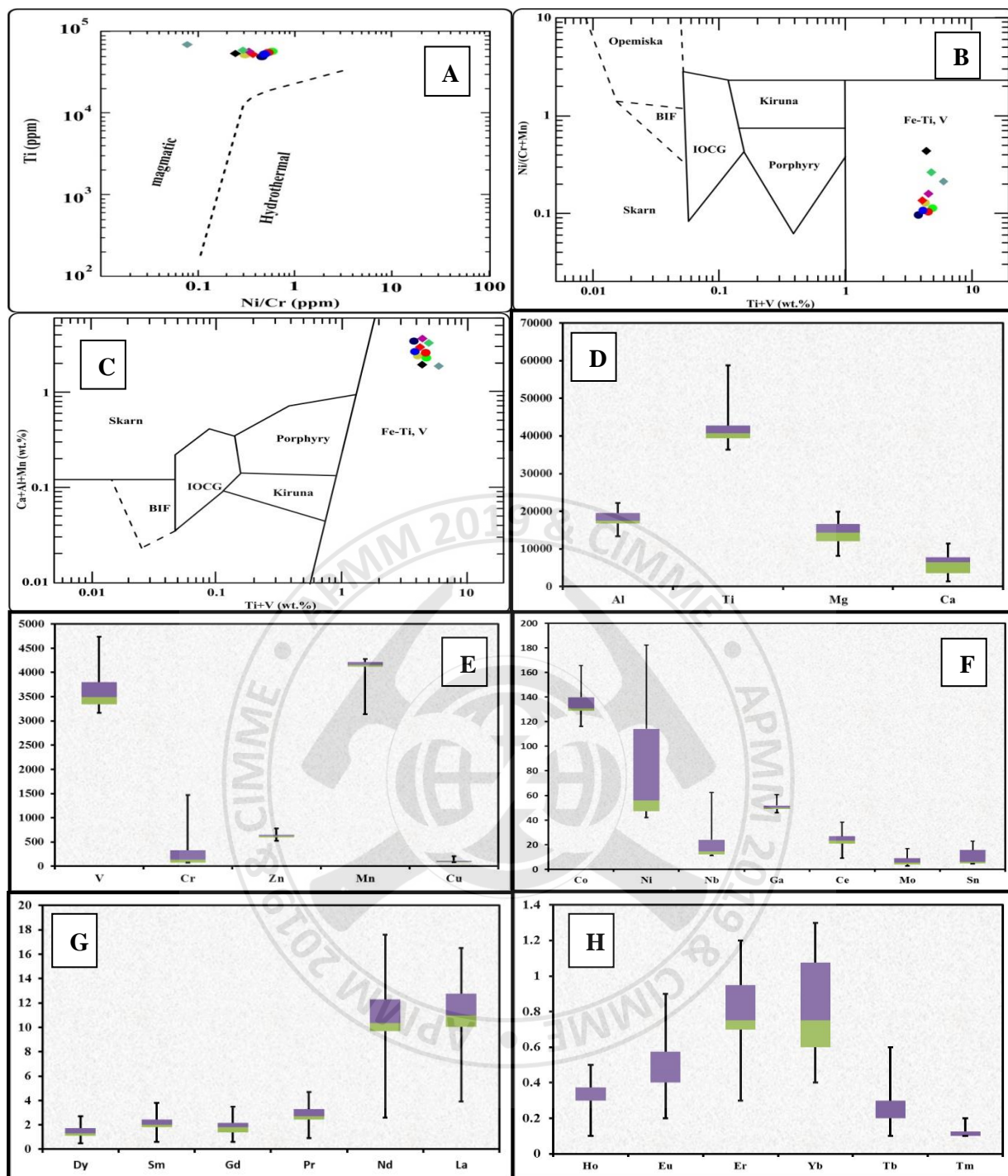Figure 3. Ni/Cr vs Ti diagram (Dare et al., 2014) (A), Ni/(Cr+Mn)   and Ca+Al+Mn vs. Ti+V

discriminant diagram to determine type of the magnetite environments (Dupuis and Beaudoin, 2011)

(B and C), Box-and-whisker plots of Al, Ti, Mg, and Ca in magnetite (D), of V, Cr, Zn, Mn, and Cu

(E), of Co, Ni, Nb, Ga, Ce, Mo and Sn (F), of Dy, Sm, Gd, Pr, Nd and La (G), and of Ho, Eu, Er, Yb,

Tb and Tm (H).

Table 1: shows the trace and rare element concentrations of magnetite analyzed by ICP-MS.

Sample No.		K.M.3 ◆	G.(6).4 ◆	L.C.6 ◆	W.5 ◆	S.h.8 ◆	F.(3).9 ●	L.(1).11 ●	W.S.B.C.12 ●	X.n.(2).13 ●	W.S.B.14 ●	Av.	St. dev.
MDL							Wt.%						
Ti	0.001	4.014	4.626	5.873	3.918	4.278	3.997	3.633	4.279	3.910	4.125	4.265	0.63
Al	0.01	1.540	2.220	1.330	1.750	2.190	1.740	1.990	1.830	1.660	1.700	1.795	0.28
Fe	0.01	>60.0	53.240	58.340	57.940	50.220	58.470	54.040	57.930	55.390	58.200	55.97	17.9
Mg	0.01	0.970	1.700	0.820	1.500	1.990	1.200	1.760	1.200	1.530	1.370	1.404	0.36
Ca	0.01	0.140	0.800	0.160	0.650	1.100	0.490	1.140	0.310	0.710	0.630	0.613	0.35
Na	0.00	0.038	0.228	0.025	0.053	0.213	0.061	0.101	0.027	0.047	0.043	0.084	0.08
K	0.01	0.110	0.170	0.050	0.060	0.180	0.080	0.100	0.030	0.050	0.050	0.088	0.05
P	0.00	0.039	0.124	0.058	0.165	0.150	0.153	0.231	0.081	0.157	0.132	0.129	0.06
S	0.04	<0.04	0.040	<0.04	<0.04	<0.04	<0.04	<0.04	<0.04	<0.04	<0.04	0.04	0.01
							Ppm						
Li	0.10	6.30	10.50	2.60	5.30	10.00	9.50	4.40	2.50	4.70	4.30	6.010	2.98
Be	1.00	<1	<1	<1	<1	<1	<1	<1	<1	<1	<1		0.00
Sc	0.10	15.80	28.30	15.50	19.50	26.30	17.50	20.60	19.40	19.60	18.80	20.13	4.15
V	1.00	4740	3352	3162	3854	3336	3961	3285	3636	3417	3575	3631.8	464
Cr	1.00	645.0	376.0	1466	137.0	183.0	142.0	74.00	70.00	80.00	75.00	324.8	440
Mn	1.00	3139	4215	4277	4136	4117	3826	4227	4143	4170	4216	4046.6	342
Co	0.20	165.5	141.8	116.0	141.5	128.3	130.4	124.6	130.6	134.8	130.9	134.44	13.3
Ni	0.10	182.3	128.6	130.2	59.10	70.80	52.60	41.90	48.20	46.80	46.30	80.68	48.7
Cu	0.10	88.50	206.0	89.90	110.3	88.60	124.7	81.60	84.70	81.90	100.1	105.63	37.9
Zn	0.20	523.8	784.9	564.7	598.5	631.0	682.2	598.6	650.8	617.4	641.9	629.4	70.7
Ga	0.02	60.52	46.46	48.94	50.13	46.06	52.54	49.57	51.50	51.93	49.95	50.76	4.04
As	0.20	7.50	25.90	9.00	7.50	24.60	16.10	11.40	6.90	14.10	15.10	13.81	6.88
Se	0.30	<0.3	<0.3	<0.3	<0.3	<0.3	<0.3	<0.3	<0.3	<0.3	<0.3		0.00
Rb	0.10	8.20	10.20	3.00	4.40	11.10	5.50	6.60	2.60	3.60	3.60	5.88	3.05
Sr	1.00	11.00	50.00	13.00	20.00	64.00	19.00	46.00	14.00	23.00	24.00	28.4	18.3
Y	0.10	2.50	11.60	7.70	7.00	12.70	6.20	9.30	4.50	7.00	6.40	7.49	3.06
Zr	0.20	22.50	79.00	80.10	38.10	63.20	46.70	38.50	41.50	39.20	41.50	49.03	18.9
Nb	0.04	23.12	31.79	62.55	11.19	24.32	14.90	11.84	11.84	12.74	14.01	21.83	15.9
Mo	0.05	16.69	10.25	9.75	6.88	4.22	6.01	4.01	2.85	3.54	5.14	6.934	4.25
Cd	0.02	0.08	0.13	0.10	0.09	0.12	0.10	0.08	0.08	0.06	0.08	0.092	0.02
Sn	0.10	17.70	16.40	22.80	5.70	13.30	6.30	4.40	5.30	4.80	4.80	10.15	6.79
Sb	0.02	1.55	3.73	1.85	1.07	1.52	0.88	0.71	0.70	0.78	1.01	1.38	0.92
Te	0.05	<0.05	0.08	<0.05	<0.05	0.07	0.06	<0.05	<0.05	<0.05	0.07	0.07	0.04
Cs	0.10	1.00	0.90	0.20	0.50	0.80	0.60	0.60	0.30	0.30	0.30	0.55	0.28
Ba	1.00	128.0	85.00	54.00	38.00	91.00	36.00	48.00	40.00	23.00	26.00	56.9	33.8
La	0.10	3.90	16.50	11.10	11.20	15.30	10.50	13.30	9.10	10.80	9.90	11.16	3.49
Ce	0.02	8.99	38.38	24.73	22.77	31.43	20.68	27.61	20.86	23.95	21.42	24.08	7.67
Pr	0.10	0.90	4.70	2.90	2.70	3.90	2.60	3.40	2.20	2.70	2.40	2.84	1.02
Nd	0.10	2.60	17.60	10.30	10.40	14.80	9.60	12.80	8.40	10.70	9.90	10.71	3.97

Sm	0.10	0.60	3.80	2.30	2.00	3.10	1.80	2.50	1.40	2.00	1.90	2.14	0.88
Eu	0.10	0.20	0.90	0.50	0.30	0.90	0.40	0.60	0.40	0.40	0.40	0.5	0.24
Gd	0.10	0.60	3.50	1.90	1.70	2.80	1.30	2.20	1.20	1.60	2.00	1.88	0.83
Tb	0.10	<0.1	0.60	0.20	0.20	0.40	0.20	0.30	0.10	0.20	0.20	0.267	0.16
Dy	0.10	0.50	2.70	1.30	1.20	2.70	1.10	1.80	0.90	1.50	1.30	1.5	0.72
Ho	0.10	0.10	0.50	0.30	0.30	0.40	0.30	0.40	0.20	0.30	0.30	0.31	0.11
Er	0.10	0.30	1.20	0.70	0.80	1.10	0.70	1.00	0.50	0.70	0.80	0.78	0.27
Tm	0.10	<0.1	0.20	0.10	0.10	0.20	0.10	0.10	<0.1	0.10	0.10	0.125	0.07
Yb	0.10	0.40	1.30	1.00	0.70	1.10	0.60	1.10	0.50	0.80	0.60	0.81	0.30
Lu	0.10	<0.1	0.20	0.20	0.10	0.20	<0.1	0.10	<0.1	0.10	<0.1	0.15	0.09
HF	0.02	1.04	2.21	2.20	1.14	1.85	1.52	1.23	1.19	1.19	1.30	1.49	0.44
Ta	0.10	1.70	1.50	4.00	0.40	1.20	0.60	0.40	0.40	0.50	0.50	1.12	1.12
W	0.10	2.30	2.70	2.50	1.30	1.50	1.10	1.00	0.90	0.90	0.90	1.51	0.72
Re	0.00	0.00	0.00	0.00	<0.002	0.00	<0.002	<0.002	<0.002	0.00	<0.002	0.00	0.00
Tl	0.05	0.06	0.08	<0.05	<0.05	0.06	0.05	<0.05	<0.05	<0.05	<0.05	0.062	0.03
Pb	0.02	11.98	72.92	21.39	18.73	53.28	29.67	17.44	24.55	23.79	35.59	30.93	18.7
Th	0.10	1.10	5.20	3.00	1.60	3.80	2.00	2.10	2.10	1.80	2.20	2.49	1.21
U	0.10	0.80	1.70	0.80	1.00	1.40	1.40	1.00	1.10	0.90	1.00	1.11	0.30
						ppb							
Ag	20	61	85	<20	34	<20	45	<20	41	37	21	46.28	28.1

Table 2: shows the comparison of trace and rare element concentrations of magnetite analyzed by ICP-MS and ICP-AES with world magnetite analyses.

Reference for sample locations	This study	Barnes et al. (2004)	Barnes et al. (2004); Tollari et al. (2008); Nabil (2003); Martin-Tanguay (2012); Méric (2011)	Dare et al. (2014)	Grigsby (1990); Razjigaeva and Naumova (1992); Audetat and Pettke (2006); Chiaradia et al. (2011)	Sawyer (2010)
location	North Taiwan	Bushveld Complex, South Africa	Bushveld Complex; Sept Iles, Canada; St. Charles de Bourget, Canadab	Lascar and El Laco stratovolcanoes, Northern Chile	Compilation from the literature	Opatica Subprovince, Canada
Description	Beach and some river magnetite	Massive magnetite, lowermost seams of the Upper Zone	Massive magnetite and massive nelsonite (mt + ap), uppermost seams of layered intrusions Anorthosite-hosted massive nelsonite dyke	Fresh calc alkaline lavas; glomerophenocrysts of magnetite, apatite, pyroxene, plagioclase, and trace ilmenite	Magnetite phenocrysts in basaltic andesite, andesite, trachyandesite	Accessory magnetite in Leucograno-diorite and leucotonalite protolith (orthogneiss)
Methods	ICP-Ms	ICP-AES	LA-ICP-Ms	LA-ICP-Ms		
Ti	4.265	1.295	6.7702	8.9789	5.6524	4.5445	0.0487
Al	1.795	-	1.3511	1.9638	1.5986	3.6145	0.0670
Mg	1.404	-	0.6569	0.9480	1.4718	2.7083	0.0039

Ca	0.613	-	0.0143	0.0024	0.0023	-	0.0039
Si	-	1.6	0.0514	0.0137	0.0490	-	0.0105
P	0.129	-	-	0.0014	0.0017	0.0099	n.a
Sc	20.13	-	34	25	26	-	1.3
V	3631.8	-	11201	3021	3291	4227	756
Cr	324.8	40.95	2916	139	586	364	212
Mn	4046.6	299.9	1853	3129	3008	1944	491
Co	134.44	32.61	212	144	213	106	35
Ni	80.68	-	489	42	308	184	34
Cu	105.63	-	43.5	3	49.5	151	12
Zn	629.4	54.63	471	710	803	1213	452
Ga	50.76	-	42	61	50	-	47
As	13.81	1.261	-	-	-	-	-
Sr	28.4	3.699	-	-	-	-	-
Y	7.49	0.355	0.43	0.09	0.17	-	n.a
Zr	28.4	-	12.5	35	55	-	1.26
Nb	7.49	16.94	1.19	4.28	10.20	-	0.17
Mo	6.934	-	0.67	3.61	0.92	-	0.41
Cd	0.092	1.436	-	-	-	-	-
Sn	10.15	27.26	1.36	2.95	5.74	-	4.25
Sb	1.38	0.110	-	-	-	-	-
Ba	56.9	1.614	-	-	-	-	-
La	11.16	0.575	-	-	-	-	-
Ce	24.08	9.360	-	-	-	-	-
Eu	0.5	0.108	-	-	-	-	-
Gd	1.88	8.006	-	-	-	-	-
Hf	1.49	-	0.59	1.40	1.53	-	0.16
Ta	1.12	-	0.10	0.24	0.57	-	0.04
W	1.51	2.741	0.12	0.08	0.09	-	0.43
Pt	-	67.61	-	-	-	-	-
Pb	30.93	37.85	1.29	0.41	0.41	-	1112
Bi	0.263	0.191	-	-	-	-	-
Ni/Cr	0.436	-	0.29	0.37	0.60	0.86	0.17

DISCUSSION

By using this diagram the studied samples plotted at magmatic field. By using these two diagrams of Dupuis and Beaudoin (2011), the studied samples plotted at Fe-Ti-V field. Magmatic magnetite that crystallized from high-temperature silicate melts, of intermediate composition, are from Fe-Ti-V-P deposits hosted in mafic-ultramafic layered intrusions (Bushveld Complex, S. Africa and Sept Iles, Canada) and massive type anorthosites (Lac St. Jean, Canada), magnetite in massive sulfide from Ni-Cuplatinum-group-element (PGE) deposits (e.g., Sudbury and Voisey's Bay, Canada) represent magnetite formed from magmatic sulfide liquid (Dare et al. 2012; Boutroy et al. 2014). So, the

magnetite at this study is similar to that at Fe-Ti-V-P deposits hosted in mafic-ultramafic layered intrusions (Bushveld Complex, S. Africa and Sept Iles, Canada).

Spinel is used as a petrogenetic mineral because its chemical composition is controlled by the environment in which it forms (Barnes and Roeder 2001). The spinel group minerals are divided in three series according to the trivalent cation): (1) the spinel series (Al3+), (2) the magnetite series (Fe3+), and (3) the chromite series (Cr3+). In the "magnetite series", magnetite (Fe2+Fe23+O4) forms a complete solid solution with magnesioferrite (MgFe2O4) and ulvöspinel (Fe2TiO4), also known as titanomagnetite (Deer et al. 1992). Temperature-dependent exchange of Fe2++Ti4+ for 2 Fe3+ between titanomagnetite and the ilmenite–hematite solid solution, and iron redox equilibrium between magnetite, ilmenite, and ulvöspinel, are the basis for the Fe-Ti thermo-oxybarometer (Buddington and Lindsley 1964; Sauerzapf et al. 2008). Magnetite displays partial solid solutions with franklinite (ZnFe2O4), jacobsite (MnFe2O4), and trevorite (NiFe2O4). Vanadium (V3+), calcium (Ca2+), and cobalt (Co2+) are also known to substitute widely in the magnetite structure. Complete solid solution of the trivalent cation (Cr3+) with chromite (FeCr2O4) and magnesiochromite (MgCr2O4) forms the "chromite series". Of the four "spinel series" end-members spinel sensustricto (MgAl2O4), hercynite (FeAl2O4), gahnite (ZnAl2O4) and galaxite (MnAl2O4), magnetite displays partial solid solution with hercynite only. Hematite (Fe2O3) forms a complete solid solution with ilmenite (FeTiO3) at high temperature (above 1,050°C), and limited solid solution with magnetite (Fe3O4), corundum (Al2O3), and bixbyite (Mn2O3) (Deer et al. 1992). Hematite replacement of magnetite is termed "martite" whereas replacement of hematite by magnetite is widely referred to as "mushketovite". The high average concentrations of some elements (Table 1) as Al, Ti, Mg, Cr, Ni, Mn and Zn may be result from: (1) substitution of Fe3+2 by Al3+2 at magnetite as show at hercynite (FeAl2O4), gahnite (ZnAl2O4), corundum (Al2O3), spinel (MgAl2O4) and galaxite (MnAl2O4). (2) Depletion of Fe3+2 at hematite and then incorporated Ti4+ at the hematite structure as ulvöspinel, or Fe3+2 substituted by Ti4+ as ilmenite. (3) Substitution of Fe2+ by Mg2+ at magnetite as show at magnesiochromite (MgCr2O4) and magnesioferrite (MgFe2O4). (4) Substitution of Fe3+2 by Cr4+ at magnetite as show at magnesiochromite (MgCr2O4) and chromite (FeCr2O4). (5) Substitution of Fe2+ by Ni2+ at magnetite as show at trevorite (NiFe2O4). (6) Substitution of Fe2+ by Mn2+ as show at galaxite (MnAl2O4) and jacobsite (MnFe2O4), and Fe3+2 by Mn3+2 as bixbyite (Mn2O3). (7) Substitution of Fe2+ by Zn2+ as show at gahnite (ZnAl2O4) and franklinite (ZnFe2O4).

Titanium is a common element in magnetite, entering as a coupled substitution 2Fe3+ = Ti4++Fe2+ favoured at high temperature in ulvöspinel-magnetite solid solutions (Buddington and Lindsley, 1964).

Titanium is very insoluble in fluids (Mysen, 2012) and its concentrations in magnetite from magma composition are also likely controlled solely by temperature.

Table 3: Correlation matrix of the studied beach and some rivers magnetite.

Relation	X	Y	r	Relation	X	Y	r
Positive correlation	Ti	Fe	0.09	Negative correlation	Ti	Al	-0.36
	Fe	Ni	0.22		Al	Ni	-0.25
		Cr	0.28			Cr	-0.57
		V	0.61			V	-0.31
		Co	0.28			Co	-0.02
		Mo	0.39			Mo	-0.33
		Nb	0.02			Nb	-0.34
		Ga	0.71			Ga	-0.57
		Sn	0.00			Sn	-0.21
		Ta	0.13			Ta	-0.45
Negative correlation	Fe	Mg	-0.89	Positive correlation	Al	Mg	0.88
		Ca	-0.85			Ca	0.79
		Li	-0.51			Li	0.64
		Sc	-0.87			Sc	0.93
		Mn	-0.45			Mn	0.28
		Cu	-0.21			Cu	0.47
		Zn	-0.41			Zn	0.67
		As	-0.77			As	0.73
		Rb	-0.65			Rb	0.70
		Sr	-0.96			Sr	0.88
		Y	-0.91			Y	0.72
		Cd	-0.50			Cd	0.55
		Sb	-0.31			Sb	0.35
		Cs	-0.31			Cs	0.51
		Ba	-0.16			Ba	0.19
		La	-0.84			La	0.73
		Ce	-0.81			Ce	0.71
		Pr	-0.82			Pr	0.73
		Nd	-0.82			Nd	0.74
		Sm	-0.81			Sm	0.69
		Eu	-0.90			Eu	0.78
		Gd	-0.80			Gd	0.72
		Dy	-0.94			Dy	0.79
		Ho	-0.78			Ho	0.70
		Er	-0.83			Er	0.76
		Yb	-0.80			Yb	0.57
		Pb	-0.66			Pb	0.73
		U	-0.68			U	0.81
		Th	-0.58			Th	0.63
				Negative	Al	Fe	-0.82

Table 4: Minimum, Lower quartile, Median, Upper quartile, Maximum values of some elements at the studied beach and some rivers magnetite.

	Minimum	Lower quartile	Median	Upper quartile	Maximum	Variation range
Ti	36330	39377.5	40695	42787.5	58730	22400
Al	13300	16700	17450	19500	22200	8900
Mg	8200	3800	2350	2225	3325	11700
Ca	1400	2150	2850	1375	3625	10000
V	3162	3340	3496	3799.5	4740	1578
Cr	70	76.25	139.5	327.75	1466	1396
Mn	3139	982.75	34.75	59.25	61.25	1138
Co	116	128.825	130.75	139.825	165.5	49.5
Ni	41.9	47.15	55.85	114.15	182.3	140.4
Cu	81.6	4.05	3.6	18.5	98.25	124.4
Zn	523.8	74.725	25.675	24.375	136.325	261.1
Ga	46.06	49.0975	50.04	51.8225	60.52	14.46
Nb	11.19	12.065	14.455	24.02	62.55	51.36
Mo	2.85	4.0625	5.575	9.0325	16.69	13.84
Sn	4.4	4.925	6	15.625	22.8	18.4
La	3.9	10.05	10.95	12.775	16.5	12.6
Ce	8.99	21	23.36	26.89	38.38	29.39
Pr	0.9	2.45	2.7	3.275	4.7	3.8
Nd	2.6	9.675	10.35	12.275	17.6	15
Sm	0.6	1.825	2	2.45	3.8	3.2
Eu	0.2	0.4	0.4	0.575	0.9	0.7
Gd	0.6	1.375	1.8	2.15	3.5	2.9
Dy	0.5	1.125	1.3	1.725	2.7	2.2
Tb	0.1	0.2	0.2	0.3	0.6	0.5
Ho	0.1	0.3	0.3	0.375	0.5	0.4
Er	0.3	0.7	0.75	0.95	1.2	0.9
Tm	0.1	0.1	0.1	0.125	0.2	0.1
Yb	0.4	0.6	0.75	1.075	1.3	0.9

The of both Ti and Al in the magnetite structure shows a positive temperature dependence (Turnock and Eugster, 1962; O'Neill and Navrotsky, 1984). Experimentally-produced magnetite in felsic igneous rock bulk compositions crystallized at temperatures above 700 °C contains greater than 10,000 and 4000 ppm Ti and Al, respectively (Canil et al., 2016). This may attribute to the temperature of magnetite forming at this study because the average of Ti and Al is 42650 and 17900 ppm respectively (Table 1). With increase the Al concentration at magnetite structure begin the magnetite series which will mention at next paragraph. Al shows a negative correlation with Fe (r= -0.82) and Ti (-0.36), but Fe shows a positive correlation with Ti (0.09). Cr and Ni show a positive correlation with Fe (r=0.28 and 0.22 respectively) and a negative correlation with Al (r=-0.25 and

-0.57 respectively). Mg, Mn and Zn show a negative correlation with Fe (r=-0.89, -0.45 and -0.41 respectively) and a positive correlation with Al (r=0.88, 0.28 and 0.67 respectively) (Table 3). This may attribute to there is large verity at magnetite series at the study area; (1) Ulvöspinel (Fe_2TiO_4), Ilmenite ($FeTiO_3$), Chromite ($FeCr_2O_4$) and Trevorite ($NiFe_2O_4$), (2) Gahnite ($ZnAl_2O_4$), spinel ($MgAl_2O_4$) and Galaxite ($MnAl_2O_4$), and (3) not Hercynite ($FeAl_2O_4$), Magnesiochromite ($MgCr_2O_4$), magnesioferrite ($MgFe_2O_4$), Jacobsite ($MnFe_2O_4$) and Franklinite ($ZnFe_2O_4$). Other elements as V, Co, Mo, Nb, Ga, Sn and Ta show a positive correlation with Fe (r=0.61, 0.28, 0.39, 0.02, 0.71, 0.00 and 0.13 respectively) and a negative correlation with Al (r=-0.31, -0.02, -0.33, -0.34, -0.57, -0.21 and -0.45 respectively) (Table 3), this attribute to enrichment of these elements on magnetite series.   Ca, Li, Sc, Cu, As, Rb, Sr, Y, Cd, Sb, Sc, Ba, La, Ce, Pr, Nd, Sm, Eu, Gd, Dy, Ho, Er, Yb, Pb, U and Th show a negative correlation with Fe (r=-0.85, -0.51, -0.87, -0.21, -0.77, -0.65, -0.96, -0.91, -0.50, -0.31, -0.31, -0.16, -0.84, -0.81, -0.82, -0.82, -0.81, -0.90, -0.80, -0.94, -0.78, -0.83, -0.80, -0.66, -0.68 and -0.58 respectively) and a positive correlation with Al (r=0.79, 0.64, 0.93, 0.28, 0.47, 0.67, 0.73, 0.70, 0.88, 0.72, 0.55, 0.35, 0.51, 0.19, 0.73, 0.71, 0.73, 0.74, 0.69, 0.78, 0.72, 0.79, 0.70, 0.76, 0.75, 0.73, 0.81 and 0.63 respectively) (Table 4), this attribute to enrichment of these elements on spinel series. REEs as mentioned at above paragraph show a negative correlated with Fe and a positive correlated with Al, and enriched on spinel series.

CONCLUSION

Magnetite concentrations are increasing in the far north of Taiwan, especially in each of the areas of Wanli, Fengyu, Laomei, White Sand Bay Creek, White Sand Bay beach and Xinzhuangzi, and decreasing toward south and west of the study area Generally, Magnetite concentrations are increase around andesite rocks. Moreover, the compositional average of the studied magnetite beach and river samples is compared with the world's average, and we noted that these samples are significantly similar in Ti, Al, Mg, Sc, V, Cr, Mn, Co, Ga, Nb, Hf and Ni/Cr of magnetite at andesite rocks of Dare et al. (2014), which reveal that these studied magnetite samples may have come from surrounding andesite rocks.The high concentration of Ti and Al at magnetite attribute to the temperature of magnetite forming at this study is 700oC (Canil et al., 2016). With increase the Al concentration at magnetite structure begin the magnetite series.According to Fe positive correlation with Ti, Cr and Ni, and a negative correlation with Mg, Mn and Zn. This may attribute to there is large verity at magnetite series at the study area; (1) Ulvöspinel (Fe_2TiO_4), Ilmenite ($FeTiO_3$), Chromite ($FeCr_2O_4$) and Trevorite ($NiFe_2O_4$), (2) Gahnite ($ZnAl_2O_4$), spinel ($MgAl_2O_4$) and Galaxite ($MnAl_2O_4$), and (3) not Hercynite ($FeAl_2O_4$), Magnesiochromite ($MgCr_2O_4$), magnesioferrite ($MgFe_2O_4$), Jacobsite ($MnFe_2O_4$) and Franklinite ($ZnFe_2O_4$) because Fe show negative correlation with Al.Other elements

as V, Co, Mo, Nb, Ga, Sn and Ta show a positive correlation with Fe and a negative correlation with Al, this attribute to enrichment of these elements on magnetite series. Ca, Li, Sc, Cu, As, Rb, Sr, Y, Cd, Sb, Sc, Ba, La, Ce, Pr, Nd, Sm, Eu, Gd, Dy, Ho, Er, Yb, Pb, U and Th show a negative correlation with Fe and a positive correlation with Al, this attribute to enrichment of these elements on spinel series. REEs as mentioned at above paragraph show a negative correlated with Fe and a positive correlated with Al, and enriched on spinel series.

REFERENCES

Lindsley, D.H. (1976a): Experimental studies of oxide minerals: Reviews in Mineralogy, v. 3, p. L61-L88.

Lindsley, D.H. (1991): Experimental studies of oxide minerals: Reviews in Mineralogy, 25, 69-100.

Ghiorso, M.S., and Sack, O. (1991): Fe-Ti oxide geothermometry: Thermodynamic formulation and the estimation of intensive variables in silicic magmas: Contributions to Mineralogy and Petrology, 108, 485–510.

Rumble, D. (1976): Oxide minerals in metamorphic rocks: Reviews in Mineralogy, 3, R1–R20.

Righter, K., Leeman, W.P., and Hervig, R.L. (2006): Partitioning of Ni, Co and V between spinel-structured oxides and silicate melts: Importance of spinel composition: Chemical Geology, 227, 1–25.

Barnes, S.J., and Roeder, P.L. (2001): The range of spinel composition in terrestrial mafic and ultramafic rocks: Journal of Petrology, 42, 2279–2302.

Ryabchikov, I.D., and Kogarko, L.N. (2006): Magnetite compositions and oxygen fugacities of the Khibina magmatic system: Lithos, 91, 35–45.

Reguir, E.P., Chakhmouradian, A.R., Halden, N.M., and Yang, P. (2008): Early magmatic and reaction-induced trends in magnetite from the carbonatites of Kerimasi, Tanzania: Canadian Mineralogist, 46, 879–900.

Rusk, B., Oliver, N., Brown, A., Lilly, R., and Jungmann, D. (2009): Barren magnetite breccias in the Cloncurry region, Australia; comparisons to IOCG deposits. In: Williams et al. (eds) Smart science for exploration and mining, Proc 10th Biennial Meeting, Townsville, 656–658.

Dupuis, C., and Beaudoin, G. (2011): Discriminant diagrams for iron oxide trace element fingerprinting of mineral deposit types. Miner Deposita, 46, 319–335.

Dare, S.A.S., Barnes, S.-J., Beaudoin, G., Méric, J., Boutroy, E., and Potvin-Doucet, C. (2014): Trace elements in magnetite as petrogenetic indicators. Mineral Deposita, 49, 785–796.

Dare, S.A.S., Barnes, S.J., and Beaudoin, G. (2012): Variation in trace element content of magnetite crystallized from a fractionating sulfide liquid, Sudbury, Canada: implications for provenance discrimination. Geochim. Cosmochim. Acta., 88, 27–50.

Boutroy, E., Dare, S.A.S., Beaudoin, G., Barnes, S.J. and Lightfoot, P.C. (2014): Magnetite composition in Ni-Cu-PGE deposits worldwide and its application to mineral exploration. J. Geochem. Explor. Doi.:10, 1016.

Barnes, S.J., Maier, W.D. and Ashwal, L.D. (2004): Platinum-group element distribution in the Main Zone and Upper Zone of the Bushveld Complex, South Africa. Chem. Geol., 208:293–317

Sawyer, E. (2010): Migmatites formed by water-fluxed partial melting of a leucogranodiorite protolith: microstructures in the residual rocks and source of the fluid. Lithos 116:273-286.

Tollari, N., Barnes, S.J., Cox, R. and Nabil, H. (2008): Trace element concentrations in apatites from

the Sept-Îles Intrusive Suite, Canada implications for the genesis of nelsonites. Chem. Geol., 252:180-190.

Nabil, H. (2003): Genèse des dépôts de Fe-Ti-P associés aux intrusions litées (exemples: l'intrusion mafique de Sept-Iles, au Québec; complexe de Duluth aux États-Unis). Université du Québec à Chicoutimi, pp 537.

Martin-Tanguay, B. (2012): Pétrographie et caractérisation des oxydes de Fe-Ti à Saint-Charles de Bourget (Québec), associé à la suite anorthositique du Lac-Saint-Jean. Université du Québec à Chicoutimi, pp 71.

Méric, J. (2011): Caractérisation géochimiques des magnétites de la zone critique de l intrusion magmatique de Sept-Iles (Québec, Canada) et intégration a une base de données utilisant la signature géochimique des oxydes de fer comme outil d'exploration Université du Québec à Chicoutimi - Université Montpellier 2, pp 48.

Razjigaeva, N.G., and Naumova, V.V. (1992): Trace element composition of detrital magnetite from coastal sediments of Northwestern Japan Sea for provenance study. J. Sed. Petrol, 62,802–809

Grigsby, J.D. (1990): Detrital magnetite as a provenance indicator. J. Sed. Petrol. 60,940–951.

Chiaradia, M., Müntener, O. and Beate, B. (2011): Enriched basaltic andesites from mid-crustal fractional crystallization, recharge, and assimilation (Pilavo Volcano, Western Cordillera of Ecuador). Journal of Petrology, 52: 1107-1141.

Audetat, A. and Pettke, T. (2006): Evolution of a porphyry-Cu mineralized magma system at Santa Rita, New Mexico (USA). Journal of Petrology, 47: 2021-2046.

Buddington, A.F. and Lindsley, D.H. (1964): Iron–titanium oxide minerals and synthetic equivalents. Journal of Petrology, 5:310–357

Sauerzapf, U., Lattard, D., Burchard, M. and Engelmann, R. (2008): The titanomagnetite–ilmenite equilibrium: new experimental data and thermo-oxybarometric application to the crystallization of basic to intermediate rocks. Journal of Petrology, 49:1161–1185.

O'Neill, H.S.C., and Navrotsky, A. (1984): Cation distributions and thermodynamic properties of binary spinel solid solutions. Am. Mineral. 69, 733–753.

Canil, D., Grondahl, C., Lacourse, T., and Pisiak, L.K. (2016): Trace elements in magnetite from porphyry Cu–Mo–Au deposits in British Columbia, Canada. Ore Geology Reviews, 72, 1116-1128.
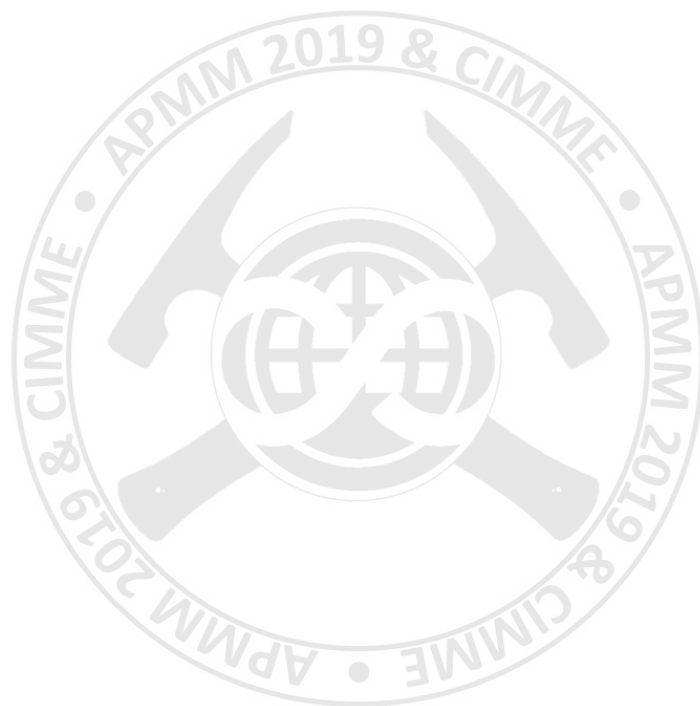
Seismic Lithology Prediction in Depth Domain

Lin, Yi-Wei and Chang, Tzy-Yi

Exploration and Development Research Institute, CPC Company, Taiwan
155829@cpc.com.tw, 155071@ cpc.com.tw

ABSTRACT

A quick technique of seismic lithology prediction has been described by a well and a seismic trace in depth domain. We referred a workflow to the application of this technique in the future. The seismic lithology trend in well location can be predicted adequately in this study. This technique will be applied to 3D seismic data in depth domain for deducing regional seismic lithology distribution in a quick way and is more precise than seismic RMS amplitude attribute, and also, can reduce the risk of hydrocarbon exploration.

INTRODUCTION

Lithology prediction is playing an important role for the primary stage of hydrocarbon exploration. By distinguishing between sandstone and shale, we can evaluate the reservoir rock and seal in a petroleum system to reduce the risk of hydrocarbon exploration.

METHOD

To predict lithology from seismic data, at first, we need to establish the well base relationship between lithology and acoustic impedance (AI). To demonstrate the idea, we use well A data. In the well A, we separate the data into 7 layers: Ko, upper D, lower D, upper K, lower K, upper M, and lower M, and calculate two relationships: AI versus shale volume and AI versus porosity. Fig. 1 shows the results from regression between AI and shale volume of well A in three layers: Ko, Upper D, Lower D. Fig. 2 shows the results between AI and porosity of well A in these layers.

After building up the relationships of the 7 layers, we extract seismic AI from the relative AI seismic cube at the location of well A to estimate lithology. Fig. 3 shows the workflow through which the seismic absolute AI can be built up and be used to estimate lithology. The absolute AI can be separated into high frequency part and low frequency part. (Barclay *et al.*, 2008)

In the high frequency part, the seismic envelope attribute (or instantaneous amplitude) proportional to the AI contrast (SEG wiki) can be calculate as (Ogiesoba and Hammes, 2010)

$$A(d) = (f^2(d) + h^2(d))^{1/2}, \qquad (1)$$

Where f(d) is the amplitude of the real seismic trace, and h(d) is the quadrature expressed by Bracewell (1965) as:

$$h(d) = 1/\pi \, d * f(d) \qquad (2)$$

where * denotes convolution. Amplitude envelope is always positive. To obtain relative AI, mean is removed from seismic envelope.

In low frequency part, the well logging AI is constructed by density and slowness. Through being filtered 1-10 Hz, low frequency AI is obtained. In 2nd pane of Fig. 4, black line is the logging AI and red line is the low frequency AI. The smooth method to gain low frequency AI is also tested, plotted in 4th pane of Fig. 4. By adding relative AI to low frequency AI, one can get absolute AI, plotted in 5th pane of Fig. 4.

To estimate lithology, the relationship between absolute AI and logging AI of each 7 layers should be found in order to mapping the scale of absolute AI to the scale of logging AI. Fig. 5 shows the relationship between absolute AI and logging AI in 3 of the 7 layers. After applying the scale of logging AI, absolute AI becomes pseudo AI. In Fig. 6, from left to right the 1st to 4th pane is the low frequency AI, relative AI, absolute AI, pseudo AI respectively.

After getting pseudo AI, we apply the both relationships between logging AI versus shale volume and logging AI versus porosity to it, and then we get estimated shale volume and estimated porosity. The criterion between sandstone and shale is:

$$\begin{cases} \text{Sandstone,} & \text{shale volume} < 38\%, \qquad (3) \\ \text{Shale} \quad , & \text{shale volume} >= 38\%. \qquad (4) \end{cases}$$

The criterion between tight sand and porous sand is:

$$\begin{cases} \text{Tight sand,} & \text{porosity} < 5\ \%, \qquad (5) \\ \text{Porous sand,} & \text{porosity} >= 5\%. \qquad (6) \end{cases}$$

After applying both criterion to estimated shale volume and estimated porosity, the estimated lithology is obtained. In pane 5th to 7th of Fig. 6 shows the estimated shale volume, estimated porosity and estimated lithology in all 7 layers of the well A. To compare difference of the estimate lithology and logging lithology, pane 8th of Fig. 6 shows the logging lithology and pane 9th shows the difference in red color and the same in white color.

CONCLUSIONS

The estimate lithology shows only the trend (mean) of the logging lithology, but cannot show the detail of the lithology because of the limit of the resolution of seismic data. The seismic lithology trend in well location can be predicted adequately in this study. This technique will be applied to 3D seismic data in depth domain for regional seismic lithology distribution in a quick way and more precise than seismic RMS amplitude attribute, and also, can reduce the risk of hydrocarbon exploration.
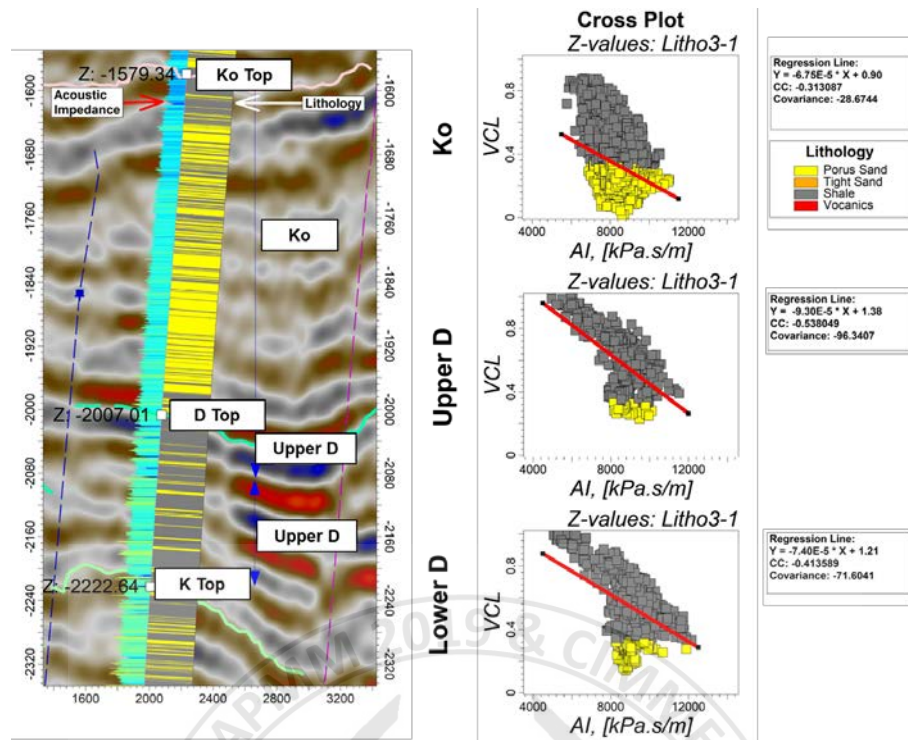
Figure 1. The regression relationship between logging AI and shale volume in Ko, Upper D and Lower D, respectivly in Well A.
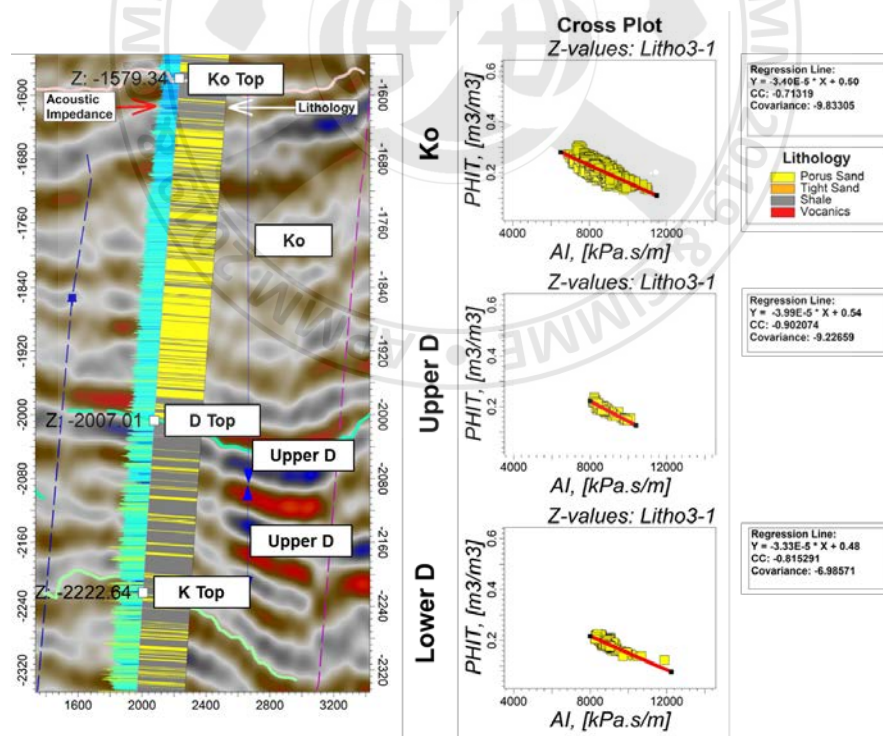

Figure 2. The regression relationship between logging AI and porosity in Ko, Upper D and Lower D, respectivly in Well A.
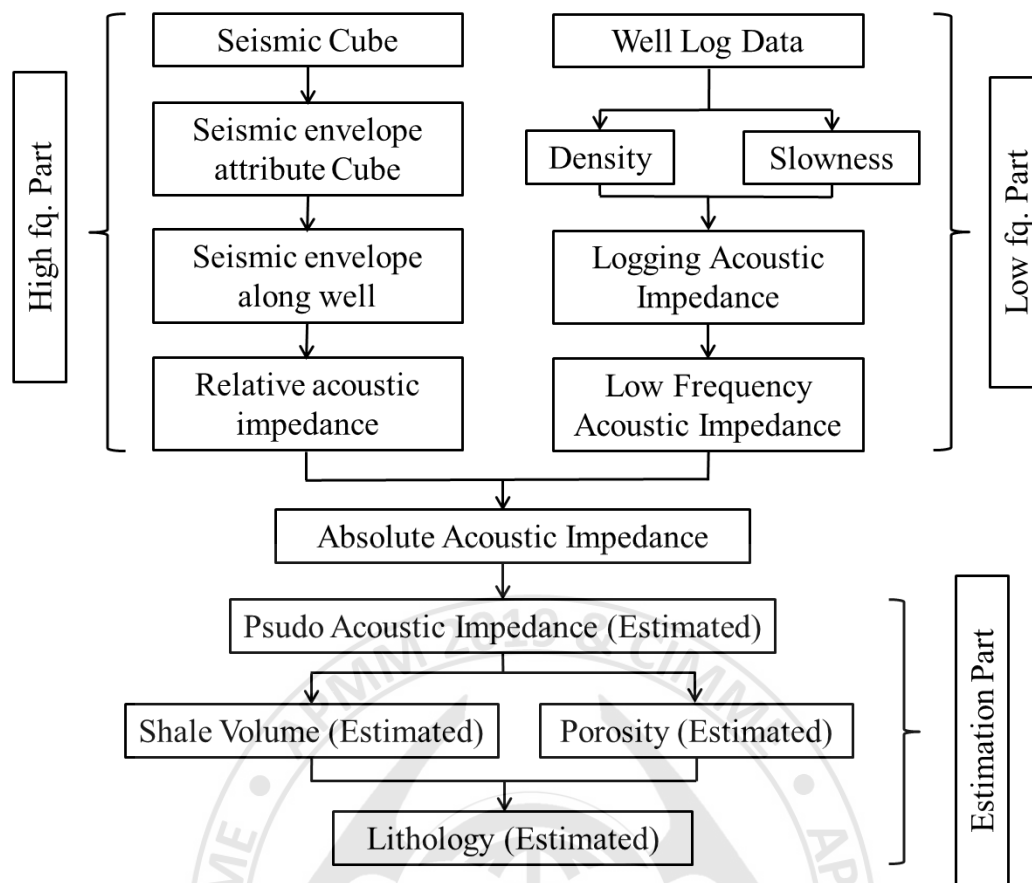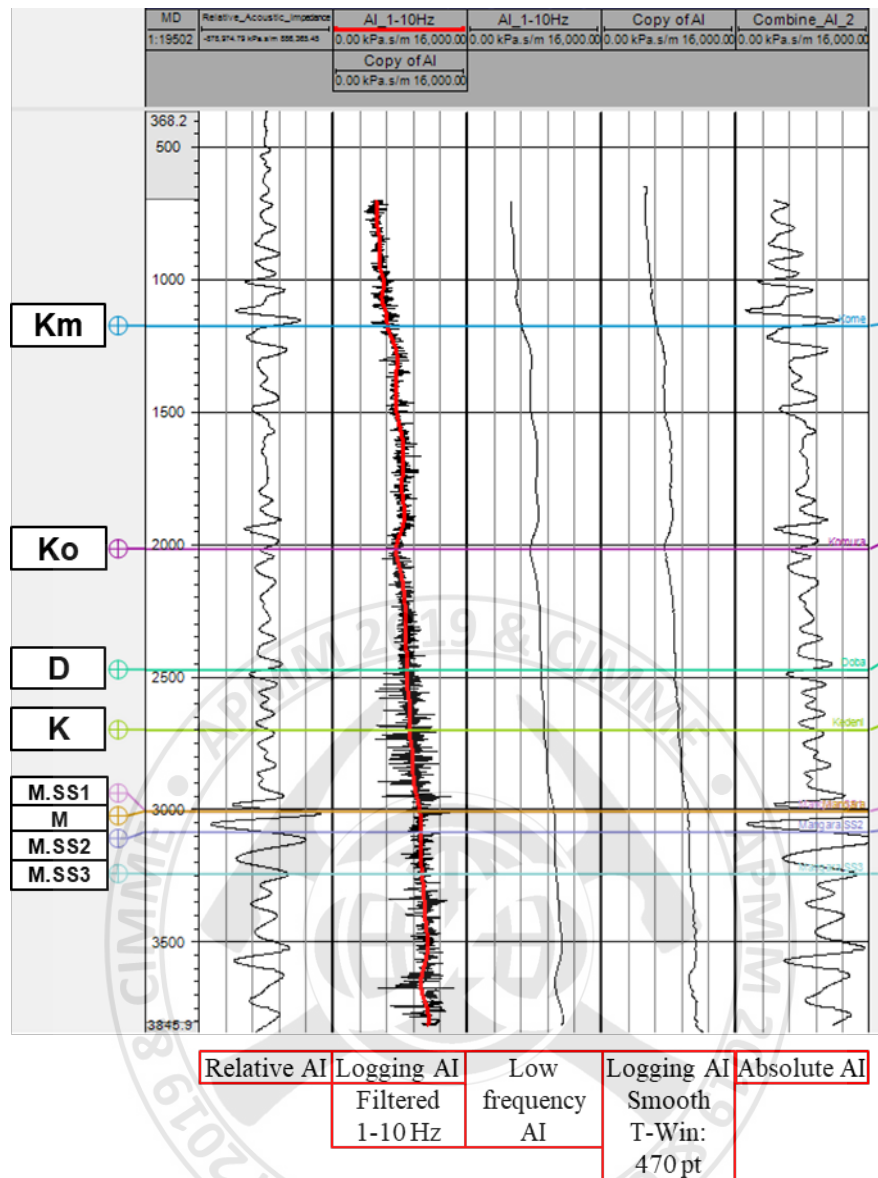
Figure 3. Seismic lithology prediction flow chart

Figure 4. Logging profile from left to right respectively: relative AI, logging AI, filtered AI, smoothed AI, and absolute AI.
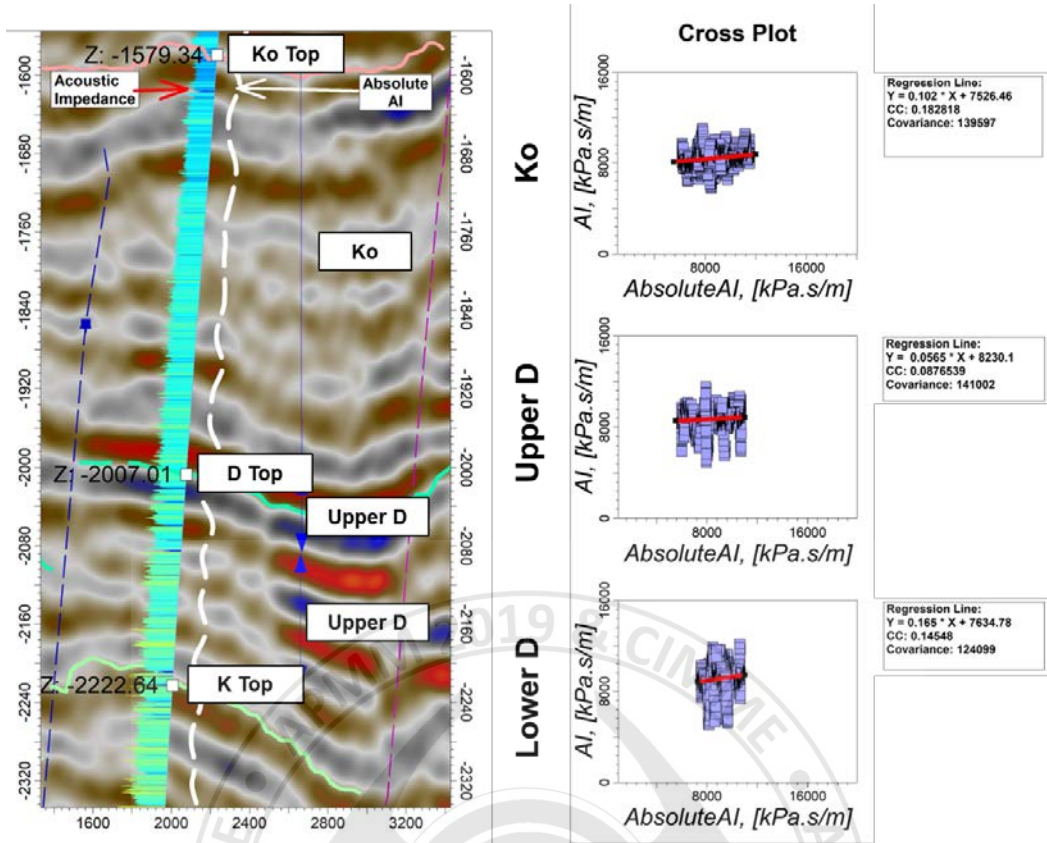
Figure 5. The regression relationship between absolute AI and logging AI in Ko, Upper D and Lower D, respectivly in Well A
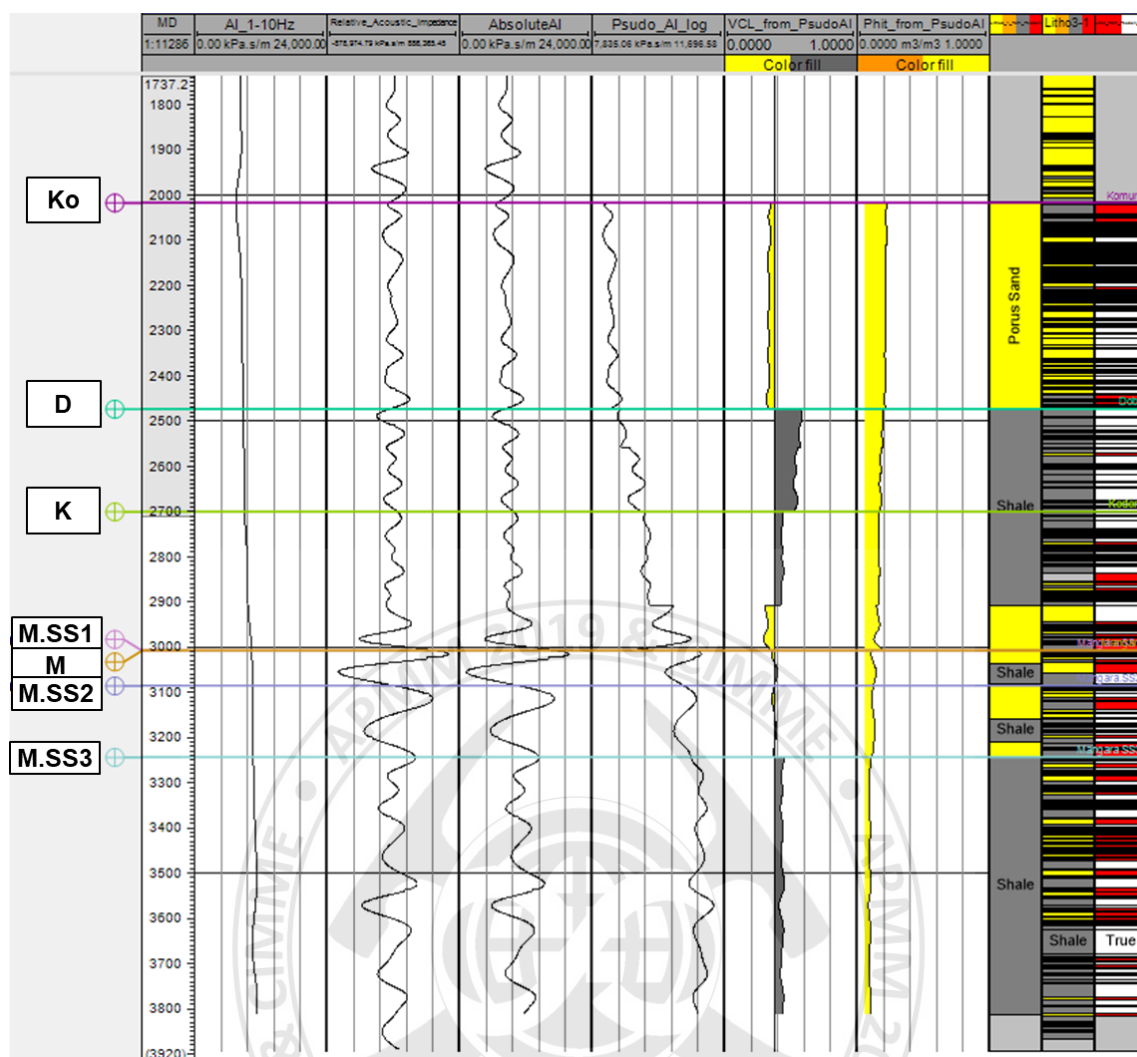
Figure 6. Logging profile from left to right respectively: low frequency AI, relative AI, absolute AI, psudo AI, shale volume estimated, porosity estimated, lithology estimated, logging lithology and matching,

REFERENCES

Barclay, F., Bruun, A., Rasmussen, K. B., Alfaro, J. C., Cooke, A., Cooke, D., ... & Özdemir, H. (2008). Seismic inversion: Reading between the lines. Oilfield Review, 20(1), 42-63.

Bracewell, R.N. (1965). "The Fourier Transform and Its Applications" McGraw-Hill, New York, 386 p.

Ogiesoba, O. and Hammes, U. (2010). "Understanding Lithologic Significance of Amplitude Envelope and Acoustic Impedance within Oligocene and Miocene Strata, South Texas Gulf Coast" AAPG Annual Convention and Exhibition, New Orleans, Louisiana, April 11-14, 2010

SEG wiki, SegDictionary:Trace envelope, https://wiki.seg.org/wiki/Dictionary:Trace_envelope

法興耐火材料

World leader in monolithic refractories 不定型耐火材料界的世界領先者

Calderys 法興耐火材料提供了廣泛性能卓越的一系列產品和解決方案。

我們的服務包括：各工業所使用的不定型耐火材料產品，及其選用、設計、施工與售後服務等。

集團客戶遍及 100 多個國家，我們不斷的創新來自於 33 個國家地區的專業人員，3 個研發中心和 11 個設計與工程中心。

法興耐火材料工業股份有限公司

屏東縣高樹鄉新南村興店路 6-6 號

Tel：(886) 8 7965562-4   Fax：(886) 8 7965816

Email：Taiwan@calderys.com   Website：www.calderys.com

元鼎耐火

鋼鐵、銅鋁、高溫窯爐、冶金業的最佳夥伴

耐火材料製造與各類窯爐之設計、施工

可鑄性耐火材料・振鑄性耐火材料・可塑性耐火材料・可鍛性耐火材料
輕質隔熱耐火材・高溫粘劑以及其他特殊不定形耐火材料
各式不定型耐火預鑄塊・高溫窯爐之設計與施工
ISO 9001:2015品質保證

元鼎耐火工業有限公司　GOOD FURNACE REFRACTORY IND. CO., LTD.
TEL：02-26223681　　FAX：02-26233630　EMAIL：GoodFurnace@gmail.com

光 和 耐 火 公 司
Kuan-Ho Refractories Industry Corporation

- 1973 年創立，台泥企業團成員，品質至上經營理念。
- 1976 年與日本品川白煉瓦株式會社技術合作，包含鋼鐵、水泥、玻璃…等工業窯爐所需之技術。
- 1991 年與德國技術合作，生產水泥旋窯用鎂鉻磚及尖晶石磚。
- 2005 年中華徵信所評為台灣耐火材料業 No.1。
- 1850℃超高溫隧道窯，先進精密研究儀器，開發各項新技術。
- 各種工業窯爐耐火材料設計、施工及維修等全面性服務。
- 外銷地區：日本、南非、中國、印度、韓國及其他地區。

一、主要產品：
1. 超高溫燒成直接鍵結式鎂鉻磚、鎂磚、尖晶石磚、鋼玉磚。
2. 高溫燒成鎂鉻磚、鎂磚、鉻磚。
3. 黏土磚、高鋁磚、謨萊石磚、鋯磚、鋁鉻磚、腊石磚。
4. 碳化矽磚、耐酸磚。
5. 鎂碳磚、鋁鎂碳磚、鋁碳磚、鋁矽碳磚。
6. 澆注材、乾濕式吹付材、塗附材、可鑄性、可塑性、搗固材、耐火泥等不定型耐火材料。

二、窯爐耐火材料：
1. 水泥廠：預熱機、旋窯、冷卻機等耐火材料。
2. 鋼鐵廠：高爐、熱風爐、煉焦爐、魚雷車、混鐵爐、轉爐、電弧爐、精煉爐、RH真空脫氣爐、加熱爐、熔解爐及石灰窯爐用耐火材料。
3. 汽電共生爐用耐火材料。
4. 焚化爐用耐火材料。
5. 煉銅、煉鋁等高溫爐用耐火材料。
6. 化工、玻璃、窯業…等高溫爐用耐火材料。

三、各式窯爐設計、檢修、爐襯預鑄成型、築爐工程承包、耐火材料技術服務。

公司:苗栗縣頭份市尖豐路 932 號　　　　　　高雄辦事處：
　　TEL：037-542873-7　　　　　　　　　　　TEL：07-8053758-9
　　FAX：037-541574　　　　　　　　　　　　FAX：07-8053703
　　E-mail:krics@kric.com.tw　　　　　　　http://www.kric.com.tw
　　業務部分機：32　　築爐部分機：57
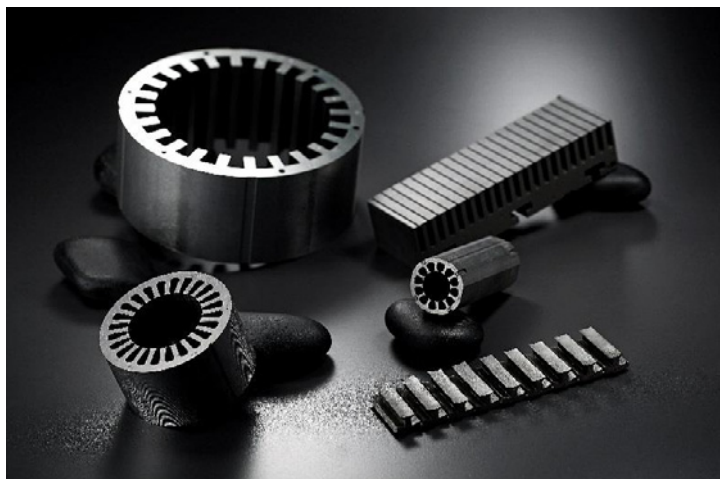
馬達鐵芯 　·　 轉子鑄鋁 　·　 模具設計

展開式
馬達鐵芯

線性
馬達鐵芯
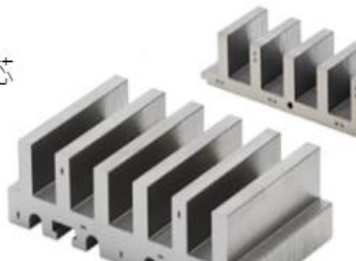
感應式
馬達鐵芯

直流無刷
馬達鐵芯

步進
馬達鐵芯

三件式感應
馬達鐵芯

蔽極式
馬達鐵芯

串激式
馬達鐵芯

特殊
馬達鐵芯

ISO 9001　ATS　REACH　RoHS　CO2　HEMA　IE3 Motor 高效率馬達聯盟

International Competitiveness

Complete career planning

Professional teachers

Department of Resources Engineering

- The Department of Resources Engineering at National Cheng-Kung University was established to address the demand for the exploitation, utilization, reclamation, management and treatment of various resources.
- The Department is the only institution in Taiwan offering advanced education in resources engineering, including minerals, energy, soil and water resources.
- The breadth of training that the Department affords resource engineers permits entry into many exciting new fields of endeavor.

Our Main Work

Training talent & Innovative research

The Department offers a four-year program leading to a B.S. degree. Advanced study may then be pursued, if desired, to achieve a M.S. or Ph. D. degree. The Department offers an integrated system for advanced education and research in resources engineering.

Research focus

- Resources development & Geological engineering
- Mineral science & Engineering
- Resource Management & Economics

Research center

- Satellite geoinformation research Center
- Georesource research center
- Petroleum strategy research center
- Nano Powder Research Center

Scholarships Information

Scholarship time frame

- Undergraduate degree students : Four year limit
- Master's degree students : Two year limit
- PhD students are limited to four years, and master's degree students who are also doing their PhD degrees are limited to five years.

Award amount

- Undergraduate degree students : the top 20% may be granted twelve months of living expenses, each monthly stipend totaling NTD 15,000; the next 20% (i.e., 20.01% to 40%) may be granted twelve months of living expenses, each monthly stipend totaling NTD 10,000.
- Master's degree students : Each applicant may receive twelve months of living expenses limited to at most NTD 8,000 a month, as well as a waiver for tuition and course credit fees.
- PhD Student : Each applicant may receive twelve months of living expenses as well as having their school fees and course credit fees waived; the maximum amount of living expenses awarded shall not exceed NTD 15,000.

Undergraduate & M.S. students

PhD students

NCKU
National Cheng Kung University

2019 CIMME Annual Convention

Assembly Date: November 19th~20th 2019 / Place: Tainan

2019 Nov. 17 – 20

International Conference on Asia Pacific Mining and Metallurgy

Call for Papers

General Information

The first International Conference on Asia Pacific Mining and Metallurgy (APMM 2019) is an international platform for scholars, researchers and participants to share and discuss interdisciplinary research and findings in the engineering fields of mining and metallurgy. APMM 2019 will take place in Tainan, Taiwan from 17-20 November, 2019.

Innovation study, full research paper, work-in-progress report and long abstract are welcomed. Abstracts and full manuscripts should conform to the required format and be uploaded on the website. Audiences are welcomed to join the conference for research exchanging and opinions discussion.

Topics

1. Geo-resource Exploration
- Geology
- Geophysical Methods and Application
- Geochemical Methods and Application
- Remote Sensing

2. Geo-resource Exploitation
- Petroleum and Gas
- Geothermal and Gas Hydrate
- Underground Storage
- Mining and Safety

3. Metallurgical Engineering
- Design of Metallic Materials
- Metal Making, Refining, and Casting
- Metal Forming Processes
- Process and Equipment Development

4. Material Science
- Structural and Functional Materials
- Nanotechnology and Nanomaterials
- Energy materials

5. Circular Economy and Sustainable Resources
- Energy Transformation
- Carbon Dioxide Reduction
- Recycle and Urban Mining
- Mineral Processing
- Geopolymer and New Sustainable Materials

Keynote Speaker

Prof. Peng, Syd S.
West Virginia Uni., USA

Prof. Yeh, Jien-Wei
Tsing Hua Uni., Taiwan

Prof. Kitamura, S.
Tohoku Uni., Japan

Dr. Tsai, Hwan-Tang
Arcelor Mittal USA

Prof. Takeshi, T.
Kyushu Uni., Japan

Important Dates

Submission Deadline	June 15
Notification of Acceptance	July 15
Early Bird Registration & Payment Deadline	September 5
Conference Date	November 17

Conference Venue

International Conference Hall National Cheng Kung University, Tainan, Taiwan
Address: 1 University Road, Tainan, Taiwan

Sponsored by

MOST 科技部 Ministry of Science and Technology · CIMME · National Cheng Kung University · TAIPEI TECH

Endorsed by

Taiwan Ceramic Society · The Society of Powder Technology, Japan · kpmi Korean Powder Metallurgy Institute · T.A.C.T. · MRS-T · VSP Vacuum Society of the Philippines · Slovak Silicate Scientific-Technological Society

Contact Us Bieng-Zih Hsieh, Ph.D. Email: APMM2019@cimme.org.tw Website : http://apmm2019.cimme.org.tw/

Sponsored and Endorsed by: